Aston University

Some pages of this thesis may have been removed for copyright restrictions.

If you have discovered material in Aston Research Explorer which is unlawful e.g. breaches copyright, (either yours or that of a third party) or any other law, including but not limited to those relating to patent, trademark, confidentiality, data protection, obscenity, defamation, libel, then please read our Takedown policy and contact the service immediately (openaccess@aston.ac.uk)

FRACTURE TOUGHNESS OF A SERIES OF HIGH CHROMIUM ABRASION RESISTANT ALLOYS.

RAYMOND WILLIAM DURMAN.

Ph.D. THESIS.

UNIVERSITY OF ASTON IN BIRMINGHAM.

AUGUST 1970.

SUMMARY.

The fracture properties of a series of alloys containing 15% chromium and 0.8 to 3.4% carbon are investigated using plane strain fracture toughness testing techniques. The object of the work is to apply a quantitative method of measuring toughness to abrasion resistant materials, which have previously been assessed on an empirical basis; and to examine the relationship between microstructure and K_{1c} in an attempt to improve the toughness of inherently brittle materials.

A review of the relevant literature includes discussion of the background to the alloy series under investigation, a survey of the development of fracture mechanics and the emergence of K_{1c} as a toughness parameter.

Metallurgical variables such as composition, heat treatment, grain size, and hot working are used to relate microstructure to toughness, and fractographic evidence is used to substantiate the findings. The results are applied to a model correlating ductile fracture with plastic strain instability, and the nucleation of voids. Strain induced martensite formation in austenitic structures is analysed in terms of the plastic energy dissipation mechanisms operating at the crack tip.

Emphasis is placed on the lower carbon alloys in the series, and a composition put forward to optimise wear resistance and toughness. The properties of established competitive materials are compared to the proposed alloy on a toughness and cost basis.

CONTENTS.

NOTATION.

a	=	Crack half length	Of Fracture Toughness Specimen.
B	=	Thickness	
W	=	Width	
$2H$	=	Height	

σ = General tensile stress symbol - specified by subscript.

σ_{ys} = Uniaxial yield stress.

τ = General shear stress symbol.

ε = Strain.

n = Work hardening coefficient.

E = Young's modulus.

G = Shear modulus.

x, y, z = Three dimensional direction symbols.

r, θ = Crack tip co-ordinates.

r_y = Radius of plastic zone.

v = Poissons Ratio.

ρ = Notch root radius.

δ = Crack opening displacement.

d = Grain size.

G = Strain energy release rate.

K = Stress intensity factor

AC = As Cast.

CC = Chill Cast.

SC = Sand Cast.

Sill = Cast in Silliminite.

HT = Hardened 975°C oil quenched.
Tempered 250°C 2 hours.

H = Homogenised 1150°C 8 hours.

F = Forged.

( ) = Numbers in parentheses refer to the Bibliography.

Additional Notation.

γ = Surface energy for unit increase in crack length.

c = Crack half length, (alternative to a).

f = Volume fraction.

σ_{app} = Applied stress.

σ_{eff} = Effective stress.

1. INTRODUCTION.

A problem often facing the supplier of abrasion resistant components for the grinding, crushing, and mineral handling industries, is how to combine optimum wear resistance with adequate toughness to resist the severe impact conditions frequently encountered. An assurance of freedom from premature failure is vital, since this can be costly, not only in replacements and repairs, but mainly in lost production during unscheduled shutdowns. Wear rate, in general a function of hardness, is a key factor in the economic working of pulverising plant and is of primary importance in instances where contamination of the product is undesirable. Thus it is a compromise between directly conflicting properties, hardness and toughness, which is required in parts such as mill liners, grinding media, crushing hammers and rolls etc., used in ore grinding, cement, coal and iron making processes.

Complexity of shape and the nature of alloys used in these applications restricts the mode of manufacture mainly to casting and forging, with little or no subsequent machining. The recent trend to the use of larger and more powerful plant has emphasized the need for improved fracture resistance, and careful selection of materials used in the more onerous conditions now prevailing.

An extensive range of ferrous alloys find application depending on the stress level of the wear process, from manganese steel, under the most severe shock loading, to high carbon white cast irons when impact resistance is of little consequence. However, it is the field between these two extremes which poses the greatest challenge to the material technologist. Here the widely used Hadfield type of austenitic steel is largely being displaced by the more abrasion resistant martensitic cast steels or alloyed white cast irons. The combination of relatively good abrasion resistance with better ductility than the white irons could make a new austenitic steel widely acceptable for many types of service. The object of this project is the examination of such an alloy with chromium as the main alloying element.

Experience in the field of wear testing has shown that this is a property best measured in production trials, laboratory tests rarely being able to adequately simulate process conditions. Progress in this aspect has led to reliable classification of many types of alloys in terms of wear rate. The problem of fracture, however, appears to have been somewhat neglected. Arbitrary measurements of toughness are made from observations during wear testing programmes, and some impact testing is carried out, but no quantitative data is available. An investigation of the fracture properties of a series of alloys, with particular emphasis on an austenitic chromium alloy was therefore considered worthwhile.

Previous work on the impact testing of abrasion resistant alloys served to illustrate the empirical nature and basic weaknesses of this method of assessment of toughness. The low fracture energy requirements of relatively brittle materials often necessitates the use of non-standard impact specimens, so eliminating any relationship to results from other sources, since there is no correlation between the impact strength of specimen and other section sizes. Also, poor sensitivity and lack of reproducibility are common features of impact testing, due mainly to the measurement of both the nucleation and propagation energy associated with cracking.

It was decided therefore, to adopt fracture mechanics as the testing technique since it reflects a combination of yield strength, work hardening rate, ductility, and is a property quite sensitive to metallurgical variations. Particular attention has been paid to the volume fraction, size, and distribution of carbides, and to the relationship between fracture toughness and microstructural variations motivated by compositional, heat treatment, solidification rate and hot working programmes.

2. CHARACTERISTICS OF ABRASION RESISTANT MATERIALS.

2.1. Types of Wear.

The rate of metal removal and the degree of impact involved in earthmoving, mineral handling, crushing and grinding plant, characterises the type of wear in a given process. Avery(1) has classified wear into three broad categories;

1. Gouging or grooving wear - in which coarse abrasive particles penetrate the working surfaces. In addition to a high rate of metal removal this type of wear is often associated with severe shock loading, as for example in earthmoving plant, hammer mill heads, jaw crushers etc.

2. High stress abrasion - where abrasive particles are crushed under the grinding influence of moving metal surfaces. In this wear process the level of stress involved is significant in governing the choice of material, and the performance of a given material for applications such as grinding media, mill liners, crushing discs and rolls.

3. Low stress scratching abrasion or erosion - predominant in abrasive handling plant such as hydro-cyclones, classifiers etc., where conditions are such that stresses are insufficient to cause penetration of the working surface or crushing of the abrasive.

The hardness of a metal can be considered as its resistance to penetration and for most wear processes, wear rate can be directly related to hardness. Exceptions occur in cases where corrosive media are being handled, when corrosion resistance can be as important as abrasion resistance. Microstructure is also a dominant factor influencing wear resistance.

In the first class of wear, the conventional choice is Hadfields 12% manganese steel. A low yield point (50,000ksi) leads to high plasticity and toughness, whilst the ability to work harden in service from an initial hardness of about 200 H_V up to 450-500 H_V on working surfaces imparts a fair degree of wear resistance. Up to 3% additions of nickel, chromium, molybdenum and tungsten increase the wear resistance and yield strength in cases where toughness can be sacrificed to a certain extent.(2) Whilst its resistance to fracture in the most severe conditions is excellent, the use of manganese steel in many applications is limited by 'spreading' due to the low yield properties. This can lead to bowing and distortion of working parts resulting in failure of holding bolts and operational difficulties in replacing worn components.

The second category of wear includes a wide range of pulverising processes, typified by the action in a ball mill, shown in fig. 2.1. Characteristic failures in liners and diaphragm plates from this type of plant are illustrated in fig. 2.2. A variety of materials have found application in this field although in many instances it is the need for adequate toughness to resist the impact forces involved that limits the maximum hardness of alloy to be employed. Choice of alloy for a given application can be influenced by several factors such as the replacement cost and availability of material, and the importance of contamination of the product. For instance the abraded metal particles may cause discoloration of paint, ceramic, and pottery pigments, or be poisonous in the preparation of foodstuffs. Further it may be detrimental in subsequent production processes such as flotation separations, where it may act as a depressant.(3.4) Thus the use of expensive abrasion resistant materials with very low wear rates is frequently justified.

Cast martensitic white irons of the Ni-Hard and Eutectic Ni-Hard types and Cr/Mo pearlitic and martensitic steels are to some extent being superceded in ball milling and similar operations by heat treated

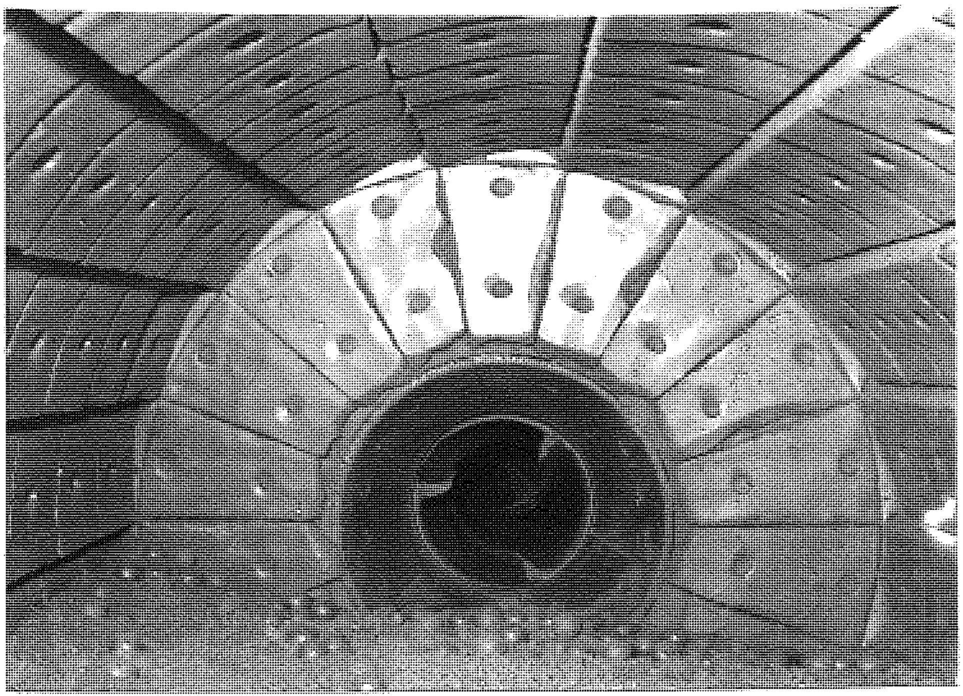

(a) View of Mineral Inlet Chute.

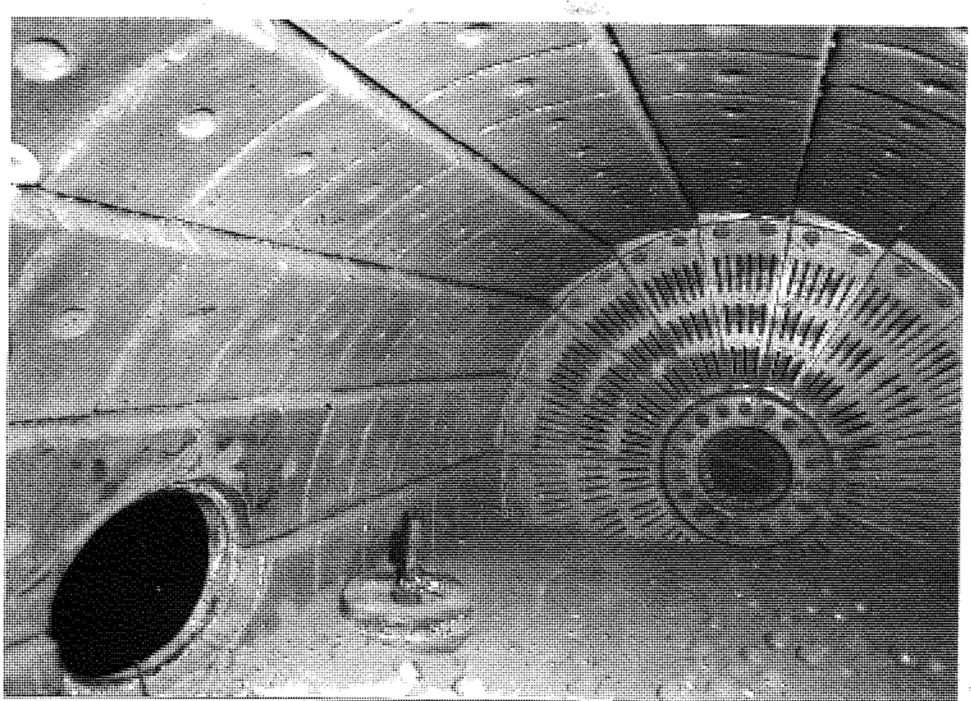

(b) Discharge Section, showing Screening Diaphragm.

Fig. 2.1. Typical Ball Mill, Grinding Cement Clinker, Internal Diameter 8 feet.

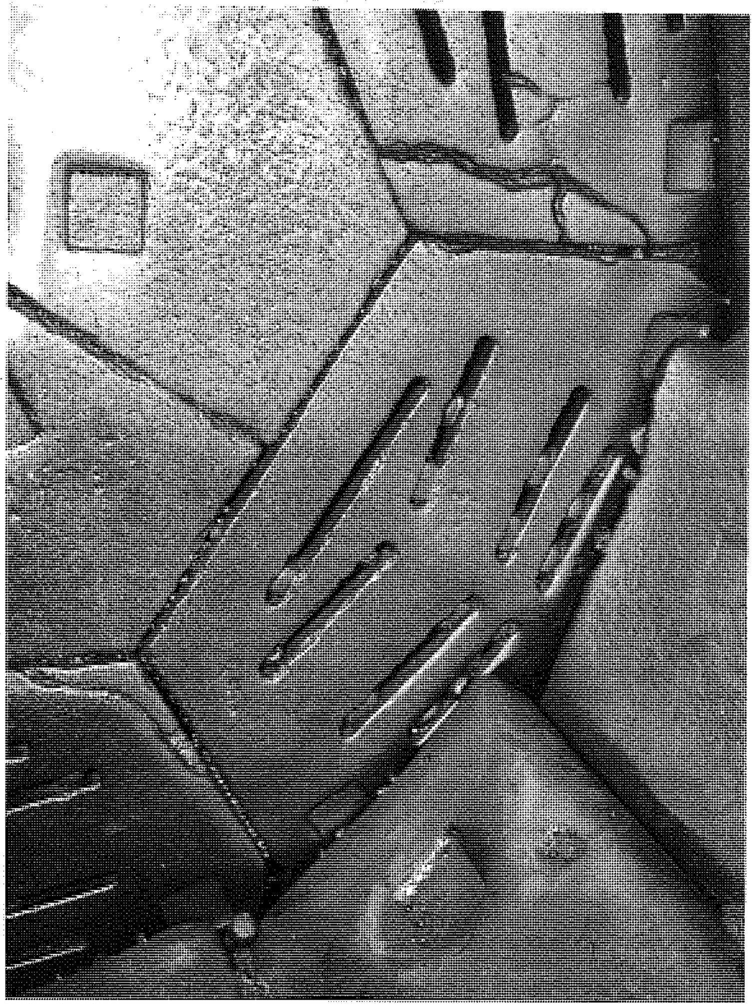

(a) Cracking in Diaphragm Plates.

(b) Fracture of Tapered Lining Plates.

Fig. 2.2. Characteristic Failures Encountered During Grinding.

martensitic and high chromium white irons. The high chromium irons covered by A.S.T.M. specification No. A 532 Type 3, containing 2.3 - 3.0% C. and 24 - 28% Cr are discussed by Dodd and Jackson,(5) and provide a convenient double approach to the problem of high stress abrasion. When cast under appropriate conditions a tough austenitic matrix can be retained at room temperature, which will work harden in service, forming a self-replacing hard surface on a comparatively soft core. In applications where insufficient metal to metal contact occurs for work hardening to take place, the high chromium irons can be heat treated, and the austenitic matrix transformed to a harder martensitic one. The fact that chromium is relatively cheap, especially in the form of high carbon ferro-chrome used in the production of these irons, means that they are no more expensive than the nickel bearing Ni-Hard types.

For the erosive type of wear when fracture resistance is unimportant, hardness is the main criterion in material selection. Martensitic materials, particularly high carbon martensitic white cast irons, are generally used, although when corrosion resistance is of consequence, high chromium irons are preferred.

Norman(6) has shown that providing fracture does not occur in service, the order of ranking of wear rate for various alloys remains unaltered when grinding different minerals, but as the abrasive conditions become more severe, the range of wear rates becomes smaller, see fig. 2.3. Thus in conditions of severe abrasion, in wet milling or the crushing of hard minerals, where wear resistance of all alloys nears a par, fracture resistance can be the controlling factor in selection of material.

The recent trend toward larger plant capable of higher output has resulted in more onerous impact conditions. In special applications where fracture in service may have disastrous consequences, high chromium irons have been reinforced with cast in high tensile steel bars. When

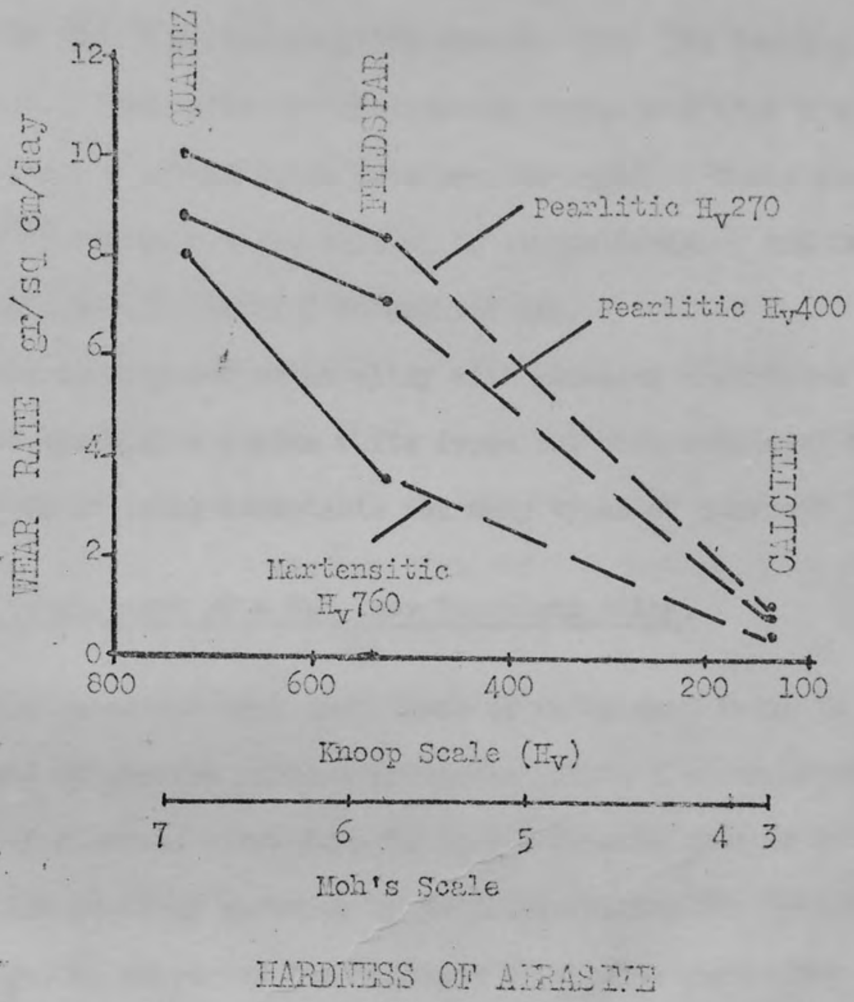

Fig. 2.3. Influence of Hardness of Abrasive Mineral on the Wear Rate of 0.8% C steel Grinding Balls at Three Hardness Levels. (After Norman(6))

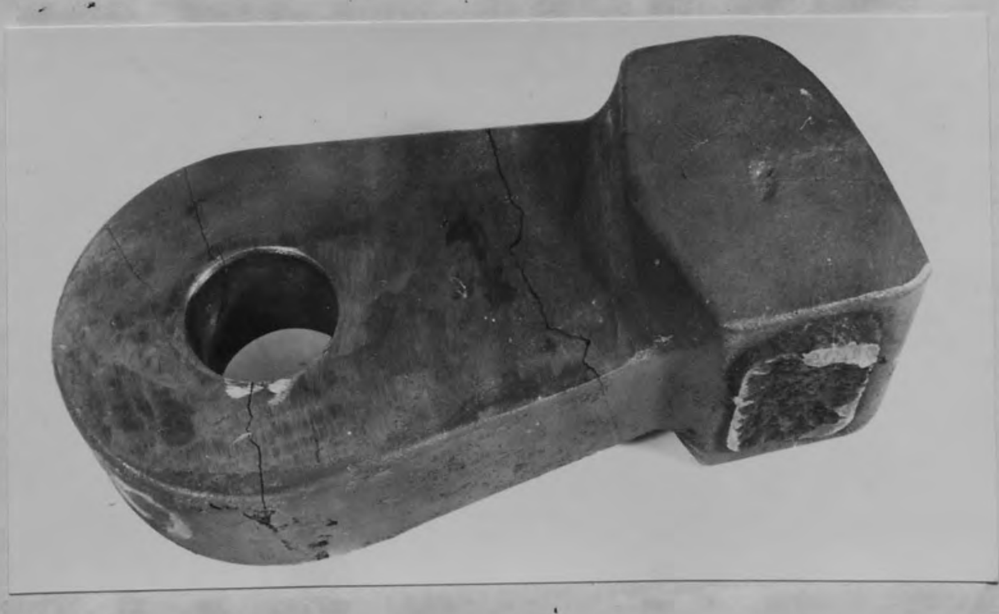

Fig. 2.4. Broken Reinforced Hammer Head.

fracture occurs the component is held together by the reinforcing, as shown in fig. 2.4, but complete success with this technique has not been attained. More recently martensitic white iron/mild steel laminates with a vacuum brazed joint have been employed. These are discussed by Kempe,(7) but as yet are limited to simple designs, and fabrication costs might well restrict widespread use.

The development of an alloy with abrasion resistance comparable to that of the high chromium white irons but with increased toughness could result in it being acceptable for many types of service.

2.2. Development of a New Wear Resistant Alloy.

The excellent wear resistance of white cast irons is imparted by the presence of massive carbide particles within the microstructure, and alloying elements contribute to this characteristic in two ways. Formation of alloy carbides by partition of carbide forming elements such as chromium, increases the hardness of carbide particles. The significance of this, however, is considered to be marginal since although the hardness of carbides may be increased from about 1200 H_V up to 1700 H_V by alloying, this is over twice the hardness of quartz (about 800 H_V) one of the most severe abrasives. It is the effect of alloying additions on the matrix which probably contributes most to wear resistance. Increasing hardenability and the formation of a hard martensitic matrix is the obvious trend in this direction, but this results in a very brittle product unless heavy tempering or very lengthy and expensive heat treatments are employed. Retention of an austenitic matrix, as in the as cast high chromium alloys, however, provides an alternative approach.

The meta-stable austenitic matrix is capable of work hardening, when operational conditions provide sufficient impact for surface deformation to occur, from an initial hardness of 400 - 500 H_V to over 1100 H_V. The depth of the work hardened layer can extend up to five mm. but, as in the work hardening of manganese steel, there is controversy over the mechanism. Most views favour either the formation of martensite or stacking fault production in the austenite. White[8] has been unable to detect martensite in deformed manganese steel, between -196 and 400°C, and suggests that it has no part in the work hardening theory of this material. Norman[6] has reported increased magnetic response in austenitic alloy grinding balls after service, indicating a martensitic transformation, although this was not confirmed. Dodd and Jackson[5] have shown that in high chromium irons deformation does not produce a magnetic change, but qualify this by pointing out that the deformation martensite of stainless steels is frequently non-magnetic.

Investigating the wear characteristics of some austenitic alloys Norman[6] has found that increasing manganese above the amount necessary to produce a fully austenitic matrix reduces the wear resistance considerably. Nickel apparently has a similar effect to manganese in reducing resistance to abrasion, although available information appears to have been obscured to a certain extent by other alloys. Chromium, however, when present in solid solution form in the austenitic matrix, resulted in a marked increase in wear resistance.

No direct evidence of the effect of copper, molybdenum or cobalt on wear properties is available, although molybdenum is a common addition to chromium irons since it suppresses pearlite formation, and has no obvious detremental effect on wear.

The presence of a network of carbides throughout the microstructure of white cast irons is an embrittling influence. Attempts to modify the morphology of carbides to isolated particles with the use of alloys, analogous to the modifications produced in spheroidal graphite cast irons, have so far proved negative. Heat treatment to spherodise the carbides have not been pursued commercially due to the high temperatures required to effect solution of the alloy carbides.

These considerations led to the instigation of the development of a

15% chromium alloy with a carbon content of between 1 - 2.5%. As martensitic alloys with complex heat treatments and molybdenum additions, this series of alloys is now competing favourably with the austenitic high chromium irons. Optimum carbon content for the austenitic version of the alloy has yet to be determined in order to combine high toughness with adequate wear resistance.

The fracture properties of this 15% chromium series of alloys has been investigated in both austenitic and martensitic conditions with carbon contents ranging from 0.8% to over 3%. Thus a discontinuous, semi-continuous and continuous carbide network has been examined. High temperature heat treatment has been carried out in an attempt to spherodise the carbides and the effects on fracture toughness observed. The grain size and toughness of cast irons is substantially influenced by solidification rate, and the influence of this variable has been investigated over a wide range, from chill casting in thin sections, to sand casting in thick sections. The effects of forging on a low carbon alloy in the series, with particular attention to directionality, have also been examined.

In austenitic alloys the work hardening mechanism has been studied, and in alloys having a less stable matrix composition a strain induced transformation detected. The effect of this transformation has been related to toughness in terms of the contribution to fracture energy requirements. The fracture micro-mechanism of austenitic and martensitic alloys has been examined fractographically and correlation between work hardening rate, carbide spacing and toughness determined on the basis of a recent fracture model.

2.3. The Iron - Chromium - Carbon System.

Literature on the liquidus surface of the iron-chromium-carbon system is fairly extensive, but there is only limited conflicting reference to vertical sections below the solidus. Early studies were made by Murakami et. al.[9] and Kinzel and Franks,[10] and the system has subsequently been reinvestigated by Bungardt et. al.[11] The shape of the relevant portion of the liquidus surface is shown in fig. 2.5. and solidification of the alloy series under investigation occurs within the austenite loop as indicated. Alloys of hypoeutectic carbon content solidify as austenite surrounded by the hexagonal chromium carbide Cr_7C_3. Bungardt et. al. suggest that the carbides are produced as a result of a peritectic reaction, but recent work by Griffing et. al.[12] and Jackson[13] has invalidated this aspect of Büngardt's work. It is now thought that the carbides are formed, together with further austenite by a eutectic reaction, and the modified vertical sections by Jackson using this approach are certainly more useful in the interpretation of many of the microstructures examined during the course of this project, see fig. 2.5.(b).

Under equilibrium conditions, and in the absence of other alloys, the high temperature austenite transforms by a peritectoid reaction, at 795°C, to soft ferrite, and the less corrosion resistant chromium carbide, $Cr_{23}C_6$, appears within the microstructure. The product of this reaction is an irresolvable granular pearlite. Balance of the ferrite and austenite stabilising elements, by the addition of small quantities (up to 1½%) of manganese or nickel, and the control of silicon and aluminium content, enables the tough austenite to be retained in the meta-stable state to room temperature. Further, it has been shown in high chromium irons[5] that the extremely brittle iron carbide, Fe_3C, is eliminated from the structure and the appearance of $Cr_{23}C_6$ can be suppressed. This is an important factor when high chromium irons are used in the as cast condition, since the wear rate of pearlitic structures can be up to four times faster than austenitic structures of similar carbon content.[14]

It is quite apparent that the composition of dendritic austenite will

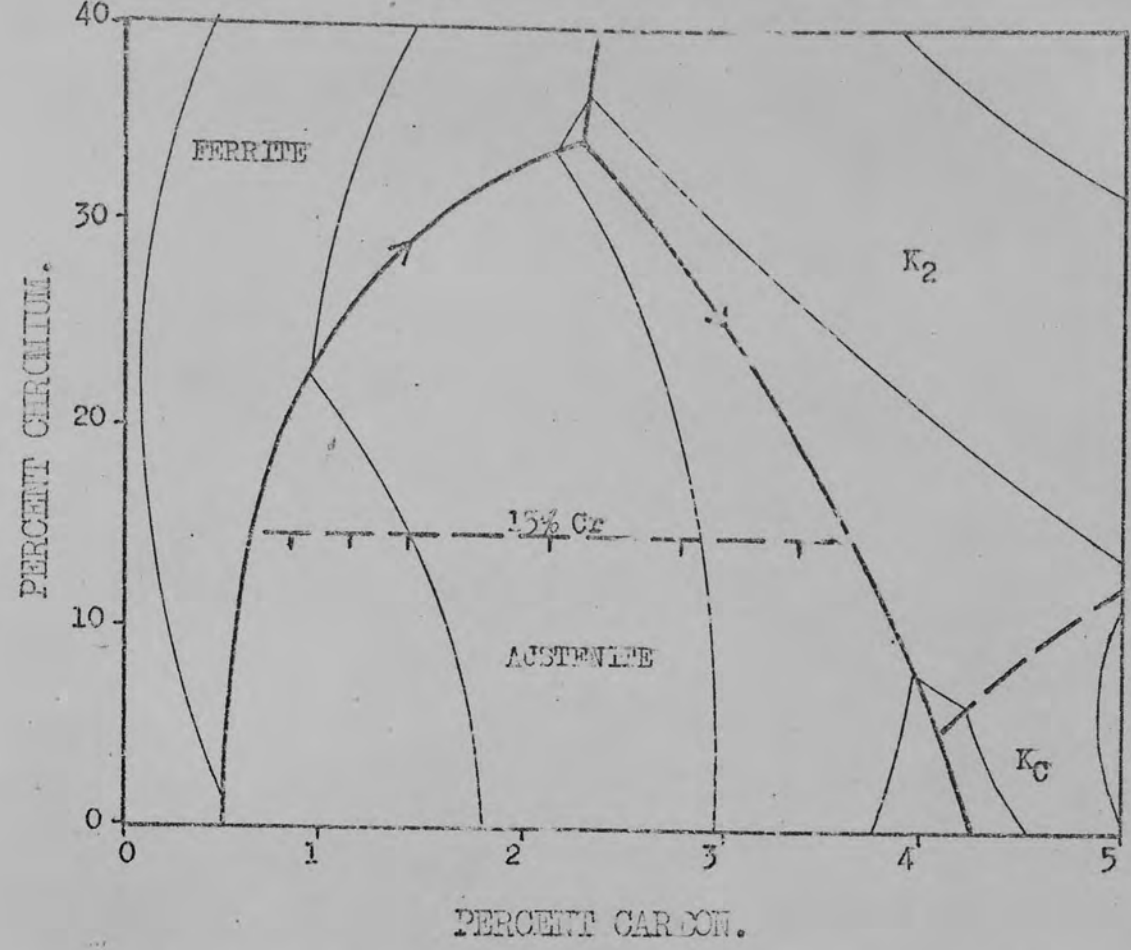

(a) Liquidus Surface, Showing Alloys Under Investigation.

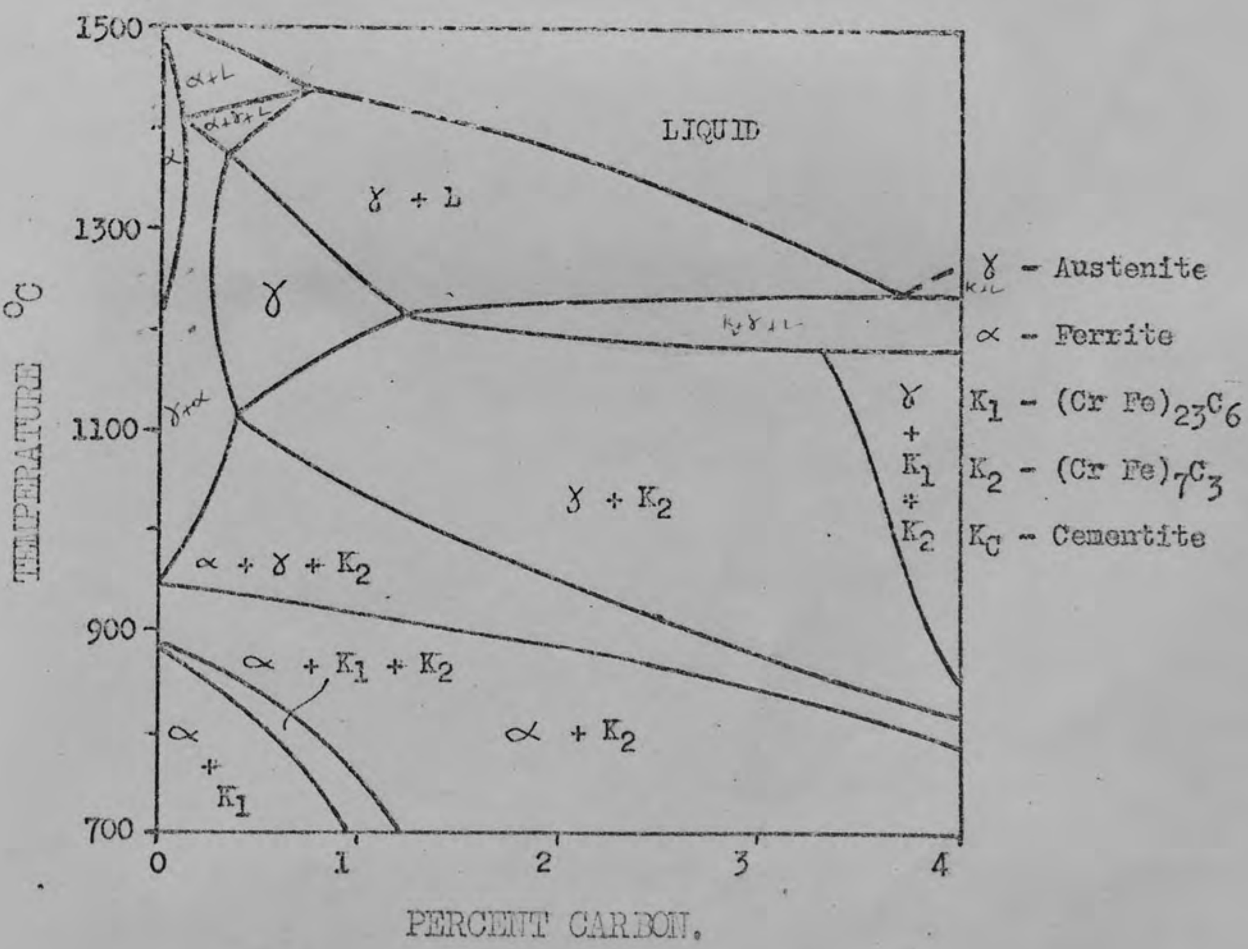

(b) Vertical Section at 15% Chromium.

Fig. 2.5. Fe/Cr/C Ternary System. (After Jackson(13)).

differ from that produced in the eutectic reaction, although the two types form a continuous phase and often cannot be separated metallographically. In fact the eutectic austenite is often depleted in carbon and chromium by an inverse diffusion gradient adjacent to the massive carbides. This results in a raising of the M_s temperature and transformation of the eutectic austenite to martensite on cooling, especially in heavy sections or slow cooling conditions. The significance of any such martensite on the fracture properties of the alloys under investigation has been examined.

The phase changes occurring during heat treatment are considered in terms of the 15% chromium vertical section of the Fe/Cr/C system by Jackson(13). At temperatures below the peritectoid reaction there is a gradual attainment of equilibrium conditions with $Cr_{23}C_6$ being present with the eutectic Cr_7C_3. In meta-stable austenitic structures the rate of transformation to ferrite is generally slow and can be ignored for the purpose of this investigation.

At temperatures above the peritectoid reaction a triple phase field is entered where ferrite, austenite and Cr_7C_3 are the equilibrium phases. Kuo(15) has confirmed that Cr_7C_3 is the only stable carbide above the peritectoid in a 12% chromium 1% carbon alloy. There is little effect on the eutectic carbides within this phase field, although spherodisation may commence after prolonged holding. Further Cr_7C_3 is precipitated from the matrix however, in the form of secondary carbide particles, which depletes the matrix in carbon and chromium. As a result the alloy becomes air hardenable and the matrix transforms to martensite on cooling. Optimum austenitizing time and temperature determinations and the effect of tempering temperature on toughness are the basis of the heat treatment programme.

On further elevation of temperature, ferrite is replaced in the structure by austenite, which with Cr_7C_3 are the stable phases. Above

1050°C significant solution of the eutectic carbide network occurs, leading to a highly alloyed stable austenite which is retained on subsequent cooling. This effect is more pronounced at higher temperatures, resulting in marked spherodisation of the carbides and breakdown of the eutectic carbide network. The stable nature and high temperature of solution is considered by Lane and Grant[16] to be a function of the relatively high melting point of this phase (1782°C).

The fact that very little change in the carbide structure is observed below 1050 - 1100°C serves to illustrate the point that grain size (or dendritic cell size) of this type of alloy is governed by the rate of solidification. Chill casting and small section sizes leads to a fine structure, whereas sand casting or large sections produces a coarse grain size. Commercially, chill casting is as yet limited to small simple shapes for ferrous alloys, but experimental graphite moulded specimens have shown a grain size of less than 0.02mm. In industrial sand castings, where section sizes are frequently over six inches, the grain size is of the order of 0.2mm. The effect of grain size is known to be a significant factor controlling the impact strength of this type of alloy.[17.18]

2.4. The Mechanical Behaviour of Retained Austenite.

A well known feature of many types of austenitic steels is strain induced martensite transformation (S.I.M.) which occurs during plastic deformation, and has been the subject of considerable research. Studies of the phenomenon have helped improve the deep drawability of austenitic stainless steels, and more recently featured in the development of high strength steels with excellent ductility and fracture properties.

Work by many authors has led to a fairly comprehensive understanding of the influence of the more common alloying elements on M_s, but very little information is available concerning M_d (the temperature at which martensite is formed during deformation). Eichleman and Hull[19] appear to cover the subject of M_d in greatest detail, studying the effects of various elements on both S.I.M. and thermal martensite formation. A number of investigators,[20,21] including Eichelman and Hull, have developed equations from which M_s can be calculated, knowing the chemical composition of the austenite undergoing transformation. Minor anomalies are present throughout the literature, but most workers put alloying elements in the following order of effectiveness in reducing M_s:

N & C; Ni; Mo; Cr; Mn; Si.

It is interesting to note that cobalt and aluminium are the only elements known to have the reverse effect (ie. raise M_s). Holloway[22] has found that M_s is raised 13.5°C/percent cobalt in a Cr/Mo die steel, which is in agreement with the results of Irvine[23] and Hawkes and Mehl[24]. Cobalt is normally added to hot working steels, since it improves hot hardness and the resistance to tempering. From the information available it would appear that the effect of alloys on M_d is similar to their influence on M_s. Table 2.1. summarises the experimental results of Eichelman and Hull, on 18/8 type stainless steel.

Table 2.1.

Relative Effectiveness of Alloying Elements on Martensite Formation Expressed as the Nickel Equivalents.

Element	S.I.M.	T.I.M.	Redn. in M_s/% element.
C	+35	+30	3,000°F
N	-	+30	3,000
Ni	+1	+ 1	110
Mn	+0.5	+0.5	60
Si	-	+0.45	50
Mo	+1.5 x Cr	-	
Cr	-	+0.68	75

Cohen discusses the mechanical and thermal aspects of S.I.M. production in a 12% Cr 1.5% C die steel, noting a general increase in S.I.M. with strain, and a marked dependence on stress. In the latter case the reaction is inhibited up to a critical stress level and then proceeds rapidly with further increase in stress. The critical stress increases significantly with the amount of thermal martensite already present as shown in fig. 2.6. The results of heat treatment are summarised in fig. 2.7, where Cohen finds a parabolic relationship between the stress required to produce a given amount of S.I.M., and austenitizing temperature. The curves pass through a minima at about 2030°F (1100°C) corresponding to the interrelation of the driving force (austenite chemistry) and barrier conditions (percent martensite). At temperatures below the minima, thermal martensite is present which acts as a barrier against S.I.M., whilst at higher austenitizing temperatures solution of carbides results in a stable austenite. A characteristic of the S.I.M. transformation noted by Cohen and other workers[26] is serrations in the tensile curve, attributed to local bursts of martensite formation accompanied by a small extension at constant stress.

Powell et. al.[27] have examined the formation of S.I.M. under the influence of different types of deformation in tensile, torsion and compression tests with 18/8 type stainless steel, and conclude that tensile deformation favours the production of S.I.M. Cina[28] has observed a similar trend and suggests that tensile deformation aids the expansion necessary for S.I.M. formation whilst compression will tend to suppress it.

Karlson and Thomas[29] have observed an increase in U.T.S. from 140 ksi. to 200 ksi, associated with S.I.M. in stainless steels and comment that carbon plays an important role in two ways. Increasing carbon has a weakening effect due to a lowering of M_s, but a strengthening effect due to solution hardening and S.I.M. formation. This accounts for the

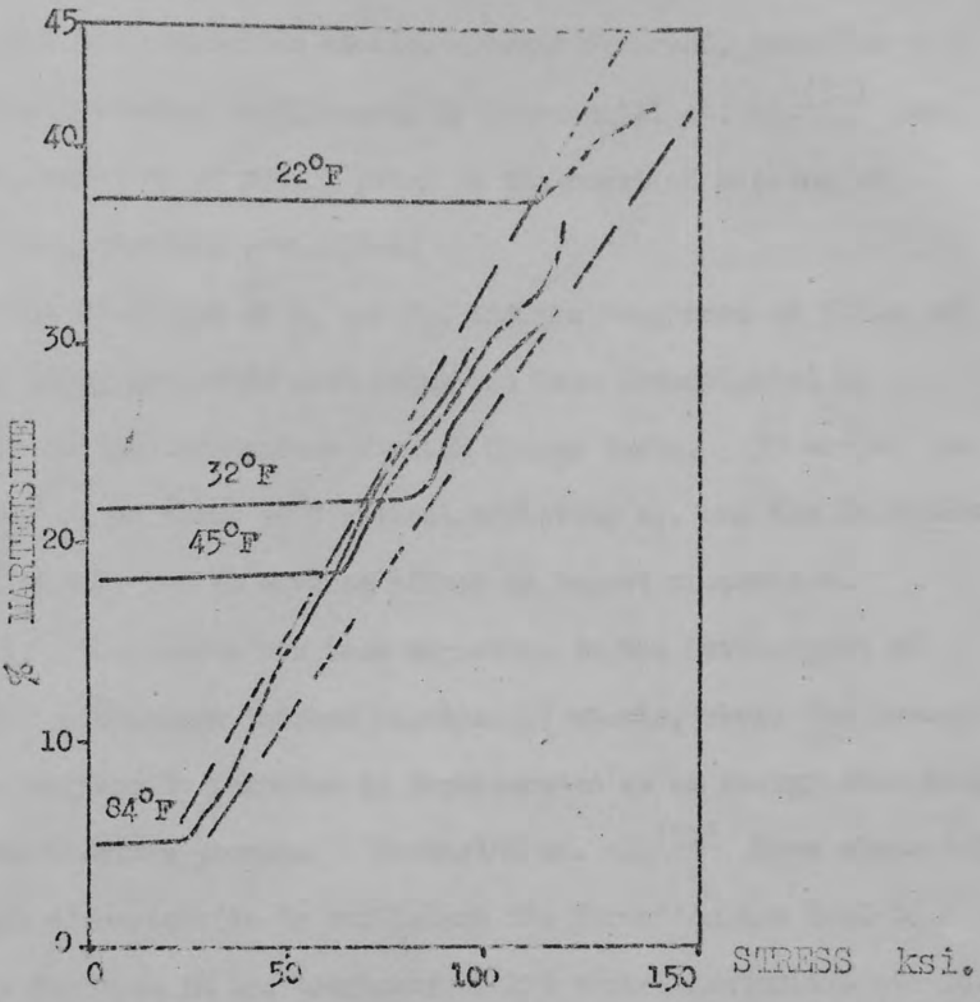

Fig. 2.6. Relationship Between S.I.M. and True Stress in Tensile Test of 1.5%C, 12%Cr Austenitised @ 2050°F and Refrigerated to Temps. Shown to Produce Various Amounts of Martensite. (After Cohen[25])

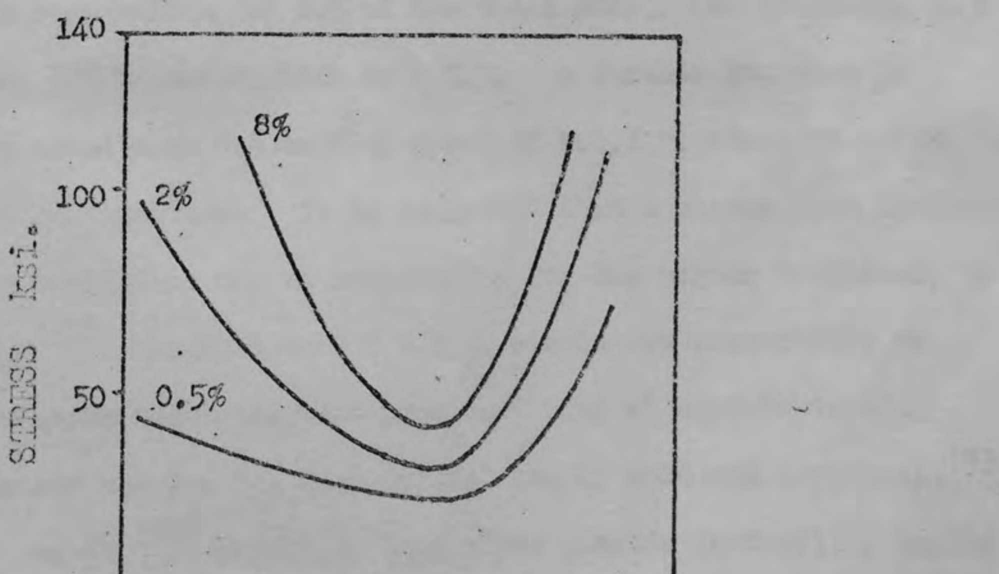

Fig. 2.7. Effect of Stress on S.I.M. in Tensile Test of 1.5%C 12%Cr Steel Austenitised as Shown. (After Cohen[25])

increased U.T.S. in austenitic steels, a trend observed, together with increased work hardening coefficient, by Bressanelli et. al.[30] who consider the formation of S.I.M. prior to the onset of necking as detrimental to mechanical properties.

The effect of copper on M_s and M_d, and the toughness of flake and nodular high alloy graphitic cast irons has been investigated by Rickard,[26] in low temperature V notch Charpy tests. 5% copper was found to lower M_s by about 30°C without affecting M_d, and the formation of about 25% S.I.M. had an adverse affect on impact properties.

The S.I.M. phenomenon has been exploited in the development of T.R.I.P. (Transformation Induced Plasticity) steels, where the invariant shear of the martensite reaction is incorporated as an energy absorbing medium in the fracture process. Gerberich et. al.[31] have shown that if the amount of martensite is sufficient its formation can lead to a considerable increase in the toughness of hot worked austenitic steels. Very good fracture toughness is reported combined with up to 40% reduction in area at a U.T.S. level of over 200 ksi. Breakdown and analysis of the various energy components leads Gerberich to believe that S.I.M. formation is responsible for 80% of the total energy for fracture, in a steel showing 30% transformation to S.I.M. A further increase in toughness is noted when the testing speed of T.R.I.P. steel is raised by three orders of magnitude. It is suggested that a change from isothermal to adiabatic conditions may be responsible for the higher toughness, by affecting M_d.[32] The fact that T.R.I.P. steels are susceptible to hydrogen diffusion and subsequent poor ductility at certain testing temperatures and speeds, has been pointed out by Gold and Koppenaal.[33]

Zackay et. al.[34] postulate that since plastic instability begins at low strains in quenched and tempered steels, the rate of strain hardening produced by dislocation interactions is inadequate to compensate for the increase in stress at the neck. Therefore barriers stronger than dislocation tangles must be introduced during plastic straining in order to delay necking so that the inherent ductility can be utilised in the form of uniform strain. Such barriers must be introduced during straining, not before, otherwise they would increase the yield strength but not necessarily the strain hardening rate. Strain induced martensite plates can act as strong barriers, particularly when the carbon content exceeds about 0.2%.

2.5. Fracture of Abrasion Resistant Alloys.

As mentioned previously little or no quantitative data on the fracture properties of abrasion resistant materials is available. It is well known from observations made on working components that the manganese steel and the pearlitic Cr/Mo steels, for instance, are tougher than white cast irons and martensitic alloy steels. Norman[35] has listed several materials in order of toughness from experience in their use as ball mill liners, but relative toughness in terms of a quantitative measurement and the mechanism of crack propagation are undetermined.

Some data has been presented by Climax Molybdenum[17] for as cast and heat treated A.S.T.M. A.532 Type 2.B. 15% chromium cast iron. This information, shown in Table 2.2. demonstrates the effects of both grain size and heat treatment on toughness, measured as breaking load multiplied by deflection, in a bend test.

For coarse grained material (sand cast) the difference between an as cast pearlitic, and heat treated martensitic structure is marginal, the as cast being slightly tougher. Whilst an increase in toughness is noted in both conditions for fine grained material (chill cast), the increase is far greater, over 100%, for the as cast pearlitic, compared to less than 50% improvement above the sand cast level after heat treatment to martensite.

TABLE 2.2.

	Sand Cast.		Chill Cast.	
	As Cast	Ht. Trtd.	As Cast	Ht. Trtd.
Transverse strength 18 inch span (lb)	2,900	2,850	4,100	3,650
Deflection at failure (inches)	0.140	0.138	0.202	0.160
Rockwell C.	51/56	60/65	52/58	62/64
Toughness (load x defln.)	406	393	823	584

In an investigation into the effects of directional solidification on a 1.2% C 12% Cr steel, Pattyn[36] finds that the direction of dendrite growth is a significant feature of the unnotched Charpy impact toughness. The results are summarised in Fig. 2.8 and indicate that when the dendrites lie along the X plane, perpendicular to the impact direction, but parallel to the test bar axis, toughness is considerably higher than for an equiaxed structure. Poorest impact properties are obtained from the Z direction when dendrite growth is perpendicular to both impact and test bar axis.

Bradley and Foster Ltd.[37] have developed a modified Izod test, to increase sensitivity in the impact testing of abrasion resistant materials. Results of the order of 80 ft-lb/in^2 are reported, for high chromium cast irons tested in the form of plain bars 1¼ in. diameter over a 5 in. span. Reproduceability is characteristically poor, however, necessitating a high level of duplication.

In addition to the more conventional 'U' and 'V' notch Charpy tests,

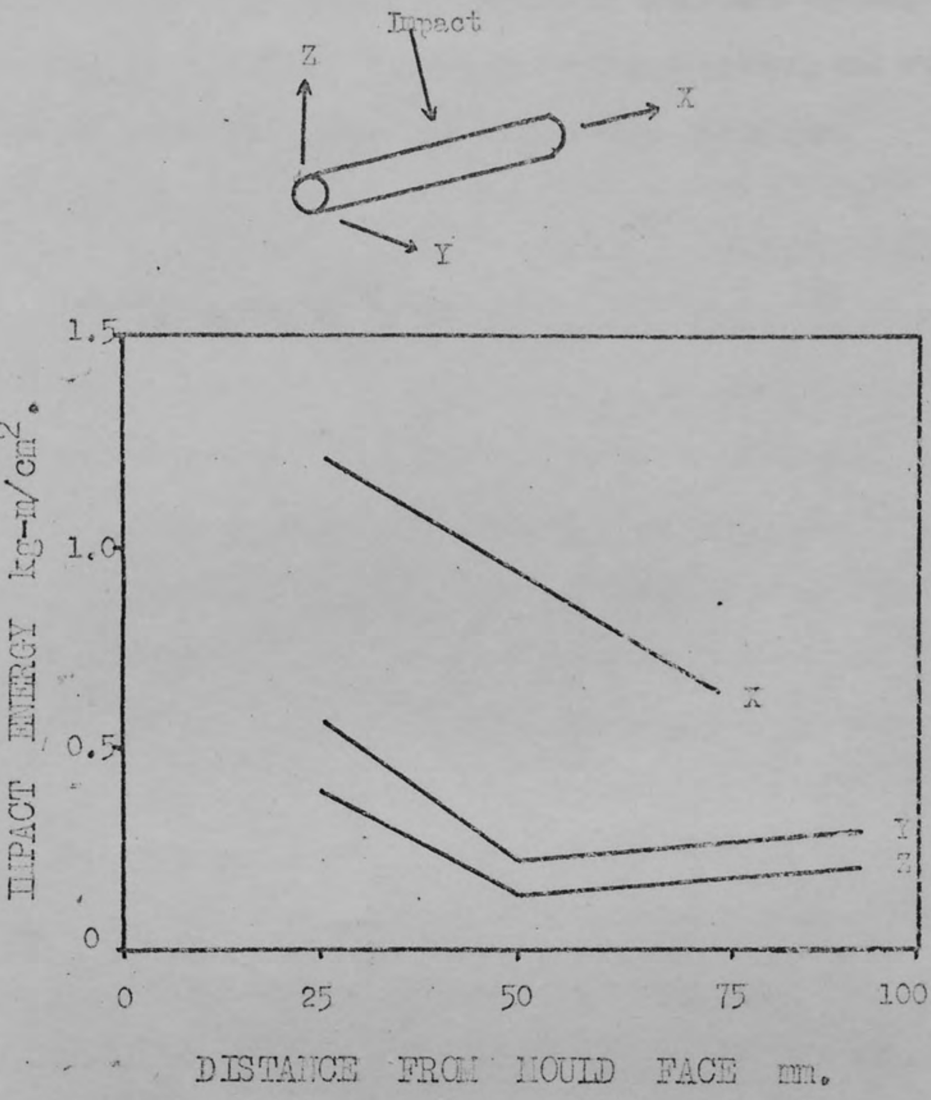

Fig. 2.8. Influence of Directional Solidification on the Impact Properties of 1.2% C, 12% Cr steel. (After Pattyn(36))

four methods of toughness assessment have now been mentioned. Whilst each might be a useful control test in a given situation, all produce empirical values which are meaningless out of their limited context. This lack of standardisation applies to toughness testing in general, not only in the field of abrasion resistant alloys, and emphasises the need for a more sensitive and quantitative technique.

3. THEORETICAL ASPECTS OF FRACTURE.

3.1. Surface Energy Concept.

The qualitative evaluation of fracture derives from the lack of precision in defining toughness. The relative brittleness or toughness of a material can be assessed by the energy required to fracture a plain or notched specimen in an impact test. Whilst a useful control test, being cheap and easy to perform, the relationship between the energy absorbed and the toughness of a component in service is of an empirical nature. Knowing that a material of given impact toughness will be suitable for a certain application, this level of toughness can be used as an acceptance value. Alternatively it is often possible to use a material above the ductile/brittle transition temperature, characteristic of many metals.

The development of Fracture Mechanics has resulted in a quantitative treatment of fracture in terms of a material property, the resistance of the material to the rapid propagation of a crack. The basis of this relatively new approach is found in the work of Griffith,(38) carried out nearly fifty years ago.

Considering an ellipsoidal crack in an infinite plate, Griffith derived the now familiar equation defining fracture stress in terms of elastic energy, and the surface energy consumed during the formation of new fracture surfaces. Assuming a half crack length, a, and a surface energy for unit increase in crack surface area γ, a positive value of $4a\gamma$ is necessary to satisfy the energy requirements of the two new fracture surfaces. The decrease in stored elastic energy, which acts as the driving force during cracking, was calculated from the work of Inglis(39), as $\frac{\sigma^2 \pi a^2}{E}$ for unit increase in crack length. This can be considered as a negative value, increasing in magnitude as the square of the crack length, as portrayed in fig. 3.1.

From Griffith's theory unstable crack extension will occur when the elastic energy release due to an increment of crack growth, da, is greater than the surface energy required for the same crack growth, ie. instability occurs when:

$$d/da \left(- \frac{\sigma^2 \pi a^2}{E} + 4a\gamma \right) = 0 \qquad \text{.... 3.1.}$$

A gross fracture stress can then be defined by the Griffith equation:

$$\sigma_f = \left(\frac{2\gamma E}{\pi a} \right)^{\frac{1}{2}} \qquad \text{.... 3.2.}$$

Whilst holding well in a general form for brittle materials such as glass, insertion of practical fracture strengths for metals, say $\frac{E}{300}$ where $E = 10^{12}$ dynes/cm^2, and surface energy, $\gamma = 2 \times 10^4$ ergs/cm^2 predicts the presence of flaws 10^{-3} cm long before the application of stress. Alternatively, extrapolation of the data to 2a values approaching atomic dimensions, suggests surface energy values well above the most optimistic estimate for ductile materials.

These anomalies in the application of Griffith's theory to metals, and evidence of plastic deformation associated with brittle cleavage fractures by Orowan,[40] led to the conclusion that in the fracture of metals the energy balance is between the elastic energy release, and the combined effects of surface energy and plastic work.

3.2. Significance of Ductility.

It is now apparent that the ability to deform plastically, rather than an increase in surface energy is responsible for any improvement in fracture strength due to environmental effects. Weiss and Yukawa[41] in their appraisal of the subject estimate that the plastic work factor is 10^4 to 10^6 times the surface energy contribution. It has been shown by Irwin[42] and Orowan,[43] independently, that in metals the energy consumed

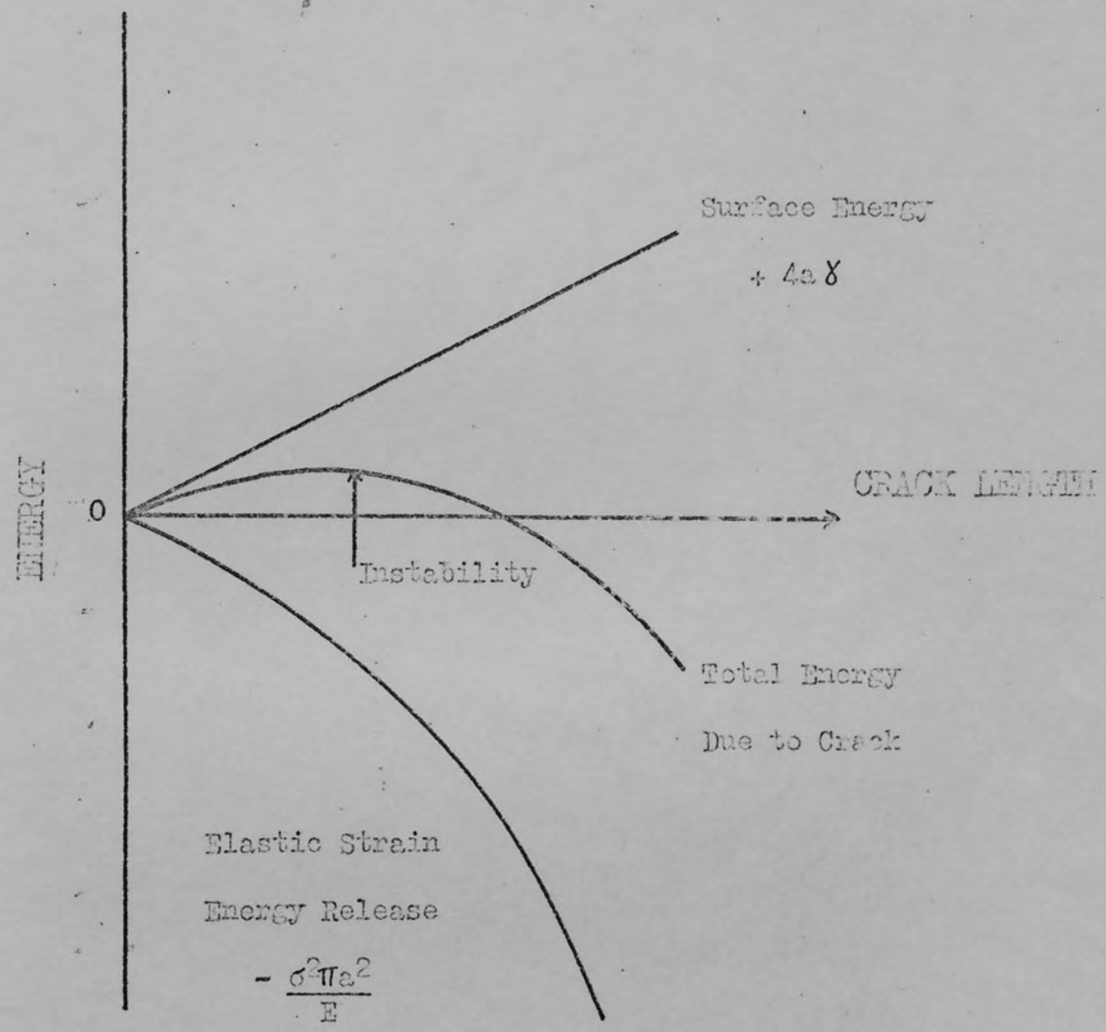

Fig. 3.1. Energy Balance of a Crack in an Infinite Plate. (After Weiss and Yukawa[41])

by plastic work during fracture is concentrated as plastic yielding in a small zone just ahead of the crack tip.

Generalisation of the situation by Irwin led to the introduction of G_c into the Griffith equation, replacing the 2γ term and representing the combined effects of surface tension and plastic yielding. By introducing G_c and rearranging, a criterion for crack propagation is achieved, since elastic modulus, surface tension, and plastic working characteristics are material constants:

$$\sigma_f \ (a)^{\frac{1}{2}} = \left(\frac{G_c \ E}{\pi}\right)^{\frac{1}{2}} \qquad \ldots. \ 3.3$$

Since G_c is the rate of release of potential elastic strain energy per unit area of crack increase, it is normally termed 'crack driving force', and is a material constant in the same way as hardness or yield strength. Indiscriminate use of equation 3.3, however, can lead to unreliable predictions of the fracture stress. In short crack situations for ductile materials, (with a high plasticity factor), use of this equation gives a fracture stress exceeding the ultimate strength of the material. The Irwin/Orowan modification to Griffith's theory can only be justified when the applied stress for crack propagation is small compared to the yield stress and when any plastic deformation is localised to a narrow zone ahead of the crack. The significance of this plastic zone is discussed to greater depth in section 3.4.

3.3. Stress Analysis Approach.

The inadequacy of the energy criterion, particularly the plasticity aspects, resulted in the development of linear elasticity relationships. Irwin(44) has pointed out that a fracture criterion expressed in terms of energy has its equivalent stress and strain criteria, and whilst this does not resolve the energy balance problems no statement concerning the use of released elastic energy is required.

Stress fields near crack tips can be divided into three basic types,[41] associated with the mode of deformation, as shown in fig. 3.2. Type I is the tensile opening mode, when the crack surfaces move directly apart. Type II, the edge sliding mode, is characterised by the crack surfaces sliding over one another perpendicular to the crack front. Type III, tearing, finds the crack surfaces shearing over one another parallel to the leading edge. A combination of one or more of these three basic modes generally describes the conditions prevailing during crack tip deformation and can be used to describe the associated stress fields. Irwin[45] has analysed the stress field for each individual case as follows:

$$\left.\begin{aligned}
\sigma_x &= \frac{K_1}{(2\pi r)^{\frac{1}{2}}} \cos {}^{\theta}/_{2} \left(1 - \sin {}^{\theta}/_{2} \sin {}^{3\theta}/_{2}\right) \\
\sigma_y &= \frac{K_1}{(2\pi r)^{\frac{1}{2}}} \cos {}^{\theta}/_{2} \left(1 + \sin {}^{\theta}/_{2} \sin {}^{3\theta}/_{2}\right) \\
\tau_{xy} &= \frac{K_1}{(2\pi r)^{\frac{1}{2}}} \sin {}^{\theta}/_{2} \cos {}^{\theta}/_{2} \cos {}^{3\theta}/_{2}
\end{aligned}\right\} \text{MODE I}$$

$$\left.\begin{aligned}
\sigma_x &= \frac{K_{11}}{(2\pi r)^{\frac{1}{2}}} \sin {}^{\theta}/_{2} \left(2 + \cos {}^{\theta}/_{2} \cos {}^{3\theta}/_{2}\right) \\
\sigma_y &= \frac{K_{11}}{(2\pi r)^{\frac{1}{2}}} \sin {}^{\theta}/_{2} \cos {}^{\theta}/_{2} \cos {}^{3\theta}/_{2} \\
\tau_{xy} &= \frac{K_{11}}{(2\pi r)^{\frac{1}{2}}} \cos {}^{\theta}/_{2} \left(1 - \sin {}^{\theta}/_{2} \sin {}^{3\theta}/_{2}\right)
\end{aligned}\right\} \text{MODE II}$$

$$\left.\begin{aligned}
\tau_{xz} &= - \frac{K_{111}}{(2\pi r)^{\frac{1}{2}}} \sin {}^{\theta}/_{2} \\
\tau_{yz} &= \frac{K_{111}}{(2\pi r)^{\frac{1}{2}}} \cos {}^{\theta}/_{2} \\
\sigma_x &= \sigma_y = \sigma_z = \tau_{xy} = 0
\end{aligned}\right\} \text{MODE III}$$

The parameters K_1, K_{11} and K_{111} are stress intensity factors for the corresponding types of stress fields, reflecting the redistribution of stress in a body due to the introduction of a crack. θ is an angular coordinate measured from the crack plane.

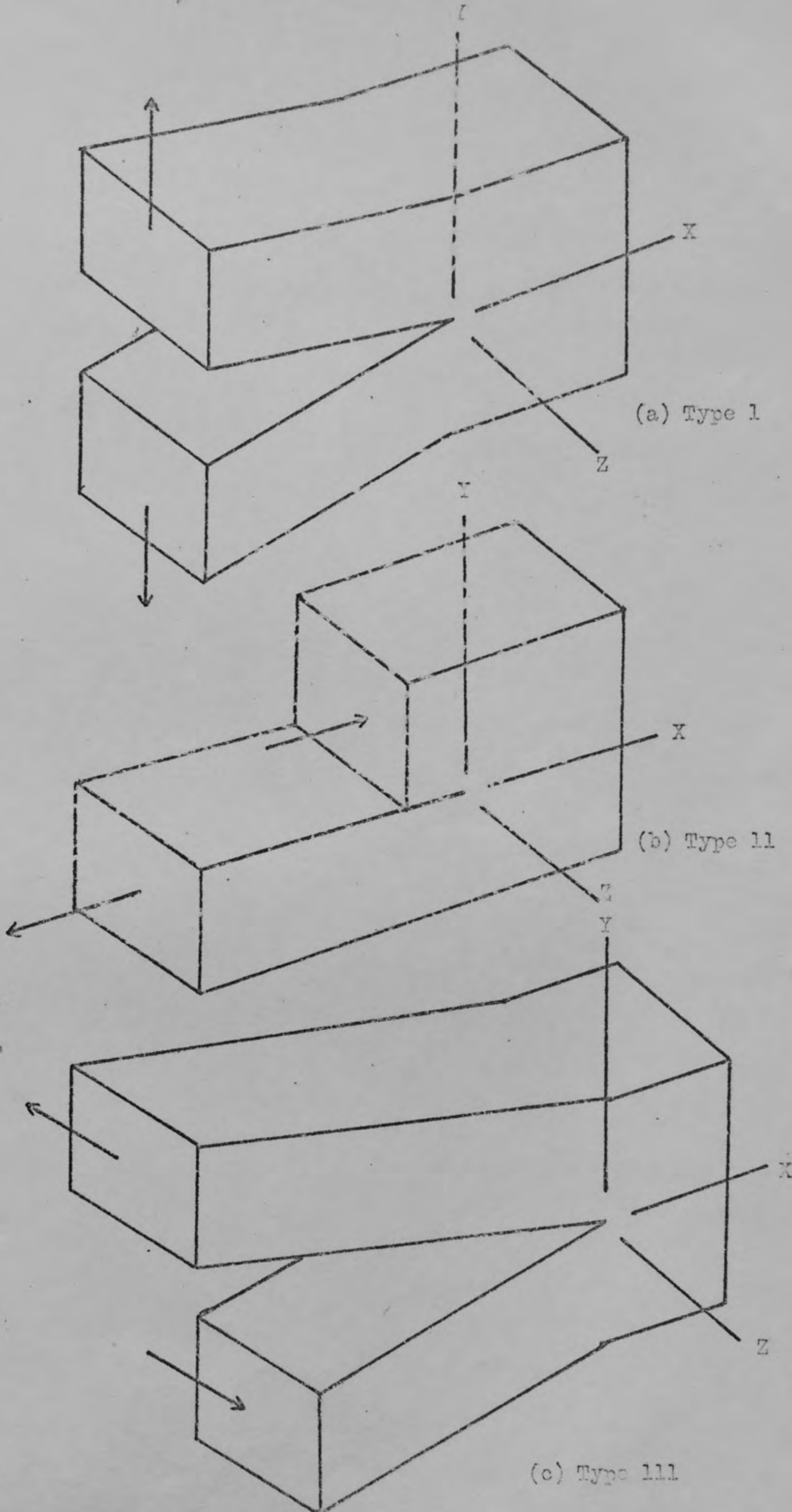

Fig. 3.2.

Basic Modes of Crack Surface Displacements. (After Paris and Sih[41])

The most noticeable feature of the stress distribution in a notched flat plate is the highly concentrated local stress σ_y in the longtitudinal direction at the notch root. Considering x as the distance ahead of the crack tip, when x = 0, σ_y is theoretically infinite and decreases with $(x)^{-\frac{1}{2}}$ according to equation 3.4. providing x remains small, ie. in a region close to the crack tip:

$$\sigma_y = \frac{K_c}{(2\pi x)^{\frac{1}{2}}} \qquad \text{.... 3.4.}$$

Since K is dependent upon the applied stress σ_a, for a given crack situation K increases with σ_a up to a critical level, K_c, when the local stress level is high enough to cause unstable crack propagation, as portrayed in fig. 3.3.

From strain energy considerations Irwin(41) has shown that energy release rate, G, can be obtained in the form:

$$G = \frac{1 - v}{2\mathcal{G}} K_1^{\ 2} + \frac{1 - v}{2\mathcal{G}} K_{11}^{\ 2} + \frac{1}{2\mathcal{G}} K_{111}^{\ 2} \qquad \text{.... 3.5.}$$

Where v is Poisson's ratio and $\mathcal{G}$ is the shear modulus.

Since $E = 2(1 + v)\,\mathcal{G}$, the separate contributions of each mode under plane strain conditions can be defined as:

$$\left.\begin{aligned} G_1 &= \frac{(1 - v^2)}{E} K_1^{\ 2} \\ G_{11} &= \frac{(1 - v^2)}{E} K_{11}^{\ 2} \\ G_{111} &= \frac{1 + v}{E} K_{111}^{\ 2} \\ \text{Where } G &= G_1 + G_{11} + G_{111} \end{aligned}\right\} \qquad \text{.... 3.6.}$$

As a consequence of these equations Irwin illustrates the direct relationship between the elastic strain energy release rate and stress intensity factor.

Other treatments leading to failure criteria have been proposed using

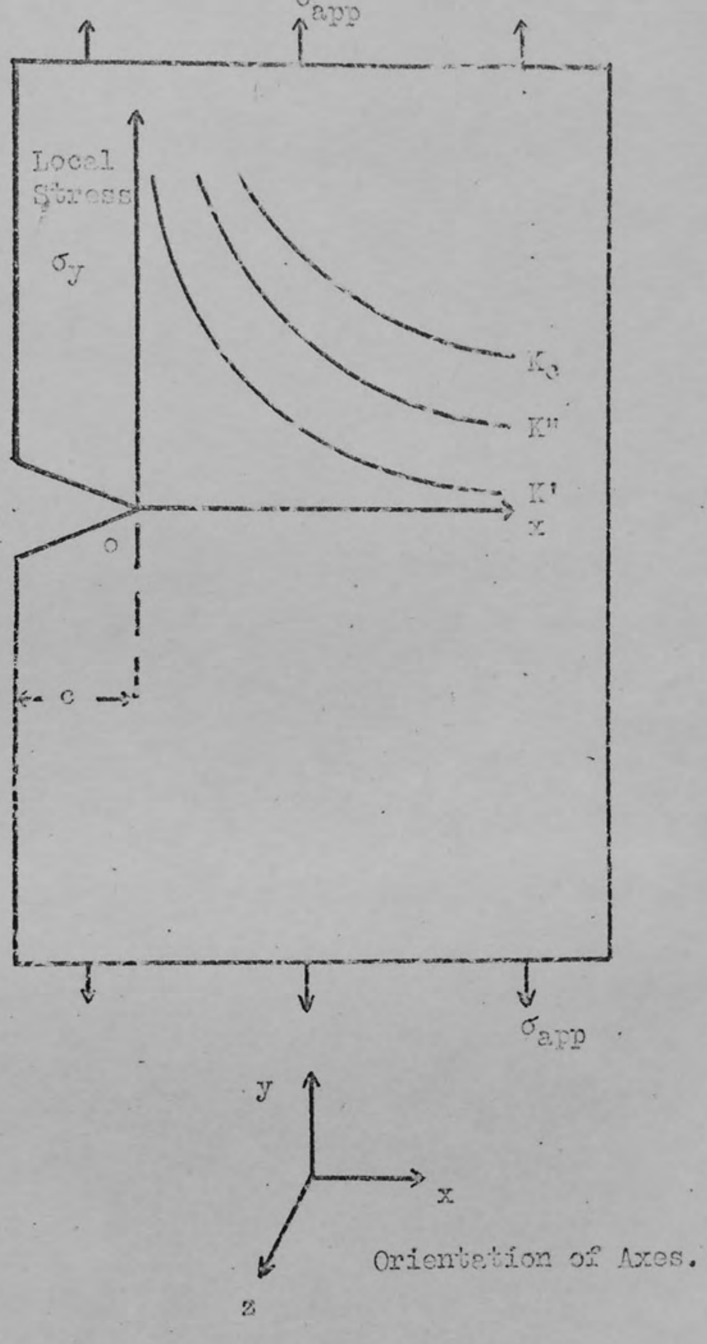

Fig. 3.3. Dependence of K on the applied stress, σ_{app}, in a given Crack situation. (After Barnby[49])

an elastic stress analysis to determine the nature of the redistributed stresses. Each is concerned with phenomena occurring at the crack tip, regarded as being essential to the attainment of a critical fracture criterion. Most notable are the methods developed by Neuber[46] (considering an enclave of critical size within the elastic stress field); Kuhn[47] (development of the ultimate stress at a specific radius from the crack tip); and Barenblatt[48] (stresses approaching the cohesive bond forces ahead of the crack with the use of 'modulus of cohesion', M, equal to $(\frac{1}{2}\pi)^{\frac{1}{2}} K_c$). However, since each of these phenomena occurs within the elastic crack tip stress field, their occurrence will always correspond to a similar distribution of elastic stresses ahead of the crack tip. Therefore they are equivalent to the current concept of fracture mechanics, and the critical stress intensity factors. Whilst being extremely useful in the fuller understanding of fracture processes these alternative theories are unnecessarily restrictive in their approach, and the absence of such assumptions in the formulation of a failure criterion is the basis of the general acceptance of fracture mechanics.

3.4. Constraint Stresses.

Consideration of fig. 3.3. has shown that the application of stress to a notched plate under elastic conditions results in concentrated local stresses in the longtitudinal y direction. In real situations three dimensional features must be accounted for.[49] The presence of the σ_y stress combined with the notched geometry causes constraint stresses in the other two dimensions of the plate, the x and z directions. These arise under the influence of σ_y because of the Poisson effect demanding contractions in these directions, whether the crack is at the surface or embedded, of simple or complex geometry. Since the local stress reduces rapidly away from the crack tip, the remaining bulk of the material is subjected to only small Poisson contractions and restrains the material at the notch root from contracting in the x and y directions, thus generating σ_x and σ_z constraint stresses.

The distribution of the σ_x and σ_z stresses will be partly dictated by the notch geometry, but generally they will tend to follow the pattern set by the σ_y stress. The level of the constraint stress will always be below that of the σ_y stress and is given by:

$$\sigma_z = v(\sigma_y + \sigma_x). \qquad \ldots. \; 3.7.$$

The fact that they are constraint stresses generated by the geometry of the situation, means that the σ_x and σ_z stresses must reduce to zero at the free surfaces, as shown in fig. 3.4. Thus σ_x follows, at a lower level, the distribution pattern set by σ_y, but falls off rapidly at the notch root, and with $(x)^{-\frac{1}{2}}$ away from the notch root.

Whilst following the distribution pattern of σ_y in the x direction, proportional to $(x)^{-\frac{1}{2}}$, σ_z reaches a constant value in the z direction through the thickness, falling off to zero at each of the free surfaces, as depicted in fig. 3.4.(c).

If the plate is thin enough then the σ_z stress has no chance to develop due to the close proximity of the free surfaces. In this situation, termed generalised <u>plane stress,</u> all the stresses lie in the plane of the plate. Alternatively in a thicker plate where the σ_z stress is developed throughout most of the section, all the strain or displacements lie in the plane of the plate surface, and none through the thickness (except very close to the plate surfaces where σ_z becomes too small to prevent displacement) and a condition of <u>plane strain</u> predominates. The yield zones characteristic of plane stress and plane strain are shown schematically in fig. 3.5.

The differences between these two important conditions are most marked when plasticity developes at the notch root. Under plane strain conditions with three principal stresses present, a component of hydrostatic

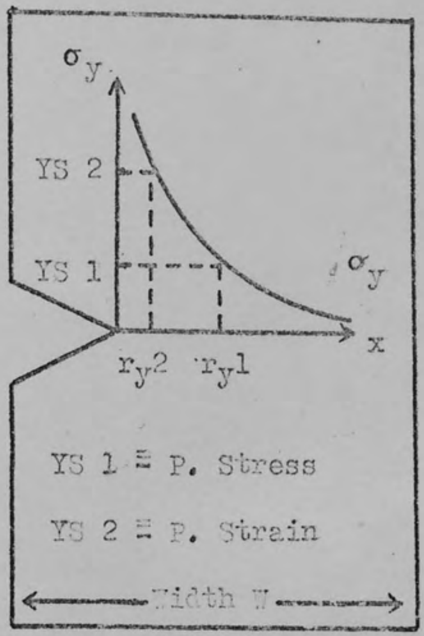

(a) Variation of σ_y across width.

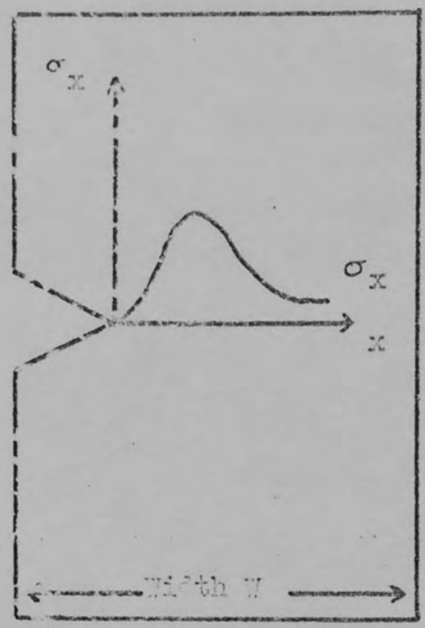

(b) Variation of σ_x across width.

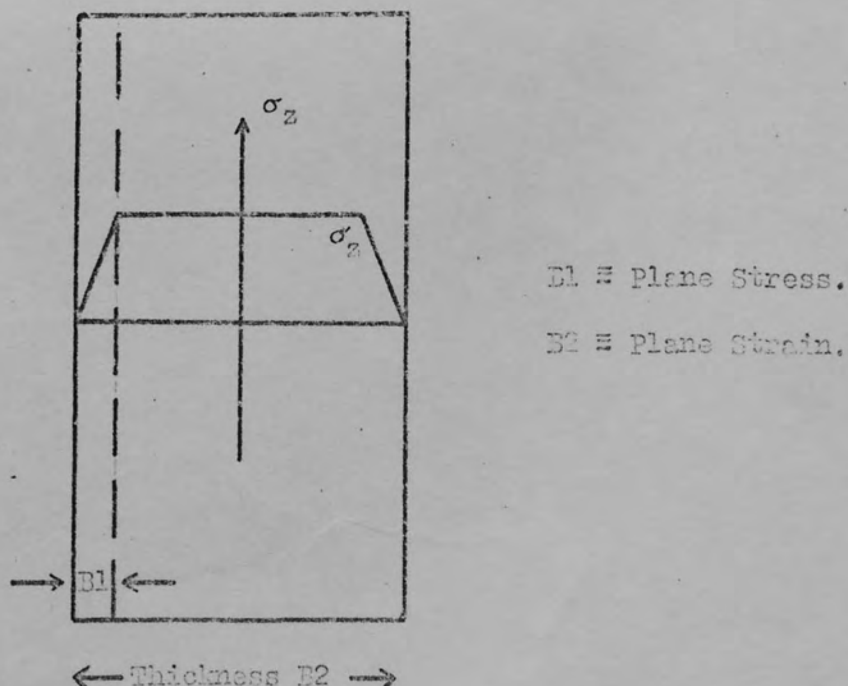

(c) Variation of σ_z through plate thickness.

Fig. 3.4. Development of Constraint Stresses through Width and Thickness of a Notched Plate. (After Barnby[49])

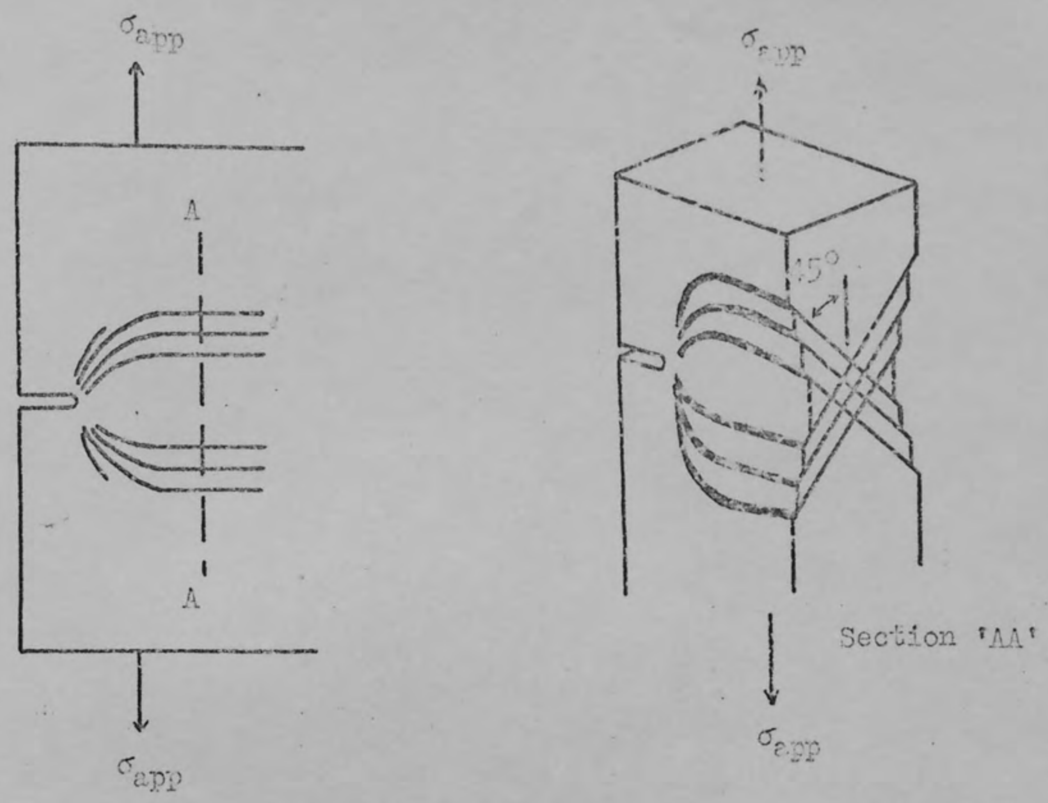

(a) Plane Stress.

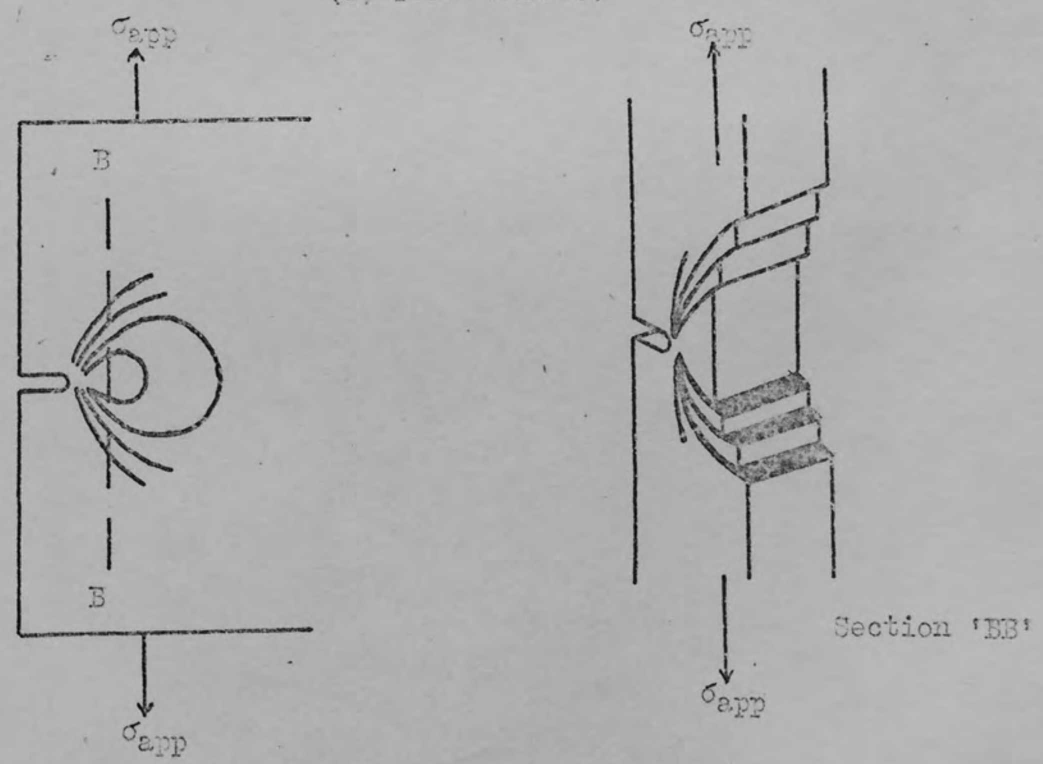

(b) Plane Strain.

Fig. 3.5. Yield Zones through the Cross Section of a Cracked Plate in Plane Stress and Plane Strain.
(After Hahn and Rosenfield[74])

tension exists in the stress field, whereas in plane stress, since the stresses through the thickness are sensibly zero, a biaxial stress system prevails. The effect of triaxial tension, in plain strain, is to increase the effective yield stress of the material subjected to the stress field by constraint (ie. at the notch root). The extent of plastic yielding can be determined from the stress distribution curve by cutting off the σ_y curve at the yield stress level, since this is the physical limit in a real situation. The distance along the x axis at which the yield stress cuts the local stress distribution, r_y, gives an estimate of the radius of the enclave which will become plastic prior to crack propagation.

It can be seen from fig. 3.4.(a) that increasing the level of σ_{ys} will reduce the extent to which plasticity occurs by limiting the size of the plastic zone. In practice the size and shape of the plastic zone will depend on the material properties and on whether the stress system is predominantly plane stress or plane strain. Under plane stress the yield strength is cut off at the uniaxial yield level, but under plastic constraint (plane strain), yielding criteria show that σ_y will be higher than the uniaxial yield strength, σ_{ys}. Using the Tresca criterion σ_{ys} must satisfy:

$$\sigma_{ys} = \sigma_y - \sigma_z. \qquad \text{.... 3.8.}$$

Where σ_y is the maximum and σ_z the minimum principal stress. Thus the effective yield strength of the material at the notch tip rises to the value of σ_y which is given by:

$$\sigma_y = \sigma_{ys} + \sigma_z. \qquad \text{.... 3.9.}$$

Irwin[41] has determined the size of the plastic zone to be, for plane stress:

$$r_y = \frac{1}{2\pi} \left(\frac{K_{1c}}{\sigma_{ys}}\right)^2. \qquad \text{.... 3.10.}$$

and for plane strain:

$$r_y = \frac{1}{5.6\pi} \left(\frac{K_{Ic}}{\sigma_{ys}}\right)^2 \qquad \text{.... 3.11}$$

During fracture the propagating crack tip is preceded through the structure by the plastic zone, which in a thick plate is small in the core where plane strain prevails, but becomes larger at the sides as the transition to plane stress occurs, shown schematically in fig. 3.6. The depth to which the larger zone extends into the thickness is approximately r_y. The smaller the plastic zone size the less energy is consumed during fracture, and since this plastic work is the major contributory factor to toughness the critical K or G is a minimum for plane strain conditions, denoted K_{1c} or G_{1c}. Under non-plane strain conditions the energy consumed in the plastic zone is greater and the values of the stress intensity factor and the corresponding strain energy release rate are higher than the minimum K_{1c} and G_{1c}. To describe these situations the general notations K_c and G_c are used. Thus K_{1c} represents the inherent resistance of a material to unstable crack propagation under the most severe conditions of geometrical constraint. Unlike the corresponding strain energy release rate, K_{1c} accounts for elastic modulus, allowing direct correlation between valid data from different materials.

3.5. Notch Acuity.

The importance of crack sharpness and its effect on the intensity of the local (σ_L) stress is expressed by Cottrell[50] as:

$$\sigma_L \propto \left(\frac{2a}{\rho}\right)^{\frac{1}{2}}. \qquad \text{.... 3.12}$$

where ρ is the notch root radius.

It is apparent that decreasing ρ, (sharpening the crack), increases the level of local stress, and as ρ approaches zero the local stress is increased toward infinity, effectively reducing the strength of the

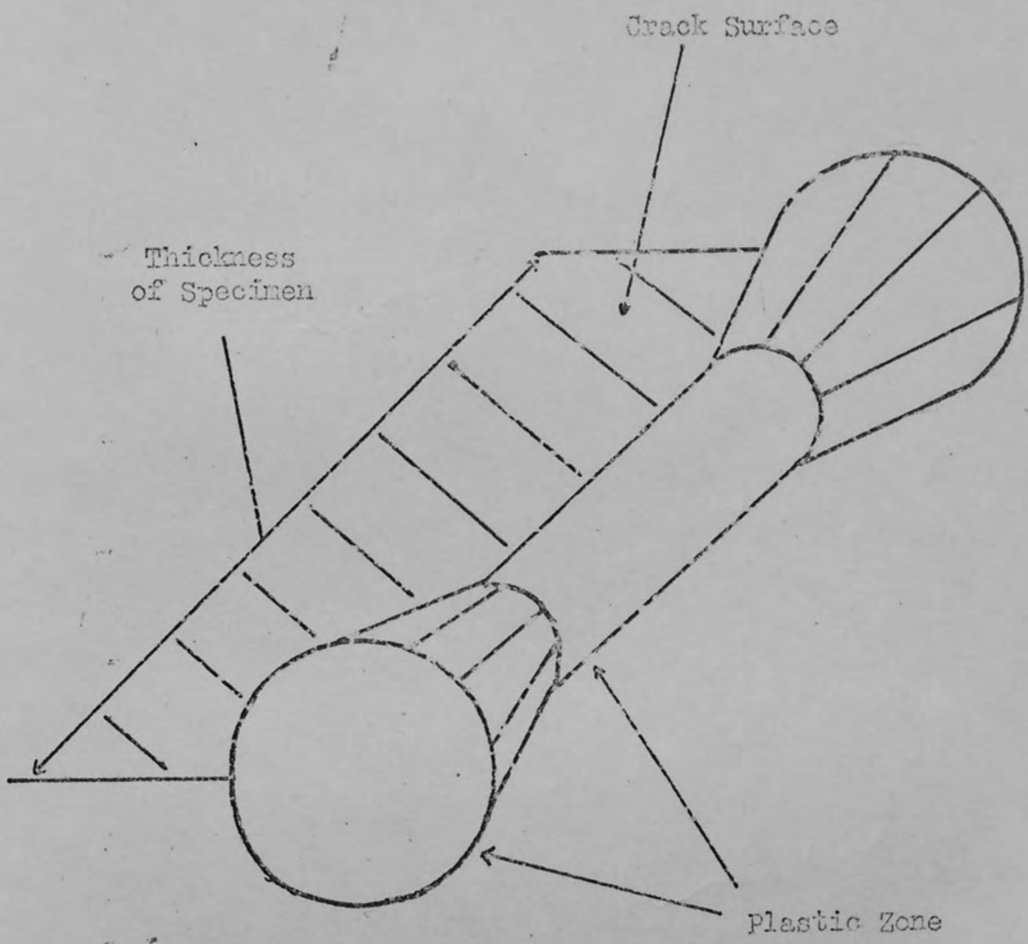

Fig. 3.6. Three Dimensional Schematic Diagram of the Plastic Zone.
(After Weiss and Yukawa[41])

material to a negligible level. For every material there is a lower limit of ρ however, below which no further increase in σ_L occurs, since plastic flow at the tip will blunt the crack. The stronger the material the lower will be the critical value of ρ, since plastic flow becomes more difficult. Greenwood(51) estimates that a crack cannot have an effective sharpness so small that the tip radius is less than about four times the inter-atomic spacing.

In an earlier analysis Irwin(52) notes the following relationship between the stress intensity factor and crack root radius:

$$K = \lim_{\rho \to 0} \tfrac{1}{2} \sigma_{max} (\pi \rho)^{\frac{1}{2}}. \qquad \ldots . \; 3.13.$$

indicating that K becomes insensitive to root radius when ρ is small compared to notch depth.

If it is considered that a critical value of strain energy release rate is the sole criterion for unstable fracture, then fracture toughness should be insensitive to root radius in the small radius range. However, experimental data by Yukawa and McMullin(53) has shown that fracture toughness values are definitely dependent on root radius. Thus it is possible, with blunt notches, to exceed the critical value of strain energy release rate without fracture occurring. This observation emphasises the importance of the size of the plastic zone, and the stress/strain relationships within it.

Weiss(54) has treated the subject by assessing the elastic stress distribution of an infinitely sharp crack, compared to cracks of finite sharpness. Jackson(55) has confirmed the results of the treatment by Weiss, in his calculations of the Neuber stress analysis, shown in fig 3.7. Both workers conclude that the stress intensification for a crack of finite root radius differs from that of an infinitely sharp crack, only in the region ahead of the crack tip approximately one fourth of the respective root radius. Therefore, for a crack of root radius 0.005in.,

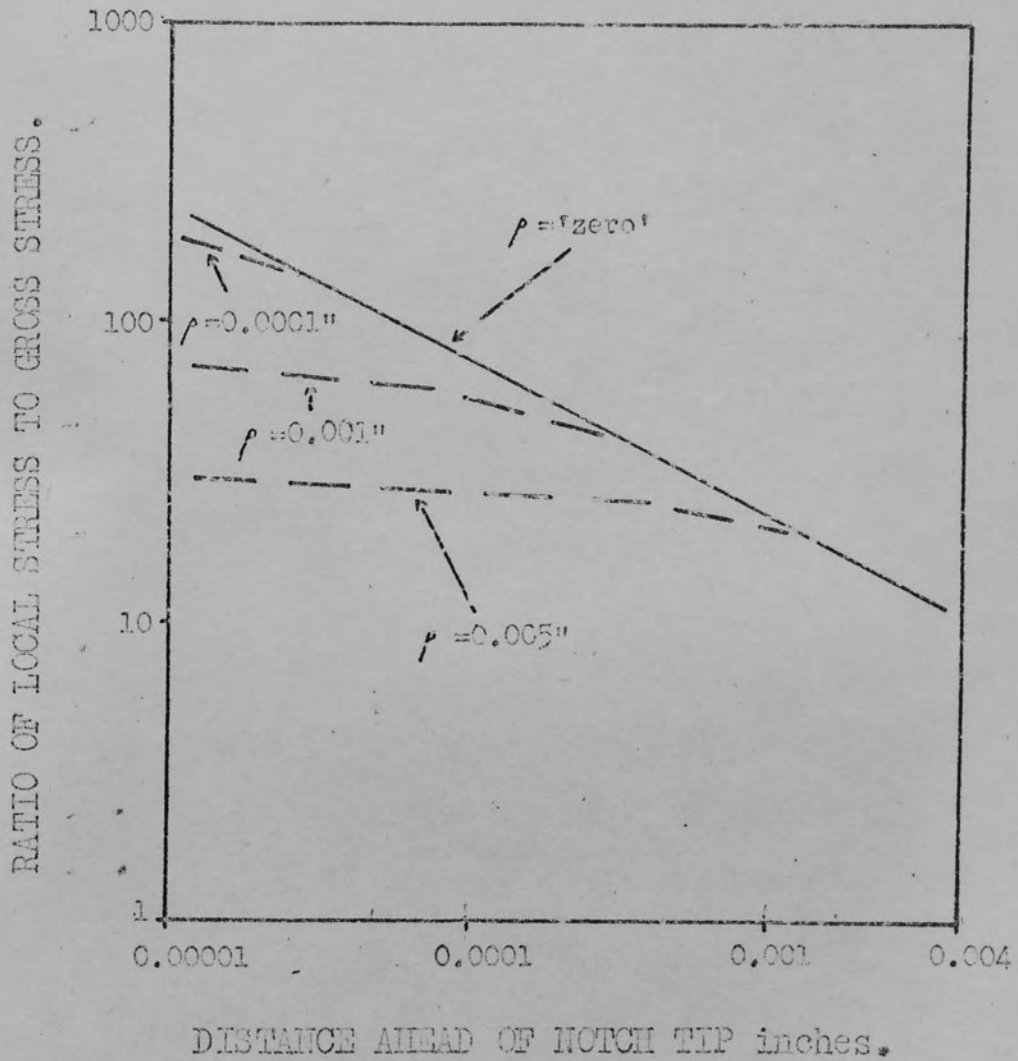

Fig. 3.7. Comparison of Local Stresses in the Vicinity of the Notch Tip. (After Jackson(55))

the crucial region is only some 0.001 in. ahead of the tip, and it is the deformation and fracture of this first micro-volume which controls the subsequent fracture of the nett section.

Two definite conditions are now specified for the unstable fracturing of a material, firstly the initiation of fracture in the small localised zone near the tip; and then the supply of stored elastic energy from regions remote from the crack tip, necessary to maintain unstable crack motion once initiation has been overcome. The problem in fracture testing is to determine which of these factors is controlling and being measured in a particular test. For example, if the crack tip is not sharper than the critical root radius for the material, it will be the initiation resistance which is controlling and being measured. This is often the case in conventional notched and unnotched impact testing.

Ideally then, in order to measure the materials inherent fracture resistance, it is desirable to perform the test under conditions where the materials resistance to the initiation stage has been reduced as low as possible. Machined notches can rarely be produced with tips sharper than about 0.002 in., but natural cracks produced by cleavage, fatigue, or fracture of secondary particles are normally sharper than this by at least two orders of magnitude in high strength materials. The affect of a blunt notch is to increase the size of the initiating plastic zone, resulting in the consumption of excess strain energy. In subsequent propagation the plastic zone size shrinks to that characteristic of a natural crack in the material. In order to avoid anomalously high values, when measuring fracture toughness, natural crack conditions are simulated by fatigue pre-cracking of a machined notch under low stress fatigue conditions.

3.6. Fracture Toughness Testing Techniques.

Formulation of stringent limits and specifications in addition to calibration data and test techniques has been issued by A.S.T.M. E 24 Special Committee, and all aspects are fully documented in S.T.P. 381 and S.T.P. 410. A brief outline of the more salient points will be given here.

Fracture Appearance. From the visual examination of fractured tensile test specimens the 'cup and cone' fracture surface has become a familiar characteristic associated with many metals. In fact the cup and cone fracture is a combination of two extreme types, referred to as 'shear' or 'slant' and 'square' or 'flat', which occur not only in tensile testing but in all instances of fracture. Slant (shear) fractures are produced in the presence of relatively large plastic strains in a situation approximating plane stress; whereas square (flat) fracture surfaces are associated with small amounts of deformation in the presence of constraint stresses, ie. in a plane strain mode.

The various types of fracture surfaces observed and their recommended descriptive terms are schematically illustrated in fig. 3.8. by Srawley and Brown.[41] Since only in the two extreme slant and square types are the fracture surfaces roughly flat, the front of an extending crack in most real situations cannot be represented by a straight line. Tests[56] in which loading of a specimen is interrupted, and the extent of crack growth marked by heat tinting, throughout the fracture process from initiation to instability, have shown that the crack front in plate specimens is parabolic with the most advanced point at the mid thickness, as shown in fig. 3.9.

This phenomenon is brought about by the influence of the free faces failing in a plane stress mode (and consuming more energy per unit increase in area), suppressing the advance of the crack in the plastically

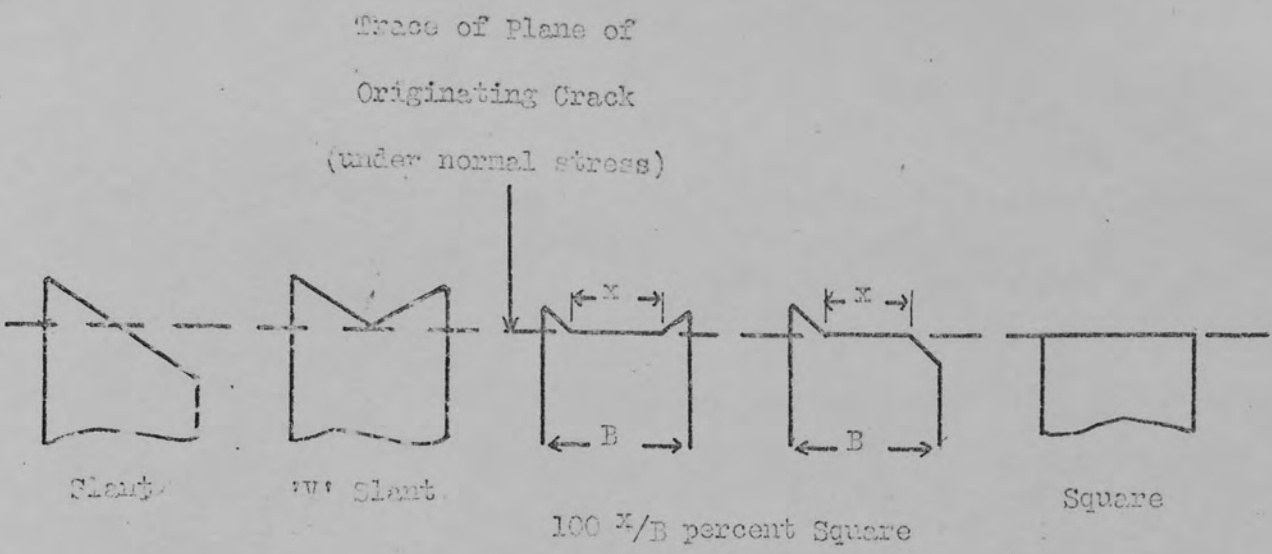

Fig. 3.8. Recommended Descriptive Terms for Types of Fracture Observed in Plate Specimens. (After Srawley and Brown(41))

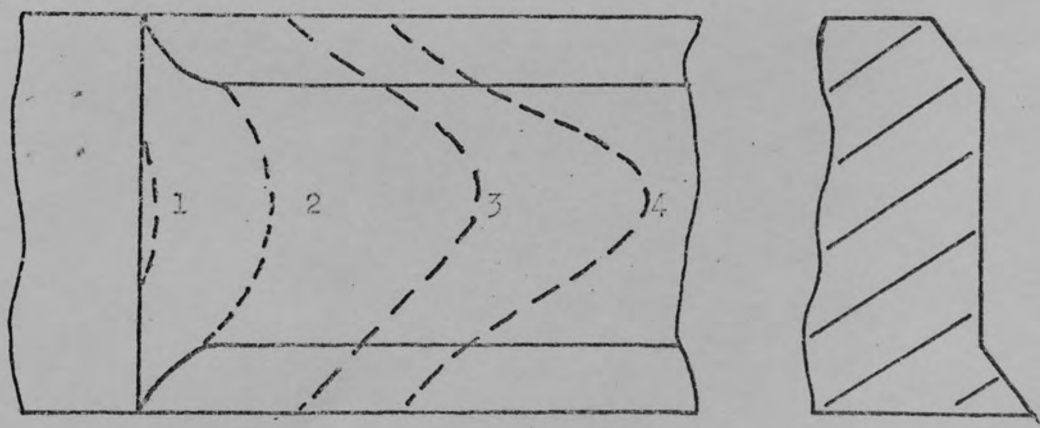

Fig. 3.9. Schematic Illustration of Successive Positions of Crack Front in Predominantly Square Fracture.
(After Srawley and Beachem(56))

constrained (plane strain) region at the centre. This type of crack is commonly referred to as a 'thumb-nail' crack, and the slant fracture area associated with the free surfaces as 'shear lips'.

Effect of Thickness. For a given material and test conditions the fracture appearance and strain energy release rate, G, show a marked dependence on section thickness, as shown for plate specimens in fig. 3.10., qualitatively typical of most metallic materials. The area of slant fracture in a given thickness is constant, and dependent on the yield properties of the material. Therefore as thickness decreases the proportion of high energy slant fracture becomes greater. For similar yield strengths (ie. same mechanical and thermal treatment) the effect of increasing thickness is to reduce the ratio of slant/square fracture. This means a reduction in energy requirements for unit fracture propagation, until the fracture is predominantly square. At this point the G_c/Thickness curve approaches a lower limiting value with minimum energy requirements, typical of an ideal plane strain situation. The level of the plateau is the plane strain toughness, G_{1c}, and is unaffected by further increase in thickness, since the extent of slant fracture is independent of plate thickness.

Effect of Width. The effect of width as distinct from thickness can best be envisaged by considering the depth of a notch in a flat plate relative to the gross section size. If the extent of unnotched material ahead of the crack is infinitely large compared to the plastic zone size, r_y, then the situation nears the ideal for the application of linear fracture mechanics. For slightly larger plastic zone sizes, or smaller widths, the contribution of the plastic zone may become significant, making it necessary to consider the plastic zone as an addition to the crack length. Under these conditions the crack length, a, is represented by $(a + r_y)$ in relevant equations. In cases where the plastic zone is large the local

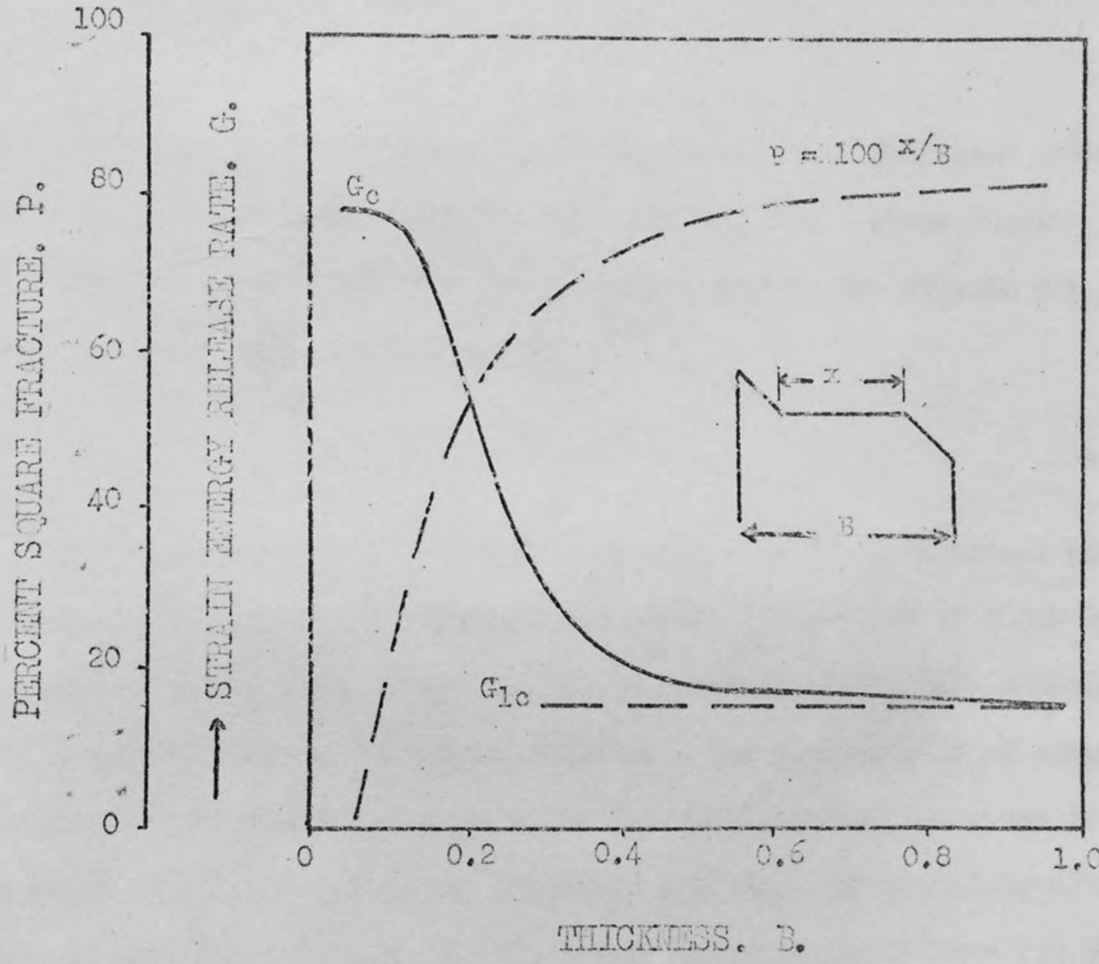

Fig. 3.10. Dependence of G_c and Fracture Appearance on Thickness of Plate Specimens. (After Srawley and Brown[41])

stress distribution may be influenced by the close proximity of the free surface and the plastic strains may actually break out to the free surface. Under these circumstances the underlying assumptions of the linear elastic stress field theories are no longer valid, and a useful determination of toughness cannot be made on these grounds. It should also be appreciated that if the crack length is too small the applied stress may well exceed the yield stress of the material before instability is reached. In all types of fracture toughness testing the nett section stress at instability should not exceed 80% of the 0.2% offset yield stress.(57)

<u>Test Procedure.</u> In section 3.3 it was shown how K_1 increases with applied stress up to the instability level K_{1c}, for a given crack situation. By introducing a geometrical factor Y, the formula can be normalised for any crack situation:

$$K_{1c} = Y \sigma (a)^{\frac{1}{2}}. \qquad \ldots .\ 3.14$$

Y is a non-dimensional polynomial incorporating the geometrical aspects of the specimen, such as thickness and width. The value of Y can be determined in two ways, theoretically by boundary collocation methods, and experimentally by compliance testing. The availability of computerised stress analysis techniques has led to the development of numerous types of specimen suitable for fracture toughness testing. It should be noted in this context that since K_{1c} is a material property, valid data can be correlated independent of the type of specimen used.

In order to determine K_{1c} therefore, from equation 3.14., since Y and a, are constants for individual tests, all that remains is to apply a tensile load across a pre-cracked notch and measure the load at which crack propagation commences. Insertion of this critical load into equation 3.14. together with values for Y and the initial crack length, a, enables K_{1c} to be calculated.

Choice of Specimen. The design of specimens for fracture toughness testing has developed rapidly over the past decade, and there is now a comprehensive range to suit many applications and test conditions. For example, three point bend specimens are ideal for quality control, since load requirements and machining costs are minimal; whereas single edge notch tensile specimens are suited to specialised testing techniques such as high temperature tests. The main factor influencing the choice of specimen and test procedure is the ultimate objective in performing the work. Fig. 3.11. shows some of the specimens available.

For plane strain fracture toughness testing it is vital that predominantly plane strain conditions should apply. A recommendation has been put forward by the A.S.T.M. E.24 committee regarding specimen dimensions, stressing that thickness and minimum crack length should exceed a characteristic of the material under test, $2.5\left(\frac{K_{1c}}{\sigma_{ys}}\right)^2$, in order that the K_{1c} value determined from that specimen be considered valid. This parameter has been empirically established by extensive testing of many materials.

Close machining tolerances are important to ensure that the geometry satisfies the calibration being used. Normally a flat bottomed notch with a root radius of less than 0.010 in. and a maximum included angle of 60° is suitable, but for special circumstances where fatigue crack initiation is difficult other techniques have been developed, such as chevron notching, and spark erosion of the notch root.

As mentioned in section 3.5. in order to simulate natural sharp crack conditions during testing, pre-cracking under low stress fatigue is employed. It is important that the fatigue cracking process be closely controlled in order that fatigue crack damage and the development of unsatisfactory fatigue cracks, (due to irregularities in the crack front contour; multi-nucleation from a blunt notch etc.), be avoided. To standardise the fatigue pre-cracking operation, A.S.T.M. E.24 committee recommend that the fatigue stress intensity $(K_f)^*$ shall not exceed 60% of

* K_f is the change in stress intensity during cyclic tensile loading.

(a) Round Notched Bar.	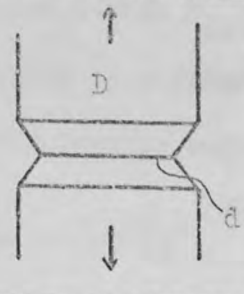	Length = 8D	Very large specimens required to obtain fracture before yield. Difficulties in fatiguing.
(b) Centre Cracked Plate.		$2a = W/6$ $B = W/4 - W/10$ Length = 4W (min)	Useful for K_c tests on thin material. Difficulties in fatiguing.
(c) Double Edge Cracked Plate.		$a = W/6$ $B = W/4 - W/10$ Length = 4W (min)	Difficulties with fatigue cracks. Generally replaced by Single Edge Notched.
(d) Single Edge Notched Plate.		a 0.6W $B = W/3 - W/8$ Length = 4W (min)	Requires only 30% material of Double Edge Notched. Useful for specialised tests.
(e) Single Edge Notched 3 & 4 Point Bend.	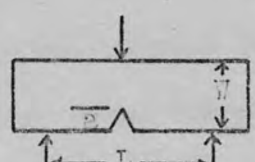	a 0.6W $B = W - W/8$ L = 4W	Easy and cheap to produce, low material and load requirement. Generally useful.
(f) Wedge Opening Load, 'C.K.S.' Type.	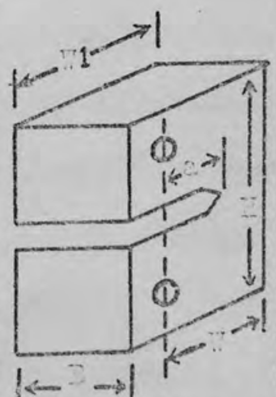	$B = W/2$ $W_1 = 1.3W$ H = 1.2W Holes = $B/2$ dia. a = 0.5W	Optimised design combines low load with small size and high measuring capacity. Ideal for directionality work.

Fig. 3.11. Various Specimens used for the Determination of Fracture Toughness.

the subsequently measured static K_{1c} value. This is achieved by limiting the amount of crack growth in a given number of fatigue cycles, which can be calculated from the following relationship by Paris:[58]

$$da/dN = C(\Delta K)^n. \quad * \qquad \ldots. 3.15.$$

In their recommendations E.24 propose that a satisfactory fatigue crack should extend not less than 0.050 in. from the notch root, in order to be outside the influence of the stress field set up by the blunt notch, and that the final 0.050 in. of fatigue crack growth should occur in not less than 50,000 cycles. It has been suggested[59], that for many materials these restrictions are too conservative and could be relaxed to a certain extent, still producing valid results.

Determination of Critical Load. Several methods have been developed for the detection of the critical load for calculation of K_{1c}, including resistivity, accoustics, photography and ink staining. The most popular method, and that recommended by A.S.T.M. E 24 committee is to plot load against the opening displacement of a notch, measured with a calibrated clip gauge. In order that the load/displacement record can be subsequently analysed, and critical load determined, it is necessary to obtain a perfectly linear response from the clip gauge. For this reason a double cantilever beam gauge incorporating four resistance strain gauges in a balanced circuit is now commonly used.

The most obvious way of measuring K_{1c} would be to test a sufficiently thick plate specimen of the material, ensuring fully plane strain conditions. This is not always convenient, however, and certainly would not be economical of material. Depending upon material characteristics, initial crack extension may take place as a rapid jump, or slow crack growth may occur throughout the nett section. In intermediate thicknesses the phenomenon of meta-instability, termed 'pop-in', can be satisfactorily employed for the determination of K_{1c}. The use of pop-in for K_{1c}

* Where C and n are material constants, and N is the number of fatigue cycles.

measurement on specimens thinner than that necessary to produce an entirely square fracture was first proposed by Boyle et. al.(60), who observed that initial extension of a crack often occurred as a distinct jump, followed by gradual extension as the load was increased. A schematic representation of pop-in behaviour in various thicknesses of material is shown in fig. 3.12. Boyle was able to show that the value of G at which pop-in occurred was the same as the value of G_{1c} determined on a sufficiently thick plate specimen.

Idealised pop-in behaviour is not always experienced in practice however, and the resulting load/displacement record is not stepped, but shows a gradual deviation from linearity. A simple analytical treatment for load/displacement records has been developed, thus eliminating the scatter introduced by individual assessment. This procedure involves detection of significant crack growth by a secant method, regardless of how the crack extension has developed, and carries with it certain qualifications to which the record must comply. It in no way affects specimen design or calculation procedures, and is analogous to the measurement of 0.2% proof stress when no distinct yield point is observed in a tensile test.

It is customary practice to determine a conditional value of K_{1c}, denoted K_Q, and from this is calculated the characteristic factor $2.5\left(\frac{K_Q}{\sigma_{ys}}\right)^2$. If this quantity is less than both the specimen thickness and crack length, and if the fatigue cracking conditions and load/displacement record are satisfactory then K_Q is taken as the required K_{1c} result.

<u>Applied Fracture Mechanics.</u> The main advantage of a fracture mechanics approach to materials assessment is that test data from laboratory specimens can be used for the selection of materials for specific design considerations. Fracture toughness will replace yield strength, or a given fraction of yield strength, as a design criterion.

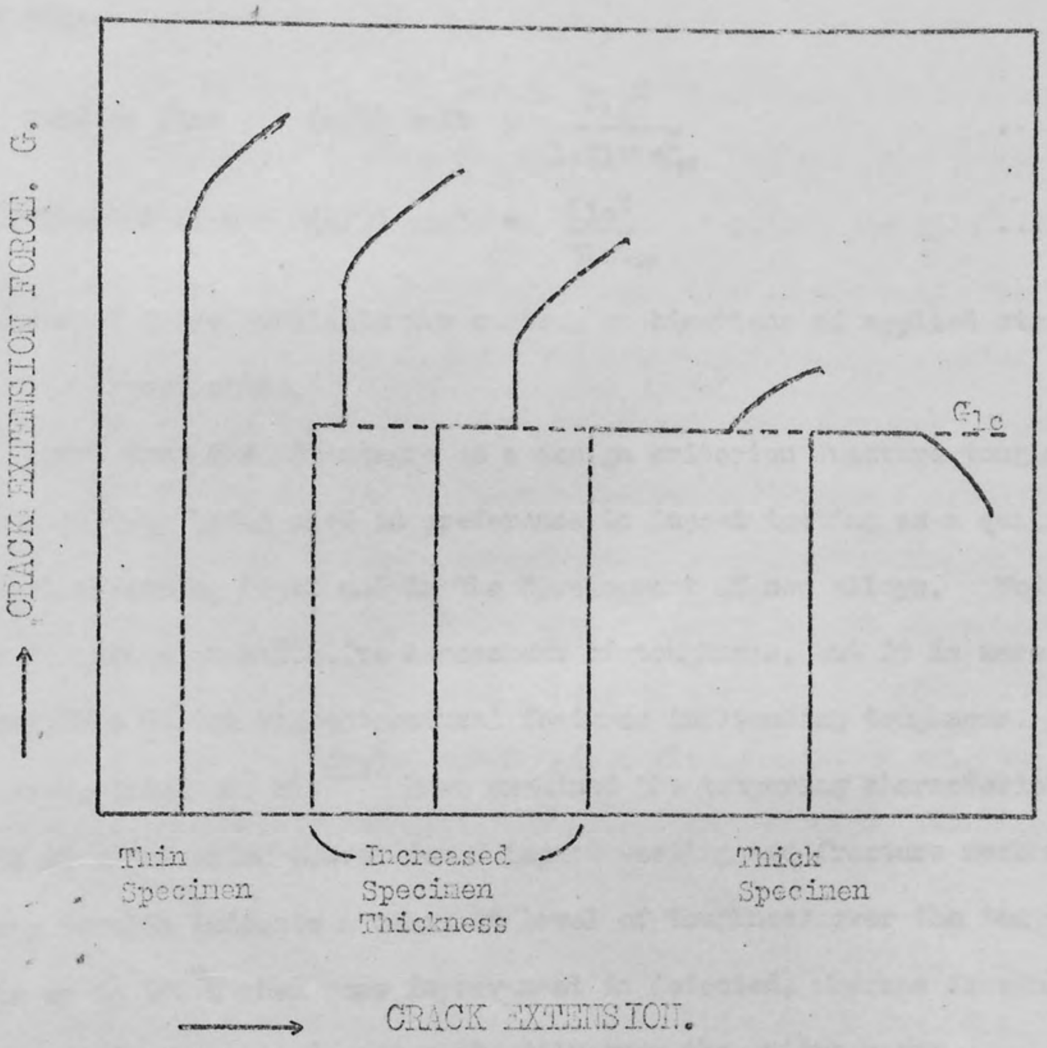

Fig. 3.12. Schematic Representation of 'Pop-in' Behaviour in Material of Varying Thickness. (After Greenwood[51])

If the plane strain fracture toughness is known, together with the stress applied to a component, it is possible to calculate the flaw size necessary for failure. Conversely, knowing the maximum size and orientation of flaw present in the component the stress for failure can be determined. Considering Q as the flaw shape parameter Irwin[61] has developed relationships between K_{1c} and σ_{app} (applied stress) and critical flaw size:

$$\text{Surface flaw} \quad (a/Q)\ \text{crit} = \frac{K_{1c}^2}{1.21\pi\sigma_{app}^2} \qquad \ldots\ 3.16$$

$$\text{Embedded flaw} \quad (a/Q)\ \text{crit} = \frac{K_{1c}^2}{\pi\sigma_{app}^2} \qquad \ldots\ 3.17$$

Values of Q are available for various combinations of applied stress and flaw aspect ratio.

Apart from its advantages as a design criterion fracture toughness is effectively being used in preference to impact testing as a quality control screening test, and in the development of new alloys. Not only does it give a quantitative assessment of toughness, but it is more susceptible to the microstructural features influencing toughness. For instance, Irani et. al.[62] have examined the tempering characteristics of EN 40 steel using conventional impact testing and fracture mechanics. Charpy results indicate a constant level of toughness over the tempering range up to 500°C when some improvement is detected, whereas fracture toughness is shown to increase steadily over the entire range.

In general many of the metallurgical features that are desired to improve fracture toughness using pre-cracked specimens are those which are effective in improving toughness on notched impact standards. The mechanism or the degree of effectiveness of a particular feature, however, may be quite different in the two situations. The pre-cracked tests will be more sensitive to factors affecting crack propagation, whereas it is likely that it will be the initiation process which is controlling tests utilising machine notched specimens.

4. METALLURGY OF CRACK INITIATION AND PROPAGATION.

4.1. Crack Initiation.

In section 3.1. it was shown that if the Griffith criterion was to hold true for metallic materials, cracks of a finite length must be present before stressing. Whilst it is known that cracks, as such, of this magnitude are not present before yielding, features are produced during deformation which are of this order. For instance slip lines across one grain leading to stress concentrations in the next approach the size of crack required to satisfy the Griffith theory. Petch(63) noted that yielding occurs at a lower stress in coarse grained than in fine grained steel, due to the large stress concentration arising from the longer slip lines in the coarse grained material, promoting unlocking of dislocations and yielding in the next grain. In both coarse and fine grained steels the unlocking stress is the same. Petch has developed a relationship connecting yield characteristics with the frictional stress resisting deformation, σ_i, and the grain size dependence:

$$\sigma_y = \sigma_i + K_y d^{-\frac{1}{2}}. \qquad \ldots . \ 4.1$$

The Petch relationship is illustrated schematically in fig. 4.1.

Stroh(64) made the first attempt to associate slip bands with the initiation of fracture by summing the stresses due to individual dislocations in a slip plane, arriving at the following equation for the initiation of a micro-crack of length L:

$$(\sigma \text{ app} - \sigma_i) = \sigma \text{ eff.} = \left[\frac{3 \pi G \gamma}{8(1 - v)L}\right]^{\frac{1}{2}}. \qquad \ldots . \ 4.2.$$

Stroh suggests that once the nucleation barrier has been overcome and a micro-crack initiated this crack would be of critical size and

Aston University

Illustration has been removed for copyright restrictions

Fig. 4.1. Schematic Illustration of the Petch Relationship(63)

result in immediate failure. In fact many micro-cracks can be present without causing failure.

In view of the inadequacy of the Stroh model, Smith and Barnby[65] have suggested an alternative mode of fracture initiation in two phase material. Consideration of dislocations piled up against a barrier such as a carbide, as in fig. 4.2, leads to the following equation for the stress to cause failure of the carbide:

$$\sigma \text{ eff} = \left(\frac{2c}{d}\right)^{\frac{1}{2}} \left[\frac{2\gamma G}{\pi(1-\nu)d}\right]^{\frac{1}{2}} \quad \ldots\ldots 4.3.$$

Thus if 2c is small and d long, (ie. long slip band and thin precipitate), the precipitate will fracture at a lower stress than postulated by Stroh. Once the crack is formed, equal lengths of slip lines cancel out leaving an unpropagated void. Unbalancing will cause the crack to propagate into the matrix on the weaker side.

Cottrell[66] discusses only the growth barrier, considering the nucleation barrier unimportant and suggests that it is growth which is the controlling factor. Cottrell proposes intersecting dislocation lines in B.C.C. metals to produce a wedge defect opening the 100 cleavage plane, as depicted in fig. 4.3. The combination of dislocations on (101) and $(10\bar{1})$ planes with Burger's vectors $^a/_2\ \bar{1}\bar{1}\bar{1}$ and $^a/_2\ \bar{1}11$ respectively, produces a dislocation of [001] with a nett lowering of the elastic strain energy:

$$\frac{3a^2}{4} + \frac{3a^2}{4} \longrightarrow a^2. \quad \ldots\ldots 4.4.$$

According to Cottrell, cracking will occur when:

$$Pnb = 2\gamma \quad \ldots\ldots 4.5.$$

(nb) can be determined from elastic strain displacements, since from fig. 4.4:

$$nb = (\sigma \text{ app} - \sigma_i)\ ^d/_\mu \quad \ldots\ldots 4.6.$$

Aston University

Illustration has been removed for copyright restrictions

Fig. 4.2. Smith and Barnby[65] Model for Initiation of Fracture at a Precipitate in Two Phase Material.

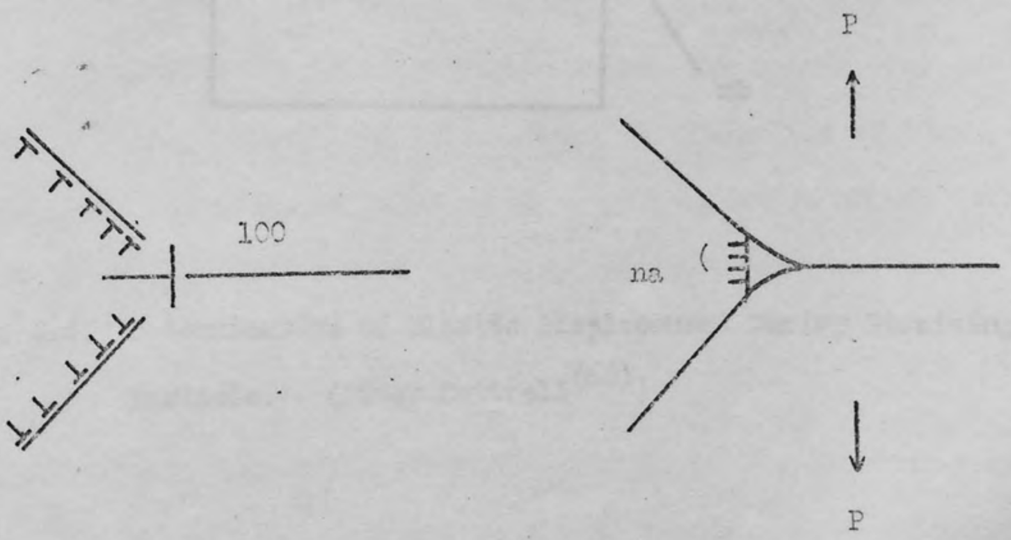

Fig. 4.3. Intersecting Dislocation Lines in B.C.C. Metals, to Produce a Wedge Defect Opening the 100 Plane. (After Cottrell[66])

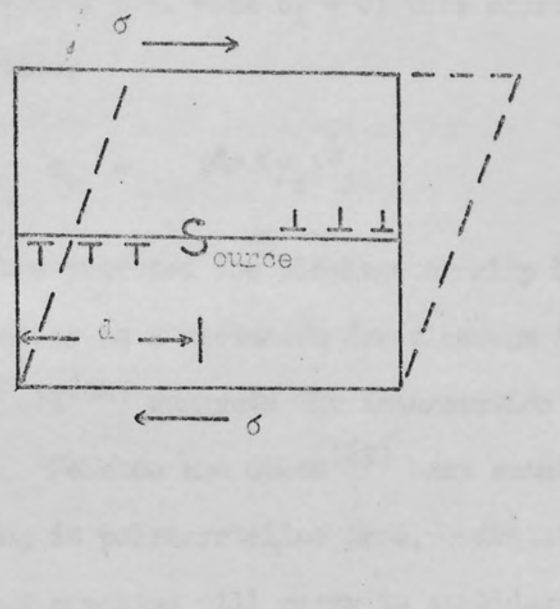

Fig. 4.4. Determination of Elastic Displacement During Straining of a Particle. (After Cottrell[66])

Substituting in Cottrell's equation and rearranging with $P = 2\sigma_y$, the condition for instability taking into account plasticity is:

$$\sigma_y (\sigma_y - \sigma_i) d = \beta \mu \gamma \qquad \ldots . 4.7$$

Where $\beta = 1$ for a plain bar, and 1/3 for a notched bar. Ignoring the effects of plasticity (ie. when $\sigma_i = 0$) this corresponds well with Griffith's equation:

$$\sigma_y = (\beta \mu \gamma / d)^{\frac{1}{2}}. \qquad \ldots . 4.8$$

Zener[67] has proposed the blockage of slip bands by precipitates and grain boundaries as a mechanism for cleavage initiation in B.C.C. metals, whilst Hull[68] suggests the intersection of mechanical twins as an alternative. McMahon and Cohen[69] have examined the initiation of cleavage cracking in polycrystaline iron, containing up to 0.035% carbon, and conclude that cracking will occur in carbides contained in quite soft pure iron during plastic straining, and the thicker the carbide the more prone it is to cleavage cracking. If the carbide is thick enough, and the micro-crack therefore long enough, it will emerge into the matrix as a Griffith crack. However, if the ferrite flows locally at the carbide/ferrite interface the local propagation into the matrix will be suppressed. Barnby[70] has compared the efficiencies of the models of Stroh, Smith and Barnby, and Cottrell, by relating K_c to the effective stress available for cracking, σ_{eff}, via the surface energy in the various models:

$$K_c = Y \sigma_{eff} c^{\frac{1}{2}}. \qquad \ldots . 4.9.$$

where Y is a geometrical parameter, and K_c is the critical stress intensity factor generated by a slip band across the cracking plane. The larger the value of Y for a given situation the greater the efficiency of the different models.

Stroh's model gave a value of 1.84, whilst those of Smith and Barnby and Cottrell gave a value of 8. The Smith and Barnby model has a Y value dependent on the precipitate size and slip band length (grain size). A large Y value will occur in coarse grained material containing thin precipitates. Y, therefore, has been shown to be a function of microstructure, and the relative efficiency of the nucleation criterion will also vary with microstructural parameters.

As an alternative to the fracture mechanics approach, Wells[71] has developed a fracture criterion based on the opening displacement of a sharp crack prior to failure, δ. At a critical crack opening displacement (C.O.D.) fast fracture will occur. Cottrell,[72] Burdekin and Stone[73], and Hahn and Rosenfield[74] have shown that a simple relationship exists between fracture toughness and C.O.D., via the yield strength:

$$G_c = \sigma_{ys} \delta_c \quad \text{.... 4.10}$$

or

$$K_c = (\delta_c \sigma_{ys} E)^{\frac{1}{2}}. \quad \text{.... 4.11}$$

This approach is currently finding wide application in low strength ductile materials where the assessment of toughness by fracture mechanics is limited by extensive plasticity. A detailed examination of the stress and strain distribution within the plastic zone, and the implications of designing on this basis are discussed by Knott[75].

4.2. Electron Fractography.

In the past, fracture has been described as 'fibrous', 'silky', 'intergranular', 'ductile' or 'brittle', but these terms are quite insufficient to describe and explain the features of most fractures. The use of electron microscopy as a tool in the examination of fracture surfaces has led to a fuller understanding and identification of individual fracture processes, such as cleavage, quasi-cleavage and micro-void coalescence.

Cleavage can be defined as the separation of a crystal along certain crystallographic planes. Metals with B.C.C. and C.P.H. structures are prone to cleavage fracture along atomic planes of high density, especially at low temperatures. Cleavage fracture in metals is always preceeded by some plastic deformation, and this combined with the fact that metal crystals are never perfect, results in the production of a stepped fracture surface, with separation taking place along parallel sets of cleavage planes. As fracture progresses these steps converge and the resulting surface examined by electron microscopic techniques exhibits typical 'river patterns'. Beachem(76) considers screw dislocations, present in the structure at grain boundaries and other features, or produced during the associated deformation, to be responsible for the formation of these cleavage steps.

In addition to grain boundaries other metallographic features such as second phases, non-metallic inclusions etc. also influence cleavage fracture in metals. In this case several fracture modes may be distinguished on the same fracture surface. A common feature of mixed mode fractures are flat facets which may comprise a considerable portion of the fracture surface, especially at temperatures near to the ductile/brittle transition. These individual facets are usually larger than fine scale metallographic features and can show river patterns and be very like true cleavage in appearance, but it has been shown that the orientation cannot be related to the cleavage planes of the matrix. The term 'quasi-cleavage' has been used to differentiate between these facets and true crystalline cleavage. Quasi-cleavage is associated with low energy fracture but shows features not normally connected with true cleavage, indicating the presence of localised plastic deformation. These are ridges and tongues which protrude from both fracture surfaces.

The fracture mode important in most ductile and tougher materials is the coalescence of micro-voids. The initiation of voids is dependent upon the existance of defects or heterogeneities present in the material or produced during plastic deformation. This can occur by fracture of inclusions and second phase particles or breakdown of the matrix/particle interface. It is known that they are initiated in the plastic zone ahead of the crack tip where they tend to develop into rounded holes. During further plastic flow the voids continue to grow, the matrix between the voids necking down and eventually separating by rupture, termed coalescence. The fracture surface created by coalescence of voids is made up of rounded concave depressions, known as 'dimples', and first identified by Crussard.(77)

Beachem has been able to show from the shape of dimples on electron fractographs, the type of stress required for their formation, and designates three types. Dimples which are roughly equiaxed or hemispherical are produced under the influence of normal plastic strain. Shear rupture dimples are produced under normal plastic strain and shear strain, and are characterised by being elongated in opposite directions on opposite halves of the fracture surface. Shear rupture dimples would be characteristically present on shear lips and the sides of cup and cone fractures. Tearing occurs under the influence of non-uniform strain, such as the tip of a crack, producing elongated dimples in the same direction on both fracture surfaces.

The size of dimples on a fracture surface is determined by two factors, the size of the initial void, which is governed by the size of the inclusion or precipitate particle, and the amount of plastic growth permitted before the void coalesces with another free surface. The latter is dependent upon the distance between voids and the characteristics of the deforming matrix.

Intergranular failure occurs in many metal systems due to segregation of impurity or alloy elements to form precipitate particles, continuous films or composition gradients at the grain boundary. This results in a variation in mechanical, physical, and chemical properties of the grain boundary from the matrix. Depending on the extent of brittle grain boundary constituents the failure may be partly intergranular and partly transgranular. The amount of plastic deformation absorbed by the adjacent grains during intergranular fracture influences the subsequent fracture surface. Beachem and Pelloux[41] have shown that intergranular failure can be associated with a variation of fracture surfaces, from being quite flat and featureless, to having a completely dimpled surface. Cleavage, fatigue markings, and other features have also been associated with intergranular separation.

4.3. Influence of Inclusions on Ductile Fracture.

The most important single structural effect on ductile fracture, is that due to second phase particles, such as inclusions, precipitates, and dispersions. In high strength steels, and high strength non-ferrous alloys, the fracture process is generally one of crack or cavity nucleation at hard second phase particles followed by internal necking of the matrix. resulting in typical dimpled rupture fracture surfaces. Since work must be done in the nucleation of the cavities, and in the subsequent coalescence process, the distribution, size, and characteristics of the dispersed particles are major metallurgical factors controlling the toughness of the alloy, since they strongly affect the level at which energy is absorbed in the plastic zone as crack propagation occurs.

Several theories have been proposed to explain the phenomenon of crack nucleation and its subsequent growth at second phase particles, most notably by Ashby,[78] Gurland[79] and McClintock.[80] Each of the models approaches the problem from a different aspect, Ashby suggesting a dislocation mechanism and the formation of a prismatic loop or vacancy loop, at the matrix/particle interface under the influence of the applied stress. Movement of the vacancy loop, by glide, away from the particle enables further loops to be produced, resulting finally in joining of the loops to form a crack. The Ashby model can be expressed as:

$$\sigma_T = \alpha \frac{\varepsilon\, d}{1} \qquad \ldots\ 4.12$$

The interface will crack when σ_T reaches a critical value, thus predicting that holes will form at larger particles at lower strains than at smaller particles.

Ashby's model does not take into account the effect of hydrostatic tension and its effect both on the flow properties of the particle and matrix, which could lead to stress relief at the interface. McClintock, however, takes these factors into consideration including the effect of work hardening, allowing effects such as notch geometry and necking to be described. The main objection to the McClintock model is that it is based on studies of plasticene containing polystyrene spheres, and therefore considers only the case where holes nucleate at zero strain by complete separation of the particle/matrix interface. Thus for most general cases where the interface retains at least a partial bond even up to high strains, or when hole formation occurs by cracking of the particle, the McClintock appreach will be inapplicable without some modification.

Gurland and Plateau[81] have examined cavity nucleation in Al/Si alloy and pearlitic steel and relate the elongation to rupture to the volume fraction of inclusions, with the micro-cracks growing into cavities by concentration of plastic strain. From this work Gurland and Plateau express the elongation to rupture as a function of the volume fraction only, for the conditions of hard precipitates and inclusions able to deform within the matrix. The model is shown to hold well for the experimental results of Edelson and Baldwin[82] on copper, strengthened with precipitates of Cr, alumina, Fe and Mo shown in fig. 4.5, and can be expressed as:

$$\varepsilon_R = \varepsilon_o + \tfrac{1}{2}\log\left[1 + \frac{K_2}{K_1}^2 \left(2/3\,\frac{1+2f}{f}\,e^{-\varepsilon R/2} - 2\right)^2\right] \qquad \ldots\ 4.13$$

where ε_R is the elongation to rupture, ε_o the elongation before cracking,

Aston University

Illustration has been removed for copyright restrictions

Fig. 4.5. Experimental Data of Edelson and Baldwin[82] on Fracture Ductility of Copper-Base Composite Alloys.

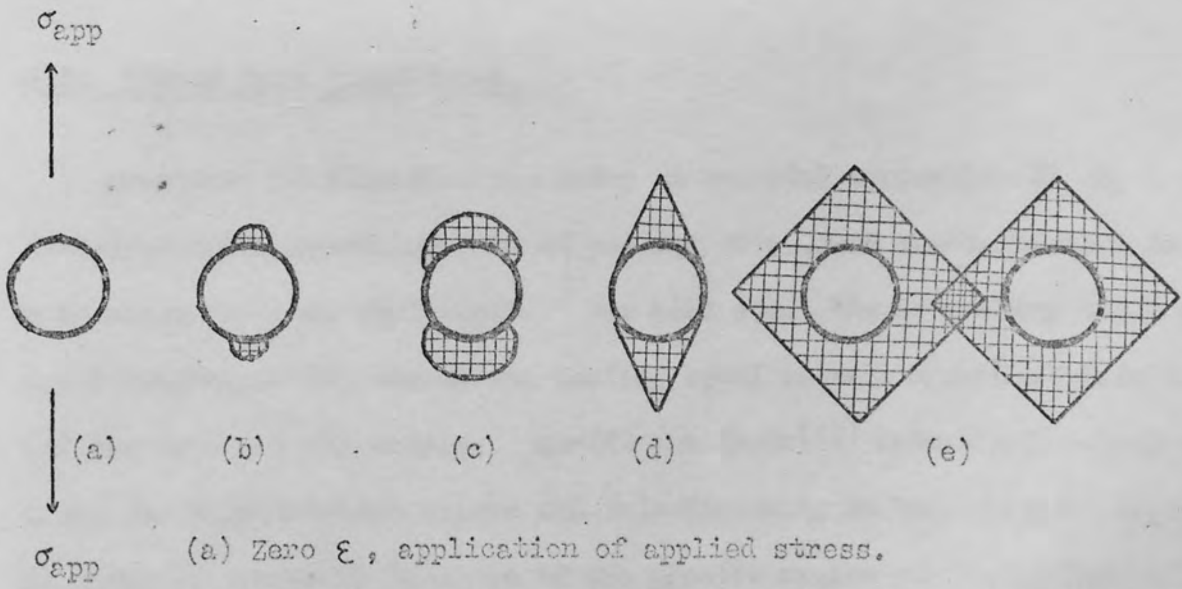

(a) Zero ε, application of applied stress.

(b) Initial separation of matrix/particle interface at low strain.

(c) & (d) Growth of holes with further strain.

(e) Coalescence of holes at high strain, close to true fracture strain.

Fig. 4.6. Void Coalescence (Schematic). (After Palmer & Smith[83], & Puttick[84])

K_1 and K_2 constants, and f the volume fraction of precipitate.

The fundamental point to emerge from all sources is that as the volume fraction of second phase particles is increased there is a rapid drop in ductility. From the studies mentioned above, and many others it becomes evident that the formation of holes at precipitates and the concentration of deformation in sharply defined bands dominates the process of ductile fracture. Either of these phenomenon may occur first, the presence of holes concentrates the strain into narrow bands emanating from the holes; whilst slip bands impinging on particles causes holes to form around the particles. It would appear that slip-induced hole formation is more typical.

Irrespective of the manner in which the cavities are initiated, with increasing stress the holes will grow by a mechanism involving plastic strain, and finally, after reaching a critical size approaching the inter-particle spacing coalescence occurs rapidly. The fundamentals of the growth and coalescence stages are not so fully understood, but are schematically represented in fig. 4.6, after Palmer and Smith,[83] and Puttick.[84]

4.4. Strain Rate Sensitivity.

Practical difficulties may arise in material evaluation if an increased crack speed, or rate of loading of a fixed crack, results in a decrease in crack resistance. For mild steel the decreasing trend of crack toughness with increasing loading speed is well known, but this is not the case for all metals. Krafft and Irwin[41] have shown a reversed trend for hard titanium alloys and this disparity in behaviour is explained in terms of the absolute slope of the plastic region of the logarithmic, stress strain curve, (θ), to changes in loading speed. For B.C.C. metals the value of θ tends to remain constant and toughness will be proportional to yield strength, which increases in all metals with increasing strain rate. Thus n and K_{1c} vary inversely with strain rate:

$$\text{Since} \quad n \sim \frac{\theta}{\sigma_f}$$

$$n \; \& \; K_{1c} \propto \frac{1}{\sigma_{ys}}$$

Beeuwkes[85] has observed in F.C.C. metals, however, that θ increases with speed of testing. If this increase in θ is a stronger effect than the increasing flow stress, σ_f, then an increasing trend in n and K_{1c} with speed of testing would follow.

Krafft[86] has demonstrated the similar dependence of n and K_{1c} upon strain rate and temperature over a wide range, using data from compression tests, which were preferred to tensile, since: (a) flow is uninterrupted by failure at low temperatures or high strain rates, and (b) compression tests are well adapted to impact testing. Making the assumptions that tensile instability and rupture occurs in a small elemental fracture cell adjacent to the crack front, illustrated in fig. 4.7, and that tensile plastic strain distribution approaching the crack can be regarded as increasing up to the elemental cell, then:

$$d_T = \frac{1}{2\pi} \left(\frac{K_{1c}}{nE} \right)^2 \left(\frac{n}{\varepsilon_T} \right)^2. \qquad \ldots.\ 4.14$$

where ε_T is the tensile strain, and d_T is a constant, representing the distance ahead of the crack front where ε_T becomes equal to n, the tensile instability strain.

By making a correction for adiabatic heating which occurs in compression testing (in fracture toughness tests the yield zone is so small that isothermal conditions prevail at all speeds), Krafft was able to match K_{1c} versus $\overset{o}{K}$ and n versus $\overset{o}{\varepsilon}$, data, shown in fig. 4.8, reaching the conclusion that d_T, the size of the individual fracture cell, is a constant related to K_{1c} and n:

$$K_{1c} = En \; (2\pi d_T)^{\frac{1}{2}} \qquad \ldots.\ 4.15$$

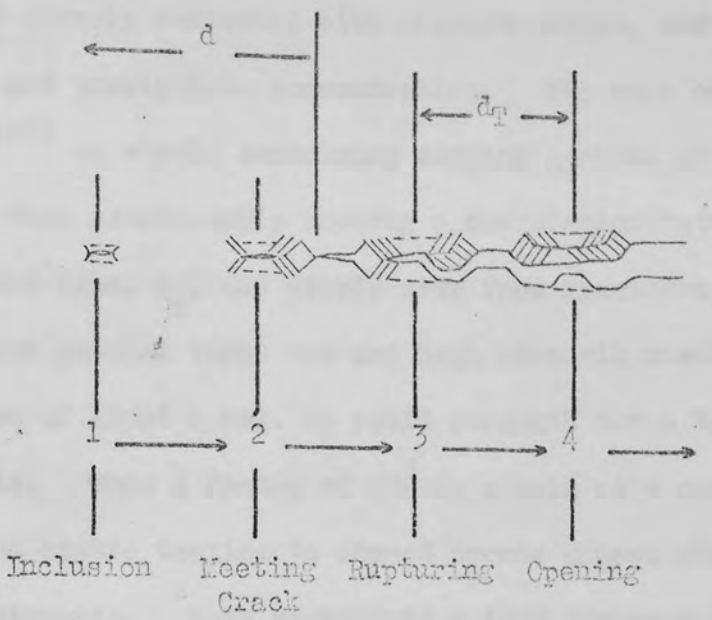

Fig. 4.7. A Model for the Interception of an Inclusion-Started Void by the Crack Front, Resulting in Dimple Formation. (After Krafft[86])

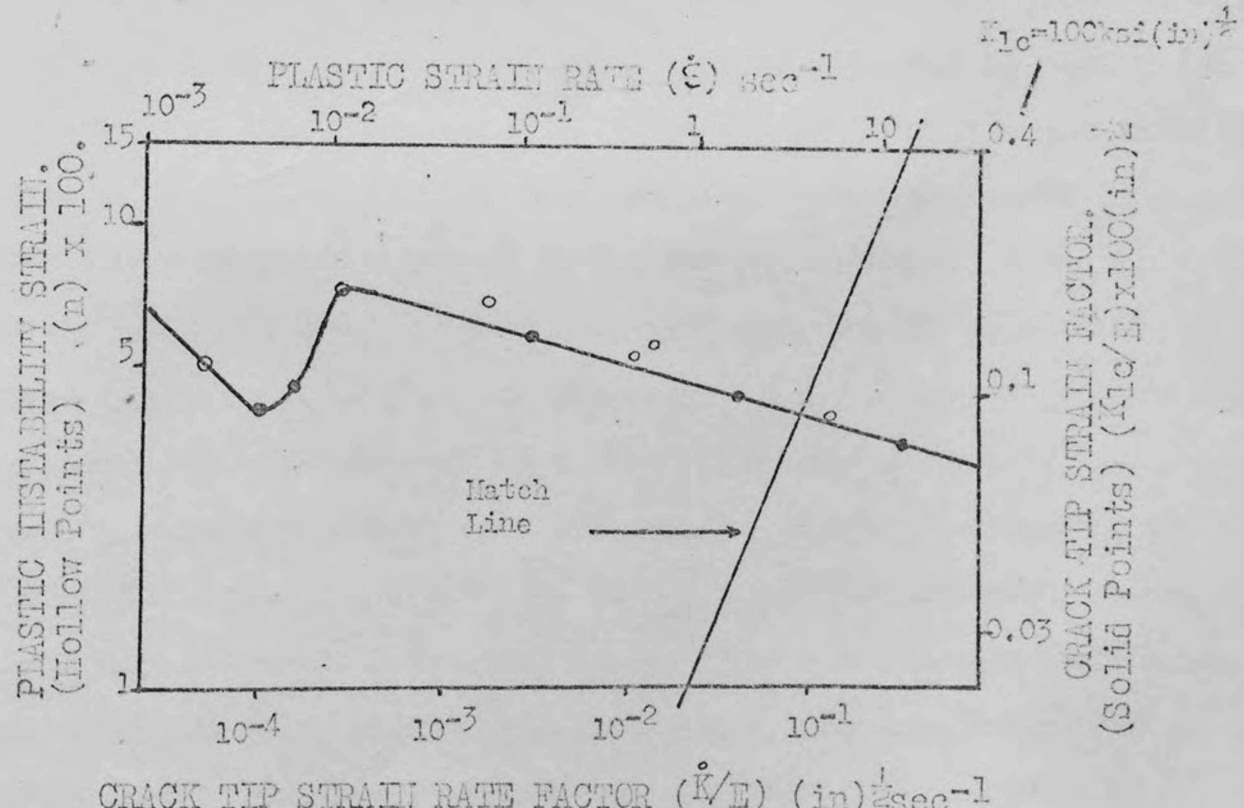

Fig. 4.8. Correlation of Crack Toughness K_{1c} with the Strain Hardening Exponent n for Mild Steel, Tested at -320°F. (After Krafft[86])

Thus according to Krafft, K_{1c} should increase directly with $(d_T)^{\frac{1}{2}}$, a constant closely connected with microstructure, and more particularly, inclusion and precipitate concentration. The work of Birkle Wei and Pellisier[87] on steels containing varying amounts of sulphur has confirmed this relationship showing a correlation between calculated process zone size, d_T, and dimple size from fractographic examination.

In more general terms low and high strength steels typically exhibit an increase of about 6 ksi. in yield strength for a tenfold increase in strain rate. Thus a factor of 10^5 in strain rate corresponding to a change from static testing to impact speeds causes about a 30 ksi. increase in yield strength. This represents a 100% increase in plain carbon steel and there will be a large effect on crack toughness. For high strength steel this may only represent a 15% increase, and K_{1c} will then be relatively insensitive to strain rate.

5. EXPERIMENTAL PROCEDURE.

5.1. Programme.

Three preliminary trials were conducted to determine the feasability of applying fracture toughness testing to cast material. Particular attention was paid to reproduceability, directionality, residual stresses, and the need for fatigue pre-cracking.

The influence of carbon content on the fracture characteristics of a basic composition of 15% chromium, less than 0.5% silicon, and 0.75% manganese was investigated over the range 0.8 to 3.4% carbon. A series of alloys at six carbon levels, within this range, was examined, all of which solidified within the austenitic loop discussed in section 2.3. A metastable austenitic matrix surrounded by an interdendritic hypo-eutectic network of chromium carbide is produced on subsequent cooling. The highest carbon level investigated (3.4%) corresponded approximately to the eutectic composition. By heat treatment of the austenitic material the effect of varying carbon content in a martensitic matrix was also investigated. Optimum heat treatment conditions were determined with respect to hardness and fracture toughness.

Breakdown of the embrittling carbide network was achieved by hot working, and by spherodisation at a temperature of 1150°C. Material of 0.8% carbon content was used in the forging trial where 50% unidirectional deformation was achieved on a drop hammer. Fracture toughness tests were carried out in the as forged condition and after heat treatment. The effects of spherodising were examined at all carbon levels. The 1.4% carbon alloy was used in an experiment involving variation of spherodisation time.

Changes in grain size over a wide range were accomplished in the 1.4% carbon alloy by the use of various moulding techniques and section sizes

Strain rate sensitivity was measured in both austenitic and martensitic material by testing over a range of speeds covering five orders of magnitude.

Structural correlation in terms of the Krafft(86) hypothesis has been observed in martensitic structures. Fractographic and metallographic evidence confirmed this relationship.

A strain induced transformation was observed in some of the austenitic alloys tested, and an attempt was made to determine the contribution of this phenomenon to plane strain fracture toughness.

The theoretical stress required to nucleate cracks in carbides has been calculated, and compared to the applied stress at which carbide cracking has been observed. The importance of carbide morphology in the determination of K_{1c} has also been demonstrated.

Optimum composition for a low carbon austenitic alloy has been proposed, and a survey made of the fracture properties of the alloys likely to be most competitive in service. A direct comparison of the relative properties of these alloys was made by determination of the critical stress levels for a given defect size.

5.2. Material Production.

Charges were made up from commercial purity raw materials and melted in a 50 kg. capacity high frequency induction furnace. Low carbon ferro-chromium (less than 0.1% C); low sulphur and phosphorus pig iron; ferro-manganese; and high quality mild steel scrap were the constituents of most heats. High carbon ferro-chromium (6%C) was used in the production of the higher carbon alloys. Pouring temperature was controlled, in the hand ladle, at 100°C above the melting point, from 1400°C at 3% carbon to 1575°C at 1% carbon.

The bulk of the material was cast as four inch square, ½ inch thick blanks, suitable for use as crackline loaded or bend specimens. Sand castings were moulded in synthetic green sand and cast horizontally in pairs, sharing a $1\frac{1}{2}$ inch square 4 inch long feeder. A swirl gate was incorporated into the running system to eliminate slag from the top surfaces of the castings, as shown in fig. 5.1.(a). All material was allowed to cool to room temperature in the mould.

Other moulding techniques were used to achieve grain size variation in the 1.4% C alloy. A 4 inch square, 6 inch long block was sand cast and allowed to cool naturally. Blanks, $\frac{1}{2}$ inch thick, were extracted from positions midway between the ends of the block and the central zone near a 4 inch diameter exothermic feeder. In this way sound material, representative of the cooling conditions in the relatively large casting was obtained in the form of fracture toughness specimens.

Chill castings were produced from graphite (Acheson Grade CS) moulds as $\frac{1}{2}$ inch thick plates, and $\frac{1}{2}$ inch thick coupons. The plates were cast individually in a vertical four part graphite mould, with a bottom in-gate and tapered feeder head, illustrated in fig. 5.1.(b). The coupons were produced in sets of three, in a two part graphite mould. A proprietary mouldcoat was sprayed onto the surfaces of the graphite moulds, which were pre-heated to 400°C prior to casting. A grain size intermediate between the chill and sand cast material was obtained by using a silliminite mould. This was pre-cast, fired, and set into a sand moulding box, using the running system described above.

Material for the hot working trial was produced as 1 inch thick, 3 inch square blanks from a 0.8% carbon melt. The forging operation was performed on a 10 cwt. drop hammer within a temperature range of 1150°C to approximately 950°C. Fifty percent reduction in thickness (1 inch to $\frac{1}{2}$ inch) was achieved after three reheating cycles with 6 to 10 blows per cycle. Four inch square crackline loaded specimens were taken from the forged stock, but subsequent tests to determine fracture toughness in the three dimensions relative to the forging direction necessitated the use of

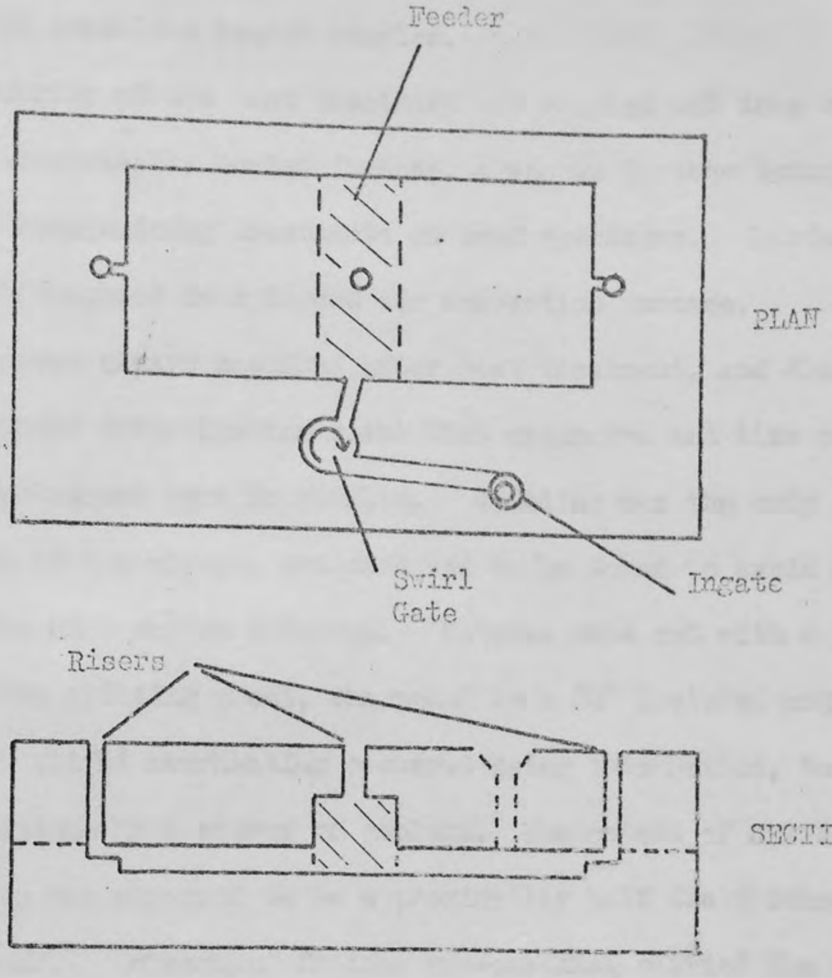

(a) Running System used for Sand Casting 4 inch Square Blanks.

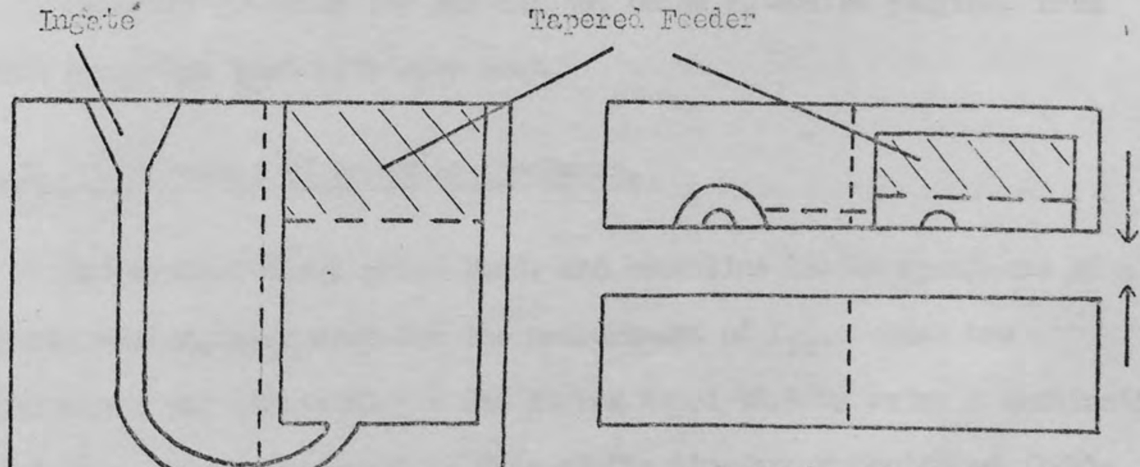

(b) Graphite Mould used for Chill Casting 4 inch Square Blanks.

Fig. 5.1. Moulding Technique for Sand and Chill Castings.

two inch span bend specimens, which were machined from the fractured halves of the crackline loaded samples.

The majority of the heat treatment was carried out in a controlled atmosphere electrically heated furnace, a vacuum furnace being used for some of the homogenising treatments on bend specimens. Hardened material was tempered in a forced air convection furnace.

Blanks were always machined after heat treatment, and the nature of the alloys under investigation meant that expensive and time consuming machining techniques were inevitable. Grinding was the only means of shaping most of the alloys, and care had to be taken to avoid grinding cracks in the high carbon material. Notches were cut with a 3/32 in. thick abrasive slitting wheel, sharpened to a 60° included angle for the final cut. Slight overheating occurred using this method, but this was kept to a minimum by a stream of coolant. The extent of overheating at the notch tip was observed to be approximately half the thickness of the slitting wheel. Subsequent fatigue pre-cracking carried the effective crack tip well beyond this point. The holes were inserted in crackline loaded specimens by spark erosion, using copper electrodes. Attempts to spark erode the notch, and experiments with hard graphite electrodes, were abandoned due to excessive electrode wear.

Chemical analysis was carried out on an automated Polyvac, from coin specimens cast with each heat.

5.3. Measurement of Fracture Toughness.

Established three point bend, and crackline loaded specimens of a recent design, were used for the measurement of K_{1c}. Each has advantages and disadvantages and it was hoped that by using a combination of both, optimum use could be made of the time and material available.

The ability of crackline loaded specimens to arrest an unstable crack in all but the most brittle of the alloys tested, facilitated the study of crack tip deformation. This was accomplished by extraction of a complete plastic enclave, containing the arrested crack tip and its associated plastic zone; or by preparation of the specimen surface before testing, and subsequent examination. The technical benefits of the crackline loaded design must be weighed against the far greater cost of production, in both material and workshop time, when compared to the three point bend specimen.

Since the crackline loaded specimen was a new design a calibration curve had to be constructed by interpolation of existing data(88) for other tensile specimens. An experimental compliance calibration was carried out as a check on the specimen design, and the entire testing procedure. A good agreement was achieved between the theoretical and experimental methods. Details of the compliance calibration are given in the Appendix. The standard W/4 calibration curve published by A.S.T.M.(88) was used for bend tests. A check on the reproducability of K_{1c} from both types was made by preparing bend specimens from the fractured crackline loaded halves.

Fatigue pre-cracking on an Amsler Vibrophore fatigue machine was carried out according to the A.S.T.M. recommended practice (final 0.050ins. in 50,000 cycles). A preliminary experiment in which faster rates of fatigue crack growth, and machined notches were used, emphasised the importance of pre-cracking. The figure of 0.0005 E suggested by B.I.S.R.A.(89) as an estimate of the propagation stress intensity range was found to be generally satisfactory. It was necessary to exceed this value for some alloys with a high K_{1c}/σ_{ys} ratio, such as the low carbon homogenised series. The load required for initiation of a fatigue crack was usually some 40 to 50% above the propagation load. Fatigue crack growth was followed with the aid of a low power binocular microscope, and the final 0.050 inch of growth estimated from graduations made on the surface of the specimen. Total fatigue crack growth for most specimens was at least 0.100 inch.

Fracture toughness testing was performed on a 5000 kg. capacity Instron machine with variable crosshead speed. A clip gauge was constructed to a design suggested by B.I.S.R.A.,[90] and illustrated in fig. 5.2. Four 350 ohm strain gauges were connected in a Wheatstone Bridge balanced circuit, and excited by a Boulton Paul C 52 transducer amplifier unit. The amplified response from the clip gauge together with the load signal from the Instron load cell, was fed into a Bryan's X - Y plotting table. A load/opening displacement record was obtained for each test. Location of the clip gauge across the notch was by means of attachable knife edges positioned accurately with a spacing shim. The clip gauge was calibrated and checked for linearity with a vernier micrometer (see Appendix).

Bend specimens were tested on a jig with friction free hardened steel rollers, supported on adjustable bosses to accommodate a span of 2 to 8 inches. The grips used for the crackline loaded specimens incorporated needle roller bearings in the head, to minimise the frictional effects due to rotation during testing.

Fatigue crack length was measured on a travelling stage microscope, an average value being taken from the furthest and least advanced points of the crack front, as recommended by B.I.S.R.A.[89]. The critical load was determined from the load/displacement record using the 5% offset procedure, which estimates significant crack growth when distinct 'pop-in' is not evident. After the preliminary trial to check reproducability of results, all tests were carried out at least in duplicate, and whenever possible in triplicate. This was in accordance with a statistical analysis of early results, which indicated that a minimum of two specimens were required for a 90% confidence limit of obtaining a K_{1c} value between $\pm$ 2 ksi $(in)^{\frac{1}{2}}$ of the mean.

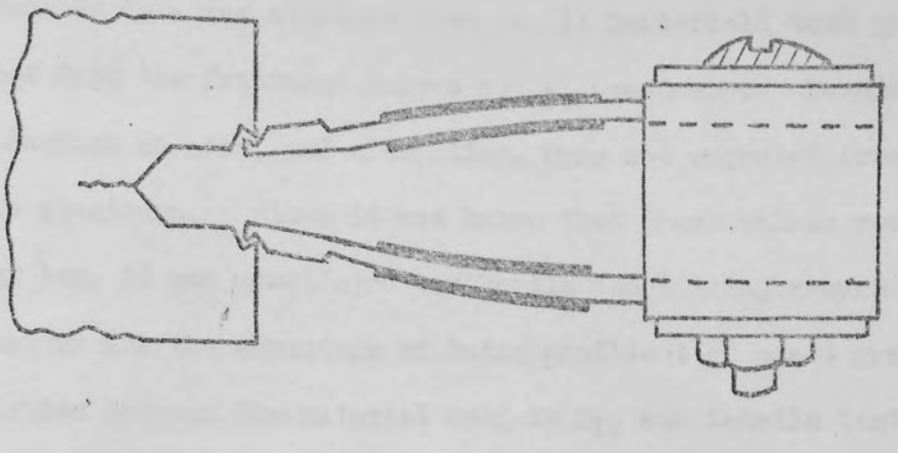

(a) Gauge Mounted on Specimen.

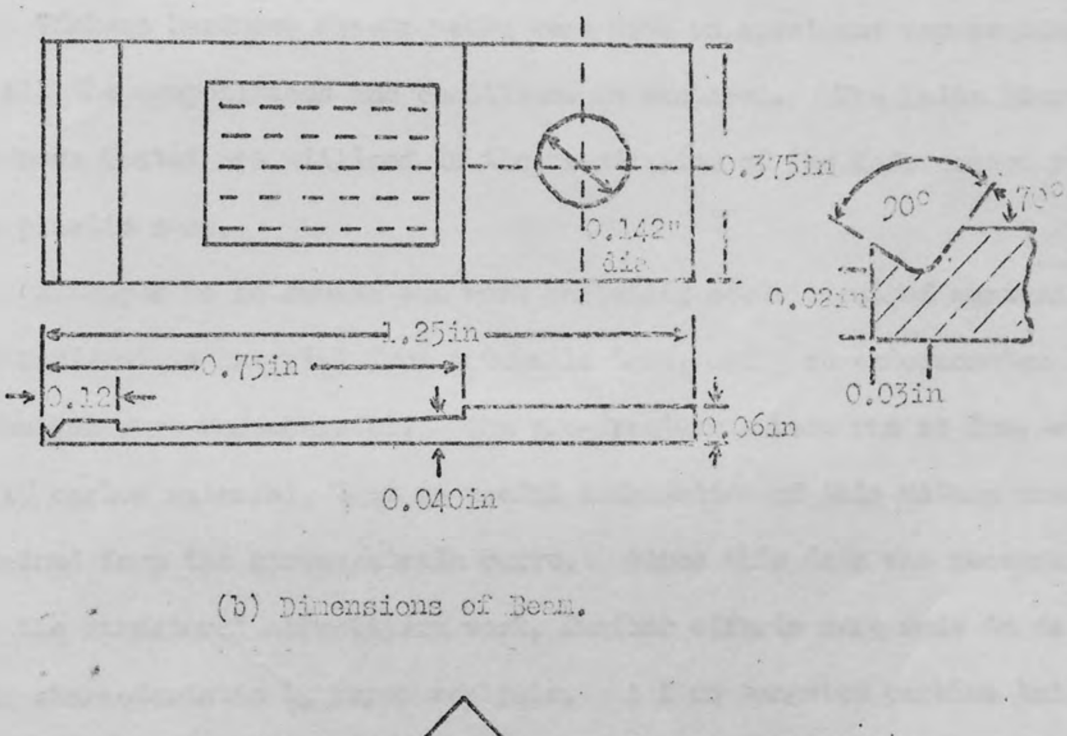

(b) Dimensions of Beam.

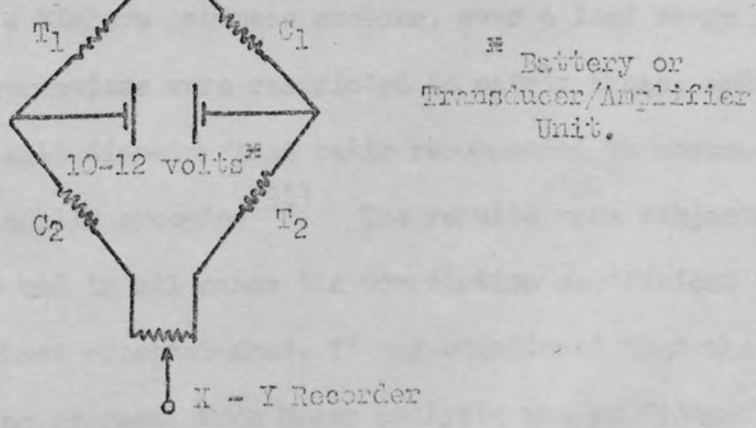

(c) Bridge Measurement Circuit.

Fig. 5.2. Details of Tapered Beam Displacement Gauge.

5.4. Mechanical Testing.

Tensile data was obtained from no. 11 Hounsfield test pieces machined from the fractured halves of K_{1c} specimens. Meaningful results for reduction in area, and elongation, were not expected from these small tensile specimens. Since it was known that these values would inevitably be very low, it was considered worthwhile sacrificing accurate data of this nature for the advantage of being confident of exact grain size correlation between the material used in K_{1c} and tensile tests. The tests were carried out at room temperature on the Instron machine, using a strain rate of 1% per minute.

Vickers hardness measurements were made on specimens representative of all the compositions and conditions encountered. The Leitz Micro Hardness Tester was utilised in the examination of the deformation within the plastic zone.

Attempts to determine the work hardening coefficient of austenitic and martensitic material from a tensile test, using an extensometer technique were unsuccessful. The pre-fracture strain was so low, even in 1% carbon material, that no useful information of this nature could be obtained from the stress/strain curve. Since this data was necessary for the structural correlation work, further efforts were made to determine this characteristic by Meyer analysis. A 1 mm tungsten carbide ball indentor was used on a Vickers hardness machine, over a load range from 15 to 50 kg. The impressions were restricted to matrix areas, and all loads were above the ball diameter/load ratio recommended to ensure that the yield point was locally exceeded[91]. The results were subjected to a regression analysis and in all cases the correlation coefficient was above 0.90. Under these circumstances, it was considered that the value of work hardening exponent from Meyer analysis was sufficiently accurate for the required purpose.

5.5. Physical Examination.

Normal metallographic techniques were used extensively. The etchant found to be most successful on the high chromium alloys was Picrol, a saturated solution of picric acid in alcohol, acidified with 4% hydrochloric acid. This solution stains austenite a light yellow colour, martensite brown, and leaves carbides and ferrite unattacked.

The volume fraction of carbides in the various structures was estimated on a Quantimet microscope. Ten areas were selected at random, at 150 X magnification, for each determination.

A limited number of two stage carbon replicas were taken, and examined in a Phillips EM 200 Electron Microscope. Difficulties were experienced in the preparation of surfaces suitable for plastic replica stripping, due to preferential etching of areas adjacent to the carbides. This effect was particularly marked during electro-polishing, although several electrolytes were tried. It also occurred to a lesser extent during chemical etching.

A comprehensive fractographic survey was made on a Cambridge Scanning Electron Microscope. Freshly cracked fracture surfaces were preserved in a dessicator, and protected with a coating of liquid plastic, prior to cutting specimens suitable for examination on the stereoscan. The plastic coating was subsequently removed with chloroform, and the fracture surface degreased and cleaned with carbon tetrachloride, in an ultrasonic bath. The stereoscan was also used for a more detailed examination of plastic zone enclaves, especially those from the free surface, where plastic deformation makes optical microscopy difficult.

6. RESULTS.

Each aspect of the work is considered as a separate experiment, and tabulated in the following order:

Table	6.1.	.. ..	Chemical Analysis.
"	6.2.	.. ..	Tensile and Hardness Tests.
"	6.3.	.. ..	Volume Fraction of Carbides.
"	6.4.	.. ..	Preliminary Trial 1 on Notch Acuity.
"	6.5.	.. ..	" " 2 on Directionality and Reproducability.
"	6.6.	.. ..	" " 3 on Residual Stress.
"	6.7.	.. ..	Fracture Toughness of Austenitic Material.
"	6.8.	.. ..	Austenitising Temperature.
"	6.9.	.. ..	Effects of Austenitising Time and Tempering Temperature on K_{1c}.
"	6.10.	.. ..	Fracture Toughness of Martensitic Material.
"	6.11.	.. ..	Rate of Application of Stress Intensity.
"	6.12.	.. ..	Forging Trials.
"	6.13.	.. ..	Effect of Common Alloying Elements on S.I.M. Formation.
"	6.14.	.. ..	Influence of S.I.M. on K_{1c}.

The thickness of all material is ½ inch, unless otherwise stated, and solidification and heat treatment procedures are described by the notation shown on page 1, and 2.

Chemical Analysis.

Six carbon levels were examined within the range 0.8 to 3.4% carbon. Details of the chemical analysis determined on an automated Polyvac from coin samples cast with each heat are shown below:

TABLE 6.1.

Heat Number	C	Si	S	P	Mn	Ni	Cr
1	0.82	0.44	0.064	0.031	0.56	0.18	16.3
2	0.78	0.75	0.028	0.037	0.73	0.22	15.5
3	0.84	0.51	0.029	0.029	0.63	0.21	16.0
4	1.06	0.77	0.038	0.030	0.77	0.20	15.5
5	1.06	0.75	0.029	0.031	0.62	0.18	14.6
6	1.16	0.63	-	-	0.88	0.18	16.7
7	1.30	0.82	0.031	0.032	0.67	-	15.5
8	1.46	0.59	-	-	0.78	0.18	16.4
9	1.47	0.47	-	-	0.72	0.18	15.8
10	2.1	0.64	0.042	0.038	2.0	0.24	14.8
11	2.82	0.58	0.034	0.048	2.89	0.11	15.5
12	3.4	0.68	0.050	0.062	2.4	0.23	14.0

Tensile Test.

Number eleven Hounsfield test pieces were machined from fractured halves of toughness specimens and tested in duplicate.

Young's modulus (E) determinations were made on modified no. 15 Hounsfield test pieces with a 2" gauge length.

The results of Vickers hardness are also included.

TABLE 6.2.

Heat No. & Treatment	% C	H_V 30	UTS ksi
1 SC/AC	0.8	425	84.5
4 SC/AC	1.1	320	74.0
7 SC/AC	1.4	350	97.0
10 SC/AC	2.1	485	110.0
11 SC/AC	2.9	510	114.0
12 SC/AC	3.4	530	*
1 SC/HT	0.8	580	144.0
4 SC/HT	1.1	630	152.0
7 SC/HT	1.4	700	161.5
10 SC/HT	2.1	750	125.0
11 SC/HT	2.9	825	122.0
12 SC/HT	3.4	850	*
9 SC 6"	1.4	355	101.0
7 SC ½"	1.4	362	96.5
9 Sill ½"	1.4	370	94.0
7 CC ½"	1.4	354	89.0
8 CC ¼"	1.4	385	77.5
		E psi x 10^{-6}	
4 SC/AC	1.1	24.4	
4 SC/HT	1.1	27.4	

* Test piece fractured during machining.

The Volume Fraction of Carbides.

The volume fraction of carbides in material of varying carbon content, grain size, and homogenisation time was estimated using the Quantimet microscope.

TABLE 6.3.

% C	% Vol. Carb.	
	AC	H.
0.8	4	1
1.1	10	4
1.4	18	9
2.1	27.5	14
2.8	35	22
3.4	37.5	27.5

1.4% C Condition.	% Vol. Carbide.
SC 6"	18
SC ½"	18
Sill ½"	17
CC ½"	17
CC ¼"	17
H ½hr.	18
H 2 hr.	18
H 4 hr.	15
H 8 hr.	9
H 16 hr.	6

Preliminary Trial 1 on Notch Acuity.

To determine the effect of notch acuity and fatigue pre-cracking, K_{1c} was measured under five different notch tip conditions varying from a blunt notch to fatigue pre-cracking under the low stress conditions recommended by A.S.T.M. Assessment of the plastic zone diameter ($2r_y$) was made on the free surface of the fracture toughness specimens after crack propagation had occurred.

Material:- Heat 6 1.1% C SC/AC.

Specimen:- 3 inch span bend.

TABLE 6.4.

Crack Tip Details.	2ry mm. Plane Stress	K_{1c} ksi(in)$^{\frac{1}{2}}$	Av. K_{1c}
Blunt Notch.	2.0	37.0	37.3
(ρ = 0.025 in)		37.5	
Sharp Notch	1.5	36.0	34.6
(ρ = 0.010 in)		33.1	
Fatigue Precracked	0.65	29.1	29.8
(last 0.050 in. - 5,000 cycles)		30.5	
Fatigue Precracked	0.65	31.3	30.3
(last 0.050 in. - 20,000 cycles)		29.2	
Fatigue Precracked	0.65	28.8	30.1
(last 0.050 in. - 5,000 cycles) *		31.4	

* A.S.T.M. Recommended Practice.

Preliminary Trial 2 on Directionality and Reproducability.

Directionality in as cast blanks has been investigated by measuring K_{1c} in three directions from the same plate. The blanks were first tested as C.L.L. specimens, and three point bend specimens were taken for subsequent tests in other directions. The direction of crack propagation is indicated below. A measure of the reproducability of K_{1c} in this material, and the variation in K_{1c} from two types of specimen can also be assessed from this work.

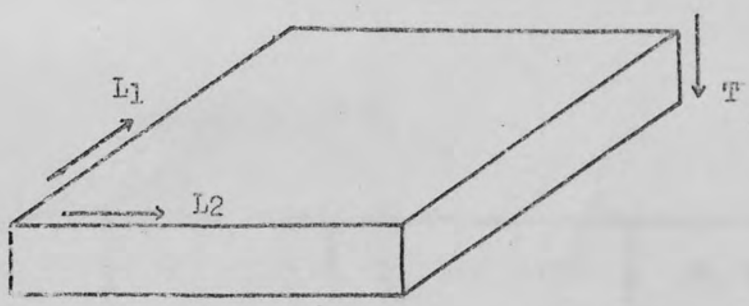

TABLE 6.5.

Heat No.	Notch Direction	Specimen	K_{1c} ksi $(in)^{\frac{1}{2}}$	Av. K_{1c}
1 SC/AC	L1	C.L.L.	39.0, 37.9, 38.3, 38.0.	38.1
0.8% C	L2	3in bend	37.6, 38.8, 37.4.	37.9
	T	2in bend	38.2, 37.2, 35.8.	37.1
5 CC/AC	L1	C.L.L.	40.0	40.0
1.1% C	L2	3 in bend	39.3, 37.4, 39.1.	38.9
	T	2in bend	38.9, 38.5, 39.0.	38.8

Preliminary Trial 3 on Residual Stress.

A tempering treatment was used to relieve any residual stress present in as cast material.

Material:- Heat 7 1.4% C SC/AC.

Specimen:- 3 inch span bend.

Treatment:- 550°C 2 hours.

TABLE 6.6.

Condition.	Av. H_v30	K_{1c} ksi $(in)^{\frac{1}{2}}$	Av. K_{1c}
As Cast	360	26.4, 25.3.	25.8
Stress Relieved	365	23.5, 26.5.	25.0

Fracture Toughness of Austenitic Material.

In this section the toughness results of all austenitic alloys are summarised, including as cast, homogenised, and the material cast to achieve grain size variation.

TABLE 6.7.

% C	Wt. No. + Condition.	Specimen Type	Gr. Size mm.	Av. Klc ksi (in)$^{\frac{1}{2}}$	No. of Tests.
0.8	1 SC/AC	CLL + Bend	0.13	37.6	11
1.1	4 + 5 SC/AC	CLL + Bend	0.11	31.7	8
1.4	7 SC/AC	CLL + Bend	0.075	26.8	8
2.1	10 SC/AC	3 in. Bend		24.6	3
2.8	11 SC/AC	3 in. Bend		21.5	3
3.4	12 SC/AC	3 in. Bend		15.9	3
0.8	3 SC/H	3 in. Bend		35.5	5
1.1	6 SC/H	CLL + Bend		44.4	3
1.4	8 SC/H	CLL + Bend		39.9	6
2.1	10 SC/H	3 in. Bend		30.9	2
2.8	11 SC/H	3 in. Bend		25.7	2
3.4	12 SC/H	3 in. Bend		23.2	2
1.4	8 SC/H ½hr.	3 in. Bend		27.5	2
1.4	8 SC/H 2hr.	3 in. Bend		30.0	2
1.4	8 SC/H 4hr.	CLL + Bend		36.5	2
1.4	8 SC/H 8hr.	3 in. Bend		39.9	6
1.4	8 SC/H 16hr.	3 in. Bend		29.0	2
1.4	8 CC/AC ½in.	2 in. Bend	0.017	34.9	4
1.4	7 CC/AC ½in.	CLL + Bend	0.030	30.0	5
1.4	9 Sill/AC ½in.	3 in. Bend	0.053	28.3	4

cont'd. overleaf....

T A B L E 6.7. cont'd

% C	Ht. No. + Condition.	Specimen Type	Gr. Size mm.	Av. K_{1c} ksi $(in)^{\frac{1}{2}}$	No. of Tests.
1.4	7 SC/AC $4\frac{1}{2}$in.	CLL + Bend	0.075	26.8	8
1.4	9 SC/AC 6in.	CLL	0.12	25.0	2
1.4	9 SC Aust'ed 6 in.	3 in. Bend		24.8	2
0.8	2 CC/AC	CLL + Bend	0.11	37.9	6
1.1	5 CC/AC	CLL + Bend	0.079	39.4	7

Austenitizing Temperature.

Optimum hardening temperature was selected from hardness determinations on specimens heat treated in a protective atmosphere and sectioned after tempering.

Specimens:- $\frac{1}{2}$ inch cube.

Treatment:- 1 hr. soak at temperature followed by oil quenching and tempering 1 hr. @ 250°C.

T A B L E 6.8.

Ht. No.	% C	Temperature °C.	Av. H_V 30.
1	0.8	950	600
		1000	600
		1050	590
4	1.1	950	620
		975	630
		1000	570
7	1.4	850	570
		900	631
		950	658

Effects of Austenitizing Time and Tempering Temperature on K_{1c}

Hardening variables were investigated in two trials to determine the effects of austenitising time (at fixed temperature) and tempering temperature on K_{1c} and hardness.

Material:- Nt. 6 SC. 1.1% C.

Treatment:- (a) Hardened 975°C ½ hr. to 16 hrs. Oil quench. Temper 250°C 2 hrs.

(b) Hardened 975°C 2 hrs. Oil quench 2 hrs. at tempering temperature.

Specimens:- 3 inch span Bend. Duplicate tests averaged.

TABLE 6.9.

Soaking Time	Av. H_V 30	Av. K_{1c} ksi $(in)^{\frac{1}{2}}$.
½ hr.	450	28.1
* 2 hr.	660	27.9
5 hr.	660	27.9
16 hr.	640	28.0
Tempering Temp. °C.		
Oil quenched	600	25.5
250	660	27.9
350	540	30.1
450	590	35.2
550	520	22.2

* Sub-zero treatment to −75°C produced no further increase in hardness in the as quenched condition.

Fracture Toughness of Martensitic Material.

The fracture toughness of martensitic alloys, including those hardened after homogenisation is summarised in this section. A standardised hardening procedure was used throughout.

Treatment:- Hardened 975°C 2 hrs. Oil quenched

Tempered 250°C 2 hrs.

T A B L E 6.10.

% C	Ht. No. & Condition.	Specimen Type.	Av. K_{1c} ksi $(in)^{\frac{1}{2}}$	No. of Tests.
0.8	1 SC/HT	CLL + Bend	26.3	9
1.1	5 SC/HT	CLL + Bend	26.9	10
1.4	7 SC/HT	CLL	26.6	3
2.1	10 SC/HT	3 in. Bend	23.5	2
2.8	11 SC/HT	3 in. Bend	20.5	2
3.4	12 SC/HT	3 in. Bend	14.5	2
0.8	3 SC/H/HT	3 in. Bend	32.1	7
1.1	6 SC/H/HT	CLL	28.0	2
1.4	8 SC/H/HT	CLL	26.8	2
2.1	10 SC/H/HT	3 in. Bend	27.9	2
2.8	11 SC/H/HT	3 in. Bend	24.8	2
3.4	12 SC/H/HT	3 in. Bend	23.8	2

Rate of Application of Stress Intensity

Sensitivity to the rate of application of stress intensity was investigated with respect to K_{1c} of austenitic and martensitic chill cast material at three carbon levels. Conversion of crosshead speed (cm/min.) to rate of application of stress intensity $\overset{\circ}{K}$, (ksi(in)$^{\frac{1}{2}}$/min.) was carried out by calibration of the load/displacement record.

Specimens:- 2 inch span bend.

Duplicate tests averaged.

T A B L E 6.11.

Heat No.	Cross Hd. Spd. cm/min.	$\overset{\circ}{K}_1$ ksi(in)$^{\frac{1}{2}}$/min.	Av. K1c ksi (in)$^{\frac{1}{2}}$. CC/AC	CC/HT
	0.005	5	36.5	
2 CC	0.02	20	37.9	
0.8% C	0.5	500	34.9	
	5.0	5,000	34.9	
	50.0	50,000	34.2	
	0.005	5	37.9	
5 CC	0.02	20	39.4	30.6
1.1% C	0.05	50	37.3	
	0.5	500	37.0	31.5
	5.0	5,000	34.8	26.2
	50.0	50,000	35.0	21.3
	0.005	5	29.2	
7 CC	0.02	20	30.0	27.7
1.4% C	0.5	500	30.5	26.0
	5.0	5,000	32.5	24.7
	50.0	50,000	31.1	20.3

Forging Trials.

(a) The effect of hot working and subsequent heat treatment on the fracture toughness of a 0.8% C alloy is shown below. K_{1c} was measured in the three planes of the plate to examine the directionality effect after forging.

(b) Variation in K_{1c} across the forged plate was investigated. The positions of K_{1c} specimens relative to the centre line of the plate are indicated in the sketch overleaf.

Material:- Heat 2 SC. 0.8% C.

Treatment:- 1 inch thick blanks forged to $\frac{1}{2}$ inch at 1150° C.

TABLE 6.12. (a).

Cond'n.	Notch Direction	Spec. Type	Av. K_V 30.	Av. K_{1c} ksi(in)$^{\frac{1}{2}}$.	No. of Tests.
	L1	CLL	450	30.9	2
F	L2	2in Bend		31.5	3
	T	2in Bend		40.9	7
F/HT	L1	CLL	560	39.2	2
	T	2in Bend		47.5	8
F/H/HT	L1	CLL	640	31.1	3
	T	2in Bend		37.5	11

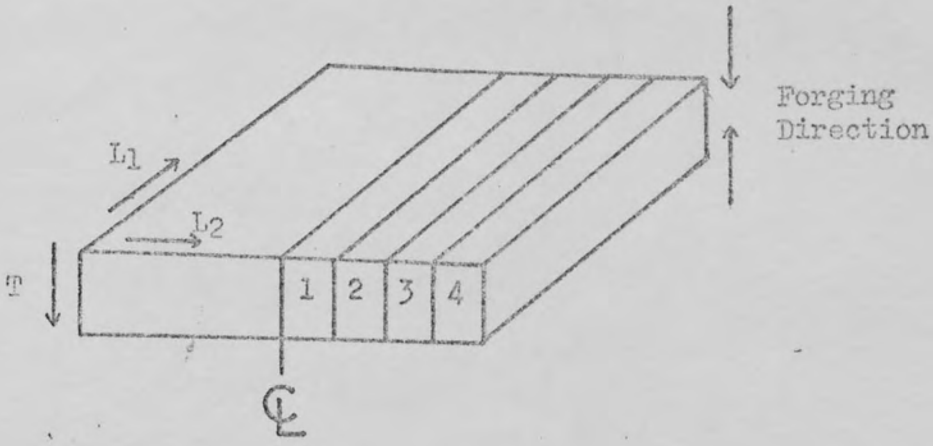

T A B L E 6.12.(b).

Cond'n.	Notch Direc.	Position of K_{1c} ksi. $(in)^{\frac{1}{2}}$					
		1.	2.	3.	4.		
F	T	37.0	43.5	41.5	39.0	40.2	36.5
	L2	30.7	31.3	30.6	32.5	31.3	40.9
F/HT	T	46.5	45.5	52.0	45.5	47.5	
F/H/HT	T	36.0	34.5	38.0	34.0	35.6	37.5

The effect of common alloying elements on S.I.M. formation.

Traces of strain induced martensite (S.I.M.) were detected in the deformed zones of several of the lower carbon alloys, particularly at the 1.1 and 1.4% carbon levels. A more detailed examination was carried out in order to observe the influence of common alloying elements on S.I.M. formation, and the effect of S.I.M. on K_{1c}. A series of eight heats were cast as $\frac{1}{2}$ inch diameter chill cast rods, covering variations in C, Mn, Ni, and Co content. The stock was homogenised at 1050° C for $\frac{1}{2}$ hour and tested as No. 11 Hounsfield tensile specimens. In all cases the pre-fracture strain was less than 5% and S.I.M. occurred in localised areas, usually close to the fracture. The amount of S.I.M. formed was estimated from a point count on the area immediately adjacent to the fracture, on longitudinal sections of tensile specimens. The results of these tests are tabulated in tables 6.13. (a) and (b).

T A B L E 6.13. (a).

Ht. No.	C	Si	S	P	Mn	Ni	Cr	Co
T1	0.73	-	-	-	1.20	-	14.8	-
T2	0.73	0.23	-	-	2.30	0.17	14.6	-
T3	0.51	0.18	-	-	0.59	1.39	15.7	-
T4	0.47	0.17	-	-	0.58	3.25	15.3	-
T5	0.82	0.33	0.011	0.030	0.52	1.38	15.2	-
T6	0.76	0.29	0.011	0.030	0.54	2.55	14.8	-
T7	1.25	0.34	0.030	0.031	0.59	0.21	15.2	0.88
T8	1.22	0.30	0.031	0.039	0.59	0.21	15.2	2.28

TABLE 6.13. (b).

Heat Nos.	Element	Range		% SIM in 5 gr. adj. to fract.		Av. UTS ksi	
		FROM	TO	FROM	TO	FROM	TO
T3-T5	C	0.51	0.82	20	TRACE	82	66
T1-T2	Mn	1.2	2.3	5	TRACE	68	63
T3-T4	Ni @ 0.5%C	1.4	3.3	20	5	82	64
T5-T6	Ni @ 0.8%C	1.4	2.6	NONE	NONE	66	68
T7-T8	Co AC	0.9	2.3	TRACE	10	73	80
T7-T8	Co H 1150°C 8 hrs.	0.9	2.3	NONE	TRACE	75	78

Influence of S.I.M. Formation on K_{1c}.

Consideration of the tensile survey led to the selection of compositions for two further heats, cast as K_{1c} specimen blanks. It was anticipated that S.I.M. formation would occur in sufficient volume to enable its influence on K_{1c} to be assessed. Cobalt was added to promote the formation of S.I.M. and each of the two heats was divided to provide a control alloy. K_{1c} was measured in the as cast condition, and after homogenisation at 1050°C for one hour.

TABLE 6.14.(a).

Ht No.	C	Si	S	P	Mn	Ni	Cr	Co.
K1-C	1.14	0.52	0.014	0.051	1.08	0.18	16.1	0.20
K1	1.11	0.59	0.013	0.062	0.97	0.18	15.8	3.84
K2-C	0.63	0.46	0.039	0.039	2.31	0.21	16.8	0.24
K2	0.60	0.52	0.041	0.050	2.20	0.20	16.3	3.97

TABLE 6.14.(b).

Ht No. & Condition	% C	K_{1c} ksi $(in)^{\frac{1}{2}}$.	Av. K_{1c}	Comments.
K1-C SC/AC	1.1	31.2, 34.0, 32.8	32.6	Trace S.I.M.
K1 SC/AC	1.1	33.4, 31.5, 35.6	33.5	Estimated 15% S.I.M.
K2-C SC/AC	0.6	32.2, 35.4	33.8)	Partly I.G. fracture
K2 SC/AC	0.6	37.3, 35.4, 36.5	36.4)	TRACE S.I.M.
K1-C SC/H	1.1	41.2, 44.0	42.6	NO S.I.M.
K1 SC/H	1.1	43.4, 41.5	42.5	Trace S.I.M.
K2-C SC/H	0.6	31.8, 27.0, 29.4	29.8)	Completely
K2 SC/H	0.6	29.6, 30.5	30.1)	Intergran. fracture.

7. DISCUSSION OF RESULTS.

7.1. Preliminary Trials.

The importance of establishing a sound working technique is vital in any project, and considerable time and effort was put to this end. Several running and feeding systems were tried in order to produce sound, clean castings. Inherent characteristics of the material and casting shape, such as directionality and residual stress were examined with regard to their effect, if any, on K_{1c}. The experimental procedure was checked by compliance calibration and the fatigue pre-cracking requirements investigated. Reproducability was observed on individual heats, on different heats of chemically similar material, and using two types of specimen. The results of the three preliminary trials confirm that plane strain fracture toughness testing is a viable technique when applied to relatively brittle cast materials.

The need for fatigue pre-cracking was demonstrated in the first of the preliminary trials. Although the results indicate a constant level of K_{1c} at higher fatigue stress levels, (see table 6.4.), the A.S.T.M. recommended practice was adhered to throughout the programme. In the absence of fatigue pre-cracking, results up to 35% high were obtained, associated with a wider plastic zone, measured at the free surface. This illustrates that the fracture process in a material containing a substantial volume fraction of brittle carbides is still influenced by plastic deformation, and is not simply controlled by the initiation of a crack within the carbide network.

The second preliminary trial, designed to examine directionality, was also used to assess the reproducability of the K_{1c} test in as cast material The implications of directional solidification and axial dendrite growth on Charpy tests were discussed in section 2.5, where the work of Pattyn[36] was reviewed. In the moulding system used in the current work, solidification occurs in the direction denoted L_1 in table 6.5, commencing at the edge opposite the feeder head. Any dendrite directionality would therefore be expected in this plane, and according to Pattyn this would lead to optimum properties in the L_2 direction, and poorest in the T direction. Macrostructural examination however, revealed a random dendrite pattern, within a narrow zone solidifying under the influence of the mould wall. This was reflected in the K_{1c} results from crack propagation in the three dimensions of the plate, (see table 6.5.) The small variations in K_{1c} on sand cast and chill cast material led to the assumption that the effects of directionality were negligible, under the conditions prevailing, and could be subsequently ignored.

Considering the project as a whole, K_{1c} was determined within an overall scatter band of 10%. A statistical analysis of the results from this trial revealed a standard deviation of 0.91 for the results of heat 1, in table 6.5, and 0.80 for the results of heat 5. For these two sets of data, a minimum of two tests are required for a 95% confidence limit of obtaining a result between ± 2 ksi.(in)$^{\frac{1}{2}}$ of the mean.

The third preliminary trial also served a dual purpose, primarily as a measure of the influence of residual stress in as cast material, but also as a check on the effect of tempering any eutectic martensite present in the 1.4% carbon alloy. The temperature selected for stress relief, 550°C, is that used commercially for high chromium cast iron castings prone to spalling and cracking in service. This treatment has been proved successful in minimising failure obviously caused by the presence of residual stress. In fact no change in K_{1c} was detected after stress relief, in the 1.4% carbon alloy tested. It has been found that the castings most likely to exhibit residual stress effects are those subjected to 'hot knockout' procedures. All castings used in this investigation, of necessity a simple shape, were allowed to cool naturally to room temperature in the mould. It is unlikely then, that a significant level of residual stress is developed in these castings.

As mentioned in section 2.3, due to micro-segregational effects it is often possible to obtain freshly formed martensite immediately adjacent to the carbides, in as cast structures. This phase was considered a likely path for crack propagation, and it was interesting to observe the effect of tempering. The bulk of the matrix, being austenite remains unaltered. The fact that no significant variation in K_{1c} was detected appears to invalidate this argument.

After the preliminary trials it was considered prudent to continue the investigation without taking elaborate precautions against the effects of directionality and residual stress.

It seems pertinent at this point to include details of a typical fracture toughness test. Fig. 7.1 shows the Load/displacement record for an as cast 1.4% carbon crackline loaded specimen, and plates (a) to (d) illustrate the crack tip conditions and slow crack growth up to the maximum load point. The fatigue crack was initiated at the root of a machined notch and the final 0.050 ins., grown in 64,000 cycles, at a mean load of 550 lb. and an amplitude of ± 550 lb. Plates (a) and (b) show the fatigue crack tip after loading to just below and just above the elastic limit. Permanent deformation in the form of a plastic zone at the crack tip is evident in plate (b). The extent of plasticity and slow crack growth at the critical, and maximum loads, is shown in plates (c) and (d). Rapid crack propagation occurs under a decreasing load beyond the maximum load point.

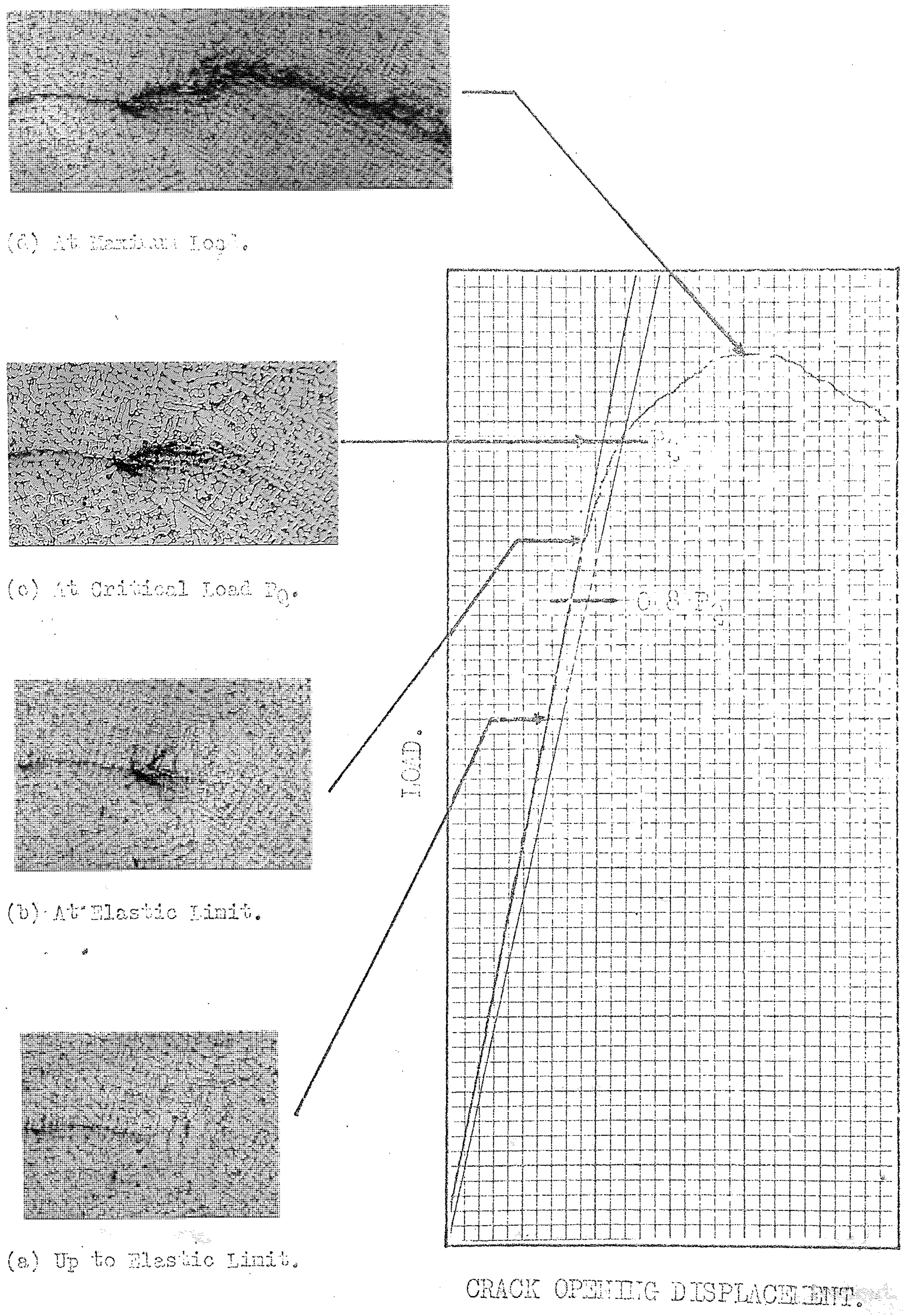

Fig. 7.1. Load/Displacement Record and Slow Crack Growth in 1.4% C, 15% Cr.

Examination of the load/displacement record shows that there is no 'pop-in' behaviour in this test, and it is necessary to construct the 5% offset line to determine the critical load, denoted provisionally P_Q. The initial crack length, a, is measured from the fracture surface, and includes machined notch plus fatigue crack. Other dimensions required for calculation of K_{1c} are width, W, thickness, B, and the geometrical factor for the specific crack situation of this test, Y.

The appropriate values for determination of a provisional fracture toughness, K_Q, are:

a (edge[1]) = 1.935 ins.)
a (edge[2]) = 1.940 ins.)   a = 1.95 ins.   B = 0.476 ins.
a (centre) = 1.965 ins.)

W = 3.375 ins. P_Q = 1900 lb. $^a/_W$ = 0.576   Y = 16.1

The calibration curve of $^a/_W$ against Y is shown in the Appendix.

From: $$K_Q = \frac{P_Q\, Y\, (a)^{\frac{1}{2}}}{BW} \qquad K_Q = 26.5 \text{ ksi.(in)}^{\frac{1}{2}}.$$

It now remains to validate the K_Q value by ensuring that the test complies with three conditions put forward by A.S.T.M. as criteria of thickness, width, and stress distribution.

(a) For a valid result the characteristic 2.5 $(^{K_Q}/\sigma_{ys})^2$ must be less than both specimen thickness and initial crack length. With a yield stress of 97 ksi. the value is 0.19, which is satisfactory, since it is less than B and a.

(b) The width criterion necessitates further analysis of the load/displacement record, at a point corresponding to 0.8 P_Q. The requirement is that the departure from linearity at 0.8 P_Q must be less than 25% of that at P_Q. Since the record in question is still linear at 0.8 P_Q, it is obviously satisfactory.

(c) The final condition refers to the fatigue crack front, and states that the difference between the most advanced and retarded points of the crack must be within 10% of the specimen thickness. Again this test fulfills the requirement, and K_Q can now be considered a valid plane strain fracture toughness value, and reported as K_{1c}.

7.2. Influence of Carbon Content.

Variation of carbon content from 0.8 to 3.4% in a base alloy containing 15% chromium is discussed in terms of microstructure, volume fraction of carbides, tensile properties, and fracture toughness.

The change in microstructure at six carbon levels is illustrated in fig. 7.2. Two important features of the as cast structure are the carbide morphology and the matrix structure. The individual carbide form is one of lamellar colonies, together with eutectic austenite. At the lower end of the carbon range, the carbide segregates into a grain boundary film, enveloping what appear to be isolated carbide colonies within large grains. Above 1% carbon this grain boundary film is not evident, and up to 1.4% carbon the carbides solidify as an incomplete interdendritic network. Further increase in carbon results in a thickening of this network and the appearance of characteristic plate like carbides. At the highest carbon level examined, (3.4%), there is a marked change in carbide morphology. Obviously this composition is very close to the ternary eutectic, with the formation of eutectic cells radiating from a nucleus, analogous to rosette graphite in grey irons. The presence of occasional primary carbide particles, characterised by their hexagonal shape, sometimes with a small pool of austenite in the centre, suggests that the alloy may be slightly hyper-eutectic.

The matrix structure reveals irregularities at the two extremes of the

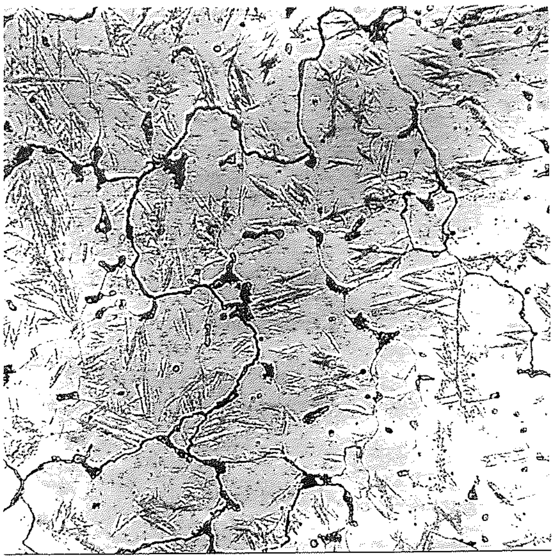

(a) 0.8% Carbon.

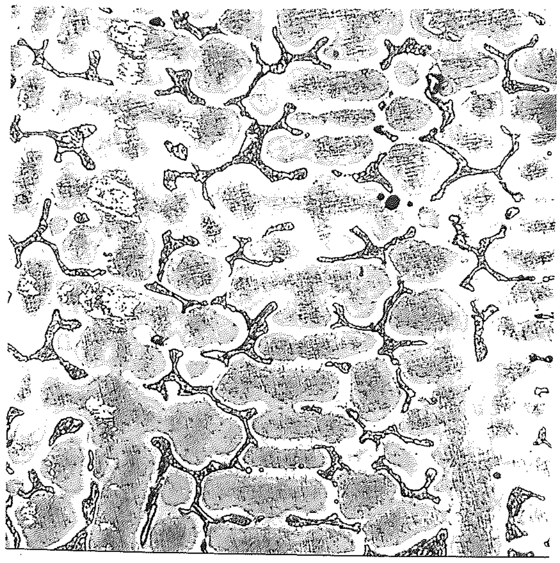

(b) 1.1% Carbon.

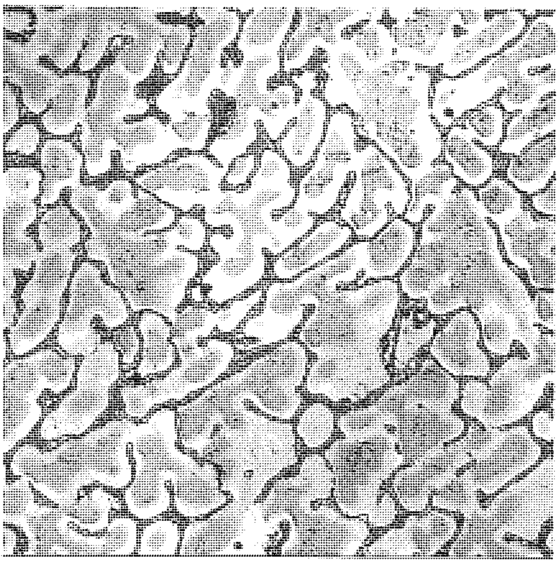

(c) 1.4% Carbon.

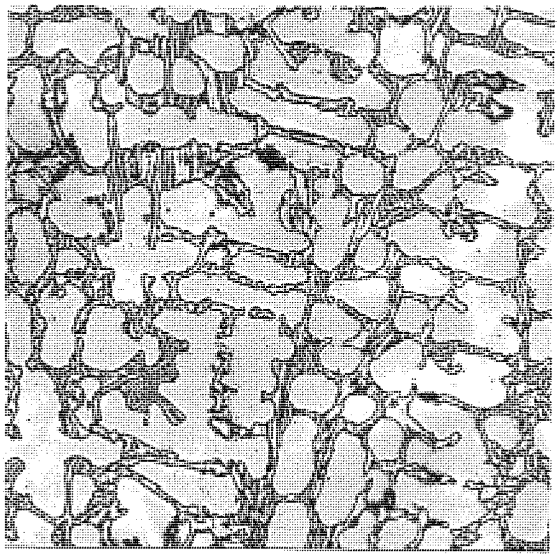

(d) 2.1% Carbon.

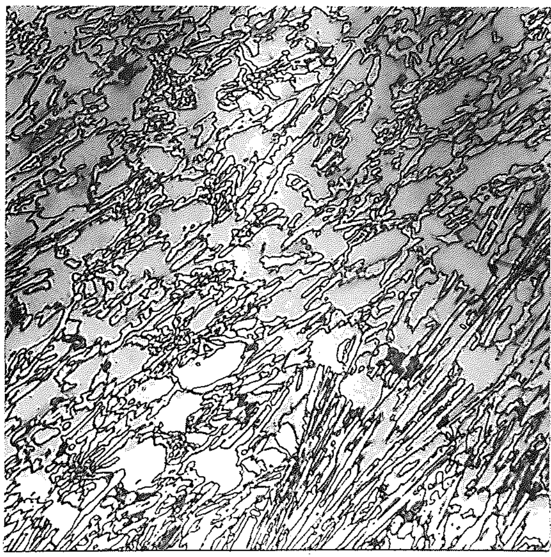

(e) 2.8% Carbon.

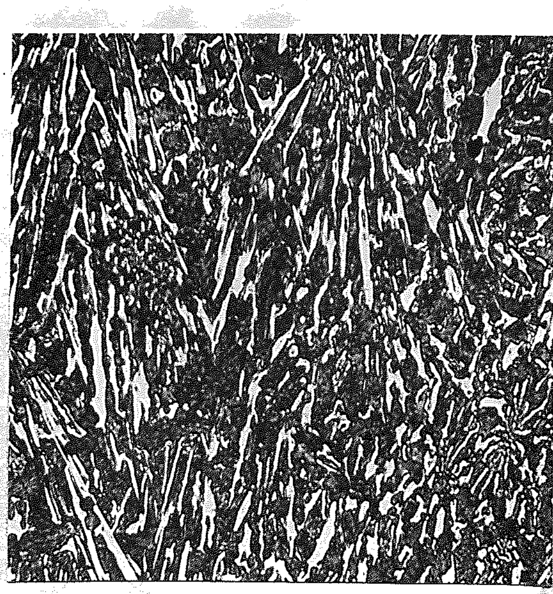

(f) 3.4% Carbon.

Fig. 7.2. Sand Cast Microstructures, X 100.

austenite liquidus phase field. At the 0.8% carbon level the composition is very close to the ferrite boundary, and the unstable austenite undergoes partial transformation to martensite on cooling. This is evident from plate 7.2. (a), which shows the coarse martensite needles. The matrix consists entirely of metastable austenite at the intermediate carbon levels. The 1.1 and 1.4% carbon alloys, which solidify through a wide freezing range, show pronounced coring. At 3.4% carbon the Cr/C ratio is so low that even the addition of 2% manganese is insufficient to prevent transformation to the equilibrium ferrite/$Cr_{23}C_6$ agglomerate. This is the dark granular pearlite type structure evident in plate 7.2. (f).

Typical heat treated microstructures are shown in fig. 7.3. Precipitation of secondary carbides, (Cr_7C_3), during austenitising leaves the matrix depleted in carbon and chromium, raising the M_s above room temperature. Subsequent cooling results in transformation of the matrix to martensite. The eutectic carbide structure remains unaffected by this treatment (975°C oil quench, 250°C temper). The presence of secondary carbides is not immediately obvious in these structures, but a more detailed examination is discussed in section 8.1.

The carbide volume at each carbon level was estimated from examination on the Quantimet microscope. The results from table 6.3. are expressed graphically in fig. 7.4., and whilst it is realised that these values may not be absolute, a useful trend is established. A linear increase of 1.8% volume fraction carbides with 0.1% carbon is evident in as cast structures up to 2.1% carbon. Above this value the increase in carbides is less pronounced as the eutectic point is neared.

Fig. 7.5. shows the tensile strength of as cast and heat treated alloys of varying carbon content. Austenitic structures exhibit a parabolic increase in tensile strength with carbon content. An exception to this pattern is the 0.8% carbon alloy, in which the U.T.S. is

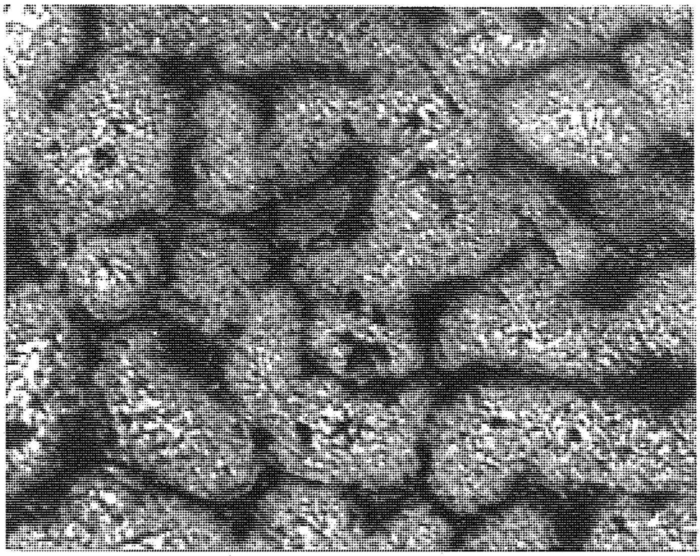

(a) 1.1% Carbon X 150.

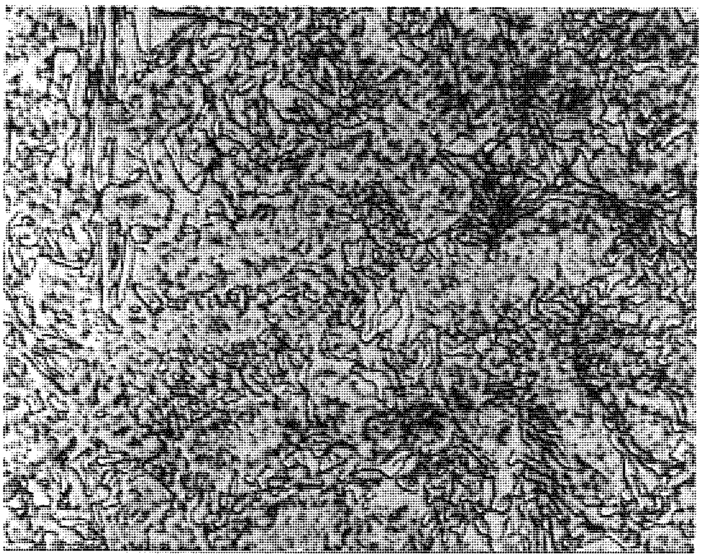

(b) 2.1% Carbon X 150.

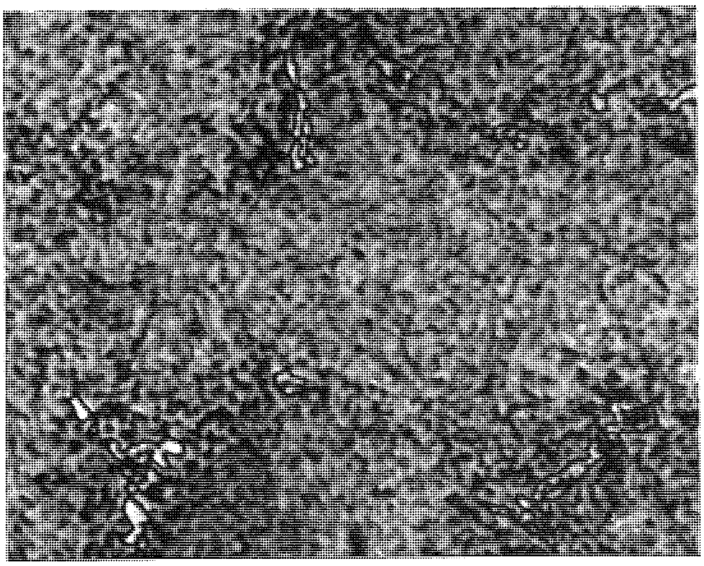

(c) 0.8% Carbon X 500.

Fig. 7.3. Typical Heat Treated Microstructures.

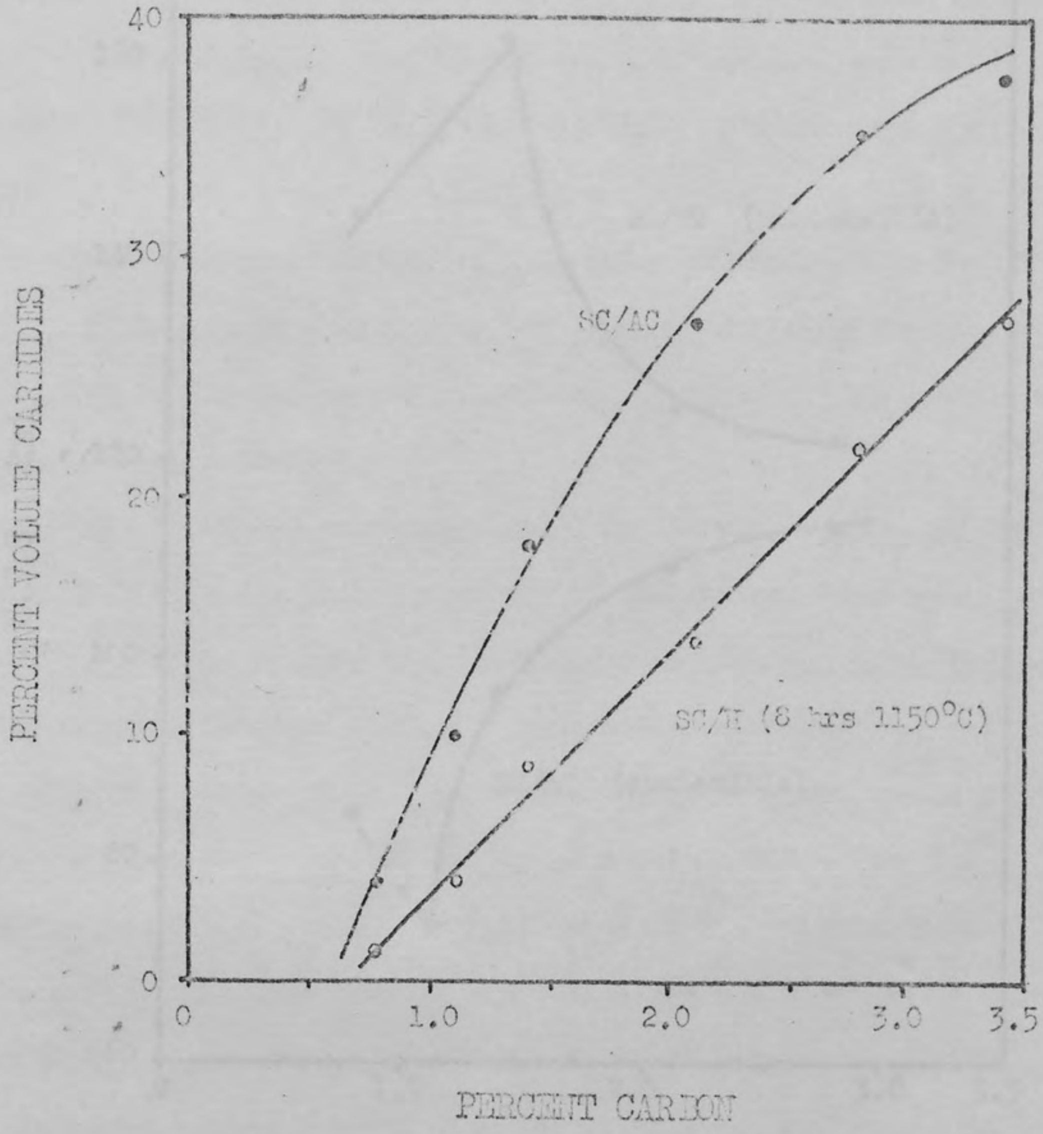

Fig. 7.4. Relationship Between Volume Fraction of Carbides and Carbon Content in As Cast and Homogenised Structures.

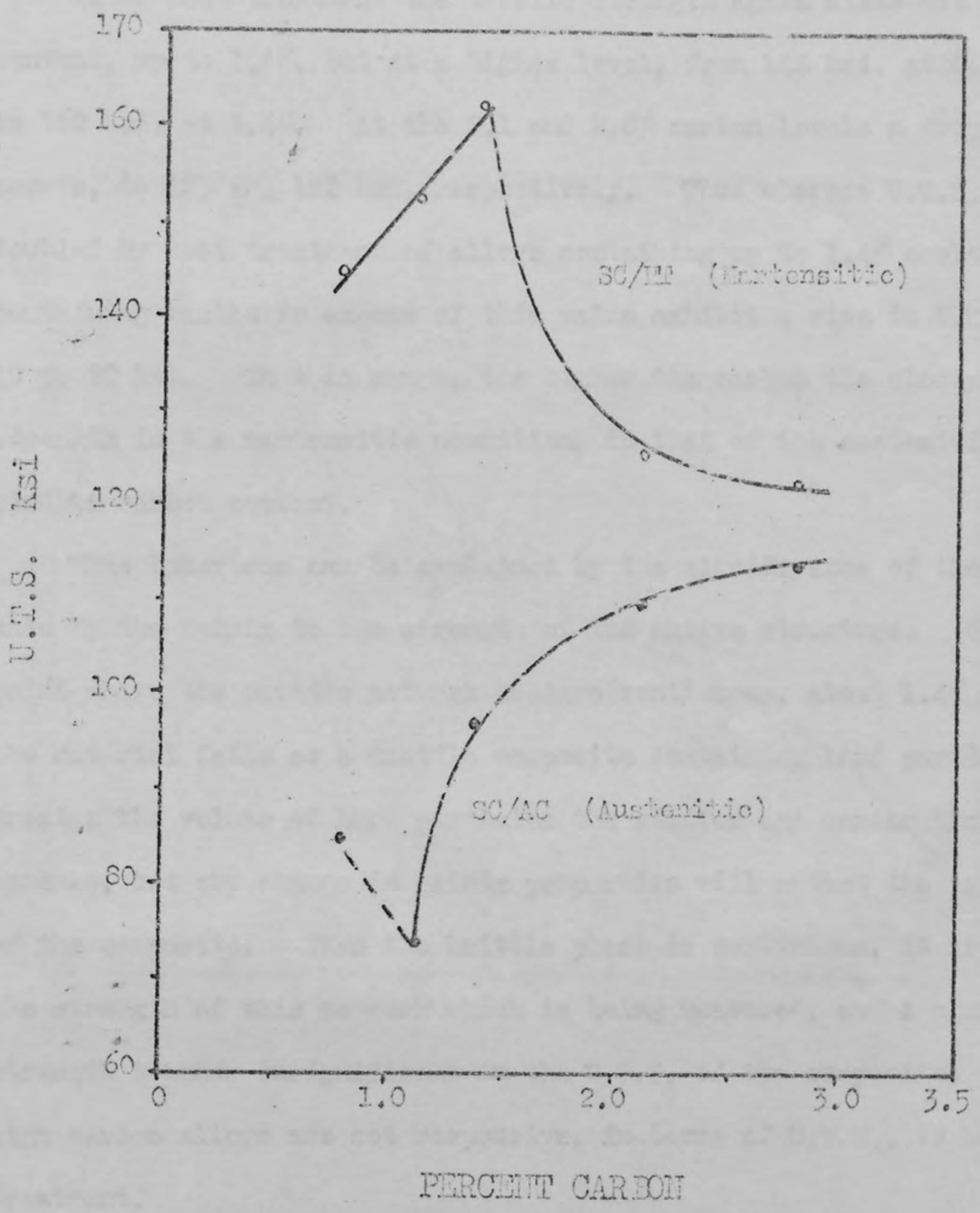

Fig. 7.5. Tensile Strength of As Cast and Hardened (250°C Temper) Material.

elevated due to the presence of martensite in the microstructure. Carbon content has a marked influence on U.T.S. up to 1.4%, with a rise from 75 ksi at 1.1%, to 97 ksi. Further increase in carbon is less effective, the U.T.S. reaching only 114 ksi. at 2.9% carbon.

After heat treatment the tensile strength again rises with carbon content, up to 1.4%, but at a higher level, from 144 ksi. at 0.8% carbon to 162 ksi. at 1.4%. At the 2.1 and 2.8% carbon levels a drop in U.T.S. occurs, to 125 and 122 ksi. respectively. Thus whereas U.T.S. is roughly doubled by heat treatment of alloys containing up to 1.4% carbon, those containing carbon in excess of this value exhibit a rise in U.T.S. of only 10 to 20 ksi. In this range, the higher the carbon the closer is the strength in the martensitic condition, to that of the austenitic alloys of similar carbon content.

This behaviour can be explained by the significance of the contribution made by the matrix to the strength of the entire structure. Up to the point where the carbide network becomes continuous, about 1.4% carbon, the material fails as a ductile composite containing hard particles. The greater the volume of hard particles the stiffer and harder the structure becomes, but any change in matrix properties will affect the properties of the composite. When the brittle phase is continuous, it is virtually the strength of this network which is being measured, and a change in matrix strength becomes insignificant in the U.T.S. of the composite. Thus the high carbon alloys are not responsive, in terms of U.T.S., to heat treatment.

The relationship between fracture toughness and carbon content of austenitic and martensitic sand cast material is shown graphically in fig. 7.6. The K_{1c} of as cast alloys shows a marked dependence on carbon content, between 0.8 and 1.4%. Over this range K_{1c} drops linearly from 38 to 27 ksi $(in)^{\frac{1}{2}}$. Just as it was for tensile properties this point appears critical in the relationship, with little further reduction in K_{1c}, to 21.5 ksi $(in)^{\frac{1}{2}}$, up to 2.8% carbon. The eutectic alloy shows a drop in

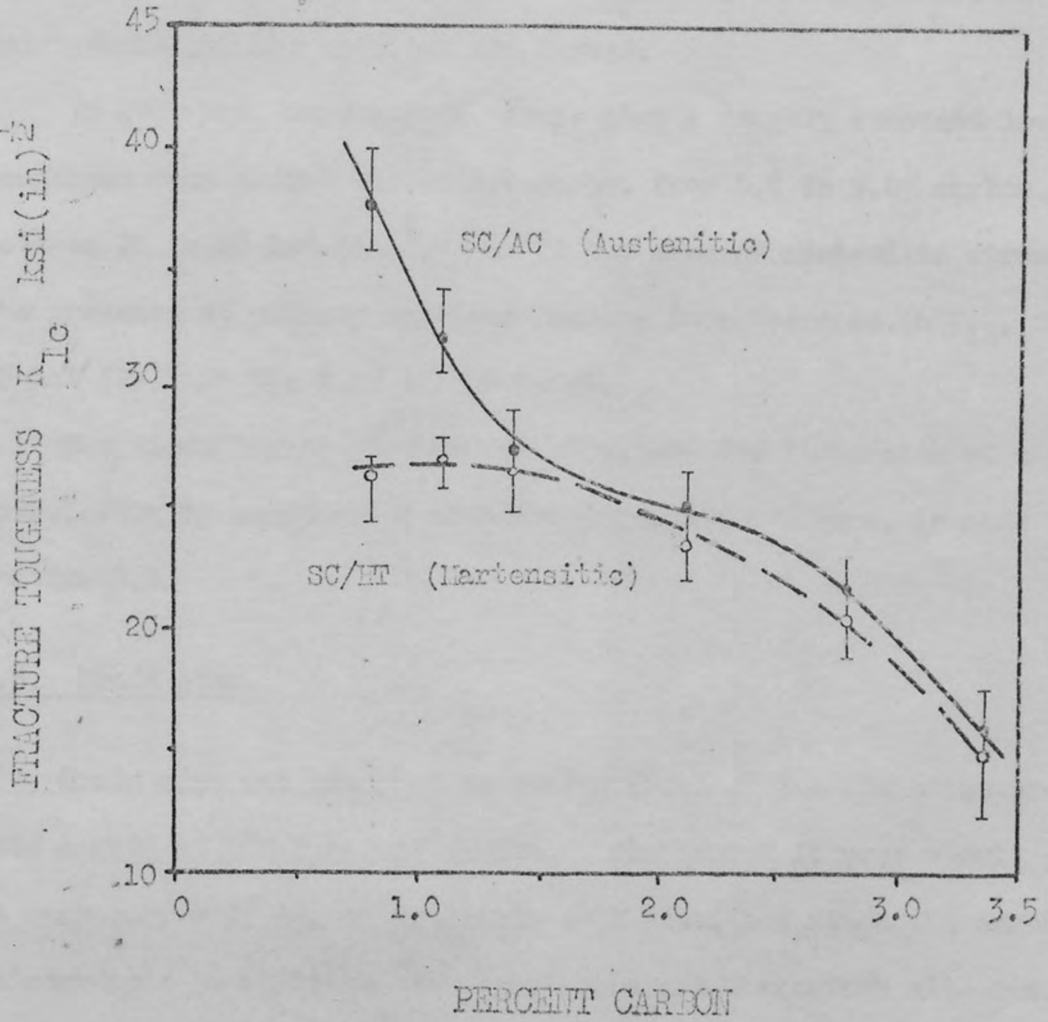

Fig. 7.6. Fracture Toughness of As Cast and Hardened (250°C Temper) Material.

K_{1c} to 16 ksi $(in)^{\frac{1}{2}}$ at 3.4% carbon. Thus, up to the point where the carbides are continuous the fracture process is controlled by the properties of the matrix, and a reduction in volume of hard carbides leads to an improvement in K_{1c}. At carbon contents over 1.4% the fracture process is dominated by the presence of the carbide network, which acts as a weak link in the structure. The addition of further weakeners in the form of excess carbides, has little effect on the overall toughness, up to the point where primary carbides are formed.

In contrast, martensitic alloys show a roughly constant level of toughness over almost the entire range, from 0.8 to 2.8% carbon, of between 21 to 26 ksi $(in)^{\frac{1}{2}}$. As in the case of austenitic structures, the presence of primary carbides results in a decrease in K_{1c}, to 15 ksi $(in)^{\frac{1}{2}}$ at the 3.4% carbon level.

The significance of these results, and the discussion of a structural correlation in conjunction with fractographic evidence, is made in section 8.1.

7.3. Grain Size.

Grain size was measured on random areas of the structure projected onto a grid at 100 X magnification. The quoted figures should probably be more correctly termed dendritic cell size, but since the carbide network acts as a dislocation barrier, crack nucleation site etc., this was considered the most pertinant measure of effective grain size. By alteration of section size and casting in three moulding materials, graphite, silliminite, and sand, a range of grain size was produced from 0.017 to 0.12 mm. This is reflected in fig. 7.7. which shows quite clearly the refinement of the microstructure with increasing solidification rate. The variation in K_{1c} and U.T.S. associated with grain refinement is shown in fig. 7.8. An increase of 30% in K_{1c}, from 26 to 35 ksi $(in)^{\frac{1}{2}}$, was observed over the complete range of grain sizes, representing sand

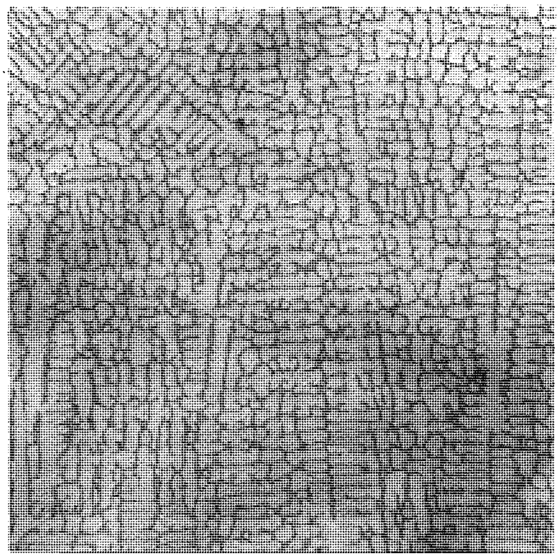

(a) CC $\frac{1}{4}$in. gr. dia. 0.017mm.

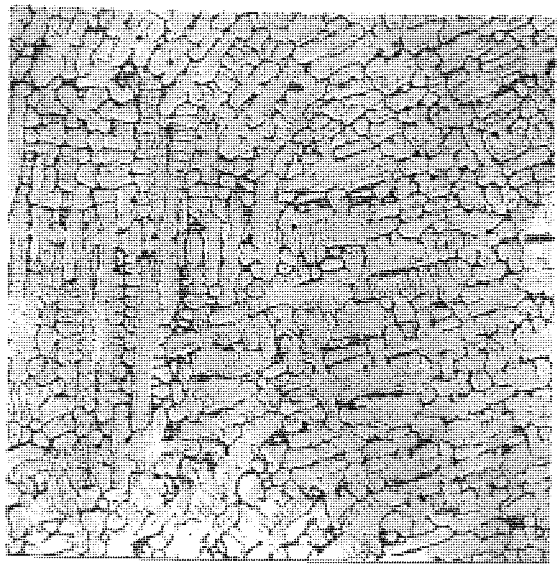

(b) CC $\frac{1}{2}$in. gr. dia. 0.03mm.

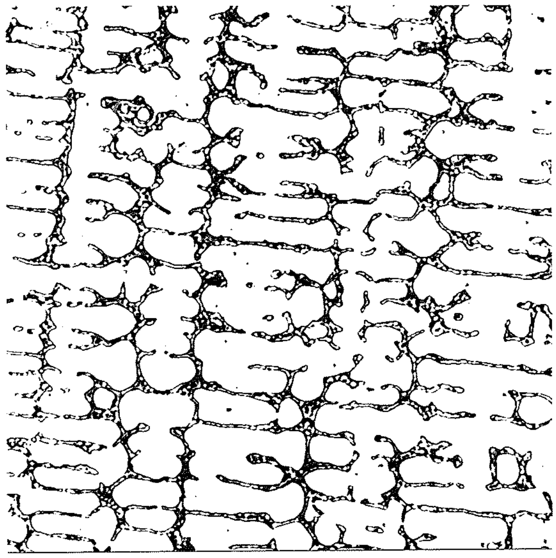

(c) Sill $\frac{1}{2}$in. gr. dia. 0.053mm.

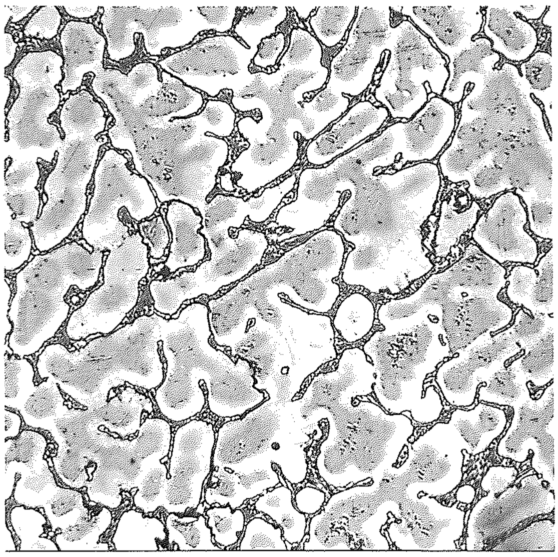

(d) SC $\frac{1}{2}$in. gr. dia. 0.075mm.

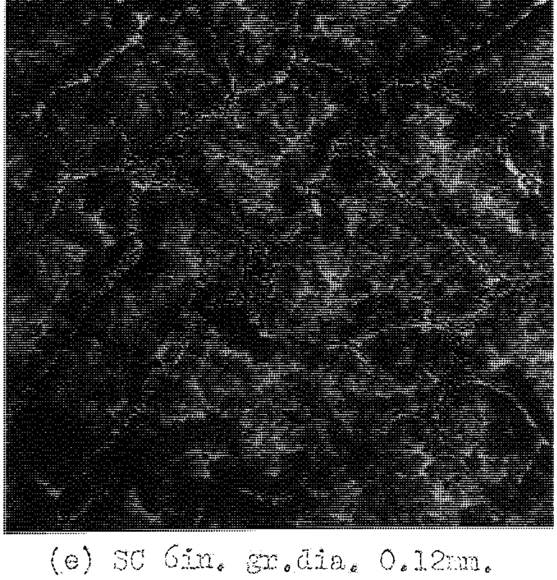

(e) SC 6in. gr.dia. 0.12mm.

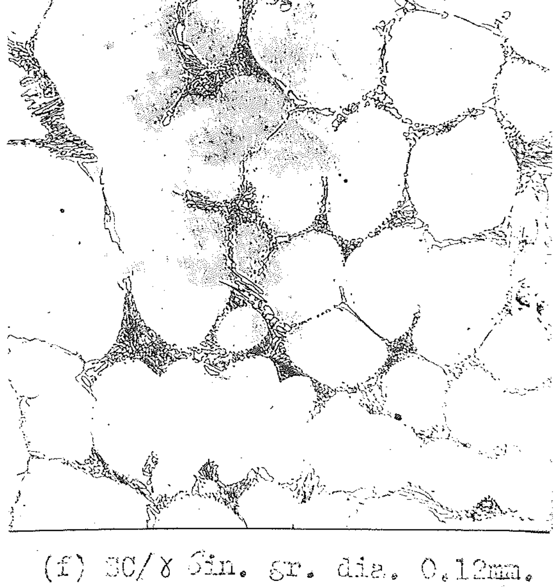

(f) SC/γ 6in. gr. dia. 0.12mm.

Fig. 7.7. Variation of Grain Size in As Cast 1.4% Carbon Material.

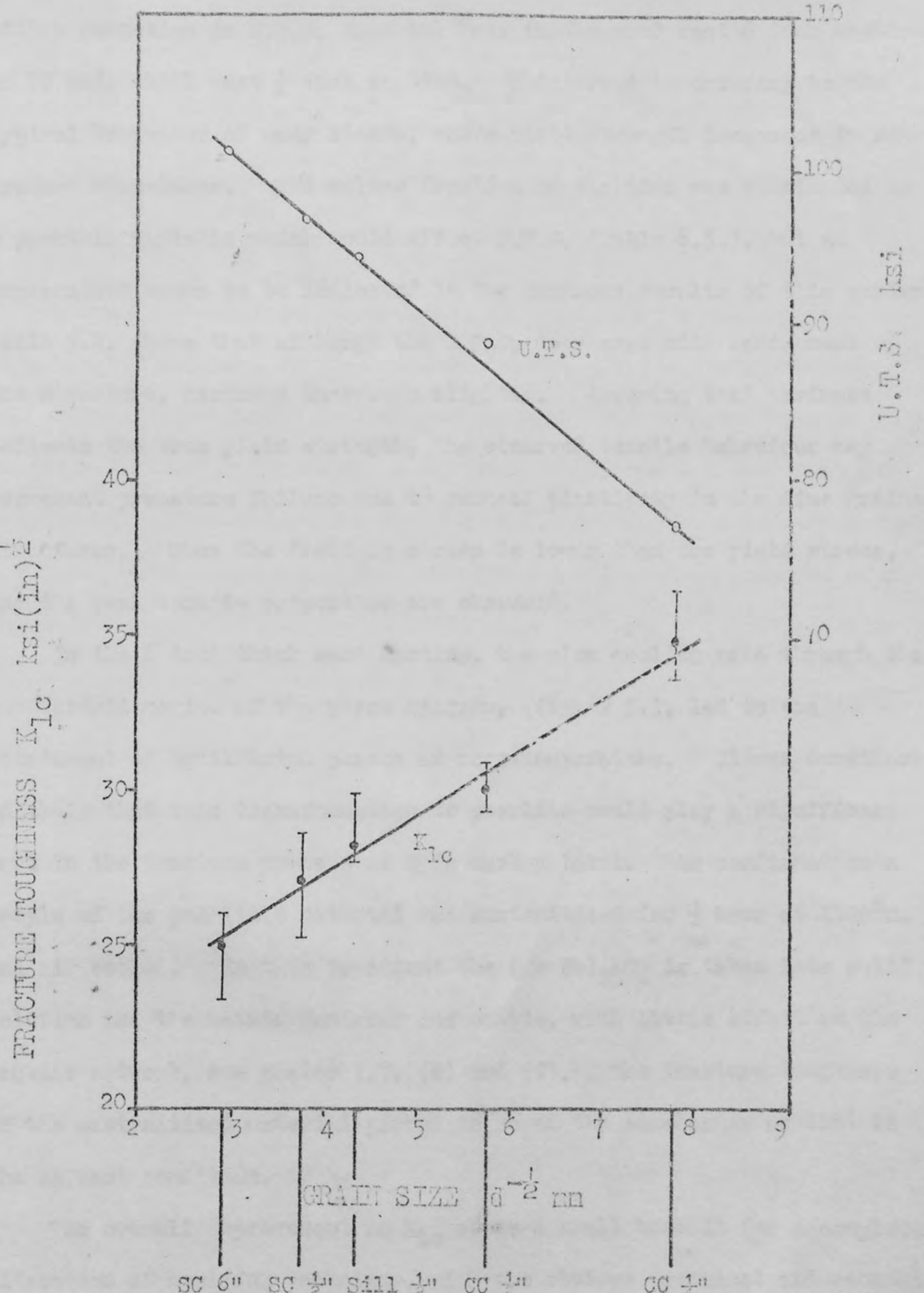

Fig. 7.8. Variation of Tensile Strength and Fracture Toughness with Grain Size in As Cast Material.

casting in 6 inch section to chill casting in $\frac{1}{2}$ inch section, respectively. Tensile properties are shown to be inversely related to fracture toughness, with a reduction in U.T.S. from 101 ksi. in the sand cast 6 inch section, to 77 ksi. chill cast $\frac{1}{2}$ inch section. This trend is contrary to the typical behaviour of many steels, where yield strength decreases in coarse grained structures. The volume fraction of carbides was eliminated as a possible variable, which would affect U.T.S. (Table 6.3.), but an explanation seems to be indicated in the hardness results of this series. Table 6.2. shows that although the U.T.S. decreases with refinement of the structure, hardness increases slightly. Assuming that hardness reflects the true yield strength, the observed tensile behaviour may represent premature failure due to reduced plasticity in the fine grained structures. Thus the fracture stress is lower than the yield stress, and the real tensile properties are obscured.

In the 6 inch thick sand casting, the slow cooling rate through the peritectoid region of the phase diagram, (fig. 2 5.), led to the attainment of equilibrium phases at room temperature. It was considered unlikely that this transformation to pearlite would play a significant part in the fracture process at this carbon level. As confirmation a sample of the pearlitic material was austenitised for $\frac{1}{2}$ hour at 1100°C, and air cooled. In this treatment the $(Cr\ Fe)_{23}C_6$ is taken into solid solution and the matrix rendered austenitic, with little effect on the carbide network, see plates 7.7. (e) and (f). The fracture toughness of the austenitised material proved to be of the same order as that in the as cast condition.

The overall improvement in K_{1c} seems a small benefit for a complete alteration of moulding technique, with the obvious technical and economic implications. Considering that a comparable improvement could be achieved by a reduction in carbon of 0.45%, at this level, a change from sand to chill casting could hardly be justified on the grounds of improving fracture toughness.

7.4. Hardening Variables.

Hardening characteristics were investigated in three experiments covering austenitising time and temperature, and tempering temperature. This aspect of the programme was confined to alloys containing less than 1.4% carbon, the range where maximum response to heat treatment was observed.

Optimum austenitising temperature (table 6.8.) for martensite formation was selected on the basis of hardness, which is reported to bear a close relationship to wear resistance, the practical function of the alloy. Highest hardness, indicating more complete transformation, was obtained at three carbon levels up to 1.4% from a soaking temperature of 975°C. This temperature was used for the subsequent hardening of all material.

Soaking time between ½ hour and 16 hours was shown to have little effect on K_{1c} (table 6.9.). The low hardness of the sample austenitised for only ½ hour indicates that precipitation of secondary carbides and subsequent transformation to martensite is probably incomplete at this stage. The specimens tested were ½ inch thick, and the shortest time in which complete transformation was achieved was 1 hour. This time will obviously be a function of section size, but a minimum of 1½ to 2 hours soak, per inch thickness, appears to be necessary for maximum hardness. No significant change in microstructure, hardness, or K_{1c} was detected on extending the soaking time up to 16 hours, indicating that the growth of secondary carbides is slow at this temperature.

The influence of tempering temperature, on the other hand, is most marked. Fig. 7.9. portrays K_{1c} and hardness as a function of tempering temperature. Peak hardness is achieved on tempering at 250°C, and after a trough in the hardness curve at 350°C, a secondary hardening effect is

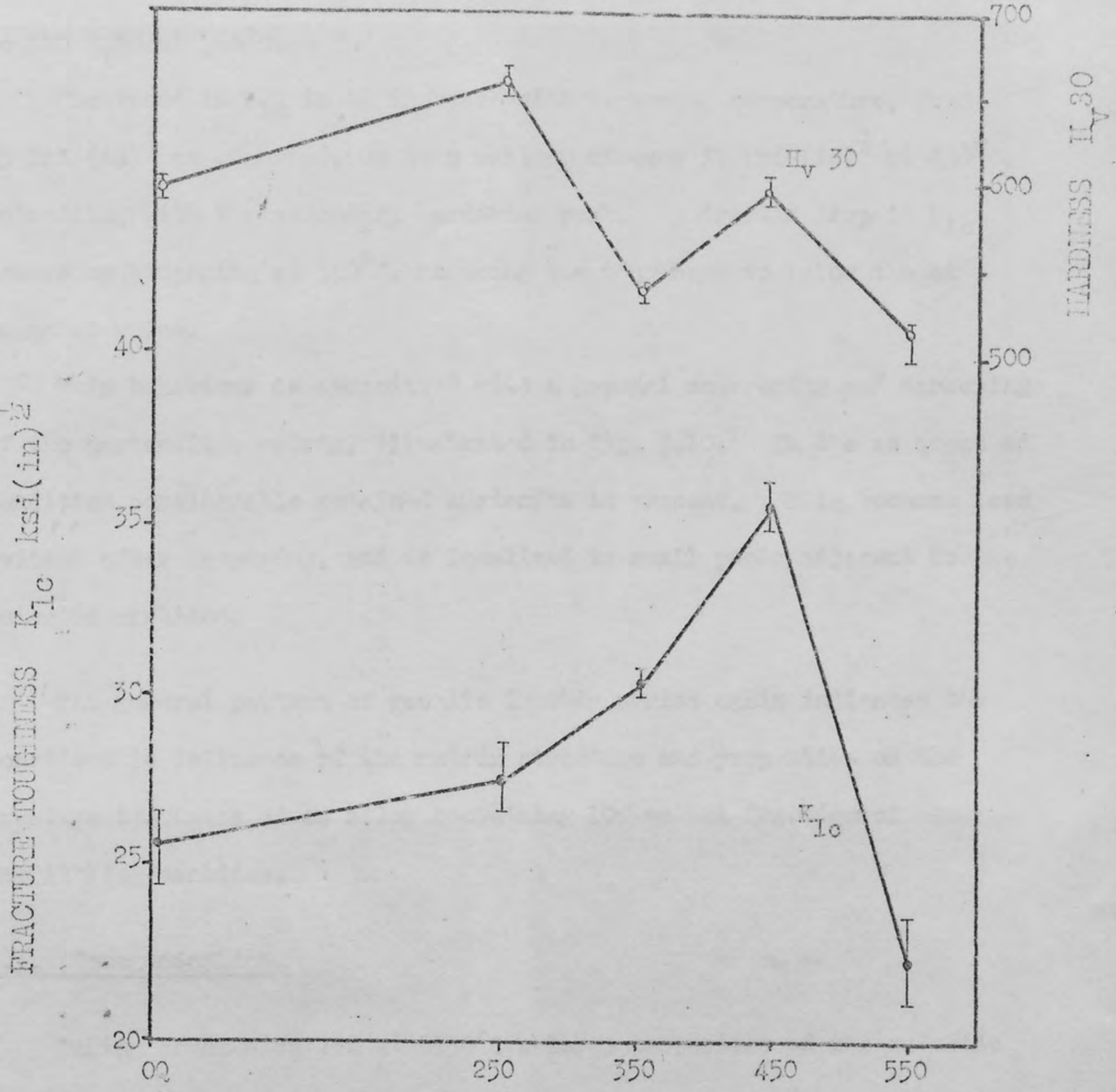

Fig. 7.9. Influence of Tempering Temperature on Fracture Toughness and Hardness.

observed at 450°C. This secondary peak reaches a level of 590 H_v30, compared to 660 H_v30 at 250°C, and 600 H_v30 as quenched. Overtempering above the secondary hardening temperature results in a fall in hardness to 520 H_v30 at 550°C.

The trend in K_{1c} is to increase with tempering temperature, from 25 ksi $(in)^{\frac{1}{2}}$ as quenched, up to a maximum of over 35 ksi $(in)^{\frac{1}{2}}$ at 450°C, coinciding with the secondary hardening peak. A drastic drop in K_{1c} occurs on tempering at 550°C, reducing the toughness to below the as quenched value.

This behaviour is associated with a gradual coarsening and darkening of the martensitic matrix, illustrated in fig. 7.10. In the as quenched condition considerable retained austenite is present. This becomes less evident after tempering, and is localised to small pools adjacent to the eutectic carbides.

The general pattern of results in this series again indicates the considerable influence of the matrix structure and properties on the fracture toughness of an alloy containing 10% volume fraction of embrittling carbides.

7.5. Homogenisation.

During homogenisation at 1150°C a large proportion of the eutectic carbides are taken into solid solution. The remaining free carbides become spherodised and the interdendritic network tends to break down into isolated particles. Solution of the alloy carbides (Cr Fe_7C_3) renders the matrix quite stable, and the austenite is readily retained to room temperature. The extent of carbide solution can be assessed from fig. 7.4., where the volume fraction carbides in alloys of varying carbon content is shown for an 8 hour homogenisation treatment. Roughly 50% of the original carbides are dissolved during this standard treatment.

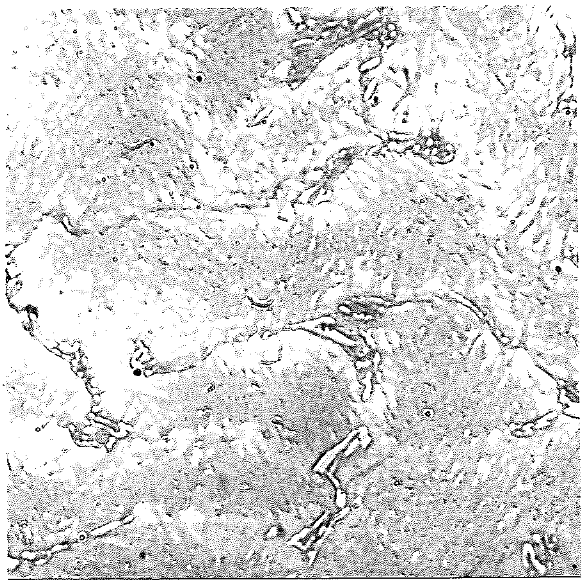

(a) As Quenched.

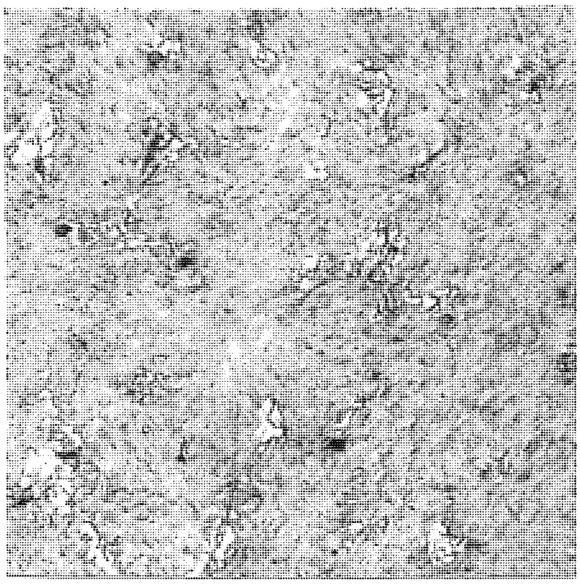

(b) Tempered 350°C.

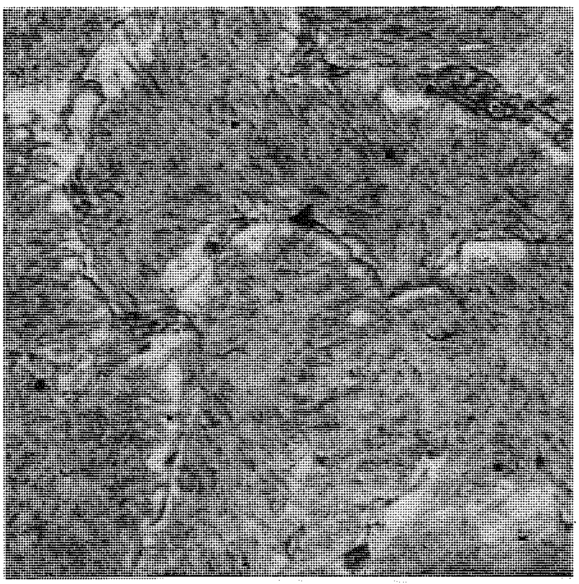

(c) Tempered 450°C.

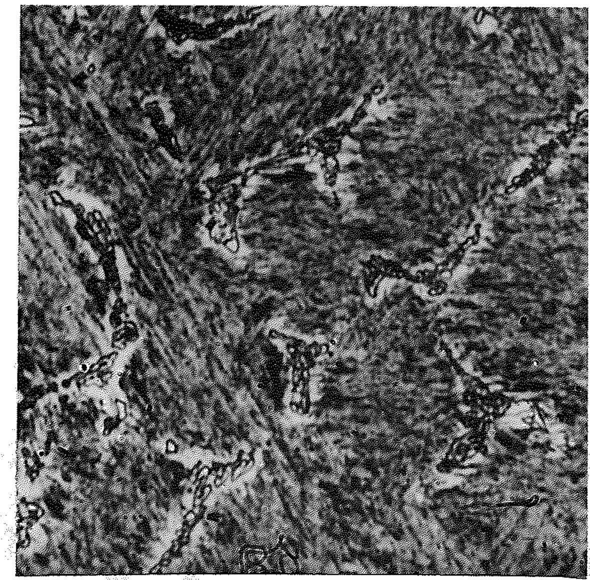

(d) Tempered 550°C.

Fig. 7.10. Microstructure of Material Tempered at Increasing Temperature, X 300.

Solution of carbides as a function of time at temperature, (1150°C), is shown in fig. 7.11. for a 1.4% carbon alloy.

Massive grain growth and segregation of undissolved carbides into a grain boundary film took place in the 0.8% carbon alloy during the standard 8 hour treatment. A similar effect occurred in the 1.4% carbon material after 16 hours at 1150°C. Individual carbide particles were observed within the grain boundary film in the 0.8% carbon structure, when almost all the free carbide was present in this form. Typical homogenised microstructures are shown in fig. 7.13 and it can be seen that the grain boundary film is beginning to develop in the 1.1 and 1.4% carbon alloys during the standard treatment.

Heat treatment to martensite after homogenisation resulted in preferential precipitation of secondary carbides at the grain boundaries and also as a sub-structure within the grains, (fig 7.14).

The trend in fracture toughness is a uniform decrease as the carbon content is raised. With one exception, K_{1c} was improved by homogenisation at all carbon levels. The 0.8% carbon alloy failed in a completely intergranular manner, the crack path following the grain boundary film mentioned above. In this case K_{1c} was reduced from 37.6 ksi.(in.)$^{\frac{1}{2}}$ as cast, to 35.5 ksi.(in.)$^{\frac{1}{2}}$ after homogenisation. The 1.4% carbon level proved to be most responsive to the 8 hour treatment, with over 50% increase in K_{1c} on the as cast value, from 26.5 ksi.(in.)$^{\frac{1}{2}}$ to 39.5 ksi.(in)$^{\frac{1}{2}}$. The plateau observed in the toughness curve for the as cast higher carbon series (fig. 7.6) was not evident after homogenisation. A constant rate of reduction in K_{1c} was revealed above 2.1% carbon, shown in fig. 7.12.

Fig. 7.11 illustrates the effect of homogenisation time on the fracture toughness of a 1.4% carbon alloy. It appears that there is a critical period in the solution of carbides where optimum toughness properties are realised. For the alloy examined, containing 1.4% carbon, the standard treatment of 8 hours produces maximum K_{1c}. Up to this time

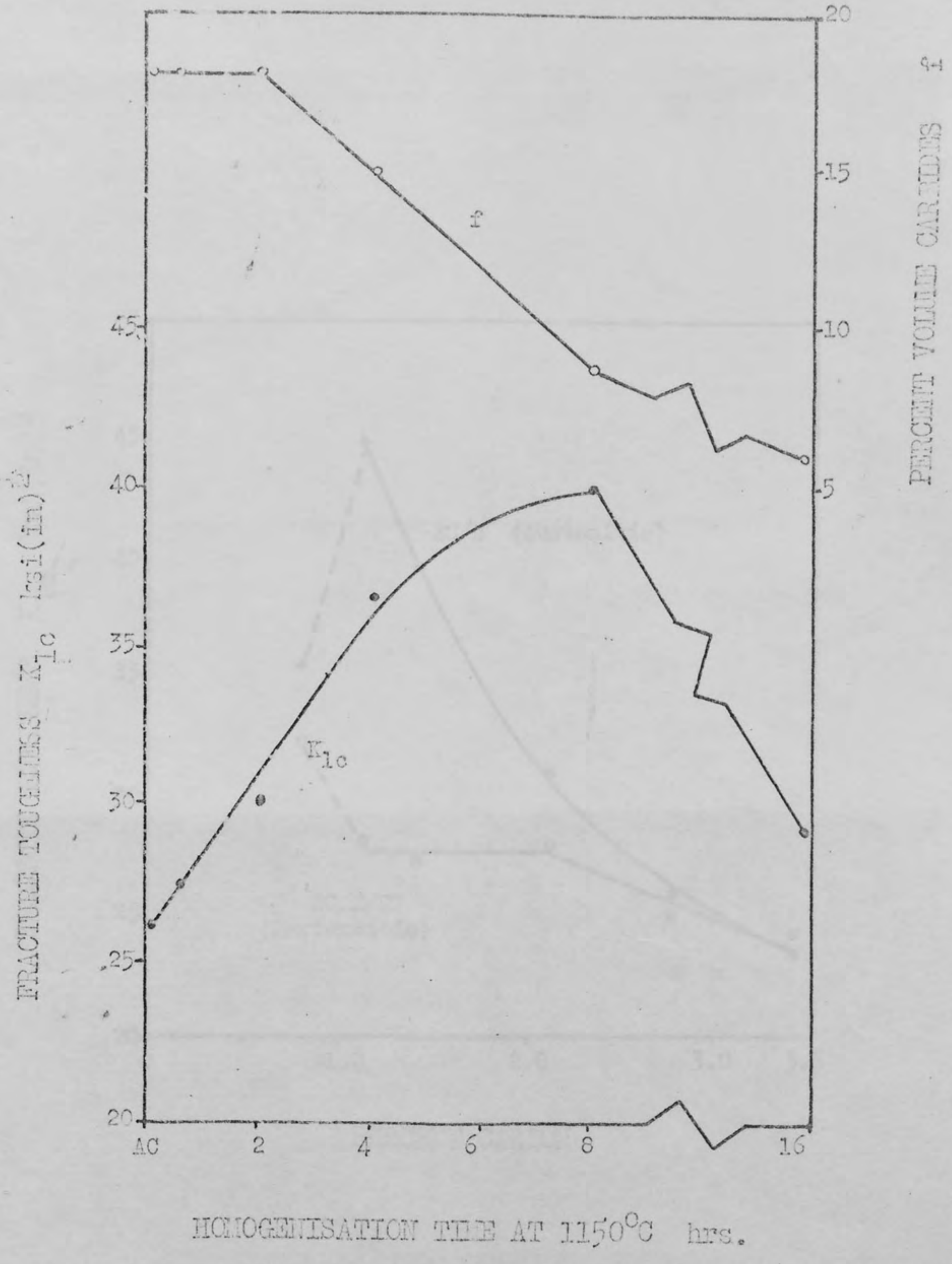

Fig. 7.11. Effect of Homogenisation Time on Volume Fraction of Carbides and Fracture Toughness.

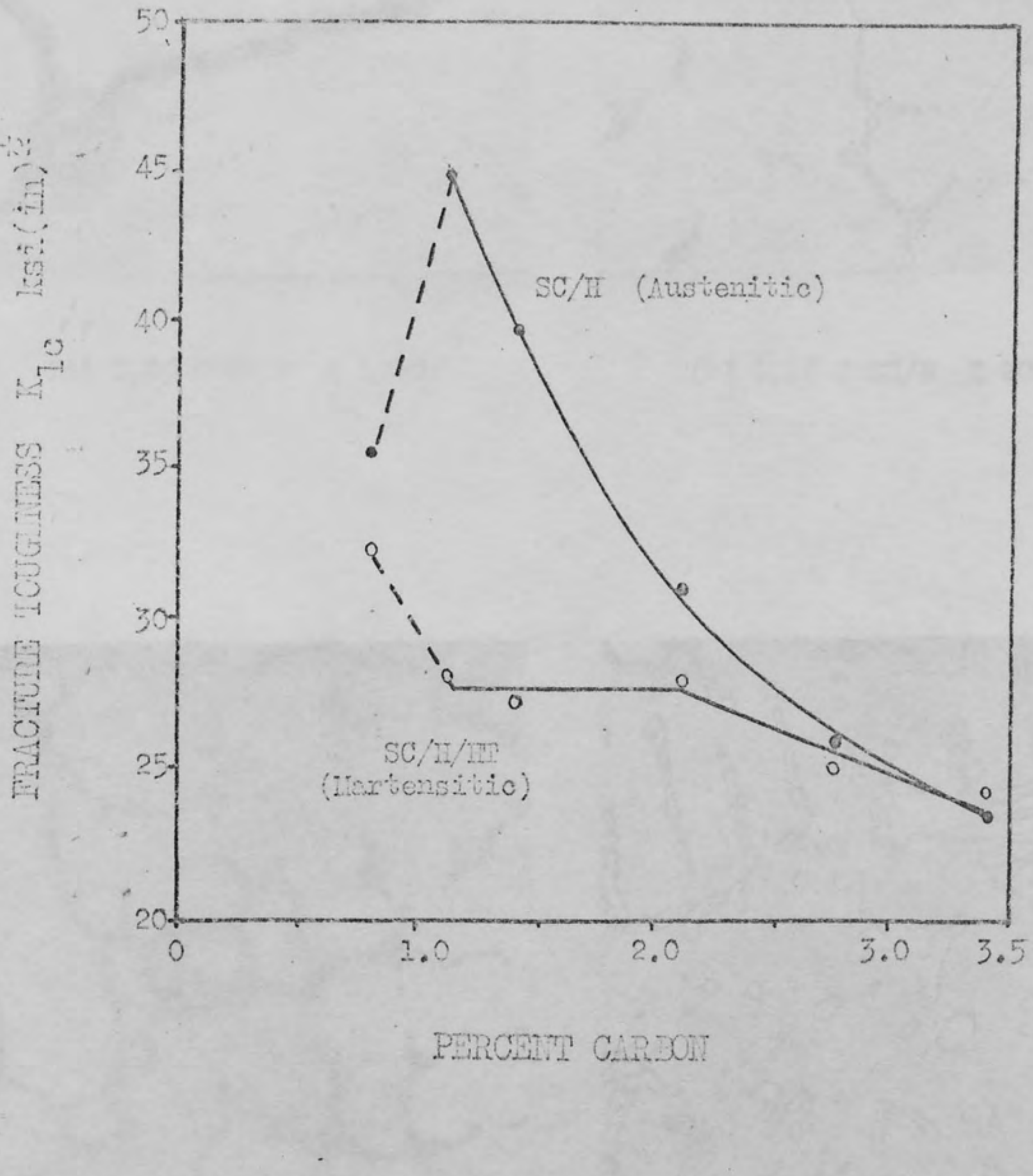

Fig. 7.12. Fracture Toughness of Homogenised and Homogenised/Hardened (250°C Temper) Material.

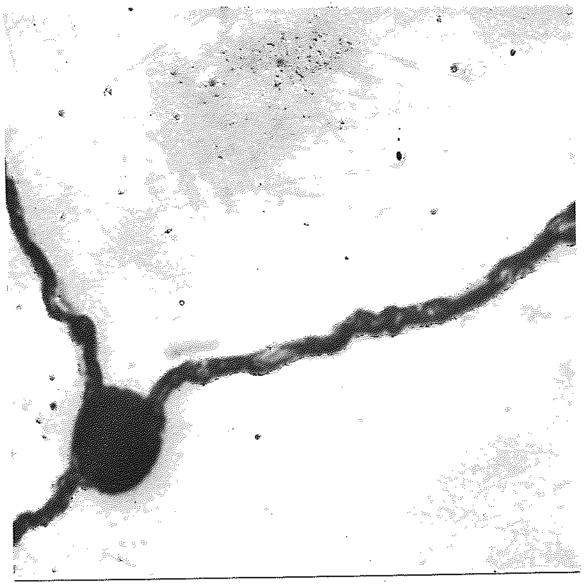

(a) 0.8% C SC/H X 1000.

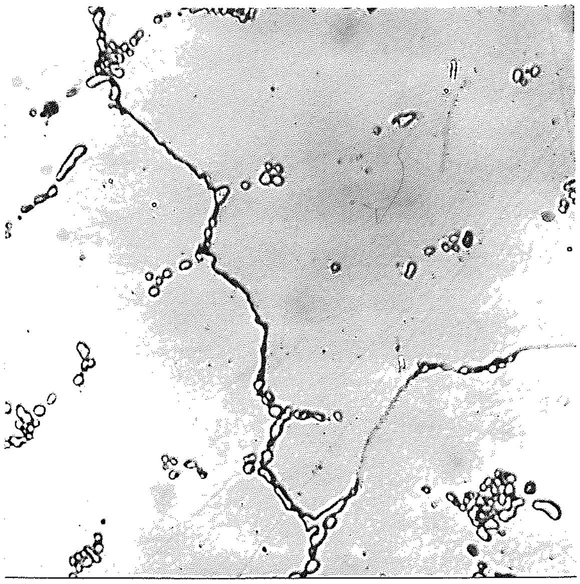

(b) 1.1% C SC/H X 200.

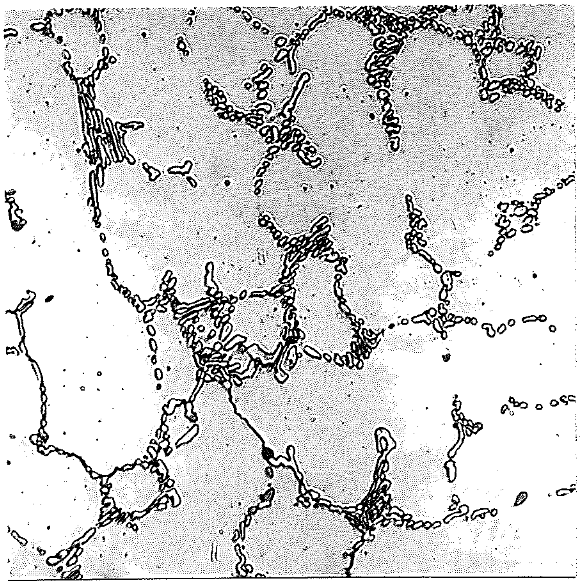

(c) 1.4% C SC/H X 150.

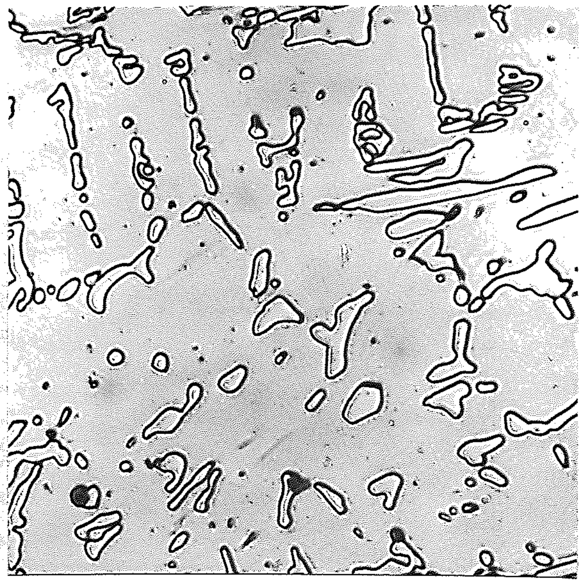

(d) 2.1% C SC/H X 200.

Fig. 7.13. Microstructure of Material Homogenised for 8 hours at 1150°C.

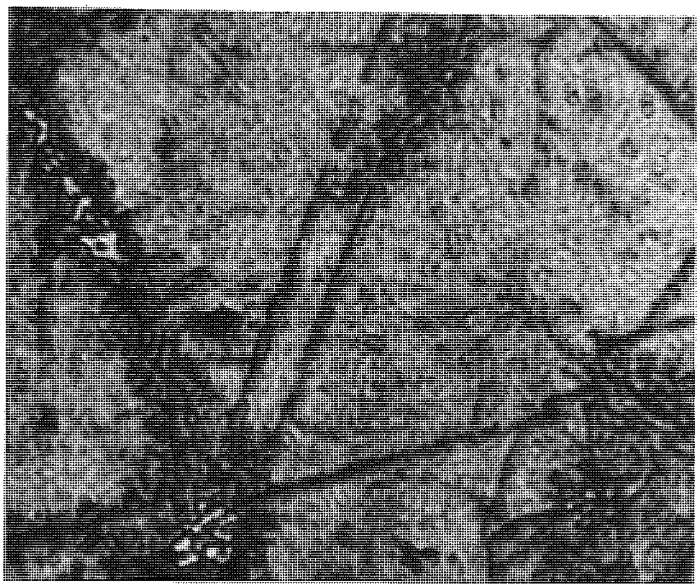

(a) 0.8% C SC/H/HT X 500.

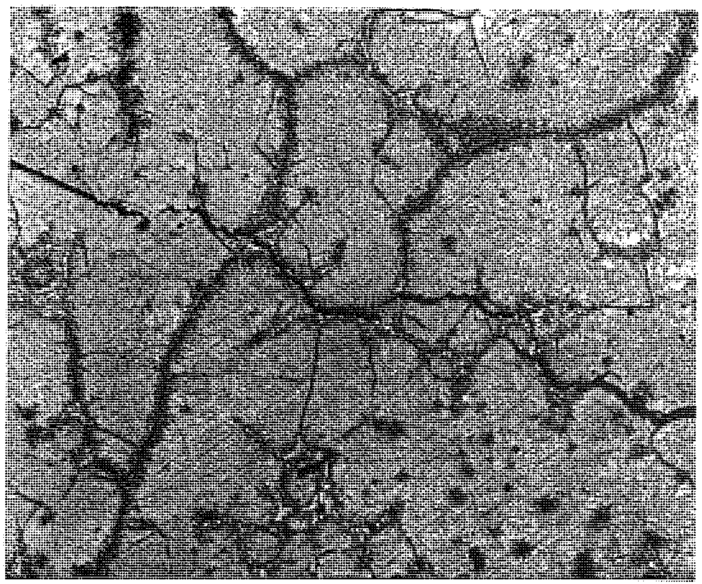

(b) 1.1% C SC/H/HT X 100.

Fig. 7.14. Typical Homogenised and Hardened Microstructures.

there is an increase in K_{1c} with soaking time from 25 ksi.(in.)$^{\frac{1}{2}}$ as cast to 36.5 ksi.(in.)$^{\frac{1}{2}}$ after 4 hours at 1150°C. The rate of increase in K_{1c} is then reduced up to 8 hours when the maximum of 39 ksi.(in.)$^{\frac{1}{2}}$ is achieved. The fall in toughness with further extension of time is associated with the formation of a grain boundary film and intergranular fracture.

Hardening of the homogenised alloys reduces K_{1c} to the level of the SC/HT series. As in the other martensitic material, there is little variation in K_{1c} over a wide range of carbon content. An interesting feature of this comparison between the two martensitic series, is that the SC/HT material exhibits a constant K_{1c} of 26.5 ksi.(in.)$^{\frac{1}{2}}$ up to 1.4% carbon (fig. 7.6), further increase in carbon reducing toughness. A similar pattern is established in the SC/H/HT structures, with a constant K_{1c} of 27.5 ksi.(in.)$^{\frac{1}{2}}$ up to 2.1% carbon. The homogenising treatment has effectively widened the range in carbon content over which matrix structure plays a significant part in fracture process.

The toughness of the 0.8% carbon alloy was hardly affected by heat treatment after homogenising, the fracture path remaining intergranular. As a result K_{1c} was somewhat higher than the level typical of martensitic alloys.

7.6. Sensitivity to Rate of Application of Stress Intensity.

The sensitivity of K_{1c} to variation in rate of application of stress intensity has been observed in austenitic and martensitic material. A range of testing speeds was used covering five orders of magnitude, from 0.005 to 50 cm/min. Crosshead speed was converted to stress intensity rate, in ksi.(in.)$^{\frac{1}{2}}$/min., by calibrating the load displacement system at 0.02 cm/min., and extrapolation. Calibration results for two specimens of different compliance functions are shown in fig. 7.15. Loading rates of 375 and 500 kg/min. were obtained for

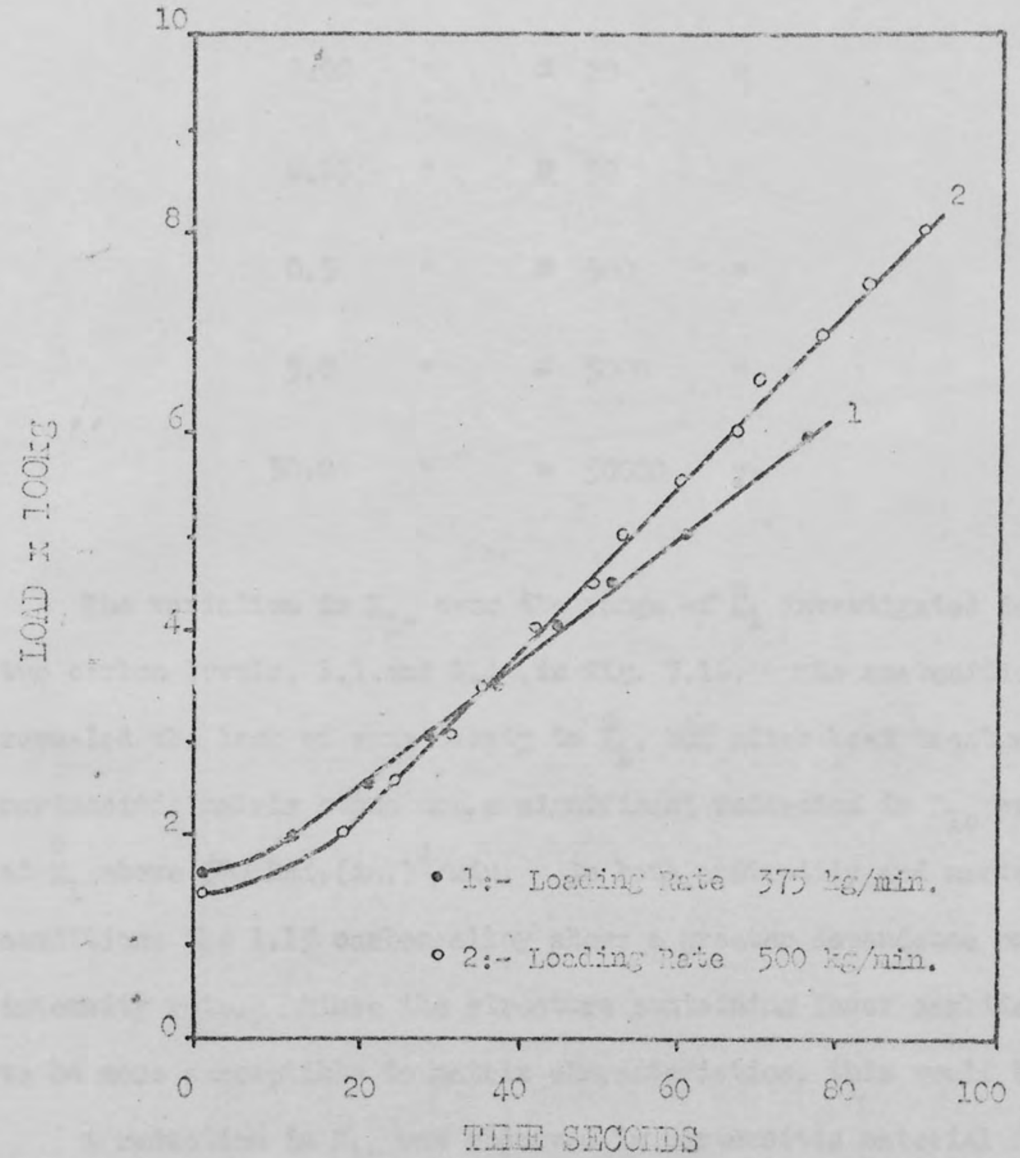

Fig. 7.15. Calibration of Loading Rate for Specimens with Geometrical Functions of 23.6 (1), and 17.5 (2).

specimens with functions of 23.6 and 17.5 respectively. Thus the rate of application of K is 19.7 and 19.5 ksi.(in.)$^{\frac{1}{2}}$/min. On extrapolation this led to the following correlation between crosshead speed and $\dot{K}_1$:

0.005	cm/min.	$\equiv$	5	ksi.(in.)$^{\frac{1}{2}}$/min.
0.02	"	$\equiv$	20	"
0.05	"	$\equiv$	50	"
0.5	"	$\equiv$	500	"
5.0	"	$\equiv$	5000	"
50.0	"	$\equiv$	50000	"

The variation in K_{1c} over the range of $\dot{K}_1$ investigated is shown for two carbon levels, 1.1 and 1.4%, in fig. 7.16. The austenitic material revealed the lack of sensitivity to $\dot{K}_1$, but after heat treatment to a martensitic matrix structure, a significant reduction in K_{1c} was detected, at $\dot{K}_1$ above 500 ksi.(in.)$^{\frac{1}{2}}$/min. In both austenitic and martensitic conditions the 1.1% carbon alloy shows a greater dependence on stress intensity rate. Since the structure containing fewer carbides is likely to be more susceptible to matrix characteristics, this would be expected.

A reduction in K_{1c} was observed in martensitic material from 30 to 21 ksi.(in.)$^{\frac{1}{2}}$, between 5×10^2 and 5×10^4 ksi.(in.)$^{\frac{1}{2}}$/min; and from 27 to 20 ksi.(in.)$^{\frac{1}{2}}$ between 50 and 5×10^4 ksi.(in.)$^{\frac{1}{2}}$/min., in 1.1 and 1.4% carbon material respectively. This behaviour is typical of B.C.C. metals, which exhibit decreasing toughness with increasing loading rate. The results of Priest and May(57) on low alloy martensitic steels show a drop in K_{1c} of between 5 to 20 ksi.(in.)$^{\frac{1}{2}}$ over a similar range of stress intensity rates.

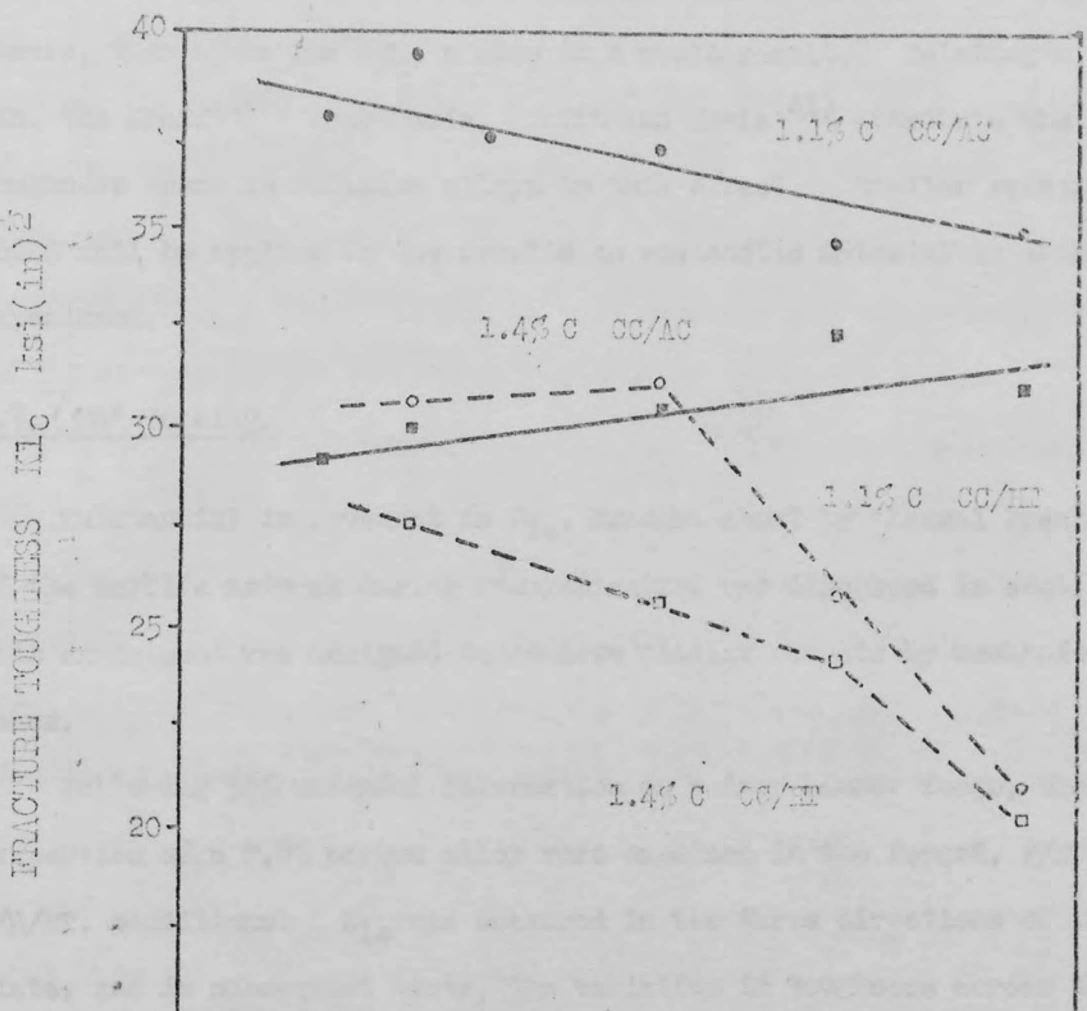

Fig. 7.16. Variation of Fracture Toughness with Rate of Application of Stress Intensity.

An almost constant level of K_{1c} was observed in the austenitic material, with a slight trend upward in 1.4% carbon, and downward in 1.1% carbon material. Beeukes[85] has noted that θ, the absolute slope of the plastic region of the logrithmic stress/strain curve, whilst remaining constant for B.C.C. metals, increases with testing speed in F.C.C. structures. If this is a stronger effect than the increasing yield stress, then since $n \propto \theta/\sigma_y$, a rise in n would result. Relating n to K_{1c} via. the Krafft[86] hypothesis, Krafft and Irwin[41] attribute the rising toughness trend in titanium alloys to this effect. Similar reasoning could well be applied to the results on austenitic material in this experiment.

7.7. Hot Working.

Substantial improvement in K_{1c}, brought about by thermal breakdown of the carbide network during homogenisation was discussed in section 7.5. This experiment was designed to achieve similar results by mechanical means.

Following 50% uniaxial deformation on a drop hammer forge, the fracture properties of a 0.8% carbon alloy were examined in the forged, F/HT., and F/H/HT. conditions. K_{1c} was measured in the three directions of the plate, and in subsequent tests, the variation in toughness across the forging was investigated.

The most significant feature of the results (table 6.12.(a)) is the high K_{1c} in the transverse direction compared to that in the longtitudinal direction. This is due to the change in the line of crack propagation relative to the elongated grains. No change in K_{1c} was observed in the two longtitudinal directions of the plate, when cracking occurred parallel to the orientated structure. In the transverse direction, with crack propagation normal to the plate fibres a rise in K_{1c} was detected in all three conditions, from 31 to 40 ksi.(in.)$^{\frac{1}{2}}$ as forged; 39 to 48 ksi.(in.)$^{\frac{1}{2}}$

F/HT; and 31 to 38 ksi.(in.)$^{\frac{1}{2}}$ F/H/HT. The orientation of the fibred structure relative to the direction of crack propagation is illustrated in fig. 7.17.

The microstructure of the forged material in the three conditions investigated is shown in fig. 7.18. In the as forged condition the structure consisted of very coarse martensite and retained austenite, K_{1c} in the transverse direction was 40.9 ksi.(in.)$^{\frac{1}{2}}$. Heat treatment led to a refined and fully martensitic structure and an improvement in K_{1c}, to 47.5 ksi.(in.)$^{\frac{1}{2}}$. The directionality imposed during deformation remained unaltered after hardening, and was still evident after homogenisation. Preferential precipitation of secondary carbides and subsequent decoration of the microstructure was evident in the F/H/HT material, and K_{1c} in this condition was reduced to 37.5 ksi.(in.)$^{\frac{1}{2}}$. The fracture path, as in previous low carbon homogenised alloys, was intercrystalline.

The abnormal level of scatter on K_{1c} results from the transverse direction led to a decision to carry out a more detailed investigation of the variation in properties across the forged plate. The spread of results on specimens taken from similar positions relative to the centre-line of the plate was within more reasonable limits. K_{1c} was measured at four positions from the centre to the edge of the plate, summarised in table 6.12.(b). A constant level of K_{1c} across the width of the plate was observed with crack propagation parallel to the orientation of the structure (longtitudinal values). In the transverse direction the K_{1c} from intermediate positions was consistently higher than from central or edge regions. This trend is illustrated in fig. 7.19. No significant variation in hardness or macrostructure was detected to explain this effect.

Recent innovations in this field, discussed by Guthrie and Jolley,(92) are encouraging for future development in the forging of white cast iron.

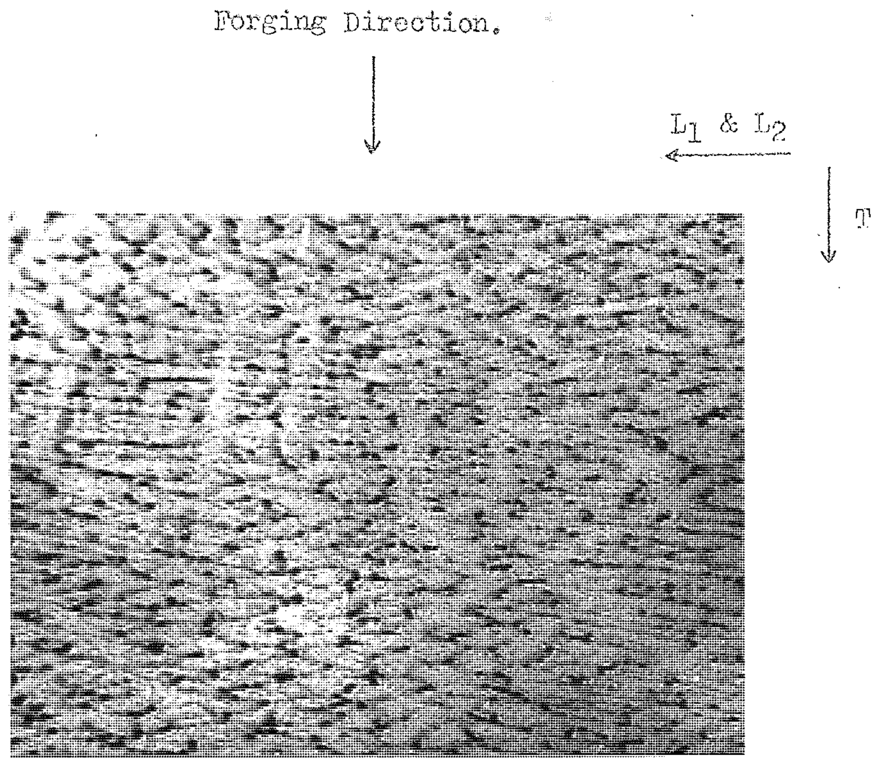

(a) 0.8% C SC/F/HT Transverse Section X 30

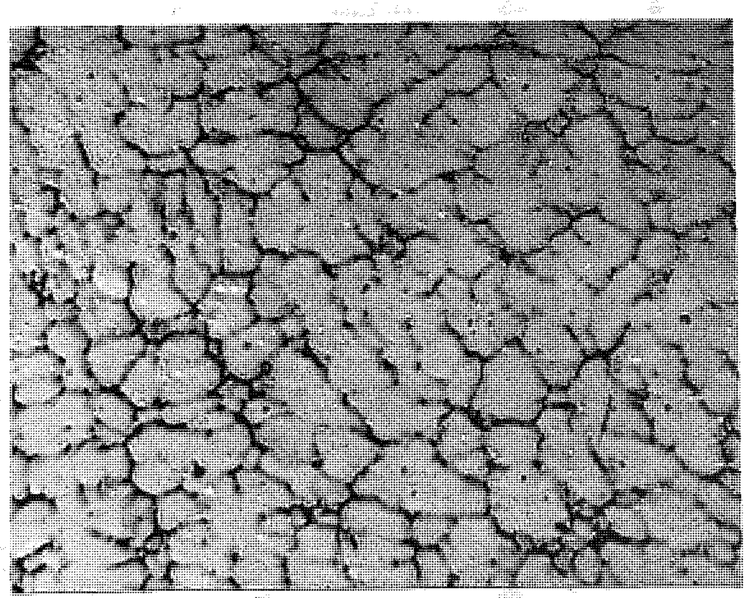

(b) 0.8% C SC/F/HT Longtitudinal Section X 30

Fig. 7.17. Orientation of Microstructure in Forged Material, Relative to the Direction of Crack Propagation.

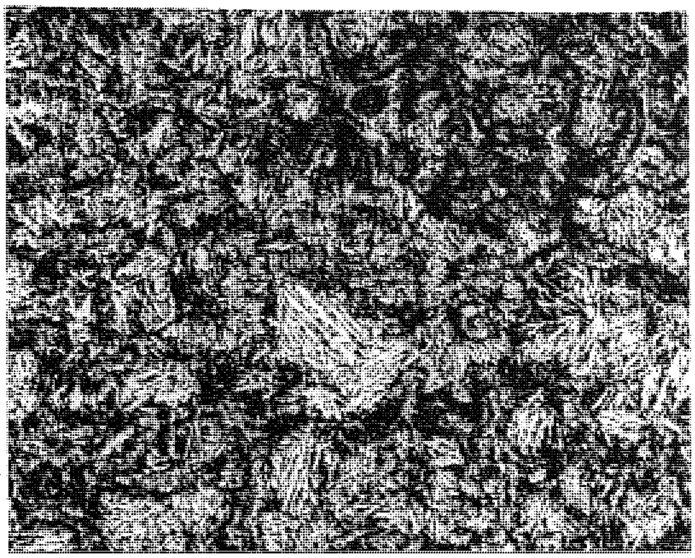

(a) 0.8% C SC/F X 100

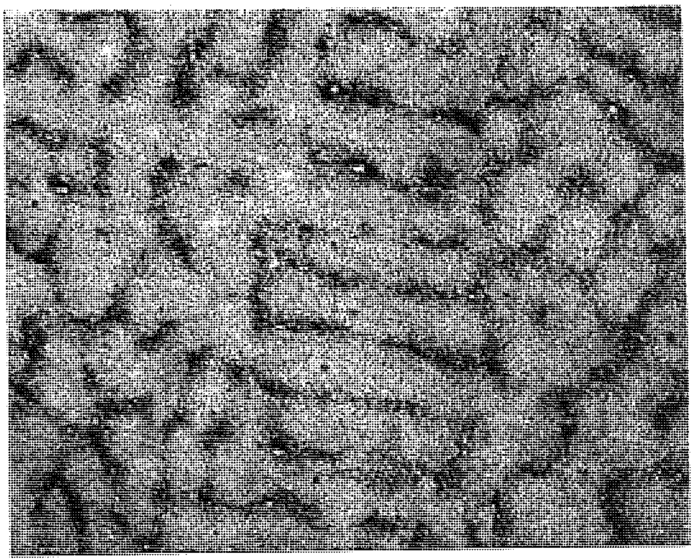

(b) 0.8% C SC/F/HT X 100

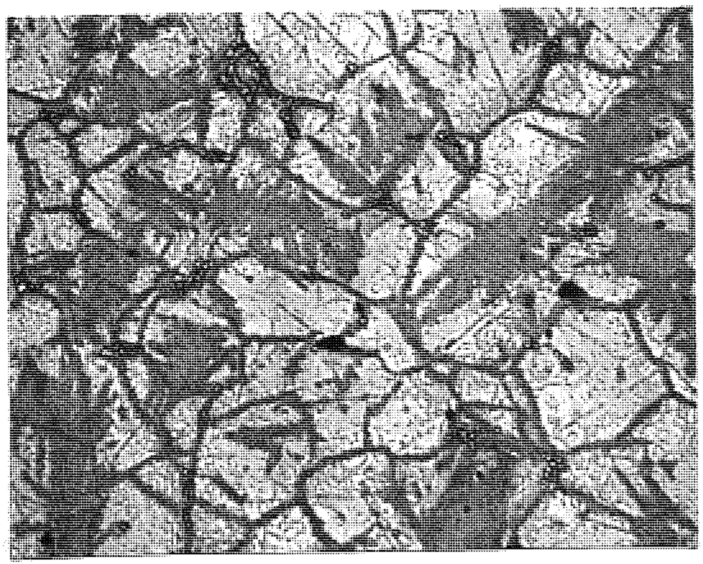

(c) 0.8% C SC/F/H/HT X 100

Fig. 7.18. Microstructure of Forged Material.

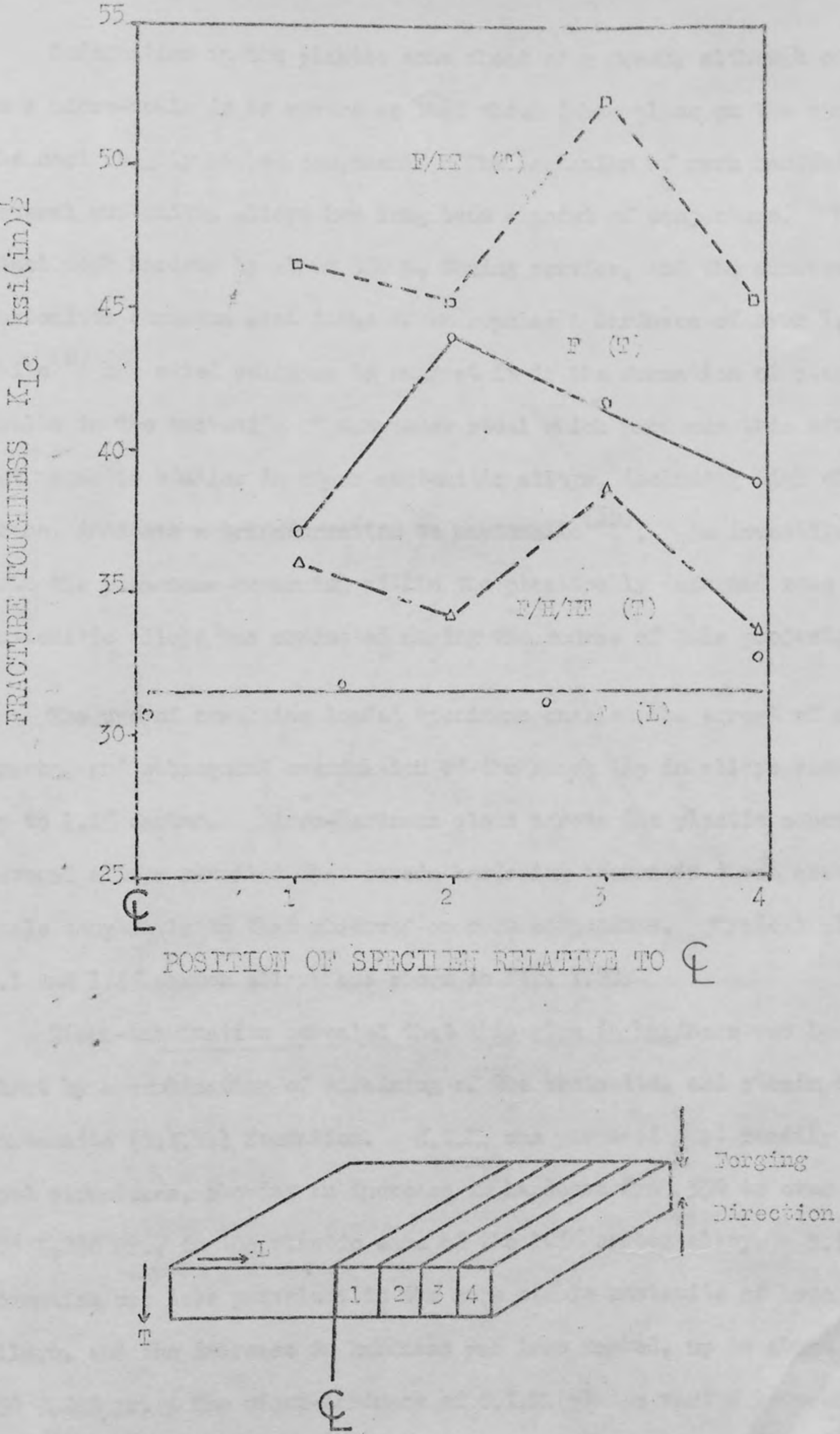

Fig. 7.19. Variation of Fracture Toughness Across Forged Plate.

7.8. Strain Hardening Phenomena.

Deformation in the plastic zone ahead of a crack, although occurring on a micro-scale is as severe as that which takes place on the surface of the most roughly worked component. The mechanism of work hardening in several austenitic alloys has long been a point of conjecture. Manganese steel work hardens by about 300 H_v during service, and the surface of austenitic chromium cast irons often reaches a hardness of over 1,000 H_v. White[8] has cited evidence to suggest it is the formation of stacking faults in the austenite of manganese steel which produces this effect, but magnetic studies in other austenitic alloys, including high chromium irons, indicate a transformation to martensite[35]. An investigation into the phenomena occurring within the plastically deformed zone of austenitic alloys was conducted during the course of this project.

The use of crackline loaded specimens enabled the arrest of running cracks, and subsequent examination of the crack tip in alloys containing up to 1.4% carbon. Micro-hardness plots across the plastic zones of several alloys revealed that strain hardening occurs in these areas on a scale comparable to that observed on worn components. Typical plots for 1.1 and 1.4% carbon alloys are shown in fig. 7.20.

Micro-examination revealed that this rise in hardness was brought about by a combination of straining of the austenite, and strain induced martensite (S.I.M.) formation. S.I.M. was produced most readily in as cast structures, showing an increase in hardness from 350 to over 800 H_v250 gr., in the plastic zone of the 1.4% carbon alloy. S.I.M. formation was less prevalent in the more stable austenite of homogenised alloys, and the increase in hardness was less marked, up to about 600 to 650 H_v250 gr. The micro-hardness of S.I.M. plates varied between 700 to 850 H_v100 gr., and in strained austenite hardness was found to increase with slip line density. At a slip line density of 100 lines/mm. the

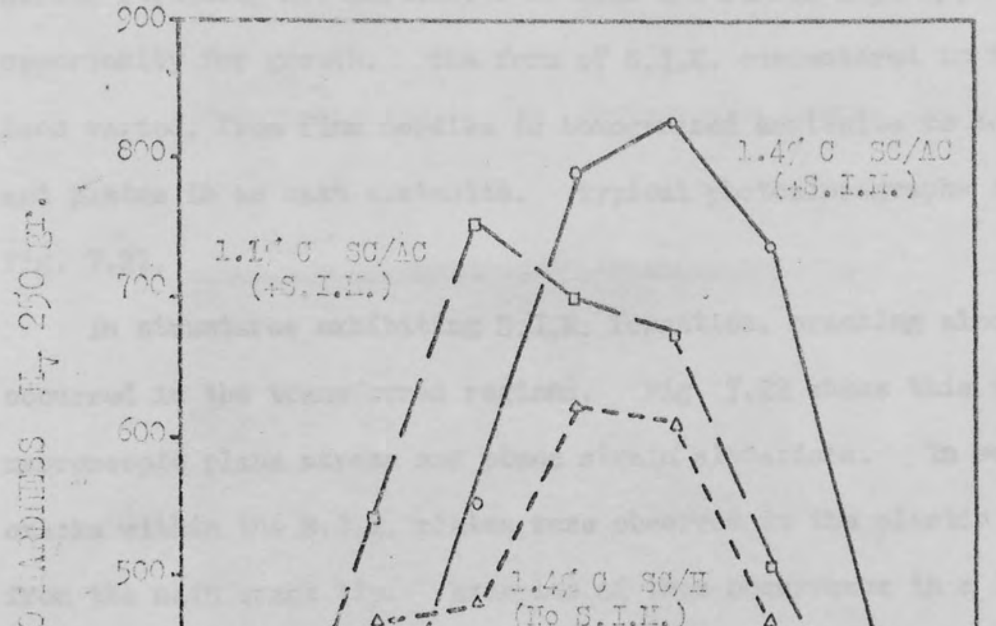

Austenite :- 350 H_v 100gr.

S.I.M. :- 700-850 H_v 100gr.

Strained Austenite :- 100 lines/mm - 450-500 H_v 100gr.

400 lines/mm - 550-650 H_v 100gr.

Fig. 7.20. Micro-Hardness Plots Across Plastic Zone (at the Free Surface) of As Cast and Homogenised Material.

hardness was 450 to 500 H_v 100 gr; at 400 lines/mm. it was 550 to 650 H_v 100 gr., compared to 350 H_v 100 gr. for unstrained austenite.

The size and shape of S.I.M. plates will depend on the stability of the austenite, nucleation and growth characteristics for S.I.M. in that austenite, and the thermal conditions prevailing. Rickard[26] has noted that S.I.M. normally occurs as fine needles, since it is likely that during straining new martensite needles are formed rapidly, with little opportunity for growth. The form of S.I.M. encountered in this work has been varied, from fine needles in homogenised austenite to coarse needles and plates in as cast austenite. Typical photomicrographs are shown in fig. 7.21.

In structures exhibiting S.I.M. formation, cracking almost inevitably occurred in the transformed regions. Fig. 7.22 shows this in both macroscopic plane stress and plane strain situations. In some instances cracks within the S.I.M. plates were observed in the plastic zone remote from the main crack tip. Examples of this occurrence in a 1.4% carbon as cast structure are shown in fig. 7.23. Plates (b) and (c) in fig 7.23 show clearly a crack in a carbide colony emanating into the matrix, and running into the martensite in preference to the austenite.

There are two points of interest concerning the practical potential of the S.I.M. transformation in austenitic abrasion resistant alloys. The development of a work hardened layer during service has always been a feature of this type of alloy, and the formation of S.I.M. in this region could be a means of increasing the surface hardness and wear resistance even further. Conflicting evidence on the effect of S.I.M. on toughness suggests that this might be a function of the alloy system. High strength, combined with high ductility and K_{1c} can be achieved when the formation energy of S.I.M. is harnessed into the fracture process, as in T.R.I.P. steels. However, the production of S.I.M. in cast irons appears to impair the impact properties,[26] possibly due to the formation of a

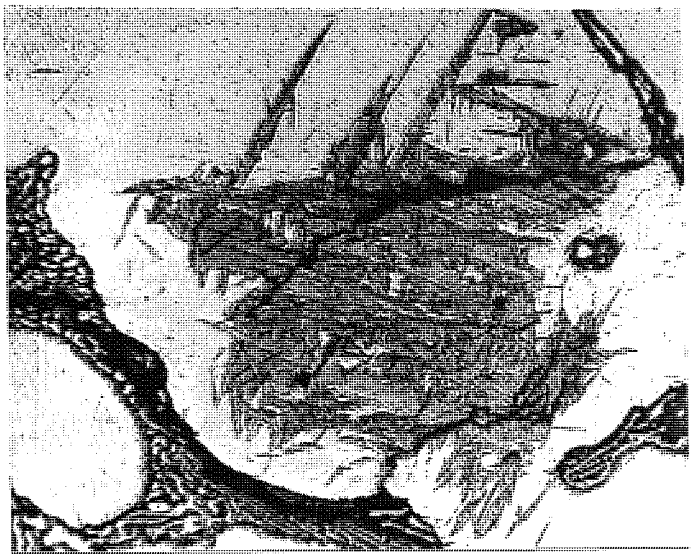

(a) 1.4% C SC/AC X 450

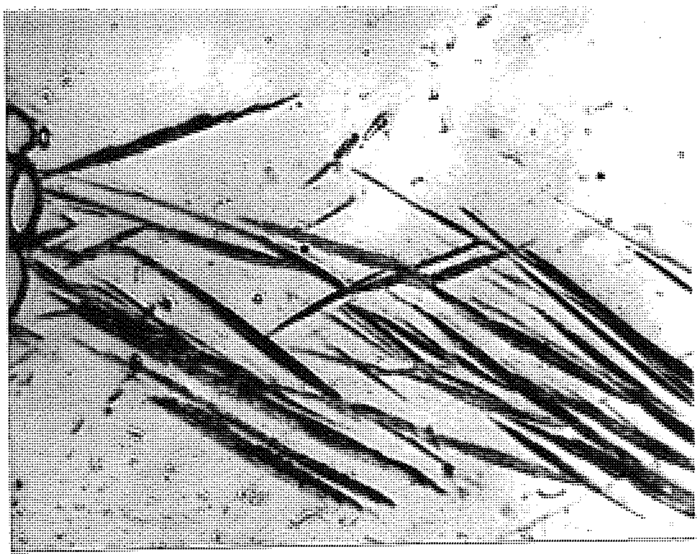

(b) 1.1% C SC/H X 1000

(c) 1.4% C CC/AC X 1500

Fig. 7.21. Typical Strain Induced Martensite.

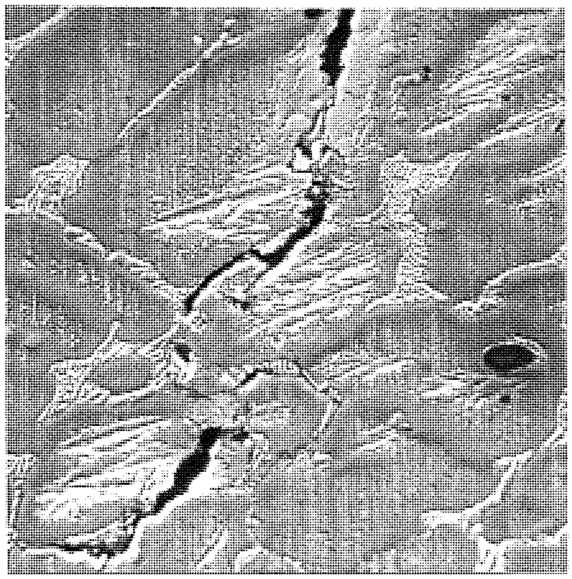

(a) 1.4% C SC/AC X 700

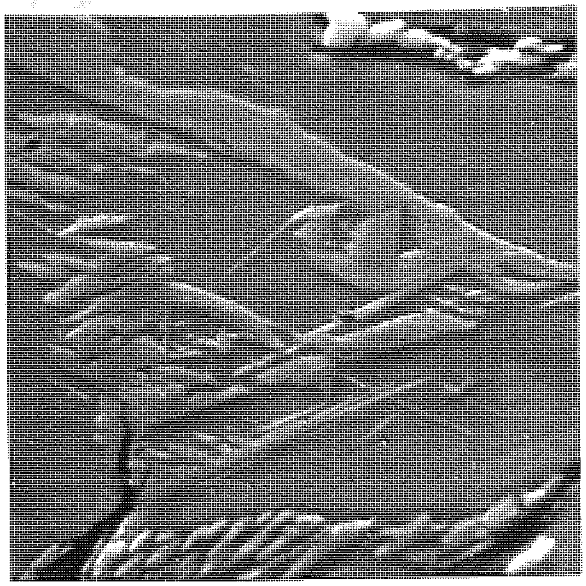

(b) 1.1% C SC/AC X 1600

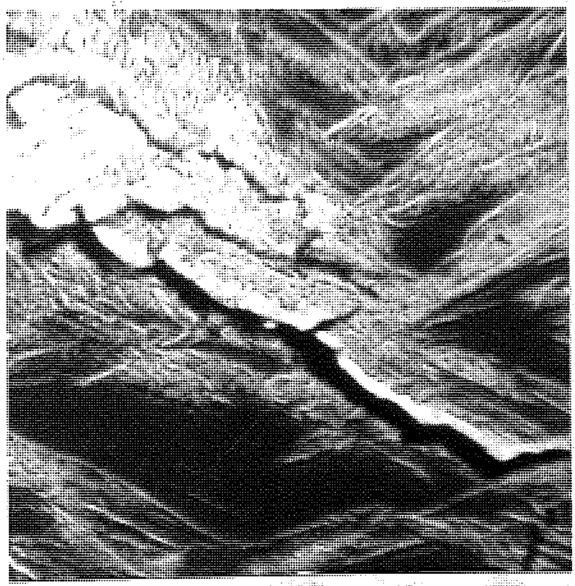

(c) 1.1% C SC/AC X 2400

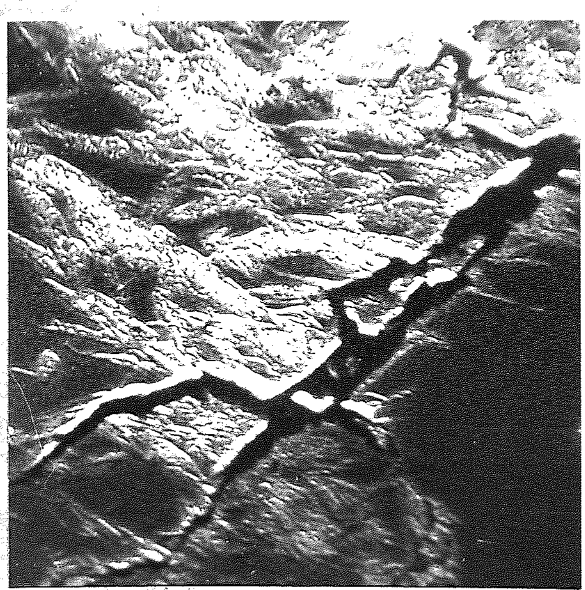

(d) 1.1% C SC/AC X 2400

Fig. 7.22. Scanning Electron Micrographs showing Crack Propagation through Strain Induced Martensite: (a) & (b) Under Macroscopic Plane Stress (on Free Surface). (c) & (d) Under Macroscopic Plane Strain (at Mid Thickness).

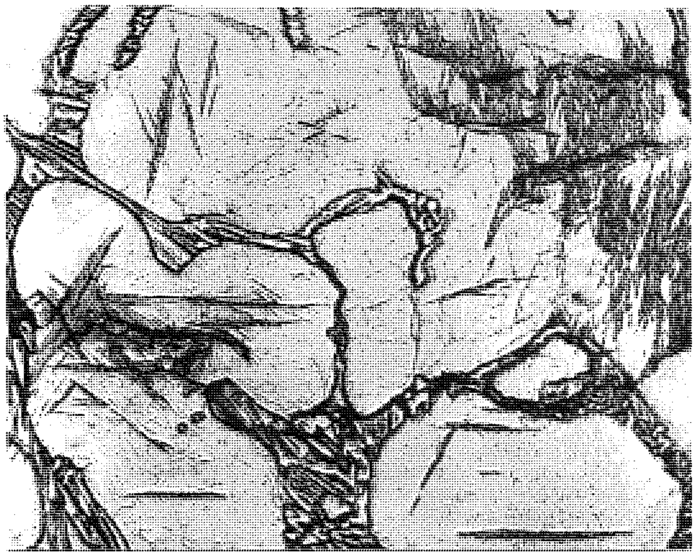

(a) 1.4% C SC/AC X 350

(b) 1.4% C SC/AC X 1000

(c) 1.4% C SC/AC X 1000

Fig. 7.23. Crack Formation in Strain Induced Martensite Plates Ahead of the Main Crack Tip.

brittle high carbon martensite. It was therefore considered pertinent to clarify the position in the 15% Cr. series of alloys.

The production of S.I.M. has been shown to be strongly dependent upon stress and strain.[25] Because of the limited strain involved in the fracture process of these alloys the most effective means of increasing the volume of martensite appeared to be raising M_d by alloying. Early investigations[27,28] showed that tensile deformation is most effective in promoting S.I.M., whereas compression opposes the expansion associated with a transformation to martensite. It was not surprising, therefore, that the tensile test was found to be the most convenient way of assessing the influence of alloying elements on M_d. The results of a survey into the effects of C, Mn, Ni and Co are summarised in tables 6.13.(a) and (b).

The scope of this survey is not sufficiently extensive as to provide quantitative information, but its purpose is fulfilled in that it indicates the trend of behaviour of the elements investigated. The results on austenitic stabilisers are in accordance with previous work, in that carbon emerged as the most potent element in reducing M_d, whereas manganese and nickel are only mildly effective. In heats T3 and 4 the low carbon was compensated for by nickel additions to retain an austenitic matrix. Cobalt was investigated on the grounds of its effect on M_s, which, with aluminium are the only elements known to raise M_s. Since aluminium is a strong ferrite stabiliser[93] in chromium alloys it was not considered with respect to M_d. The addition of 2% cobalt increased the volume of S.I.M. from a trace to 10%, measured empirically in a tensile test.

The survey provided two opportunities to assess the influence of S.I.M. formation on tensile properties, at a constant carbon level. In each case the production of S.I.M. was accompanied by an increase in U.T.S. from 64 to 82 ksi. in heats T3 and T4; and from 73 to 80 ksi. in heats T7 and T8, corresponding to a 15% and 10% increase in S.I.M. volume respectively.

In the relatively ductile alloys such as the 18/8 stainless and T.R.I.P. steels used by many workers, S.I.M. formation has taken place throughout the gauge length of tensile specimens. The low ductility of the alloys investigated here, confined the S.I.M. to the area immediately adjacent to the fracture. Only rarely was the transformation observed in areas remote from the fracture surface. This means that the stress required to produce S.I.M. is also sufficient to initiate failure under the prevailing stress conditions, where yielding is almost coincident with fracture. In the 0.5% carbon alloy, heat T4, the region between yield and failure was extended and a feature characteristic of S.I.M. formation was revealed. Serrations were produced in the load/extension curve, attributed to the formation and subsequent deformation of spontaneous bursts of S.I.M., causing a local extension at constant stress. This effect is illustrated in fig. 7.24., and typical longtitudinal microsections of tensile specimens are shown in fig. 7.25.

Two heats were subsequently produced from which it was hoped to determine the influence of S.I.M. on the K_{1c} of 15% chromium alloys. The first heat was of the basic 1.1% carbon composition with 4% cobalt added. In the second heat, also containing 4% cobalt, the carbon was reduced to 0.6%, and 2% manganese added to maintain the austenitic matrix. To produce a control alloy of identical composition, both heats were cast in two parts, the cobalt being added to the second half of each. Chemical analysis and the results of K_{1c} tests in the as cast condition and after homogenisation are tabulated in tables 6.14.(a) and (b).

Unfortunately the 0.6% carbon alloy failed in an intergranular manner, an undesirable feature evident in many of the low carbon alloys tested. This resulted in little plastic deformation and only traces of S.I.M. in the fracture process. A direct assessment was possible, however, from heat K1 in the as cast condition, where no significant variation in K_{1c}

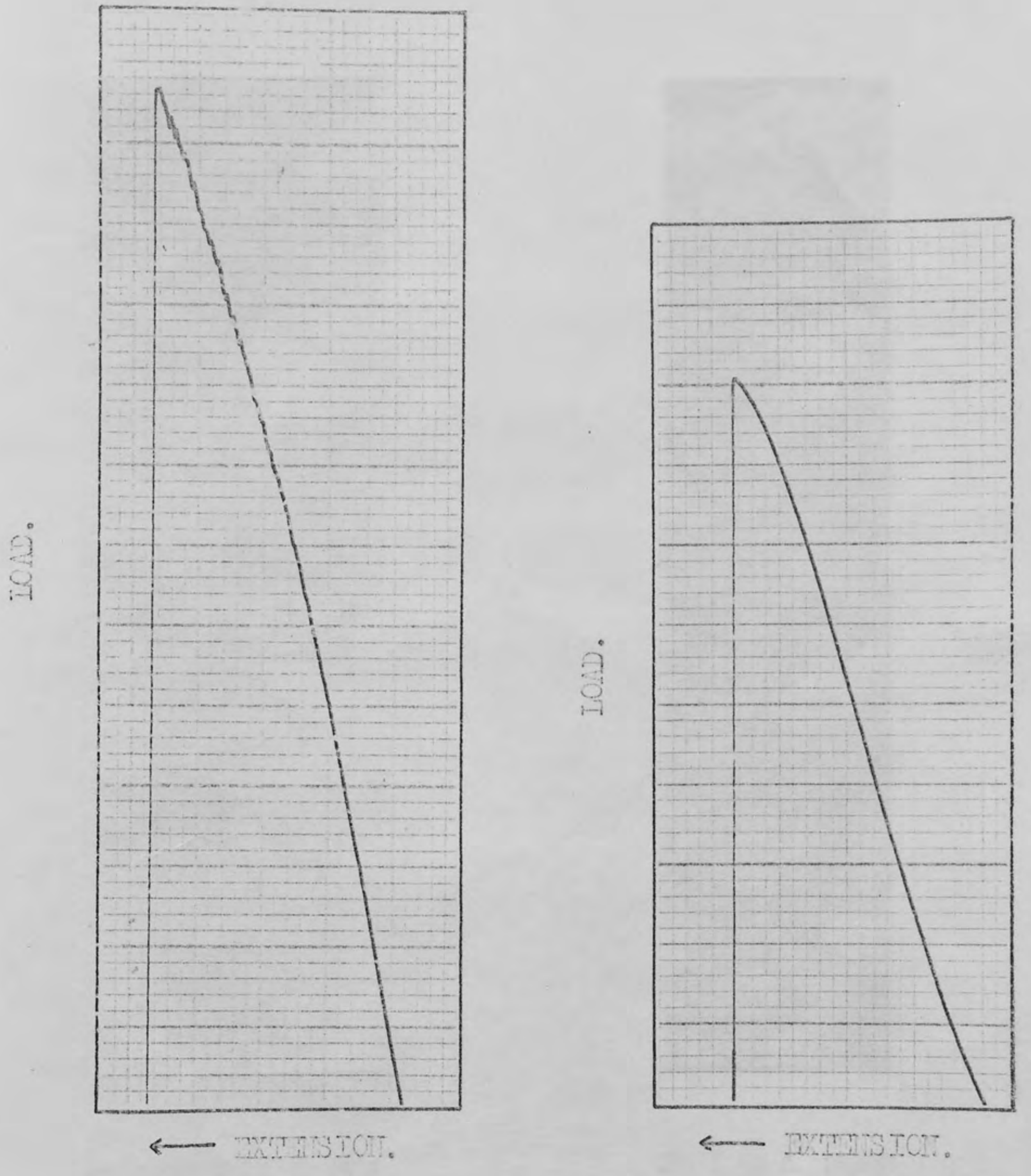

(a) Heat T4 0.5% C. Showing Serrations Corresponding to S.I.M. Formation.

(b) Heat T5 0.8% C. No S.I.M. Formation.

Fig. 7.24. Influence of Strain Induced Martensite Formation on the Load/Extension Curve.

(a) Heat T.4. 0.5% C

20% S.I.M.

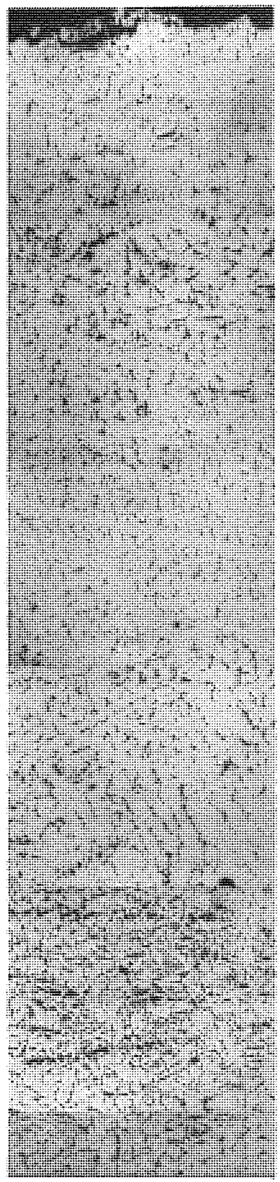

(b) 1.4% C SC/AC

Showing Band of S.I.M. Remote from Fracture.

Fig. 7.25. Longtitudinal Sections of Tensile Specimens showing Strain Induced Martensite Formation.

was detected when an estimated 15% of the matrix in the plastic zone transformed to martensite.

The relationship between plastic energy dissipation and S.I.M. formation is discussed in section 8.2.

7.9. Fractographic Examination.

A comprehensive fractographic survey of the 15% chromium series of alloys under investigation was made on a Cambridge scanning electron microscope. Fracture surfaces from the six carbon levels and all the heat treatments utilised were included in the examination. Sample preparation was discussed in section 5.5.

The area studued in all cases was that adjacent to the crack tip, where rapid crack propagation is initiated. In low carbon alloys the fatigue crack was easily discernable as a flat striated region, showing interconnected fracture facets on different planes, illustrated in fig. 7.26. In the higher carbon alloys, particularly 2.9% and 3.4%, it was often difficult to distinguish between the rapid crack and fatigue cracked region. The direction of macro crack propagation in all the fractographs is from left to right, as shown in fig. 7.26.

Fig. 7.27 shows fractographs of the six alloys in order of increasing carbon content in the as cast condition. Up to 1.4% carbon, plates (a), (b), and (c), the fracture surface consists of ductile tearing and fractured carbides, with the latter becoming more evident at the higher carbon levels. At 1.4% carbon, carbides constitute about 75% of the fracture surface. At 2.2% carbon and above, plates (d), (e), and (f), the fracture surface is completely dominated by the cleavage fracture of carbide colonies. Plate (f) shows a fractured primary carbide surrounded by the lammellar eutectic carbide colonies. This evidence confirms the assumptions made in section 7.2, concerning the fracture process in austenitic structures. It was suggested that up to 1.4% carbon, the

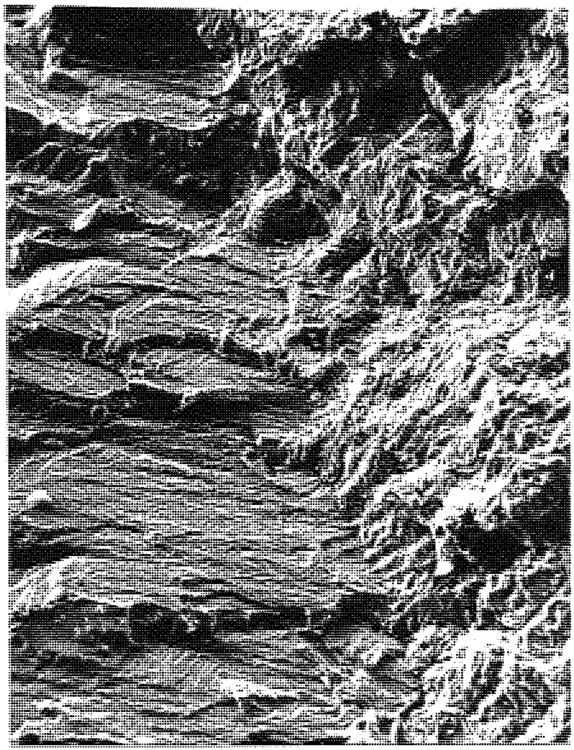

(a) 1.1% C SC/AC X 150

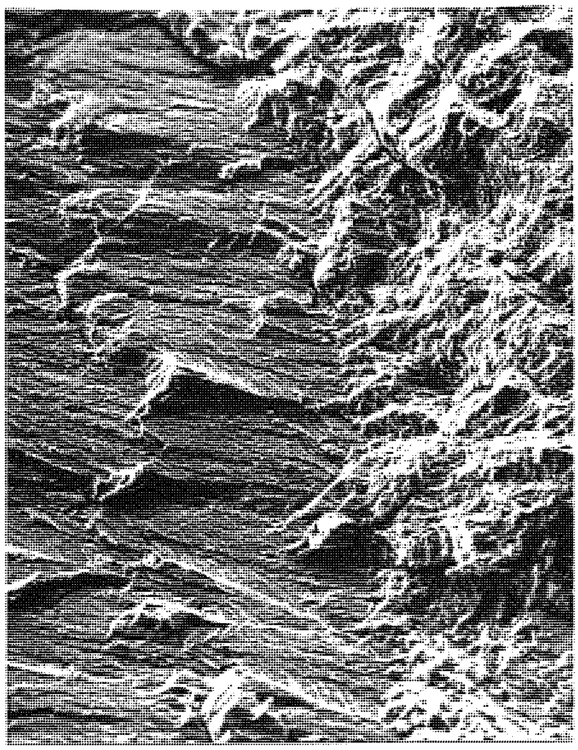

(b) 1.4% C SC/H X 150

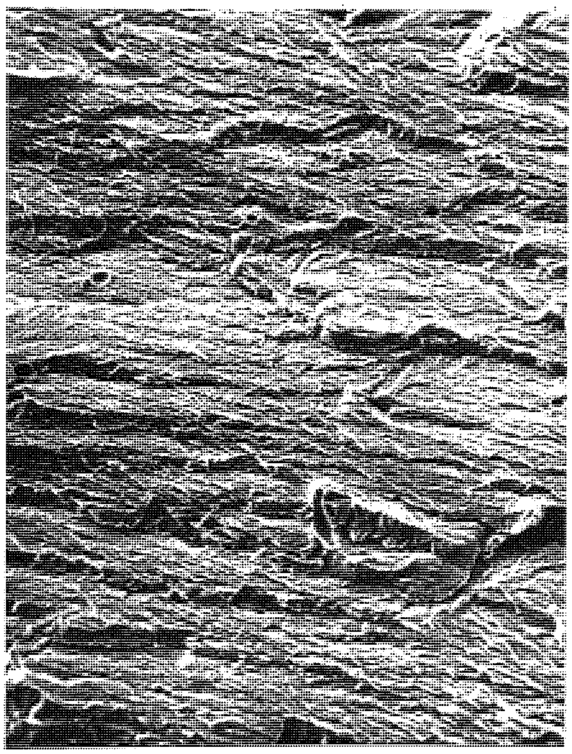

(c) 1.1% C SC/AC X 350

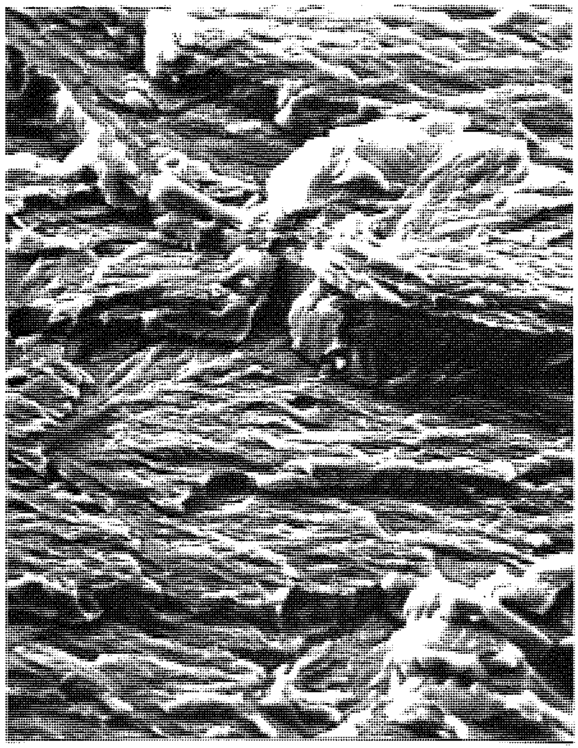

(d) 1.1% C SC/AC X 1700

⟶ Direction of Crack Propagation.

Fig. 7.26. Scanning Electron Fractographs showing: (a) & (b) Fatigue Crack Tip. (c) & (d) Details of Fatigue Crack.

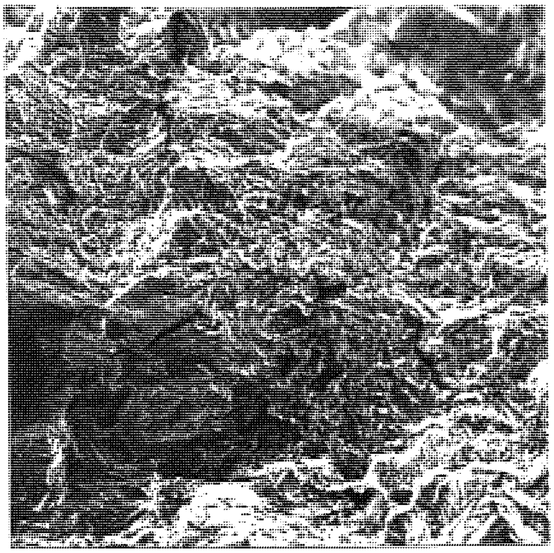

(a) 0.8% C SC/AC

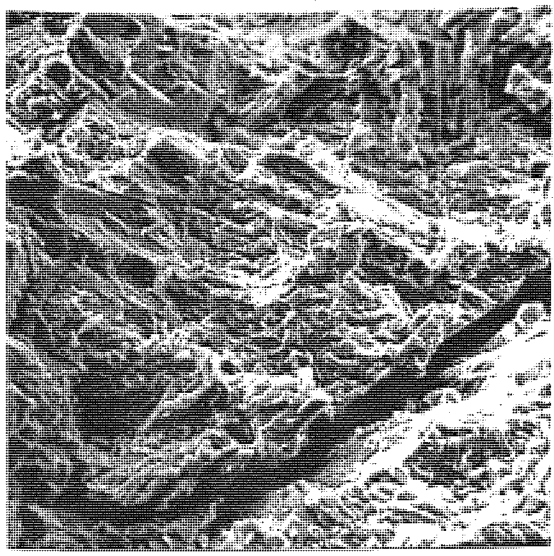

(b) 1.1% C SC/AC

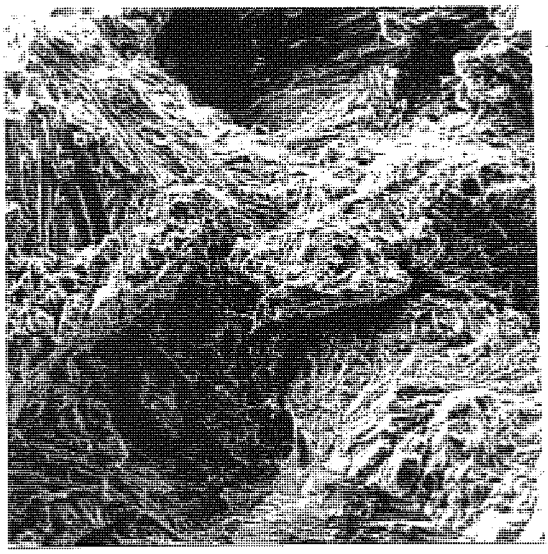

(c) 1.4% C SC/AC

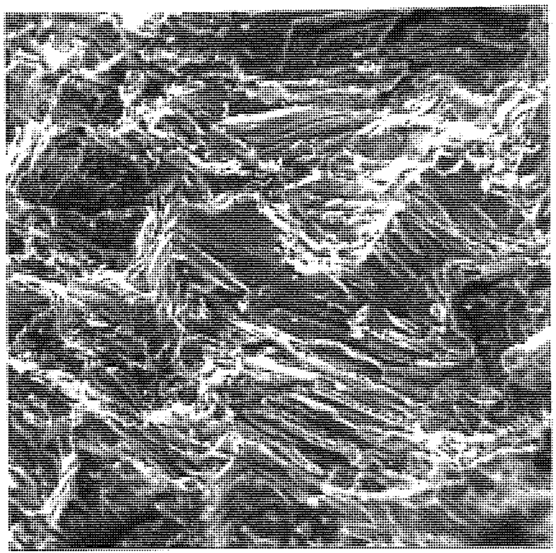

(d) 2.1% C SC/AC

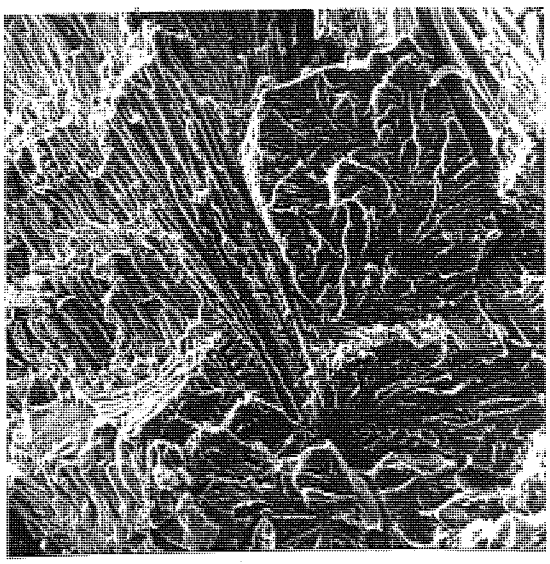

(e) 2.9% C SC/AC

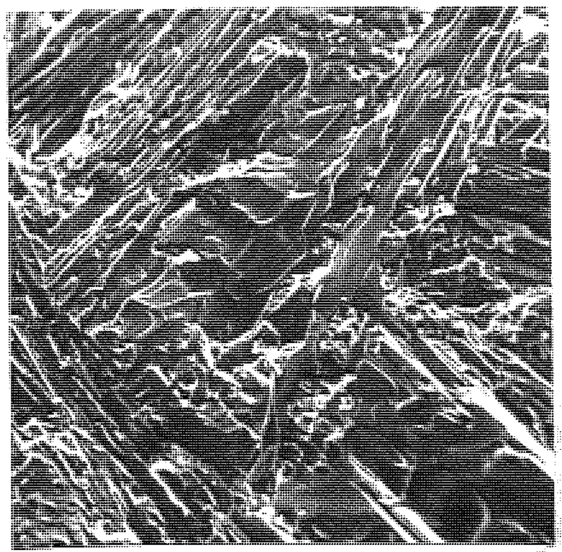

(f) 3.4% C SC/AC

Fig. 7.27. Fractograph of As Cast Material of Varying Carbon Content X 500.

matrix structure is the controlling factor, but at higher carbon contents the continuous carbide network dominates the fracture process.

Details of the ductile tearing associated with austenitic structures are shown in fig. 7.28. A feature of the sand cast austenitic fracture surfaces is what appears to be a series of coarse overlapping tongues, presumably produced by tearing, shown in plates 7.28.(a) and(b). In some cases the formation of these tongues is angular, and their appearance suggests fracture with limited plastic deformation. These points and the size of the angular features, shown typically in plate 7.28.(b), suggest that they might represent the fracture of brittle high carbon strain induced martensite plates. Further evidence of plastic deformation is shown in plate 7.28.(c) where distinct elongated dimples are revealed on the austenite dendrites.

Characteristics of fractured carbides, the flat facets and river markings typical of cleavage fracture, are illustrated in fig. 7.29. Plate (a) shows a 90° change in direction of the crack path, associated with a transformation from flat cleavage of a carbide to matrix fracture. River markings on the fracture surface of a primary carbide particle in 3.4% carbon material are shown in plate (b). These markings indicate the initiation of cleavage on different planes, which run into each other as fracture progresses. Thus fracture of this particle has occurred from bottom to top of the picture, normal to the macroscopic cracking direction (L to R). In contrast note the featureless cleavage of carbides in the same alloy in plate (d). Plate (c) illustrates the longitudinal fracture of a carbide/austenite eutectic colony, in 1.4% carbon material.

Heat treatment causes a marked refinement in the area of the fracture surface which fails with a ductile micro-mechanism. (fig. 7.30.). Alloys exhibiting a fracture surface consisting predominantly of carbide cleavage in the as cast condition, (ie. greater than 1.4% carbon), remained unaltered after heat treatment. Comparison of plate 7.30.(d) with the high carbon

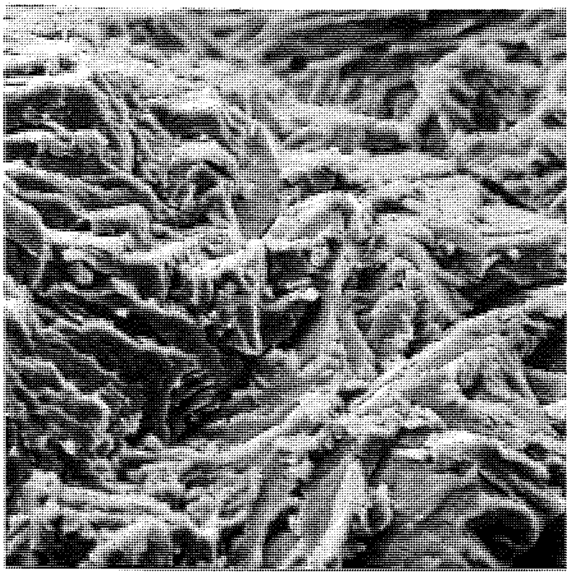

(a) 1.1% C SC/AC X 1600

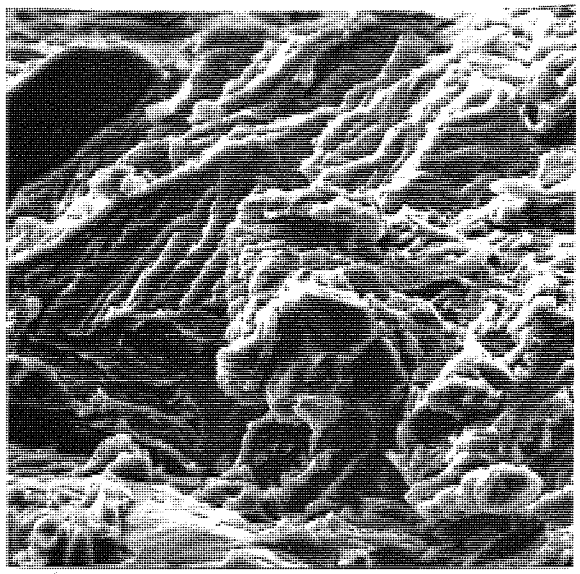

(b) 1.4% C SC/AC X 1500

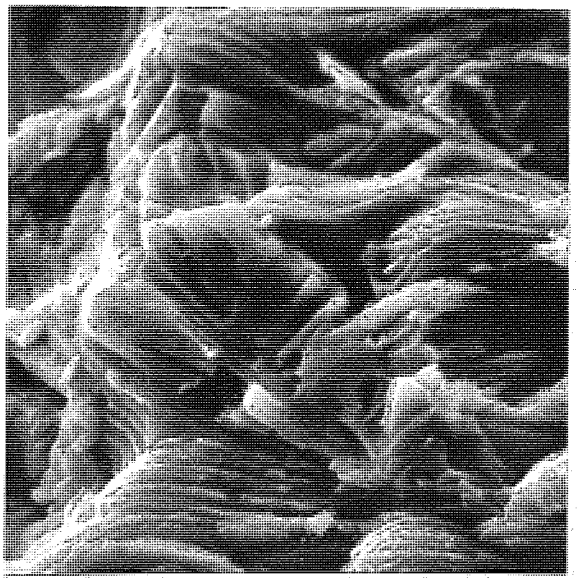

(c) 1.4% C CC/AC X 3200

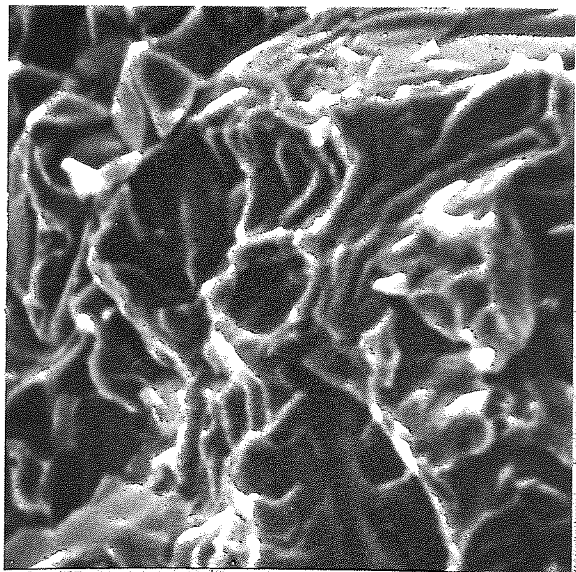

(d) 0.8% C SC/AC X 6000

Fig. 7.28. Fractographs of Austenitic Cast Material. (a) and (b) Coarse Surface produced by Tearing, and Failure of S.I.M. Plates. (c) and (d) Plastic Deformation of Austenite.

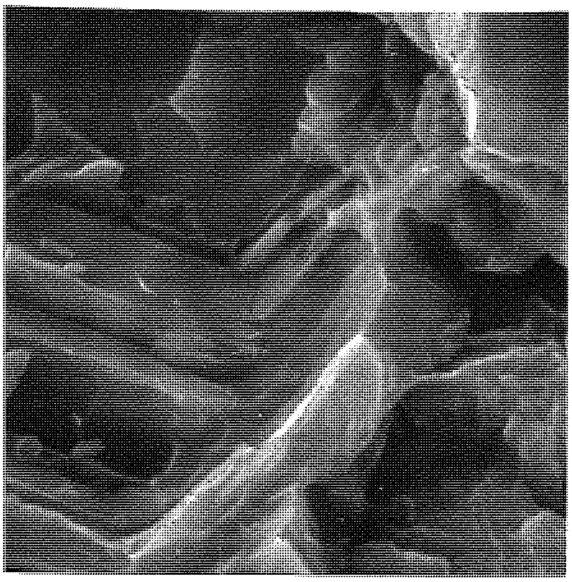

(a) 1.4% C X 2400

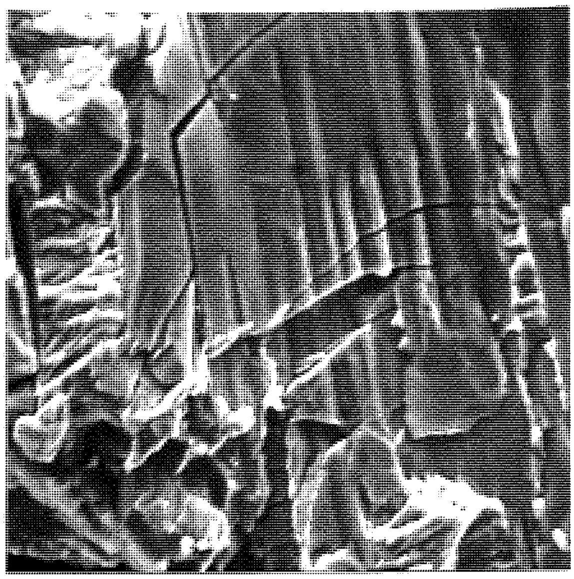

(b) 3.4% C X 1400

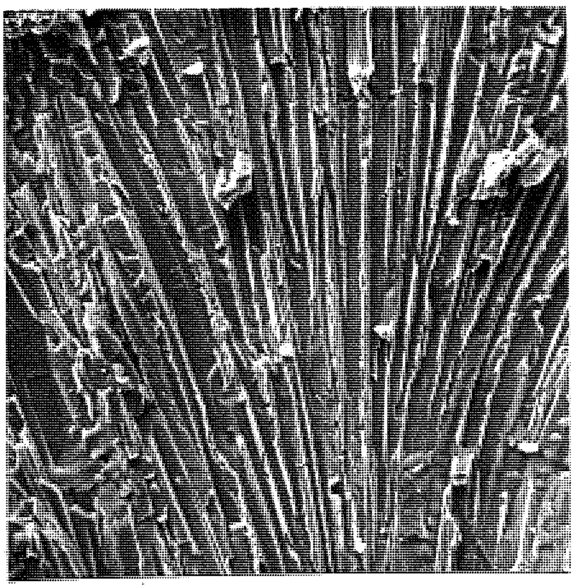

(c) 1.4% C X 750

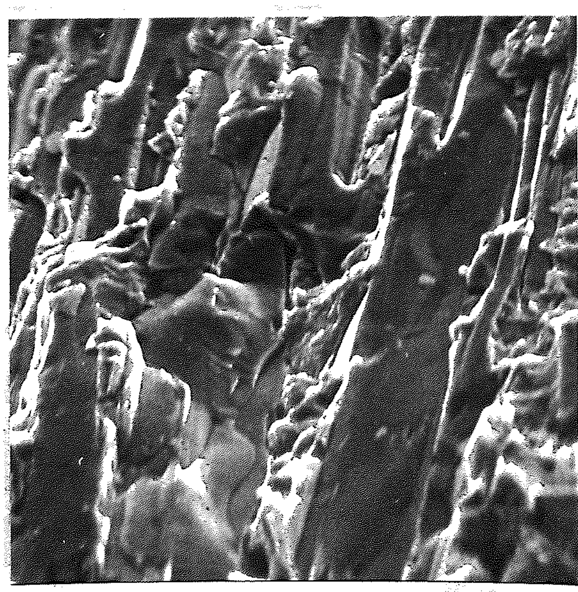

(d) 3.4% C X 1300

Fig. 7.29. Fractographic Features of the Cleavage Fracture of Carbides.

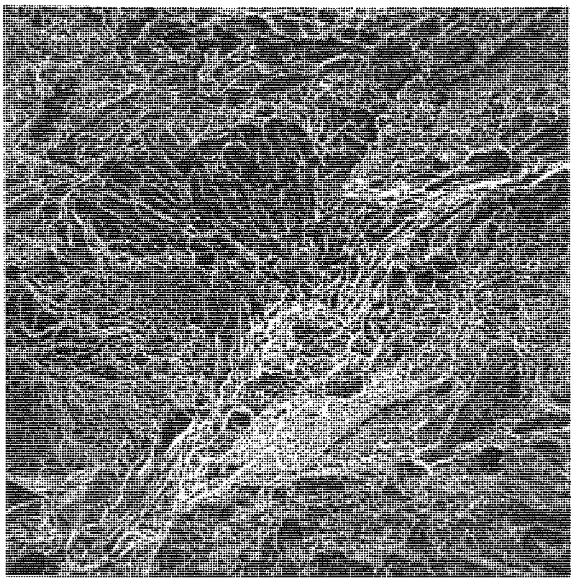

(a) 0.8% C SC/HT X 700

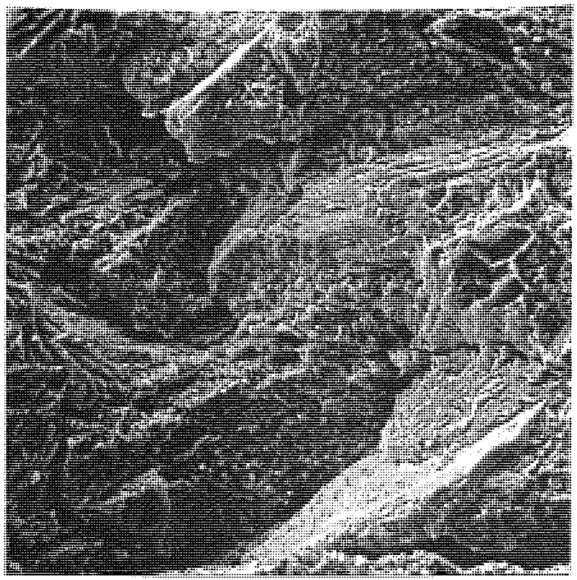

(b) 1.1% C SC/HT X 700

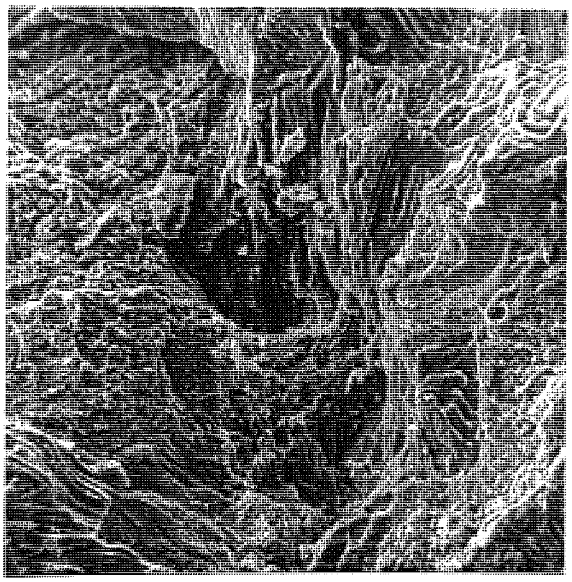

(c) 1.4% C SC/HT X 700

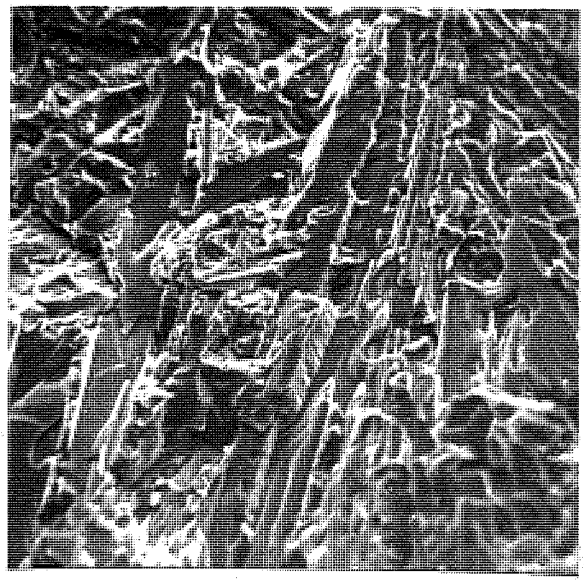

(d) 2.9% C SC/HT X 700

Fig. 7.30. Fractographs of Heat Treated Material of Varying Carbon Content.

as cast fractographs (fig. 7.27.(d), (e), and (f)) demonstrates this effect. The examination of heat treated material was therefore concentrated on the three carbon levels up to 1.4%.

At 0.8% carbon, shown in plate 7.30.(a), the fracture surface consists almost entirely of dimpled rupture, characteristic of micro-void coalescence. Eutectic carbides become more evident on the fractographs at 1.1 and 1.4% carbon, plates (b) and (c), occupying 40 to 50% of the fracture surface at 1.4%. This is significantly lower than the amount of carbide fracture in the as cast condition at the same carbon level. It is clear from this fractographic evidence that there are two different micro-mechanisms operating in the fracture of as cast austenitic, and heat treated martensitic, material. This is discussed at greater length in section 8.1.

Metallographic examination has revealed the migration of carbides into a grain boundary film during homogenisation of 0.8% carbon alloys. Heat treatment of this low carbon homogenised structure leads to the precipitation of secondary carbides on preferential planes, within a martensitic matrix. In both SC/H and SC/H/HT conditions at the 0.8% carbon levels the fracture surface showed evidence of a low energy failure, shown in fig. 7.31. Plate (a) illustrates the intergranular fracture, or grain boundary separation, in the austenitic alloy. The presence of carbide particles within the grain boundary film is confirmed in plate (b), which also shows the elaborate patterns produced during fracture of the grain boundary film.

The fracture surface of the 0.8% carbon SC/H/HT alloy, shown in plates (c) and (d), is quite different. Although still a low energy fracture, the crack path appears to be along transgranular cleavage planes. This produces flat featureless facets, with occasional river markings, connected by areas of dimpled rupture.

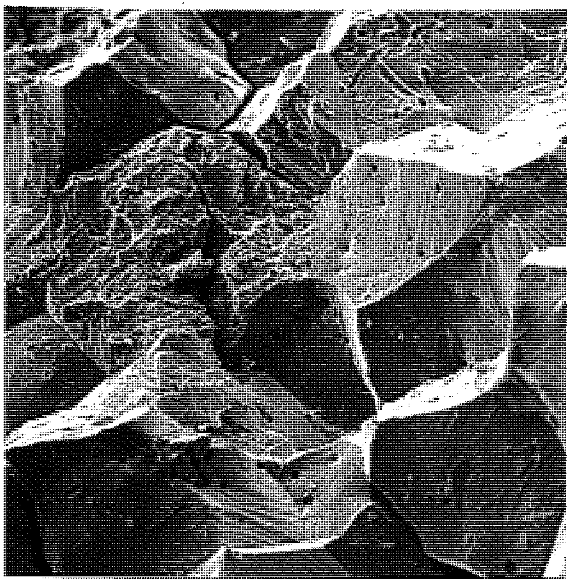

(a) 0.8% C SC/H X 150

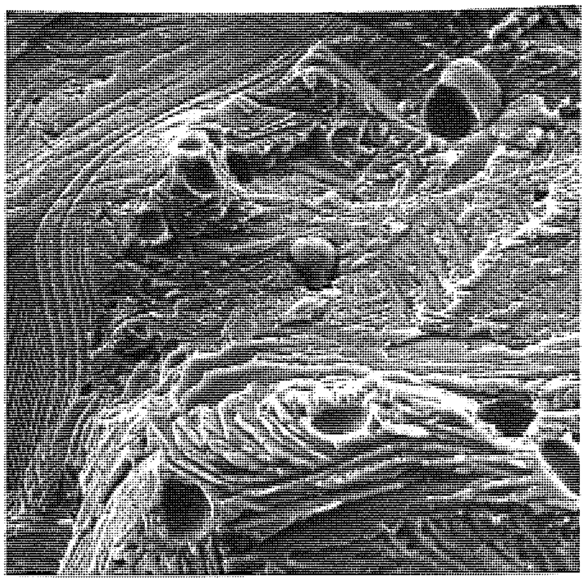

(b) 0.8% C SC/H X 750

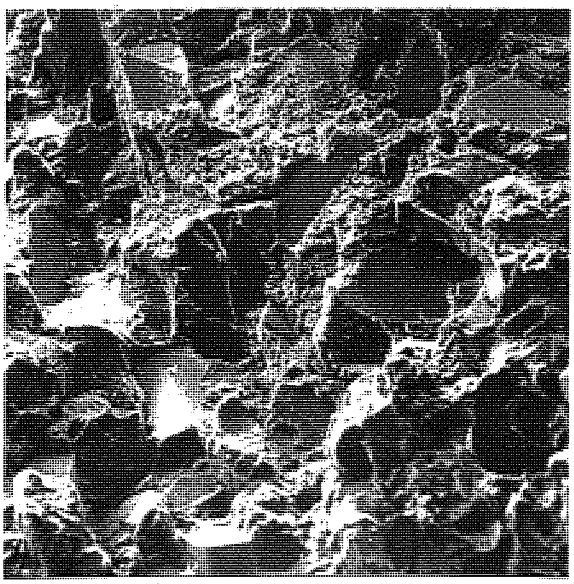

(c) 0.8% C SC/H/HT X 150

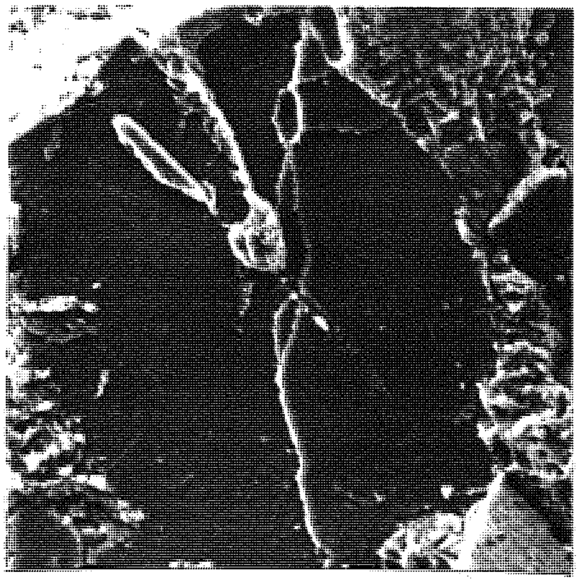

(d) 0.8% C SC/H/HT X 800

Fig. 7.31. Fracture Surface of Low Carbon Homogenised Structures.

The fractography of higher carbon homogenised structures is depicted in fig. 7.32. Two points of interest are immediately evident; a change in the fracture micro-mechanism of austenitic material before and after homogenisation; and the marked difference in dimple size between austenitic and martensitic material in the homogenised condition.

The first point is quite clear from a comparison of plates 7.28(a) and 7.32(b), which show the same 1.1% carbon alloy in the austenitic condition, before and after homogenisation. The major differences between these two structures are the volume fraction of carbides present, and the stability of the austenitic matrix. Since in each case the carbides are present as a discontinuous network, it is difficult to envisage them affecting the fracture process of the interconnecting matrix. It seems likely therefore, that the stability of the austenite, and even slight transformation to martensite during cracking may play a significant role in determining the fracture micro-mechanism.

The second point, regarding dimple size, can be appreciated from plates (b) and (d) in fig. 7.32. It is sufficient to note here that there is a significant difference in the size of dimples between austenitic and martensitic material, although the micro-mechanism of fracture is the same. The relevance of this variation is discussed in section 8.1.

In addition to partially dissolving the eutectic carbides, the homogenisation treatment has apparently weakened the carbide/matrix interface. Fracture of the carbide particles has been a feature of the fractography of as cast and heat treated material. After homogenisation however, cracking of the interface between carbide and matrix takes place revealing entire carbide particles rather than cleavage facets. This is most evident in plate 7.32.(d).

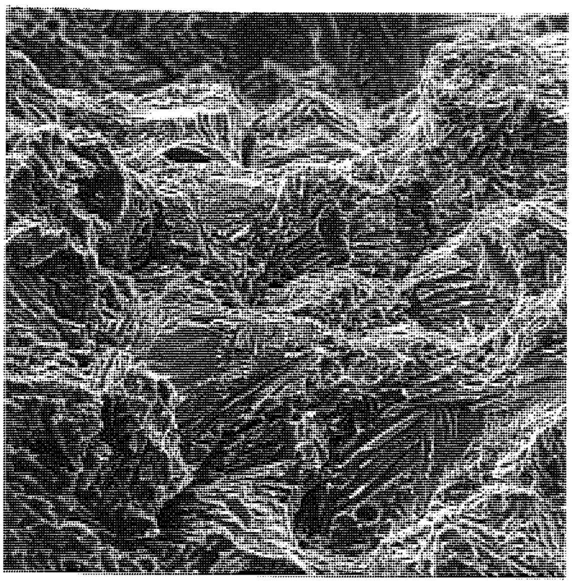

(a) 1.1% C SC/H X 300

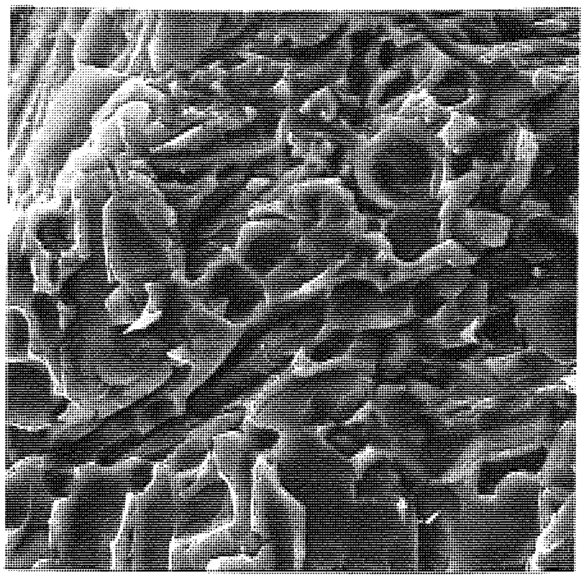

(b) 1.1% C SC/H X 1500

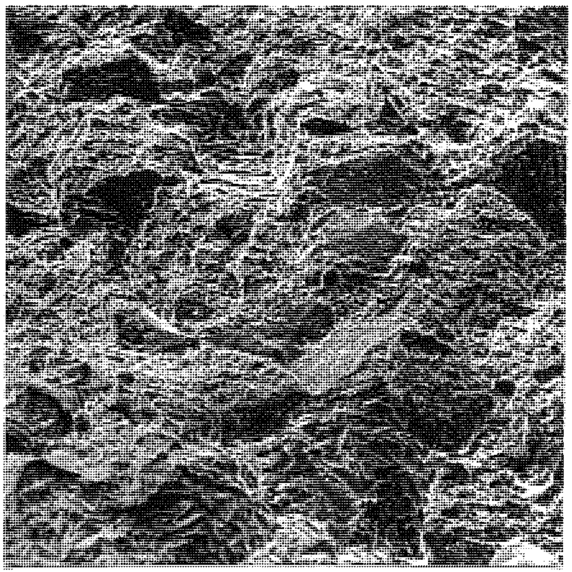

(c) 1.1% C SC/H/HT X 300

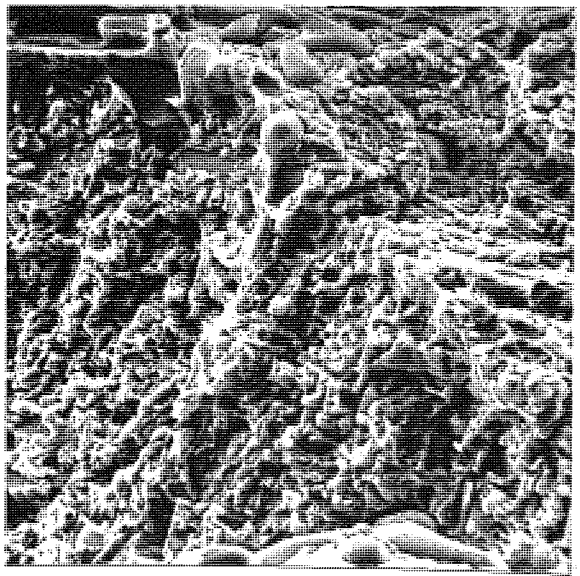

(d) 1.1% C SC/H/HT X 1500

Fig. 7.32. Dimpled Rupture of Higher Carbon Homogenised Material.

8. THEORETICAL CONSIDERATIONS.

8.1. Structural Correlation.

The model proposed by Krafft,(86) correlating K_{1c} with work hardening coefficient (n), and the elemental fracture cell (d_T), was outlined in section 4.4. This hypothesis is based on the 'tensile plastic-flow instability' condition being attained, (ie. the achievement of strain equal to 'n', the necking strain), in coherent ductile ligaments ahead of the crack tip. When crack loading is increased sufficiently to establish the strain for ductile rupture of the cell a distance ahead of the crack, corresponding to the average cell size d_T, crack growth becomes unstable. When cleavage is predominant, Krafft suggests that the critical process is tearing of the interconnecting ductile ligaments. Hipper(92) maintains that cleavage facets are formed well in advance of the crack, and as in normal rupture, the separation of the ductile ligaments connecting cleavage facets might be expected to be governed by strain hardening characteristics. In this case the instability zone size is limited by confinement between cleavage facets, which may explain why some steels with excellent strain hardening properties attain only a moderate level of toughness.

According to Krafft then, crack extension occurs by void nucleation and subsequent growth and coalescence, until plastic flow instability occurs at the critical cell size. Thus the dimples observed on ductile fracture surfaces are considered to be representative of the elemental fracture cell, or 'process zone'. Nucleation of voids can result from the fracture of inclusions or second phase particles, and since nucleation rate will govern, to a large extent, the size of the process zone, the distribution of nucleii will play a significant part in determining fracture toughness.

It was decided to attempt to correlate the fracture toughness of the 15% chromium alloys with microstructure in terms of the Krafft model. The fractographic survey has shown that up to the point where a continuous carbide network is produced, a considerable proportion of the fracture surface is of a ductile nature. The structural investigation was concentrated mainly on these alloys, containing up to 1.4% carbon, and exhibiting a fracture process controlled by plastic deformation.

Consider first the situation in martensitic alloys. A constant level of toughness was observed, independent of carbon content and volume fraction of carbides. The predominant fractographic feature of material in this condition was the dimpled rupture of the matrix. Detailed fractography revealed that in fact dimple sizes for all martensitic structures were very similar, including the alloys heat treated after homogenisation. This is illustrated in Fig. 8.1., which shows the uniformity of dimple size at three carbon levels up to 1.4%. The experimental fracture cell size was estimated from the following formula:

$$d_T = (A/N)^{\frac{1}{2}} \qquad \ldots\ 8.1.$$

where N is the number of dimples in an area A. In these calculations allowance was made for the foreshortening produced by tilting of the specimen in the scanning electron microscope. In all the martensitic structures, the experimental fracture cell size was found to be approximately 1 micron.

Having determined d_T experimentally it was necessary to measure Young's modulus and the work hardening exponent for this material in order to predict a theoretical tensile instability zone size from the Krafft equation:

$$K_{1c} = E\,n\,(2\pi d_T)^{\frac{1}{2}} \qquad \ldots\ 8.2.$$

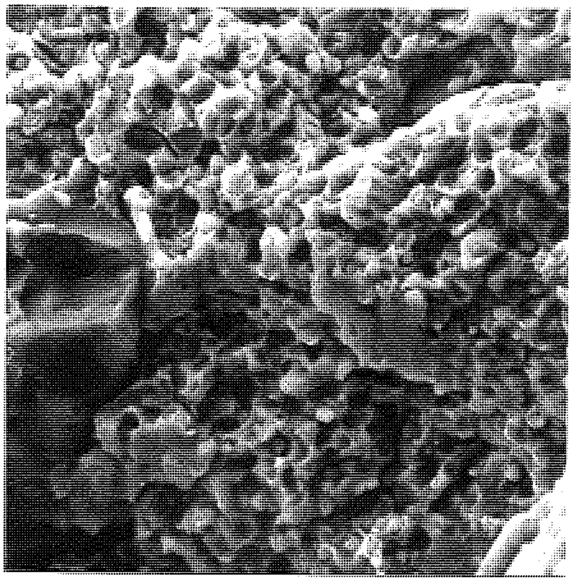

(a) 0.8% C SC/HT

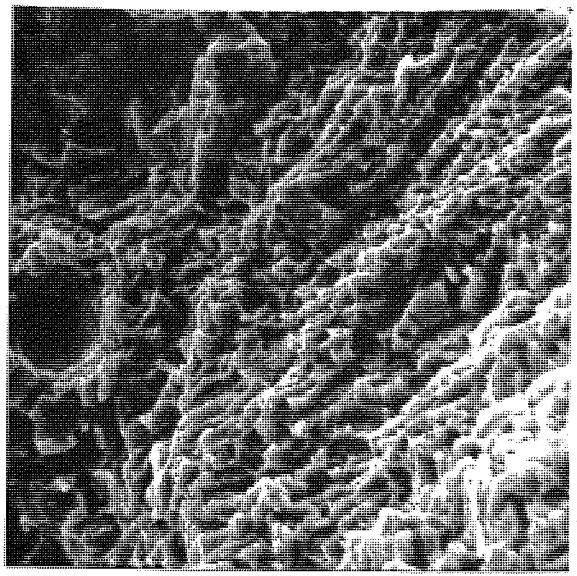

(b) 1.1% C SC/HT

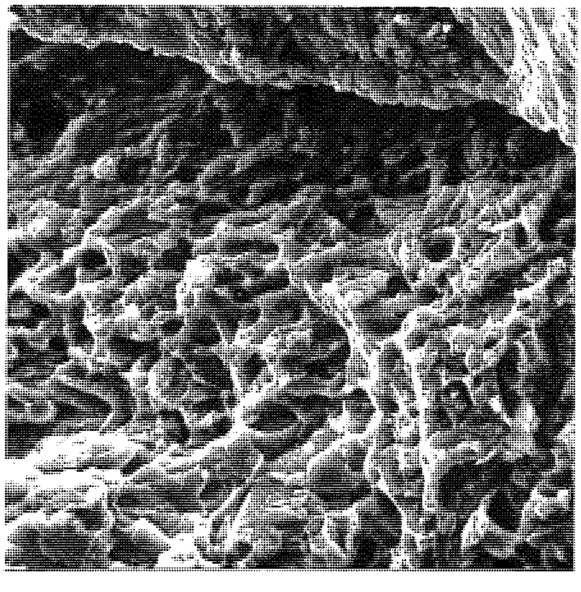

(c) 1.4% C SC/HT

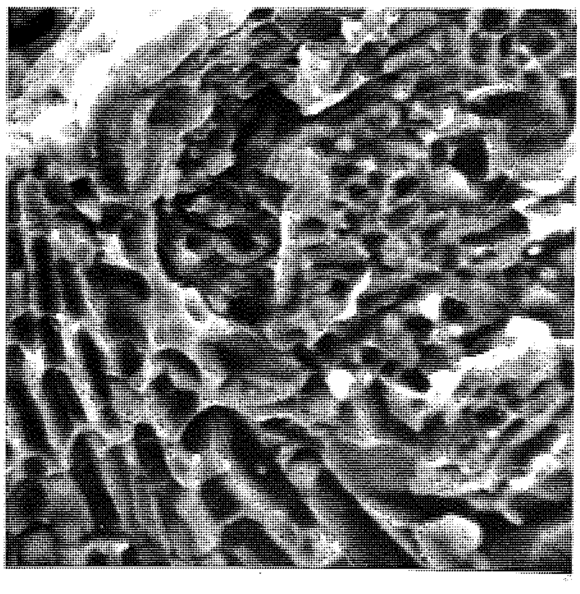

(d) 1.4% C SC/H/HT

Fig. 8.1. Uniformity of Dimple Size in Martensitic Alloys X 3000

Young's modulus (E), was readily obtained during a tensile test, using an extensometer technique, (table 6.2.). However, owing to the very small pre-fracture strain the values of n, calculated by the conventional log/log plot of the stress/strain curve were anomalous. The work hardening exponent was estimated, therefore, by the Meyer analysis technique, described in section 5.4.

Thus, using figures of 27.4×10^6 psi. for E; 24 to 27 ksi.$(\text{in})^{\frac{1}{2}}$ for K_{Ic}; and 0.075 to 0.09 for n, a value between 0.5 to 0.8 microns was predicted for d_T, in martensitic material. This is in extremely good agreement with the experimentally determined fracture cell size of between 0.8 and 1.0 microns. Detailed results are tabulated in table 8.1 below.

The invariance of d_T, on the basis of Krafft's extensive experimental results, suggests that it may be related to some characteristic dimension of the microstructure. Birkle et. al.[87] showed that this dimension was the spacing between sulphide inclusions in Ni-Cr-Mo-steels. The most pertinent characteristic of the martensitic structures under investigation, appeared to be the dispersion of secondary carbide particles. The average secondary carbide spacing $\bar{\bar{d}}$ was determined by electron microscopy, using two stage carbon replicas, and found to be very close to the average dimple spacing on the fracture surface, illustrated in fig. 8.2 and recorded in table 8.1.

TABLE 8.1.

% Carbon & cond'n	Av K_{Ic} ksi$(\text{in})^{\frac{1}{2}}$	E psi $\times 10^{-6}$	n	d_T μ	Av Dimple Spacing μ	Sec Carb Spacing $\bar{\bar{d}}$ μ
0.8 SC/HT	26.3	N.D.	0.083	0.6	0.9	0.8
1.1 SC/HT	26.9	27.4	0.089	0.6	0.8	1.0
1.4 SC/HT	26.5	N.D.	0.072	0.8	0.9	0.8
1.1 SC/H/HT	28.0	N.D.	0.084	0.7	0.9	0.9
1.4 SC/H/HT	26.8	N.D.	0.092	0.5	1.0	0.7

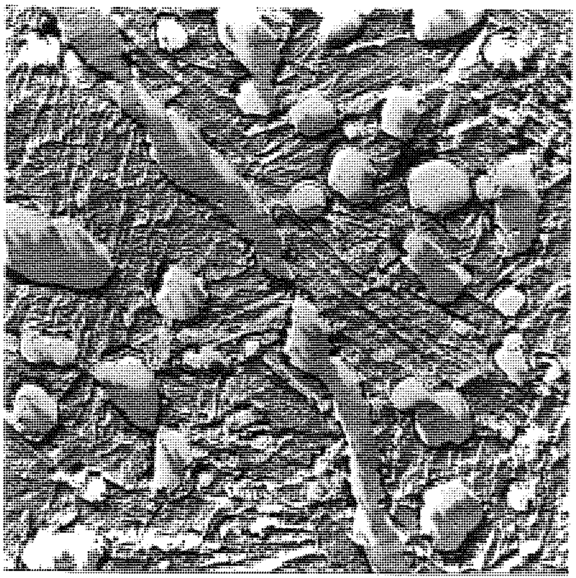

(a) 0.8% C SC/HT X 12,500
$\bar{d}$ = 0.8

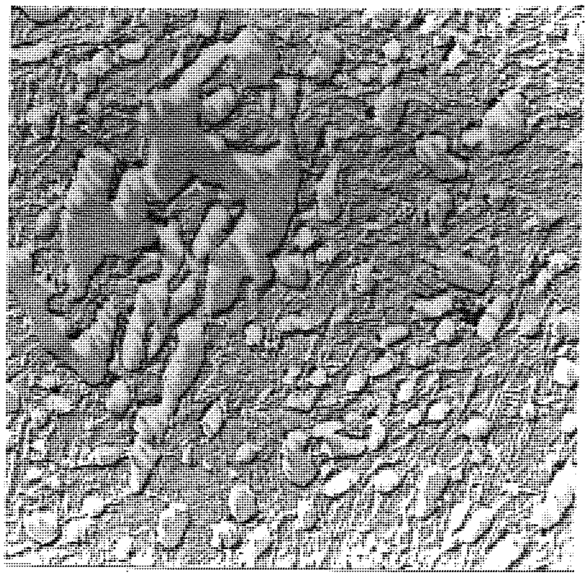

(b) 1.1% C SC/HT X 5,500
$\bar{d}$ = 1.0

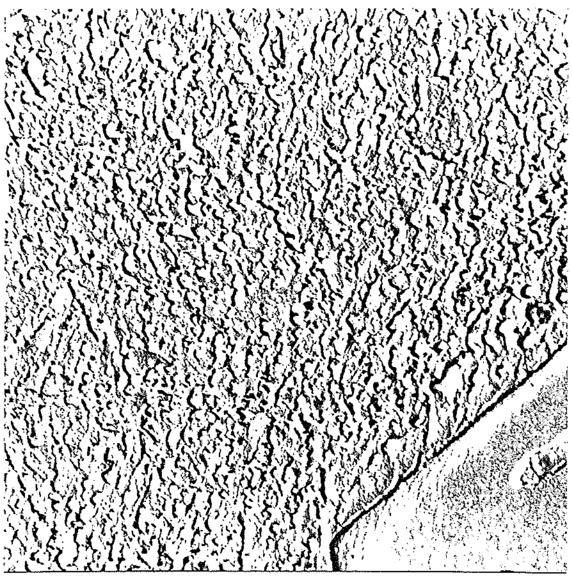

(c) 1.4% C SC/HT X 2,650
$\bar{d}$ = 0.8

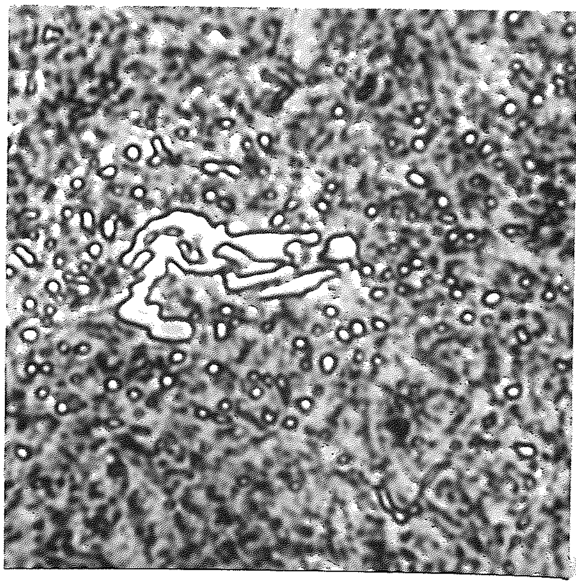

(d) 1.1% C SC/H/HT X 1,500
$\bar{d}$ = 0.7

Fig. 8.2. Distribution of Secondary Carbide Particles in Martensitic Structures. (a), (b) & (c) Electron Micrographs using Two Stage Carbon Replicas. (d) Optical Micrograph.

The match between dimple spacing and secondary carbide dispersion data indicates that the sites for void nucleation are probably the secondary carbide particles. This assumption was confirmed by further fractographic evidence, showing dimples to be centred on secondary carbide particles 0.2 to 0.75 microns in diameter, illustrated in fig. 8.3.

These observations suggest that the onset of plane strain fracture instability is controlled by the dispersion of secondary carbide particles, and that the instability zone size corresponds to the average distance between these precipitates. The uniformity of secondary carbide dispersion explains the constant level of K_{1c} in all the martensitic structures.

In austenitic structures a high rate of work hardening, associated with only moderate K_{1c}, results in predicted process zone sizes of 0.1 to 0.2 microns, as listed in table 8.2. In homogenised alloys where the fracture process is micro-void coalescence, the dimple spacing was an order of magnitude greater than this value. A closer correlation was revealed in as cast material, when a dimpled fracture surface was produced. An example is shown in fig. 8.4, where the dimple spacing is 0.5 microns in 1.4% carbon chill cast material. A structural feature of similar size was observed in the eutectic austenite of the same alloy in the sand cast condition. Fig. 8.4.(c) shows the fracture surface of a eutectic colony, where a crack in a carbide lamella has propagated into the adjacent austenite. Void formation and local necking during the fracture of the austenite has produced a single line of dimples in this region. The spacing of these dimples is 0.46 microns, and whilst this is of the same order as the dimples on primary austenite it shows only moderate correspondence with the theoretical process zone size, d_T.

Also included in table 8.2 is the spacing of other features observed on the fracture surface, such as the overlapping tongues discussed in section 7.9.

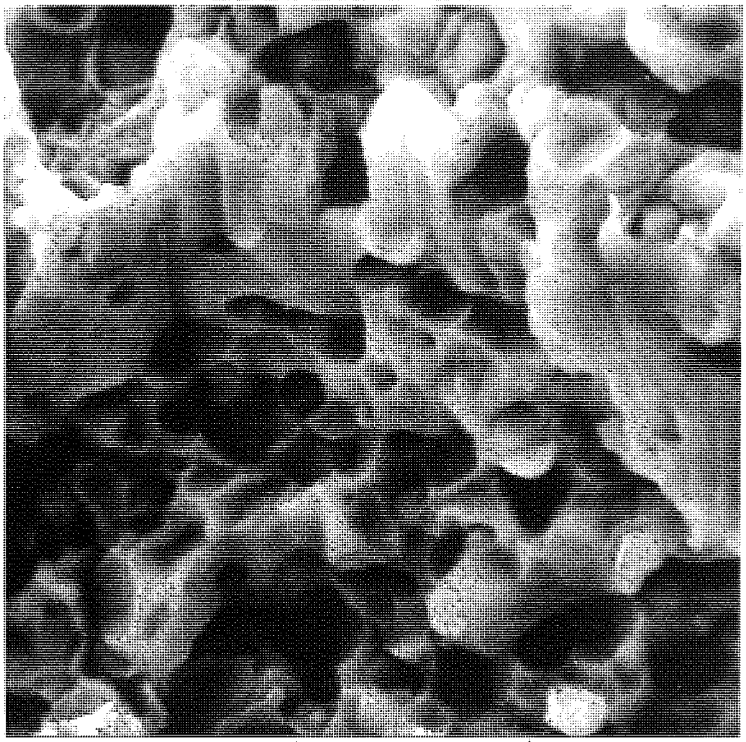

(a) 0.8% C SC/HT X 7,500

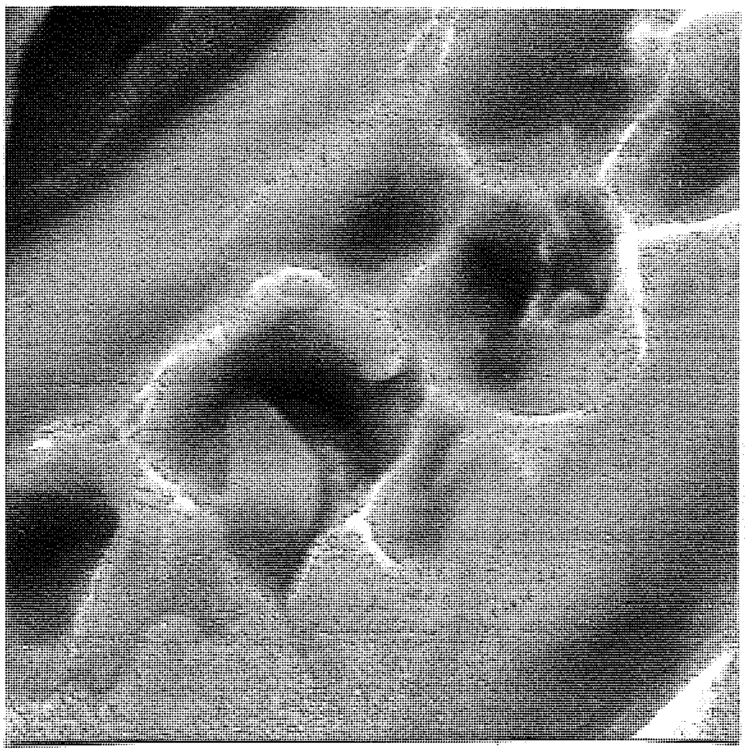

(b) 1.1% SC/HT X 20,000

Fig. 8.3. Secondary Carbide Particles within Dimples of Martensitic Fracture Surfaces.

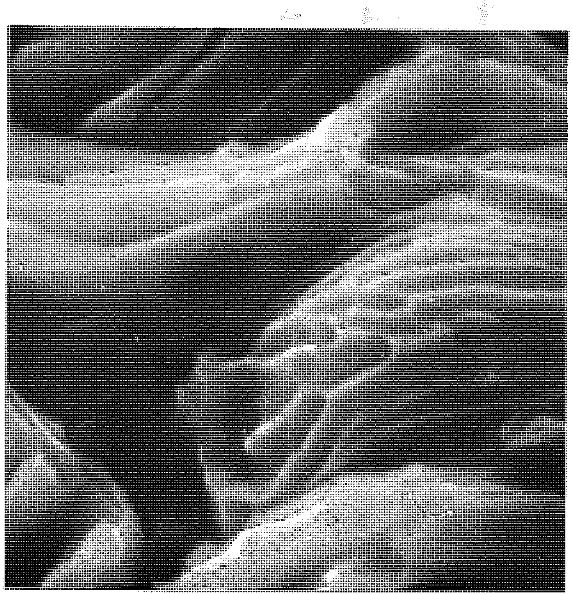

(a) 1.4% C CC $\frac{1}{4}$ in.

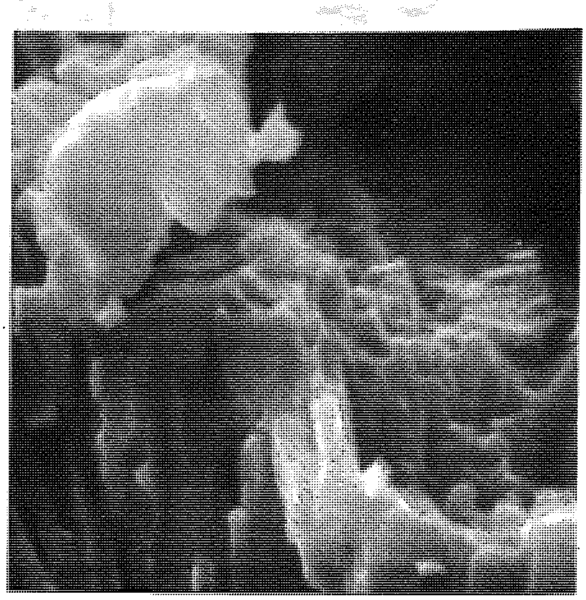

(b) 1.4% C CC $\frac{1}{4}$ in.

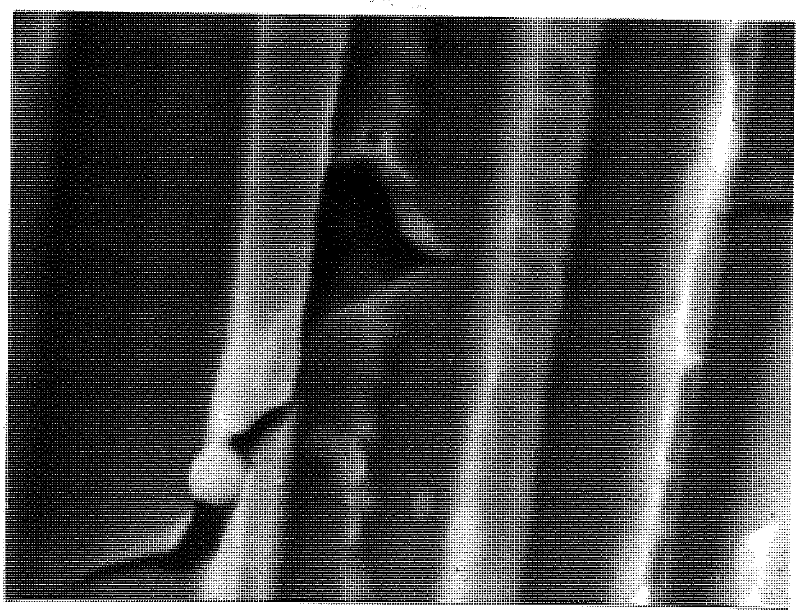

(c) 1.4% C SC/AC

Fig. 8.4. Dimpled Rupture of Austenite. (a) & (b) Fracture surface of Primary Austenite. (c) Void and Dimple Formation in Eutectic Austenite. X 9000.

TABLE 8.2.

% C & Cond.	Av K_{1c}, ksi(in)$^{\frac{1}{2}}$	E	n	d_T μ	Av Dimple Spacing μ	Spacing of other Features μ
0.8 SC/AC	38	N.D.	0.22	0.23	-	2.5
1.1 SC/AC	32	24.4	0.29	0.10	-	3.0
1.4 SC/AC	27	N.D.	0.24	0.10	0.46	2.8
1.1 SC/H	45	N.D.	0.30	0.16	2.0	-
1.4 SC/H	40	N.D.	0.26	0.17	1.[illegible]	-
1.4 CC/AC ($\frac{1}{4}$ in.)	36	N.D.	0.24	0.16	0.5	-

The arguments and theories concerning the nucleation of voids ahead of a crack were discussed in section 4.3.(78,79,80). It was concluded that slip induced cavity formation was the most typical mechanism operating during this process. Fig. 8.5 shows such cracking at carbide particles within the plastic zone of 1.1 and 1.4% carbon austenitic alloys. Krafft(86) postulates that in the presence of cleavage cracks the controlling factor in the fracture process is the ductile failure of interconnecting ligaments. Fractographic evidence has shown that by comparison, martensitic alloys contain fewer eutectic carbides on the fracture surface, than austenitic alloys of similar carbon content. It is suggested that in martensitic alloys where the nucleation of voids within the matrix is easier, due to the presence of secondary carbide particles, the fracture process is not so dependent upon the eutectic carbides. On the other hand, in austenitic alloys where the matrix is more ductile and has a higher work hardening rate, the eutectic carbides play a more important role. The interlamellar spacing of eutectic colonies in 1.4% carbon alloys has already been shown to have some significance.

(a) 1.1% C SC/AC X 450
(0.01 in. ahead of crack tip).

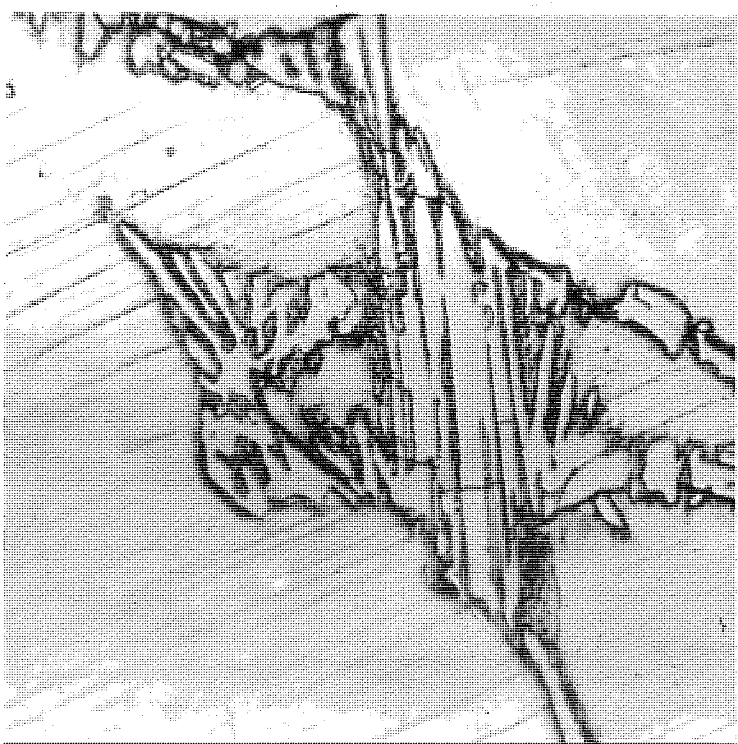

(b) 1.4% C SC/AC X 1500
(0.015 in. ahead of crack tip).

⟶ Direction of Crack Propagation.

Fig. 8.5. Slip Induced Cracking in Austenitic Structures.

A further complicating factor in the matrix failure of lower carbon austenitic alloys is the formation of strain induced martensite. The tendency for the crack path to be through the S.I.M. plates indicates that it might be the work hardening characteristics of this phase which should be considered rather than those of the austenite. Gerberich et. al have noted a change in the fracture process when S.I.M. is formed, from dimpled rupture to wavy glide, in T.R.I.P. steels(31). The higher carbon martensite produced in the 15% chromium series, fractures in a mode of restricted plastic deformation, and the process zone size would be larger by at least an order of magnitude due to the low work hardening rate. Assuming a value of 0.08 for n, in the 0.8% carbon sand cast condition, results in a theoretical process zone size of 2.3 microns, which is in good agreement with the spacing of the overlapping tongues observed on this fracture surface.

To summarise, in martensitic alloys which failed by dimpled rupture good correlation between K_{1c} and work hardening was observed on the basis of Krafft's tensile plastic flow instability hypothesis. The distribution of secondary carbides was found to correspond with the fractographic dimple size and the theoretical process zone size. These three characteristics were shown to be constant at all the carbon levels examined, explaining the uniform toughness over this range.

Structural correlation in austenitic alloys was complicated by the fact that the fracture process shows greater dependence on the carbide network, and the presence of strain induced martensite in some alloys. The interlamellar spacing of the eutectic colonies in higher carbon alloys has been shown to be significant, and a correlation based on the properties of the strain induced martensite appears to be more relevant in lower carbon alloys.

8.2. Plastic Energy Dissipation.

Controlled strain induced martensite formation during cracking in steels of balanced chemical composition is the basis of the combined high strength, ductility, and toughness achieved in T.R.I.P. steels. An analytical treatment of the energy dissipation in T.R.I.P. steels by Gerberich et. al.[31] indicates that the invariant shear of the martensite reaction is about five times as effective as the plastic dissipation processes normally occurring at the crack tip.

In their analysis, Gerberich et. al. treat the shear transformation to martensite as an energy absorbing mechanism, since it takes place to minimise the strain energy of the system. The separate contributions of martensite, austenite, and the invariant shear as energy absorbing media are computed from the volume fraction of martensite, the strain energy density of the martensite, and the size and shape of the plastic zone. Treating these three factors individually, from magnetic field strength measurements the volume fraction of martensite, V, is found to be proportional to strain;

$$V_{\alpha'} \simeq 1.2\,\varepsilon^{\frac{1}{2}}. \qquad \ldots.\ 8.3.$$

The strain energy density is approximated to (σ_{ys} E), and a tensile analogy taken which describes the plastic strain distribution in the plastic zone as:

$$\varepsilon = \frac{\sigma_c}{E}\left(\frac{R_p}{r} - 1\right) \qquad \ldots.\ 8.4.$$

where σ_c is the yield point of the austenite/martensite composite, and R_p is the length of the plastic zone. By assuming a plastic strip height of $\frac{1}{2}$ R_p a shape factor of $^{\pi}/_{8}$ is obtained.

Combination of these three factors results in the following equations for the plastic energy absorption, U, of the separate dissipation media:

Martensite: $U_{\alpha'} = 0.56\ \sigma_{\alpha'} (\frac{\sigma_c}{E})^{3/2}\ R_p^{\ 2}t.$ .... 8.5.

Invariant Shear: $U_{is} = 0.185\ \sigma_{\alpha'} (\frac{\sigma_c}{E})^{\frac{1}{2}}\ \varepsilon_{is}\ R_p^{\ 2}t.$ .... 8.6.

Austenite: $U_{\gamma} = (0.196\ \frac{\sigma_\gamma \sigma_c}{E}\ R_p^{\ 2}t) - (0.55\ \sigma_c\ (\frac{\sigma_c}{E})^{3/2}\ R_p^{\ 2}t)$ .... 8.7.

where σ_γ is the austenite yield stress (approximated to σ_c), $\sigma_{\alpha'}$ the martensite yield stress (estimated from other sources), ε_{is} the transformation strain, and t the plate thickness.

Enumeration and summation of equations 8.5, 8.6, and 8.7 leads to a total plastic energy absorption, U_p, in terms of R_p. Plastic strip height is measured as a function of crack length, related to R_p, and estimates of U_p calculated at various stages of the slow cracking process. The plastic energy dissipation rate, G_p, is obtained from:

$$G_p = \frac{dU_p}{da} \qquad \text{.... 8.8.}$$

and expressed in terms of stress intensity by:

$$K_p = (E\ G_p)^{\frac{1}{2}}. \qquad \text{.... 8.9.}$$

Good correlation (within 15%) between derived and experimental values of K was achieved by Gerberich et. al., for two materials undergoing transformation to martensite.

The model, as proposed by Gerberich et. al., applies to a plane stress situation, and requires modification to deal with the alloys investigated here. Under predominantly plane strain conditions, the radius of the plastic zone will be approximately 1/3 of that measured at the free surface. The energy associated with this smaller zone will be correspondingly less, in proportion to the volume of the plastic zone. A factor which must also be taken into consideration is the elevation of the yield stress due to plastic constraint, when a condition of plane strain prevails. This effect can increase the value of the uniaxial tensile yield stress by up to approximately three times, (2.8 using the Von Mises yield criterion). Under these conditions it seems reasonable to apply upper and lower bounds to the analysis, (a) assuming no elevation of the yield stress due to plastic constraint, where σ_{ys} equals the uniaxial tensile yield stress; and (b) assuming maximum constraint, where σ_{ys} equals three times the uniaxial tensile yield stress.

In the first case the following parameters are appropriate in the application of the analysis to the 1.1% carbon alloy of heat K1 in the current investigation, ($K_{Ic} = 33.5$ ksi.$(\text{in})^{\frac{1}{2}}$):

$$\sigma_{\alpha'} = 180 \text{ ksi.} \qquad \sigma_c = \sigma_\gamma = 61.5 \text{ ksi.} \qquad t = 0.5 \text{ in.}$$

$$E = 27.4 \times 10^6 \text{ psi.} \qquad \varepsilon_{is} = \tan 19^\circ = 0.344$$

The value of $\sigma_{\alpha'}$ was obtained by extrapolation of data on the 0.8% carbon sand cast alloy. This material was partially transformed to an acicular thermal martensite, similar in appearance and micro-hardness to the S.I.M. produced in cast structures.

The major axis of the martensite regions in T.R.I.P. steel tensile specimens was observed to be very close to the theoretical shear angle of $54^\circ\ 44'$. Similar measurements on chromium alloys revealed an average angle of 53° with the tensile axis. It was considered pertinent therefore, to use the same value of ε_{is}, the transformation strain, as used in the Gerberich analysis.*

The formation of S.I.M. is more sensitive to strain, in T.R.I.P. steels than in chromium alloys. From the information presented by Cohen[25] on 12% chromium steels, the following relationship between volume fraction of martensite and strain was deduced:

$$V = 0.8\,\varepsilon^{\frac{1}{2}}. \qquad \text{.... 8.10.}$$

* (ie. 19° the typical mechanical shear displacement of many types of martensite.)

Using this modified data the following values were obtained for the energy absorption of martensite, austenite, and the invariant shear:

$$U_{\alpha'} = 7.5\ R_p{}^2 t.\ \text{psi.}$$

$$U_{is} = 465\ R_p{}^2 t.\ \text{"}$$

$$U_{\gamma} = 24.5\ R_p{}^2 t.\ \text{"}$$

$$U_p = 497\ R_p{}^2 t.\ \text{" for one enclave.}$$

$$= 994\ R_p{}^2 t.\ \text{" for entire plate.}$$

The increase in plastic strip height with slow crack growth is shown in fig. 8.6 for heat K 1 SC/AC. Estimations of R_p were made, and values of U_p calculated. The graph of U_p against slow crack growth, Δc, is shown in fig. 8.7. The most significant region during slow crack growth, relative to K_{1c}, is the first 0.05 in., and graphical differentiation over this region results in a value of 192 lb/in. for G_p. This figure is representative of the energy associated with the plastic zone at the free surface. According to Irwin[41]:

Under plane stress:- $$r_y = \frac{1}{2\pi}\left(\frac{K_{1c}}{\sigma_{ys}}\right)^2 \quad \ldots\ 8.11.$$

Under plane strain:- $$r_y = \frac{1}{5.6\pi}\left(\frac{K_{1c}}{\sigma_{ys}}\right)^2 \quad \ldots\ 8.12.$$

where $2r_y = R_p$, leading to plastic strip heights of 0.090 and 0.033 ins. for plane stress and plane strain conditions respectively. Assuming the volume of the plastic zone to be $\left(\frac{\pi R_p{}^2 t}{4}\right)$, the corresponding plastic zone volumes are 32×10^{-4} and 4.3×10^{-4} cu. ins. These values are slightly higher than the observed dimensions of the plastic zone, probably due to the restraining influence of the carbides, but this should not affect the ratio, which is being used here. Thus the energy absorbed under plane strain is roughly $^1/_8$ of that under plane stress.

Applying this correction gives a value of 24 lb/in. for G_p, and

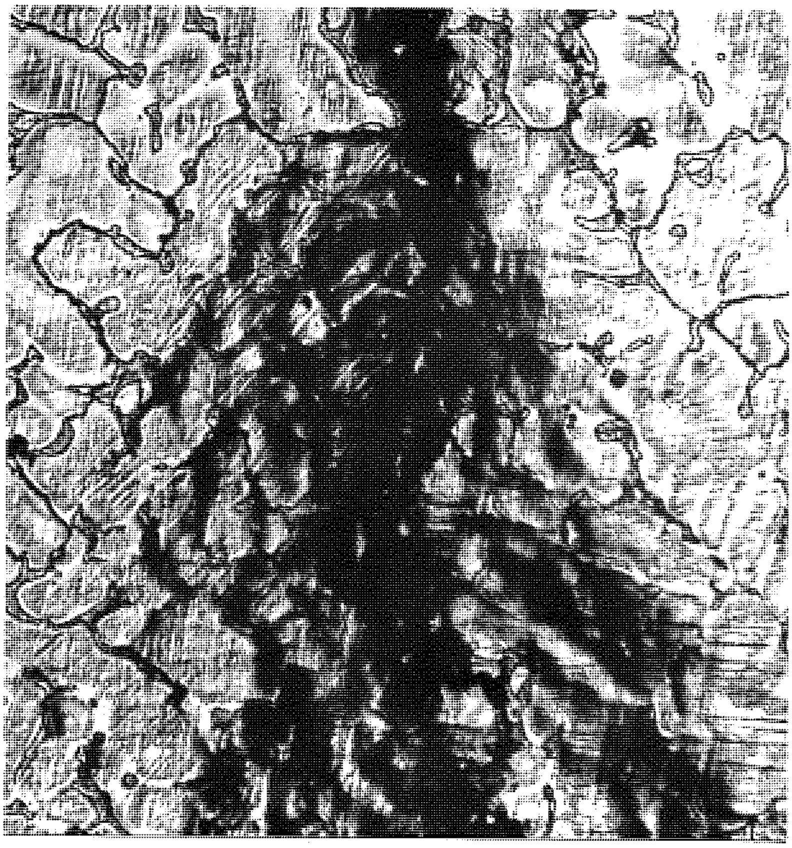

Heat K.1. 1.1% C X 100

Fig. 8.6. Slow Crack Growth and Plastic Zone Formation, in austenitic material.

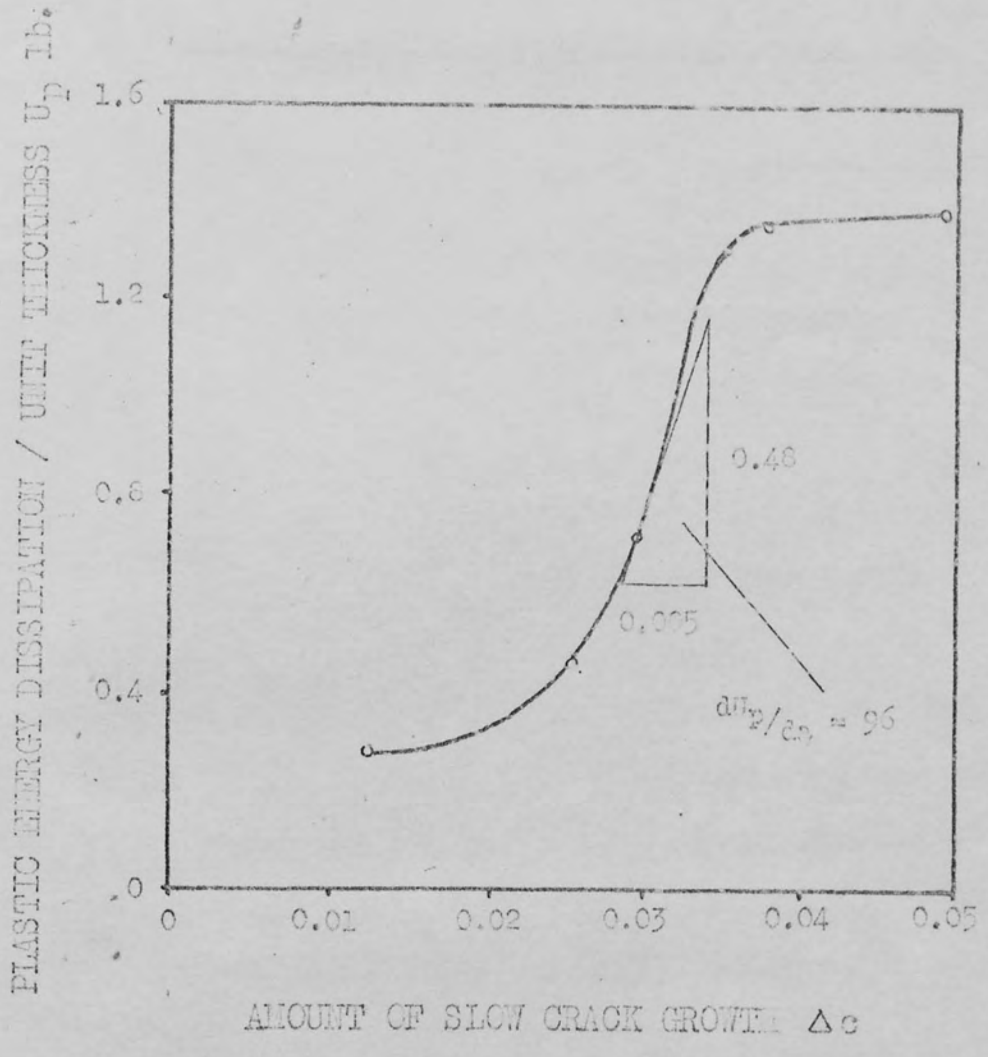

Fig. 8.7. Estimate of Plastic Energy Dissipation as a Function of Crack Length, by Graphical Differentiation.

26.5 ksi.$(in)^{\frac{1}{2}}$ for K_p.

For the upper bound solution, a similar procedure is followed, using the elevated yield stress data given below:

$$\sigma_c = \sigma_\gamma = 184.5 \text{ ksi.} \qquad \sigma_{\alpha'} = 540 \text{ ksi.}$$

and:

$$U_{\alpha'} = 62\, R_p^2 t \text{ ksi.}$$
$$U_{is} = 2840\, R_p^2 t \text{ "}$$
$$U_\gamma = 210\, R_p^2 t \text{ "}$$

$$U_p = 3112\, R_p^2 t \text{ " for one enclave.}$$
$$= 6224\, R_p^2 t \text{ " for entire plate.}$$

After correcting for the smaller plastic zone this results in a figure of 200 lb/in. for G_p, or converting to stress intensity, 76 ksi$(in)^{\frac{1}{2}}$ for K_p.

In this treatment the energy required for cracking of the carbides has not been taken into account. The specific energy requirement for carbide cracking is about $^1/_{10}$th that for matrix fracture, but since the invariant shear of the martensite reaction provides over 90% of the total energy, the nett effect would be only a very slight decrease in U_p, and consequently K_p.

In summary then, by examining the two extremes of plastic constraint, derived values for K_p of 26.5 and 76 ksi.$(in)^{\frac{1}{2}}$ are obtained, compared to the experimental figure of 33.5 ksi.$(in)^{\frac{1}{2}}$, for K_{1c}.

8.3. Crack Initiation.

The influence of applied stress on crack nucleation was discussed in section 4.1. Petch[63] has shown that a proportion of any stress causing yielding in a crystalline structure is employed in overcoming the frictional effects resisting deformation. This frictional stress will vary with the grain size dependence of the yield stress in the structure under investigation. In their modification of the Stroh[64] approach Smith and Barnby[65] estimate the stress required to cause cracking in a hard precipitate embedded in a deforming matrix. The effective stress, σ_{EFF}, is expressed as a function of the length of dislocation pile up, d, acting on a precipitate of thickness 2c:

$$\sigma_{EFF} = \left(\frac{2c}{d}\right)^{\frac{1}{2}} \left(\frac{2\gamma G}{(1-v)d}\right)^{\frac{1}{2}} \qquad \ldots .\ 8.13.$$

The Smith and Barnby model is shown schematically in fig. 4.2 and is typified by the situation illustrated in fig. 8.5. Consider the circumstances of plate 8.5.(a), where a crack has been nucleated 0.01 ins. ahead of the main crack tip, at maximum load in a fracture toughness test; $2c = 4.5 \times 10^{-4}$in., $d = 3 \times 10^{-3}$in., $G = \frac{1}{2}E = 13 \times 10^{6}$psi, $\gamma = \frac{Gb}{10}$, where b, Burgers vector of a dislocation, $= 1.2 \times 10^{-8}$ins., and $v = {}^{1}/_{3}$.

The theoretical shear stress required to crack the precipitate, the value of σ_{EFF} obtained using equation 8.13 is 2.5 ksi. To compare this figure with the applied stress it is necessary to estimate the stress level within the plastic zone at a given point. The shear stress can be calculated from Irwin's basic definition using the co-ordinates x and θ, where x is the distance ahead of the crack tip and θ is the angle of displacement from the crack plane, in this case 20°:

$$\tau_{xy} = K \frac{\cos \theta/2}{(2\pi x)^{\frac{1}{2}}} \cdot \quad \sin {}^{\theta}/_{2} \cdot \quad \cos {}^{3\theta}/_{2} \cdot \qquad \ldots .\ 8.14$$

For this material, the maximum load condition corresponds to a K value of 35 ksi.$(in)^{\frac{1}{2}}$, and at a distance 0.01 ins. ahead of the crack tip, the shear stress acting on the precipitate is 22.5 ksi. Since the effective stress required to crack the carbide is only 2.5 ksi., almost 90% of the applied stress is needed to overcome the frictional resistance to deformation. This is in accordance with the results of Barnby(94) on stainless steel containing 3% volume fraction of $(Fe\ Cr)_{23}\ C_6$, attributed to the small grain size dependence of the yield stress in F.C.C. alloys.

Cracks formed in hard particles in the plastic zone will remain as unpropagated voids, until the applied stress reaches a level sufficient to cause propagation into the matrix. This is the next stage in the fracture process, the voids acting as initiation sites for ductile failure. Fig. 8.8 shows the main crack connecting with fractured carbides, and the emergence of the new crack tip into the matrix. The crack path in plates (a) and (b), is outlined by strain induced martensite, and the formation of S.I.M. ahead of the crack tip is evident from plate (c).

Several workers have demonstrated the decrease in ductility with increasing volume fraction of brittle phase added to a ductile matrix. The predominant feature of much of this work is the proportion of brittle constituent present. Gurland and Plateau(81) relate ductility directly to the volume fraction of second phase particles. However, this can only be considered as a general approach since it does not take into account the morphology of the second phase, or the interaction between the mechanical properties of the second phase and the matrix.

The deformation characteristics of the matrix, in particular the frictional resistance to slip, has been shown to be significant in determining the applied stress required to nucleate cracks in brittle precipitates. Fig. 8.9, where K_{1c} is expressed as a function of volume fraction of carbides in austenitic structures, illustrates the influence of second phase morphology. Since the ability to deform plastically controls

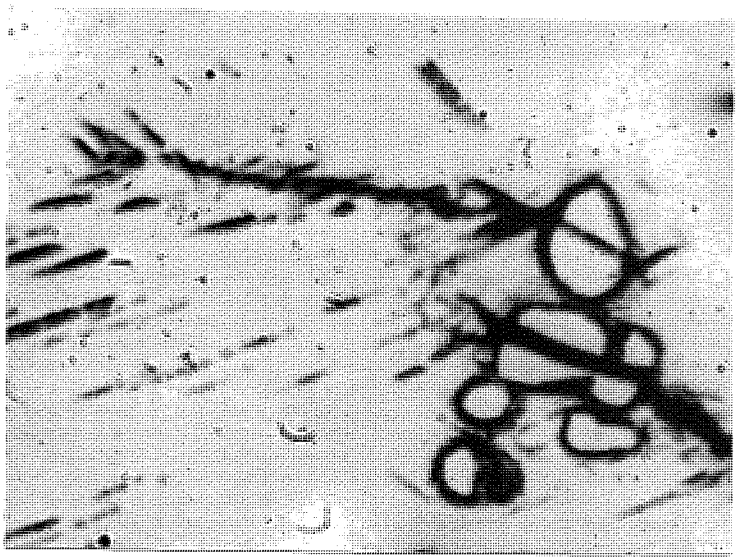

(a) 1.1% C SC/H X 1000

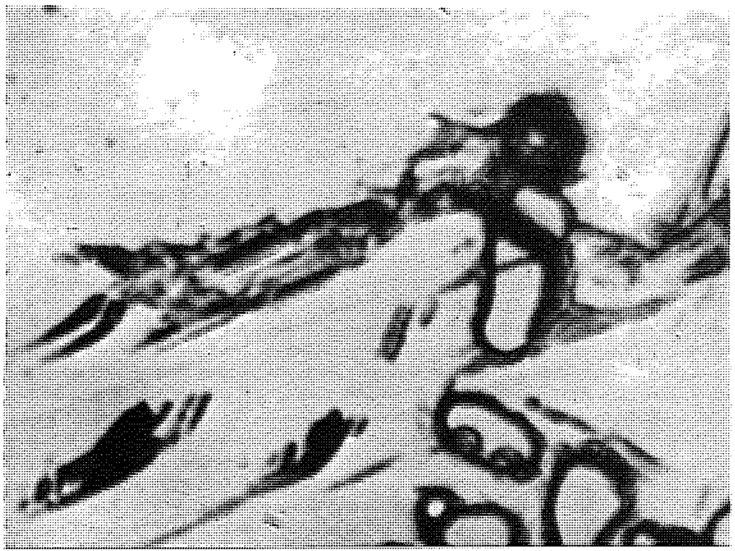

(b) 1.4% C SC/H X 1000

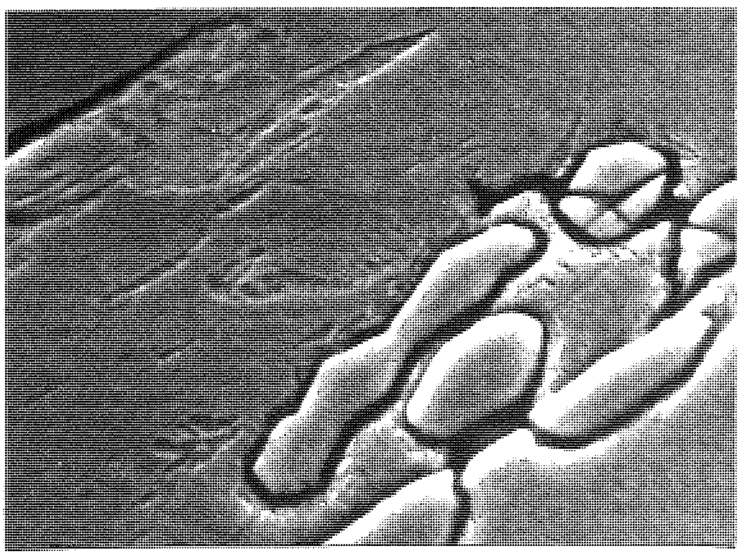

(c) 1.4% C SC/H X 3200

Fig. 8.8. Crack Propagation into the matrix from Cracked Carbides.

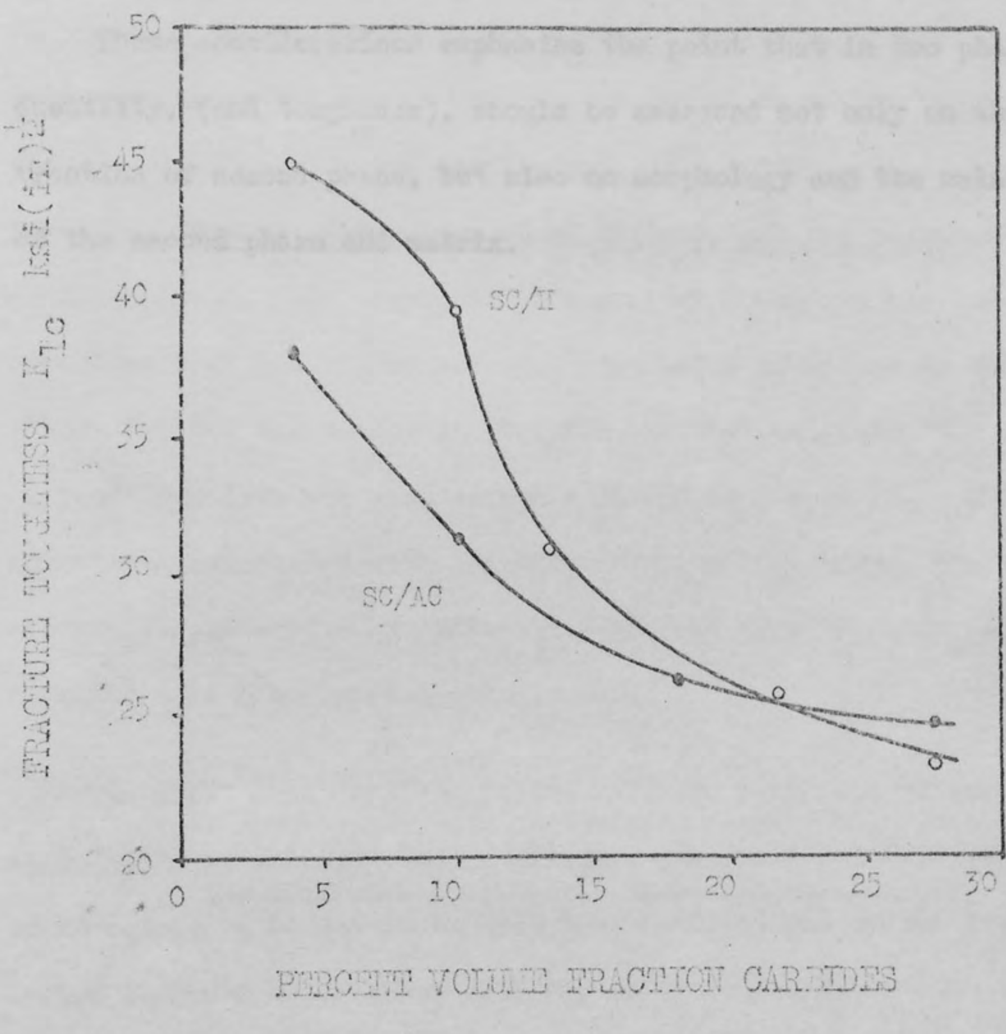

Fig. 8.9. Variation of Fracture Toughness with Percent Volume Fraction Carbides.

toughness, a drop in ductility generally corresponds to a reduction in toughness. K_{1c} decreases most rapidly with the first 15% volume fraction of carbides, but it is the variation in K_{1c} over this range between as cast, and homogenised structures which is important. For instance 10% by volume of interdendritic eutectic carbides have a greater embrittling effect than the same proportion of spherodised particles.

These considerations emphasise the point that in two phase material ductility, (and toughness), should be assessed not only on the volume fraction of second phase, but also on morphology and the relative properties of the second phase and matrix.

9. COMMERCIAL SIGNIFICANCE OF RESULTS.

9.1. The 15% Chromium Alloys.

It is probably worthwhile at this stage to briefly restate the reasons for investigating the 15% chromium series of alloys.

One of the most widely used abrasion resistant alloys employed currently in medium impact loading situations is 25% Cr 2.5% C austenitic white cast iron. Recent developments in grinding and crushing plant are resulting in more onerous impact conditions, and the search for an alloy with comparable wear properties but greater toughness has led to the development of the 15% Cr series. The major advantage in using a 15% Cr alloy, besides the saving in chromium, is that an austenitic structure can be readily maintained with carbon contents as low as 1%. Thus one of the advantages associated with the high chromium cast irons, the ability to produce an austenitic or martensitic product from the same alloy, is retained in a lower carbon alloy.

The first consideration is the relative toughness of austenitic and martensitic material. From a fracture toughness point of view there is no advantage to be gained by heat treatment, at any carbon level. At carbon contents below about 1.5% the alloy is tougher in the as cast condition than after heat treatment to produce optimum hardness. The fracture toughness of martensitic material can be improved by increasing tempering temperature, but at the expense of hardness and probably wear resistance. If heat treatment is necessary for other reasons, such as the type of wear process involved, there is little benefit in reducing carbon content below 2%, except when combined with a high tempering temperature. It should be noted that the tempering conditions necessary for significant improvement in toughness are fairly critical, and there is a danger of over tempering, associated with a drastic drop in both hardness and toughness.

In the as cast condition only marginal improvement in toughness is achieved by reducing carbon from about 3%, just below the eutectic level, to 1.5%. Below 1.5% there is a steady increase in toughness with reduction in carbon to 0.8%, the limit of the austenitic phase field.

In the low carbon alloys there is a tendency for the carbides to segregate in an embrittling grain boundary film, and the optimum combination of hardness and fracture toughness appears to be at about 1% carbon. Reduction in carbon is accompanied by a drop in hardness, but it may be possible to counteract this by adjusting the composition to promote the formation of martensite in the deformed surface layer, without impairing toughness.

Economically a high carbon content is favourable for two reasons, both connected with production. It enables the use of pig iron in the furnace charge in place of more expensive low carbon steel scrap, or low carbon ferro-chromium. Melting temperature increases from 1275°C at 3% carbon to 1450°C at 1% carbon, and this is associated with a widening of the solidification range. Thus a low carbon alloy will not only be more costly to melt but will also be more susceptible to unsoundness due to feeding problems. The increased feeder head material necessary for lower carbon alloys would reduce the yield of the casting process. As far as moulding technique is concerned, any process which refines the grain structure by increasing solidification rate (such as chill casting) will improve toughness. However, this improvement is not considered sufficient to be the sole justification for a change in moulding practice.

An important factor in the choice between an austenitic or martensitic alloy may be the sensitivity of fracture toughness to the rate of application of load. Over the range of testing speeds used (the fastest of which is well below that involved in impact loading), martensitic structures have exhibited a drop in toughness with increasing loading rate. No change was detected in the as cast condition.

The embrittling carbide network formed during solidification can be broken down in two ways, thermally and mechanically. High temperature heat treatment at 1150°C spherodises the carbide particles, and can increase fracture toughness by up to 50%. Soaking time is important in the attainment of maximum toughness, and increases with carbon content. Excessive grain growth and the formation of a grain boundary film occurs if soaking time is extended past the optimum. A protective furnace atmosphere is essential at 1150°C to prevent decarburisation and scaling, and the cost of the treatment prohibits a large scale commercial proposition. In special circumstances, however, spherodisation of a limited number of small castings might be attractive.

Forging of low carbon alloys (less than 1½% C) shows greater promise for further development. The production of small simple shapes, such as grinding media (balls or slugs), would be ideally suited to this process. Uniform deformation followed by heat treatment to a homogenous martensitic or austenitic structure should result in a very acceptable product.

9.2. Fracture Toughness of Competitive Alloys.

An accurate and dependable measure of the toughness of a new alloy is of little significance without a perspective view of the materials with which it is to compete. A brief survey was carried out on six alloys which are likely to be most competitive in the field of application envisaged for the 15% Cr 1% C alloy. The group of alloys investigated comprised: (a) Manganese steel (still the conventional choice in severe impact conditions); (b) alloyed manganese steel (lower wear rate than (a) in similar circumstances); (c) EF 253 (proprietry high Cr white cast iron); (d) Maxichrome (proprietry 12% Cr, 1.5% C martensitic alloy).

Chemical analysis and mechanical properties, including K_{1c} are presented in tables 9.1.(a) and (b). Quoted K_{1c} values are the average of a minimum of two tests.

TABLE 9.1. (a).

ALLOY.	C	Si	Mn	Ni	Cr	Mo	Co
BF 253.	2.2	0.35	1.1	0.25	23.4	-	-
Manganese steel.	0.97	0.60	10.5	0.06	0.04	-	-
Alloyed Mn. steel (1)	1.23	0.82	9.4	1.56	4.04	-	3.6
(2)	1.30	0.55	11.2	3.0	3.3	-	0.25
Maxichrome	1.30	0.5	1.4	0.12	12.5	0.6	-

TABLE 9.1. (b).

ALLOY.	ORIGIN	U.T.S. ksi.	Hv 30	K_{1c} ksi.(in)$^{\frac{1}{2}}$	COMMENTS.
BF 253. AC.	Worn lining	116	500	25.7	)Rapid crack)
H.T.	plate.	125	750	25.5	)propagation
Mn. steel	"	46	220	27.0	))
Alloyed (1)AC Mn. St.	Virgin	86	280	29.0	)slow crack))growth through
(1) H	material	-	220	40.3	))entire nett)
Alloyed (2)AC Mn. st.	"	72	270	30.3	)section.))
(2) H		-	200	38.4	)
Maxichrome	New lining plate	164	450	35.3	Rapid cr. prop.
1%C 15%Cr AC	Virgin	70	330	35	Some sl.cr.grth.
H.T. 250°C.	Material	150	650	26	Rapid cr. prop.
H.T. 450°C.		-	570	35	" " "
H. 1150°C.		-	250	45	Some sl.cr.grth.

Three main groups of alloys are covered by the materials investigated in this survey, namely martensitic, and hard and soft austenitic. The results indicate that a 1% C, 15% Cr alloy could compete favourably, especially with the first two types.

Two alloys constitute the martensitic group, BF 253 H.T. and Maxichrome. The BF 253 was subjected to a straightforward hardening (975°C) and tempering (250°C) treatment, which has no effect on as cast toughness. This is consistent with results on the 15% Cr series. The normal procedure for Maxichrome alloys is a complex and expensive heat treatment including prolonged annealing. However, the resulting level of fracture toughness can be attained in the 15% Cr alloy by simply increasing tempering temperature from 250°C to 450°C.

The fracture toughness of the as cast 15% Cr alloy is some 40% higher than the as cast BF 253, representing the hard austenitic category. This margin would probably be greater for a more typical BF 253 containing 2.7 to 2.9% carbon. Undoubtedly the wear resistance of the harder BF 253 will be superior to that of the 1% carbon material. The performance of lower carbon alloys in a dry cement mill production trial initiated some 3½ years ago, and still proceeding, indicates that a reasonable level of wear resistance is maintained. In more severe abrasive conditions, such as wet grinding, the wear rate should compare even more favourably with that of the higher carbon alloys.

In the third general group, soft austenitic, although the K_{1c} of the manganese steels is slightly lower than the 15% Cr material, they have a very slow rate of crack propagation. In effect this means that after the critical stress intensity has been exceeded, and crack growth initiated, a high stress level must be maintained to cause complete failure. This feature is illustrated in fig. 9.1, which includes typical load/displacement records of the alloys under investigation. Thus, for a given crack situation, a higher stress is required to initiate crack

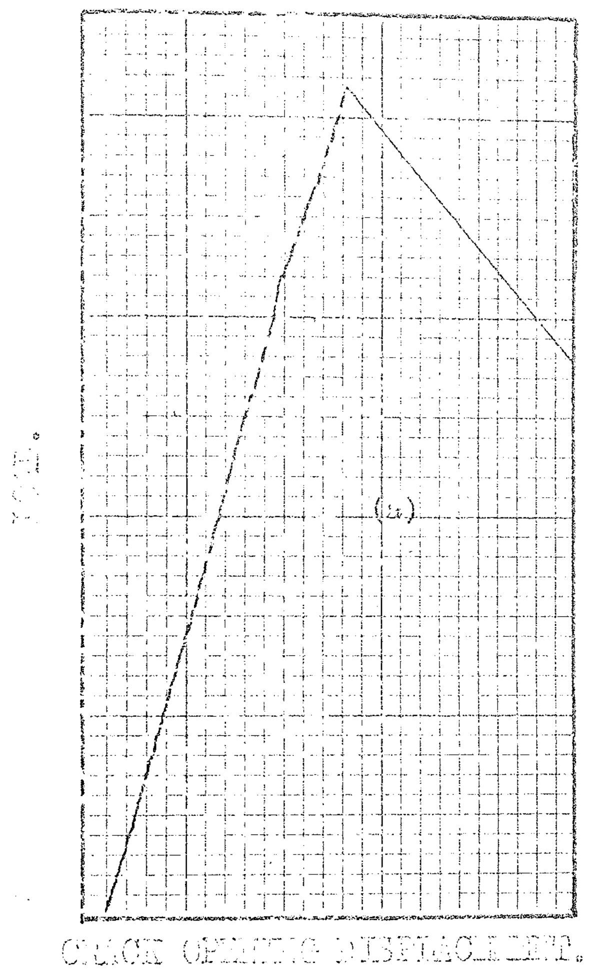

(a) High Carbon Material.

(b) Low Carbon Martensitic Material.

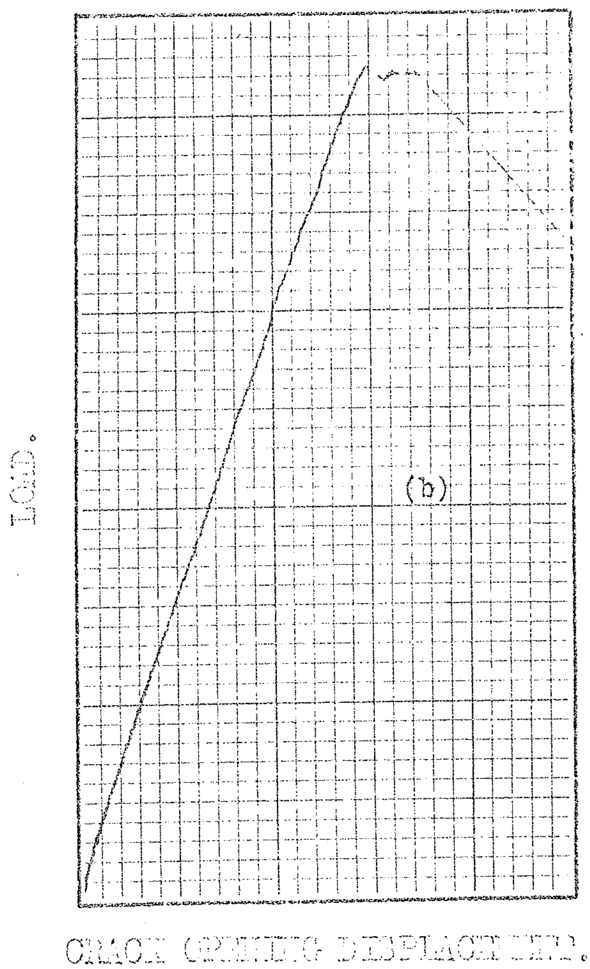

Fig. 9.1. (a) & (b). Typical Load/Displacement Records for Material with Negligible Slow Crack Growth.

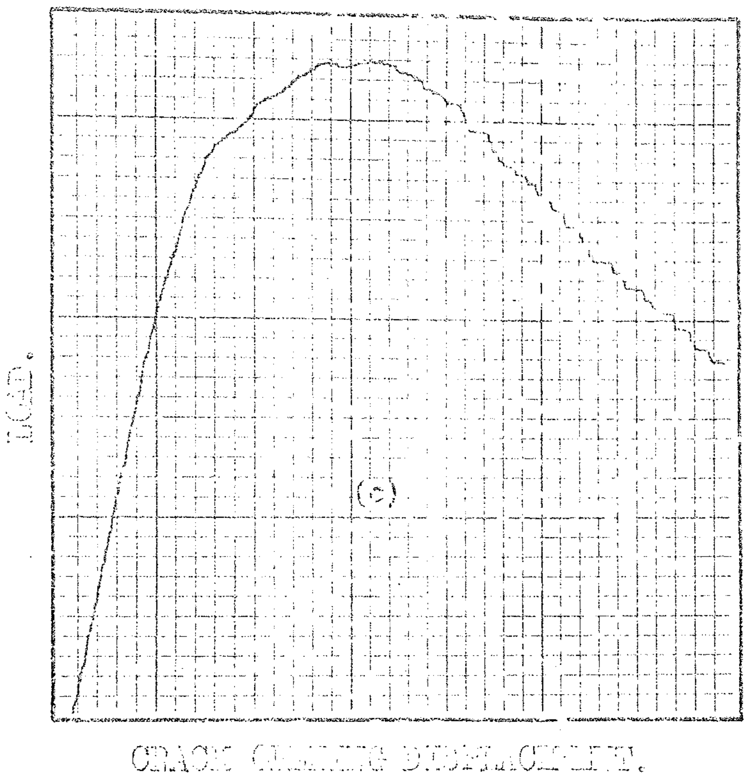

(c) Low Carbon Austenitic Material.

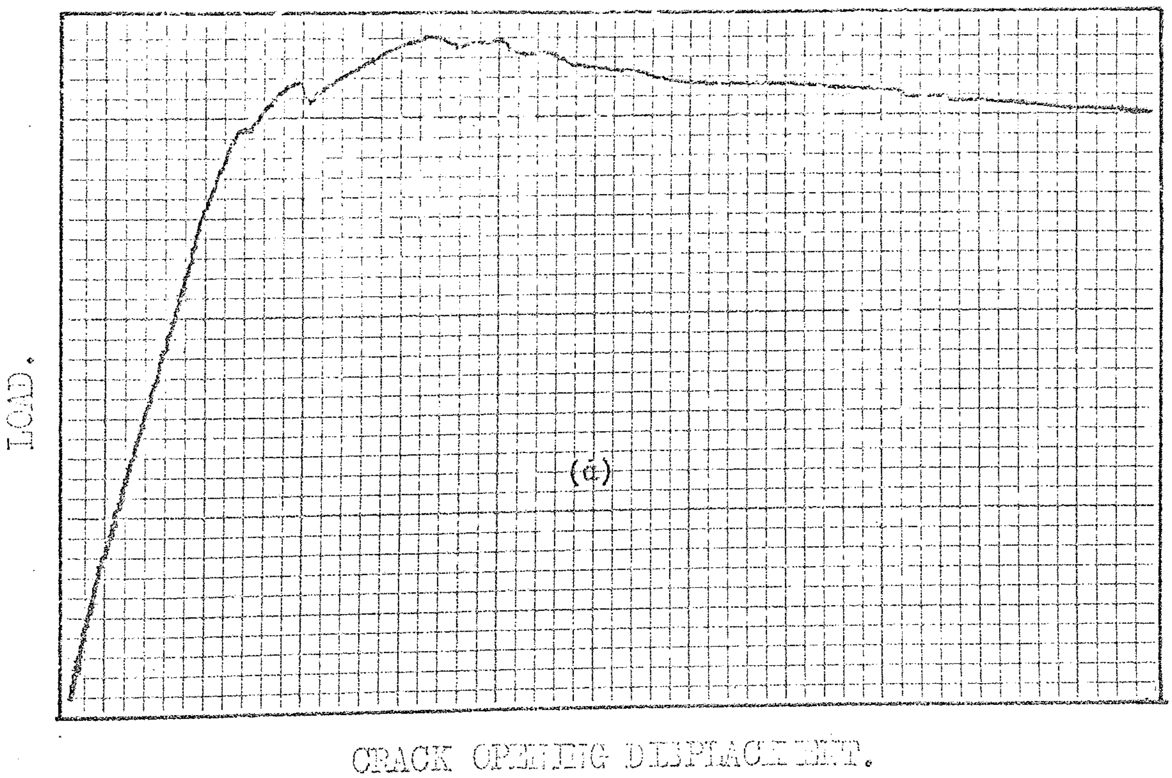

(d) Manganese Steels.

Fig. 9.1. (c) & (d). Typical Load/Displacement Records for Material showing Significant Slow Crack Growth.

growth in the low carbon 15% Cr alloy. Subsequent propagation through the nett section is relatively fast, but still associated with some slow crack growth. In contrast, high carbon and martensitic alloys exhibit rapid crack propagation immediately critical stress intensity conditions are reached, with little or no slow crack growth.

Although several factors influence the choice of alloy for a given application, in components which are continually wearing, cost is always important. A comprehensive economic analysis would include the separate costs of pattern making, moulding, raw materials, melting, fettling, scrap, machining and heat treatment. For reasons such as the fluctuations in the price of raw material, and special requirements of the customer, it is common practice to quote costs on a contract basis. However, most suppliers have a range of tonnage prices which can be used as a general guide for comparison purposes. The following survey gives an estimate of the relative costs of the alloys under consideration in terms of these current selling prices.

Manganese Steel. General difficulties associated with the production of manganese steel are reflected in the comparatively high selling price. For instance in the molten state manganese steel reacts with normal silica sands, necessitating the use of expensive neutral mould facings.

Materials and heat treatment: £110 - £120 / ton.

Selling Price: Up to £350 / ton.

BF 253. A high chromium white cast iron marketed in the as cast, stress relieved, and hardened and tempered conditions.

Materials and Melting: £70 / ton.

Selling Price (as cast): £180 - £190 / ton.

Additional Heat Treatment Costs:-

Stress Relieving: £30 / ton.

Hardening: £45 / ton.

Tempering: £25 / ton.

Maxichrome. Molybdenum additions and prolonged annealing during heat treatment cycle, contribute to the rather high selling price of this alloy.

Materials and Melting: approximately £80 / ton.

Selling Price: approximately £250 / ton.

15% Cr 1% C.

Materials and Melting: £55 - £60 / ton.

A selling price is not available for this alloy, but accounting for decreased yield due to extra feeding requirements it should still sell at around £170 - £180/ton in the as cast condition.

In general then, the proposed 1% C, 15% Cr composition appears to have commercial potential, at a competitive price, with a wider range of application than most of the alloys of its type at present on the market.

9.3. Critical Defect Size.

In applications where there is a danger of unstable brittle failure the gross stress field is generally elastic at the operational load, and the failed component is characterised by the absence of a large amount of plastically deformed material. This observation is fundamentally important and emphasises the risk involved in estimating the strength and operational life of a component on conventional strength analyses, assuming plastic yielding prior to failure. It should be recognised that fabricated, wrought, and cast components all contain defects and flaws of various kinds. The operational life of any structure is governed by the defect size required to cause failure at the operating stress level (ie. the critical defect size), the initial defect size, and the sub critical crack growth characteristics of the material.

The A.S.T.M. E 24 committee have categorized the types of defects likely to be encountered as surface, embedded, or through thickness cracks. For surface and embedded defects the degree of constraint at the crack front is high and plane strain conditions generally prevail. The mode of fracture for through thickness cracks will depend upon material strength and thickness. In thin sections plane stress is generally predominant, but with increasing thickness the fracture changes from slant to square under essentially plane strain conditions.

In the failure of abrasion resistant castings a likely initiation site for brittle fracture is central unsoundness. It is common practice when producing thick sections to accept a certain amount of drawing, provided it is restricted to the interior of the casting. Normally the examination of failed components from grinding and crushing plant is hampered by destruction of the fracture surface due to contamination and post-fracture abrasion. However, when observed on the fracture surface this type of defect has been the apparent cause of failure. A typical example of shrinkage cavities on the fracture surface of a low carbon 15% Cr alloy is shown in fig. 9.2, taken from an unreported test casting, produced with insufficient feeding capacity.

In this situation, determination of the critical stress for an embedded defect of given size and shape was considered the most appropriate way of comparing the relative toughness of the alloys under investigation.

The mathematical model for the prediction of critical defect size assumes an elliptical (or semi-elliptical), defect shape. The relationship between defect shape, denoted Q, and aspect ratio is normally presented as a function of the applied stress level, shown in fig. 9.3. For an embedded flaw[61]:

$$\left(\frac{a}{Q}\right) \text{crit} = \frac{1}{\pi} \times \left(\frac{K_{Ic}}{\sigma_{app}}\right)^2. \qquad \ldots\ 9.1.$$

(a) X 50

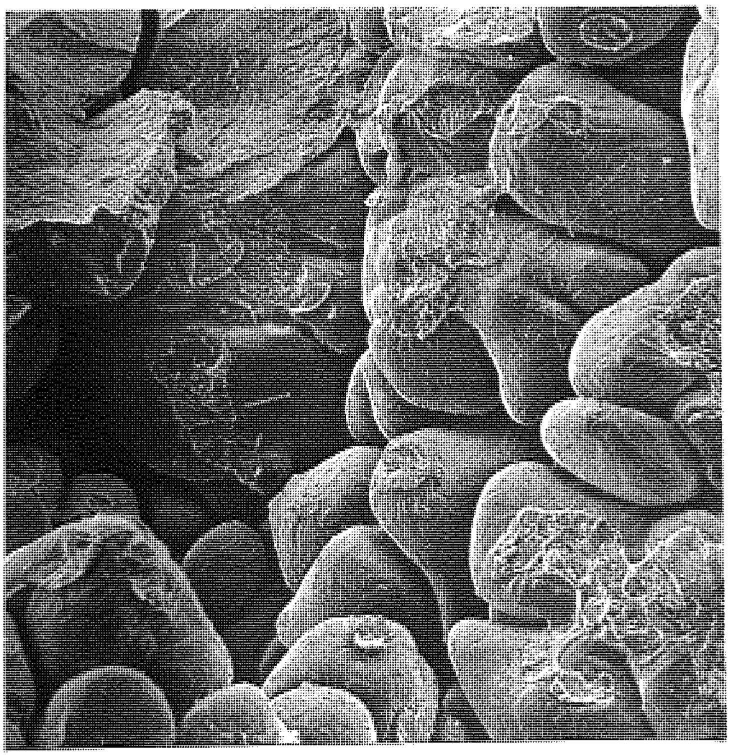

(b) X 200

Fig. 9.2. Shrinkage Porosity on Fracture Surface of 1.1% C 15% Cr Test Casting.

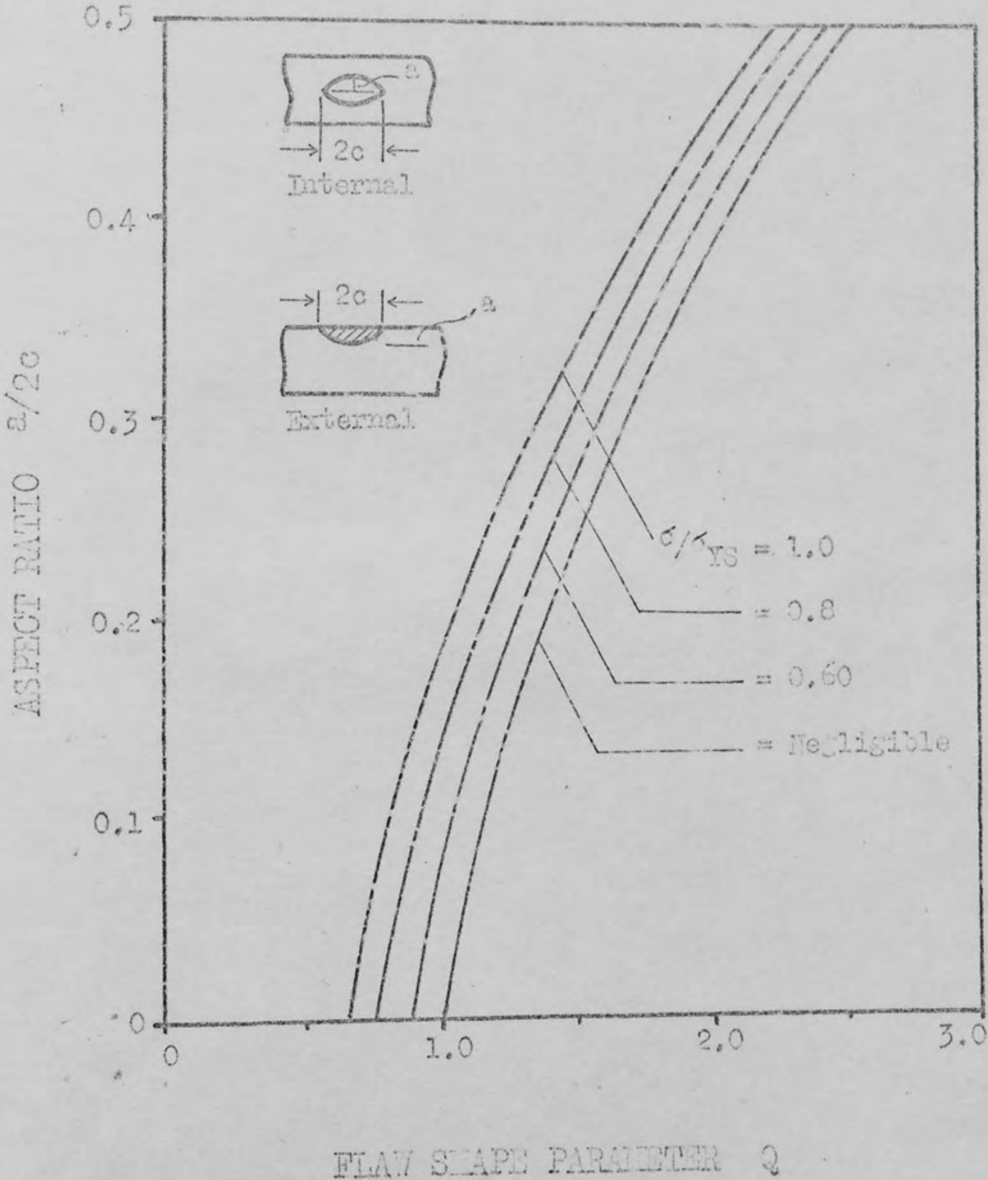

$K_{1c} = 1.1\ (\pi)^{\frac{1}{2}}\ \sigma\ ({}^{a}Cr/Q_{Cr})^{\frac{1}{2}}$

$Q = \phi^2 - 0.212\ (\sigma/\sigma_{YS})^2$

Q = Flaw Shape Parameter.

ϕ = Complete Elliptical Integral.

σ = Gross Stress.

σ_{YS} = 0.2% Offset Tensile Yield Stress.

Fig. 9.3. Flaw Shape Parameter Curves for Surface and Internal Cracks(41).

or

$$\sigma \text{ crit} = \frac{K_{1c}}{\left[\left(a/Q\right)\pi\right]^{\frac{1}{2}}} \qquad \ldots\ 9.2.$$

The term $\left(\frac{a}{Q}\right)$ describes the defect size in terms of the aspect ratio, $\frac{a}{2c}$, where 2c and 2a are the major and minor dimensions of the defect with respect to the direction of crack propagation. Considering an area of porosity three inches in diameter, and extending $1\frac{1}{2}$ inches through the thickness (not uncommon in, say, a 4 inch thick casting), the aspect ratio, $\frac{a}{2c}$, is 0.25. Thus the Q value will vary from 1.3 to 1.5 depending on the yield stress of the material. Assuming that no sub critical crack growth occurs, the load required to attain critical stress intensity conditions, σ_{crit}, and initiate unstable cracking in this given situation, is proportional to K_{1c}, and indicated in table 9.2, below.

TABLE 9.2.

Critical stress requirements for an embedded defect, aspect ratio 0.25, where a = 0.75 ins.

Alloy.	U.T.S. ksi.	K_{1c} ksi(in)$^{\frac{1}{2}}$	Critical stress ksi.
15% Cr 1% C AC.	70	35	27.5
H.T. 250°C.	150	26	20.1
H.T. 450°C.	-	35	27.6
H. 1150°C.	-	45	35.6
BF 253 (2.2%C)	116	25	19.8
15% Cr 2.8% C.	115	21.5	16.8
15% Cr 3.4% C.	-	16	12.5
Maxichrome	164	35.3	27.8
Manganese steel.	46	27.0	21.0

10. CONCLUSIONS.

Plane strain fracture toughness testing techniques have been used to study the fracture characteristics of relatively brittle abrasion resistant alloys. The investigation was based on an austenitic cast iron, containing 15% chromium and 0.8 to 3.4% carbon. Particular attention was paid to the tougher low carbon alloys in this series. Carbon content, grain size, hardening variables, homogenisation, rate of application of stress intensity, and hot working, have all been examined, and the effects on fracture toughness, microstructure, and tensile properties observed.

Variation of carbon content has been shown to be a major factor influencing the fracture process, and the point at which the eutectic carbide network becomes continuous, about 1.5% carbon, found to be particularly important. At carbon contents above this value, toughness is controlled by the volume fraction of carbides, and is unaffected by matrix characteristics. Lower carbon alloys, in which the carbide network is discontinuous, are responsive to heat treatment and sensitive to matrix structure. Heat treatment to a martensitic matrix leads to a constant level of toughness, independent of carbon content, and generally below the as cast value.

In the low carbon series the following treatments have resulted in an improvement in fracture toughness:

(a) Reducing the volume fraction of eutectic carbides in austenitic alloys, from the level at which a continuous carbide network is formed.

(b) Decreasing the grain size at a given carbon content.

(c) Increasing tempering temperature of martensitic alloys.

(d) Spherodisation of the eutectic carbides by heat treatment at temperatures approaching the melting point.

(e) Deformation of the as cast structure.

A structural correlation was observed in martensitic alloys, in terms of a recent fracture model based on a plastic instability concept. The spacing of secondary carbide particles was found to correspond to the fractographic dimple size and the theoretical process zone size. The uniformity of secondary carbide distribution at varying carbon contents, is thought to be responsible for the constant level of toughness recorded in martensitic material.

In austenitic structures a strain induced transformation to martensite has been detected within the deformed zones of fracture toughness and tensile specimens. This transformation was shown to raise the U.T.S. with little influence on K_{Ic}. In an analysis of the fracture mechanisms occurring at the crack tip, the experimental K_{Ic} result was observed to be between the upper and lower bounds of a value derived from a modified energy dissipation model.

A survey of the materials likely to be most competitive with a proposed 1% carbon, 15% chromium alloy, indicates that this alloy would compete favourably, as far as toughness and cost is concerned. Variation of the microstructure by heat treatment widens the possible range of application beyond that characteristic of other wear resistant alloys.

APPENDIX

Two methods are available for the measurement of the geometrical constant Y, which determines the level to which K_{1c} is raised by a given situation. Theoretical values of Y for many types of geometry have been calculated by complex stress analysis techniques, but practical calibration can be made for any specimen geometry by compliance testing, which also tests the experimental rig and procedure.

Since the crackline loaded specimen used in this investigation is a relatively new design it was decided to check the Y calibration by a compliance experiment.

Irwin and Kies (95) express the strain energy release rate in terms of load and spring compliance of the specimen.

$$d\varepsilon/_{da} = \tfrac{1}{2} P^2 \, d/_{da} \, (1/_M).$$

where ε is the strain energy, a, crack length, P load, and M spring compliance. Strain energy release rate, however, is G_1, which is related through E, Young's modulus, to K_1:

$$d\varepsilon/_{da} = G_1 = \frac{\left[K_1(1 - v^2)\right]^2}{E}$$

Hence, for unit thickness B, where v is Poissons ratio:

$$\frac{\left[K_1(1 - v^2)\right]^2}{EB} = \tfrac{1}{2} P^2 \, d/_{da} \, (1/_M).$$

and:

$$K_1 = P \left[\frac{EB}{2(1 - v^2)} \, d/_{da} \, (1/_M)\right]^{\frac{1}{2}}. \qquad \ldots\ldots (A1)$$

In stress analysis K_1 is normally expressed in terms of Y as:

$$K_1 = \frac{YP(a)^{\frac{1}{2}}}{BW} \qquad \ldots\ldots (A2)$$

where W is the width of the specimen. Combination of equations A1 and A2 leads to a formula for the polynomial Y:

$$Y = W \left[\frac{EB}{2a(1 - v^2)} \, {}^{d}/_{da} \left({}^{1}/_{M} \right) \right]^{\frac{1}{2}}. \qquad \ldots\ldots \text{(A3)}$$

W, B, E, and v, are constants, so by varying a, and measuring ${}^{d}/_{da} ({}^{1}/_{M})$, the Y value for any crack length can be determined.

The experimental procedure followed was similar to that described by Sullivan (96). The clip gauge was first checked for linearity by attaching it, with the knife edges, to a vernier micrometer. The response to opening and closing the gauge, was measured on the Bryans X - Y plotter, and is shown in fig. A1. A mild steel specimen was made, to the design in fig. A2, with an initial crack length of 0.5 ins. The compliance, $({}^{1}/_{M})$, was determined by loading and unloading, within the elastic region, up to 200 kg., measuring the slope of the load/displacement record, and taking the reciprocal. This procedure was repeated at twelve crack lengths, up to a final crack length of 2.5 ins. Ten duplicate compliance measurements were made at each increment of crack extension. The variation in $({}^{1}/_{M})$ with crack length is shown in fig. A3.

Boundary collocation data for this type of specimen is calculated from the theoretical displacements at the load line, and it is necessary to correct experimental data to compensate for measurement at the specimen edge, (97). The values of $({}^{1}/_{M})$ to which the correction graph applies are shown in table A1.

Compliance was expressed as ${}^{d}/_{da} ({}^{1}/_{M})$, by graphical differentiation of the compliance versus ${}^{a}/_{W}$ curve at four crack lengths. This procedure is shown schematically in fig. A4. Insertion of this data into equation A3 gives the Y values shown in table A2. Experimental results are shown, superimposed on the theoretical analysis by Srawley and Gross (98) in fig. A5.

The compliance calibration is in good agreement with the computed analysis, and correlates well with the experimental results of Wessel [99] and Terry and Richards [100] on compact tensile specimens.

Compliance Calibration Results for Crackline Loaded Mild Steel Specimen.

$W = 3.375$ ins. $B = 0.489$ ins. $2H = 4.0$ ins. $v = 0.29$.
$E = 30 \times 10^6$ lb/in^2. Notch width $^3/_{32}$ in. Hole at crack tip 0.08 in. dia.

TABLE A1.

a.	a/W	$^1/_M \times 10^6$ in/lb	$^1/_M$ Corrected to L.E.
1.02	0.302	1.648	1.030
1.20	0.355	1.937	1.282
1.39	0.412	2.316	1.618
1.59	0.472	3.202	2.350
1.76	0.522	3.854	2.88
1.98	0.586	5.300	4.10
2.17	0.642	7.347	5.76
2.34	0.684	10.48	8.41

TABLE A2.

a/W	$^d/_{da}\ (^1/_M)$	$\left[^d/_{da}(^1/_M)/a\right]^{\frac{1}{2}}$	Y
0.65	11.1	2.28	21.6
0.57	5.9	1.76	16.5
0.45	2.78	1.35	12.7
0.33	1.36	1.11	10.6

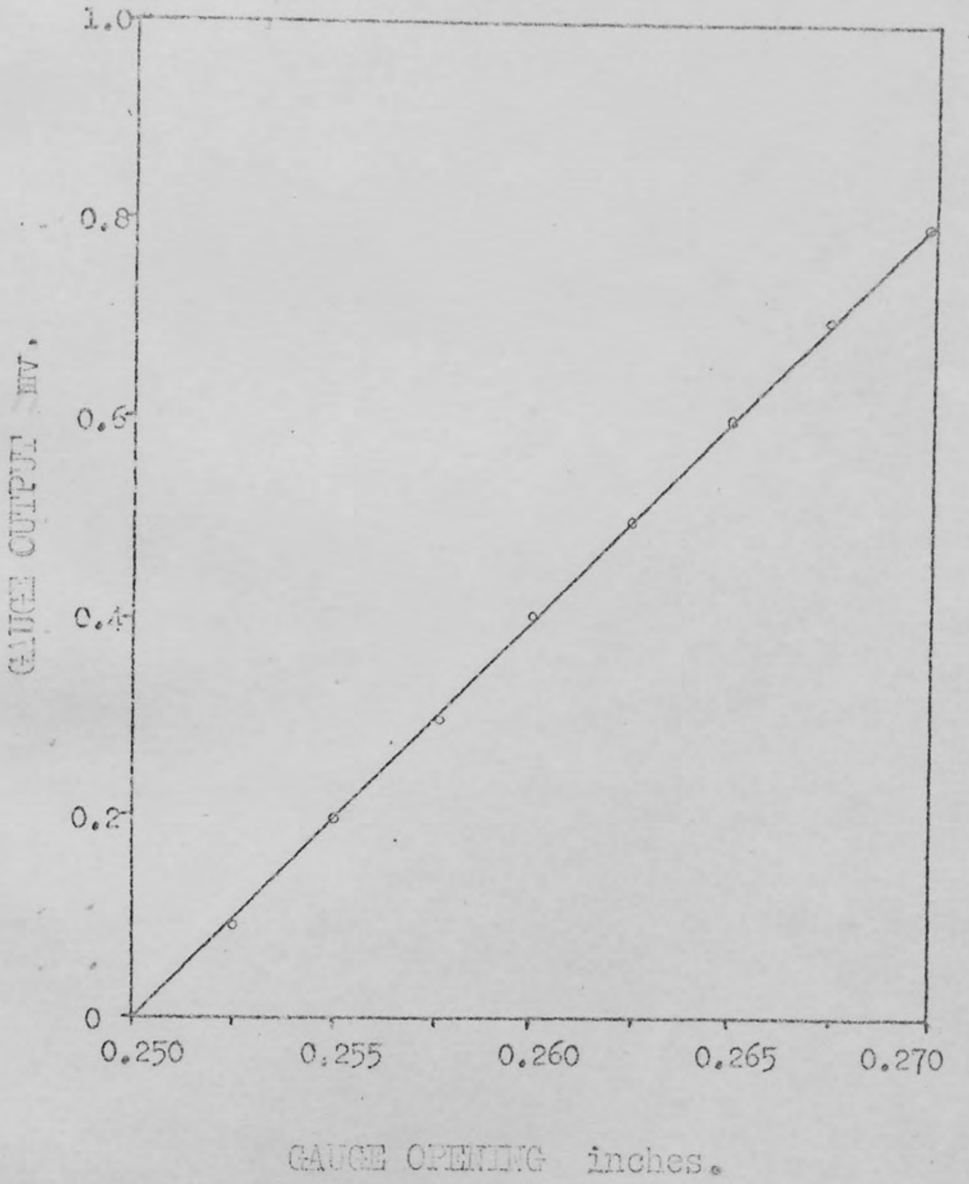

Fig. A1. Clip Gauge Calibration Curve.

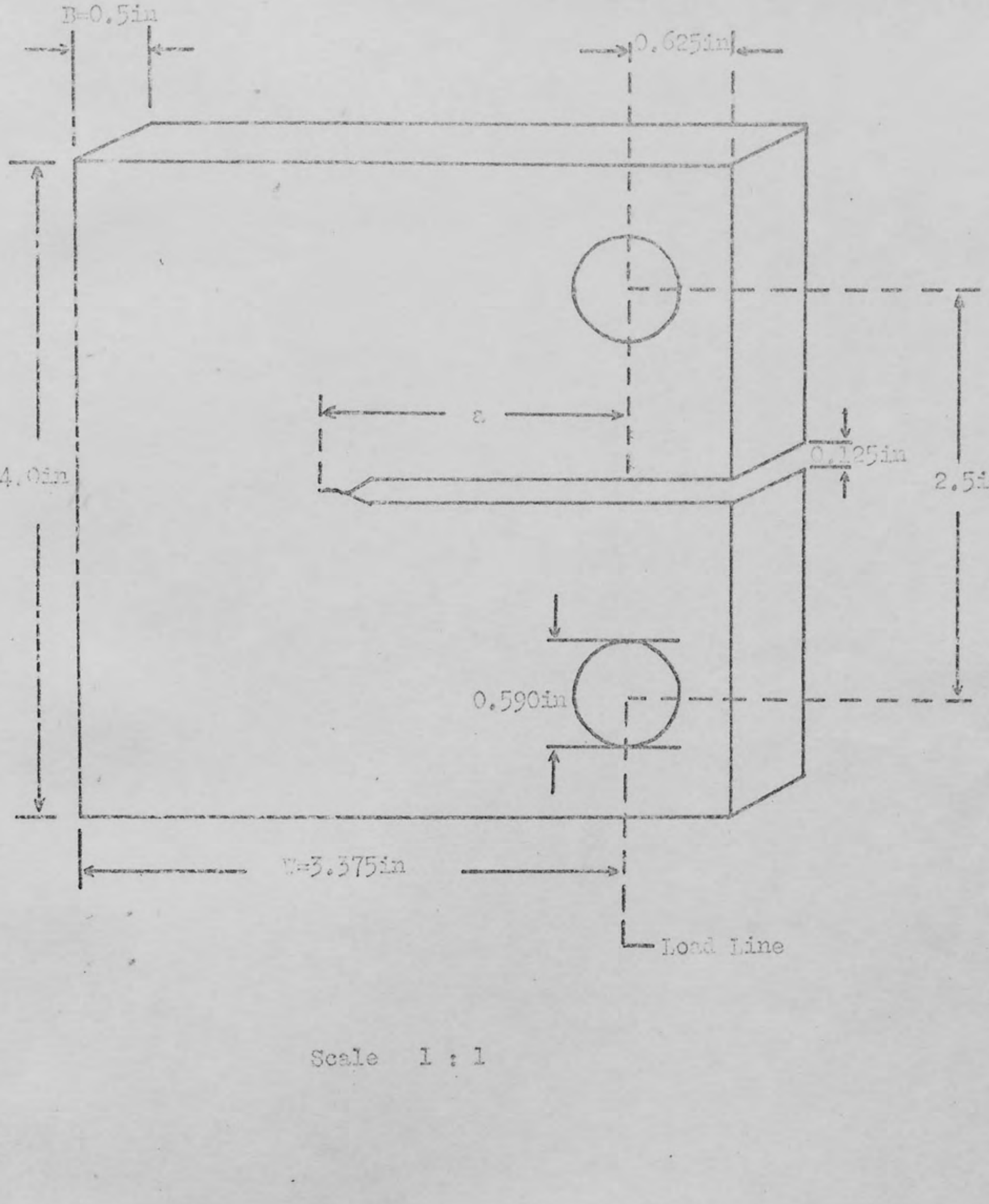

Scale 1 : 1

Fig. A2. Crackline Loaded Fracture Toughness Specimen.

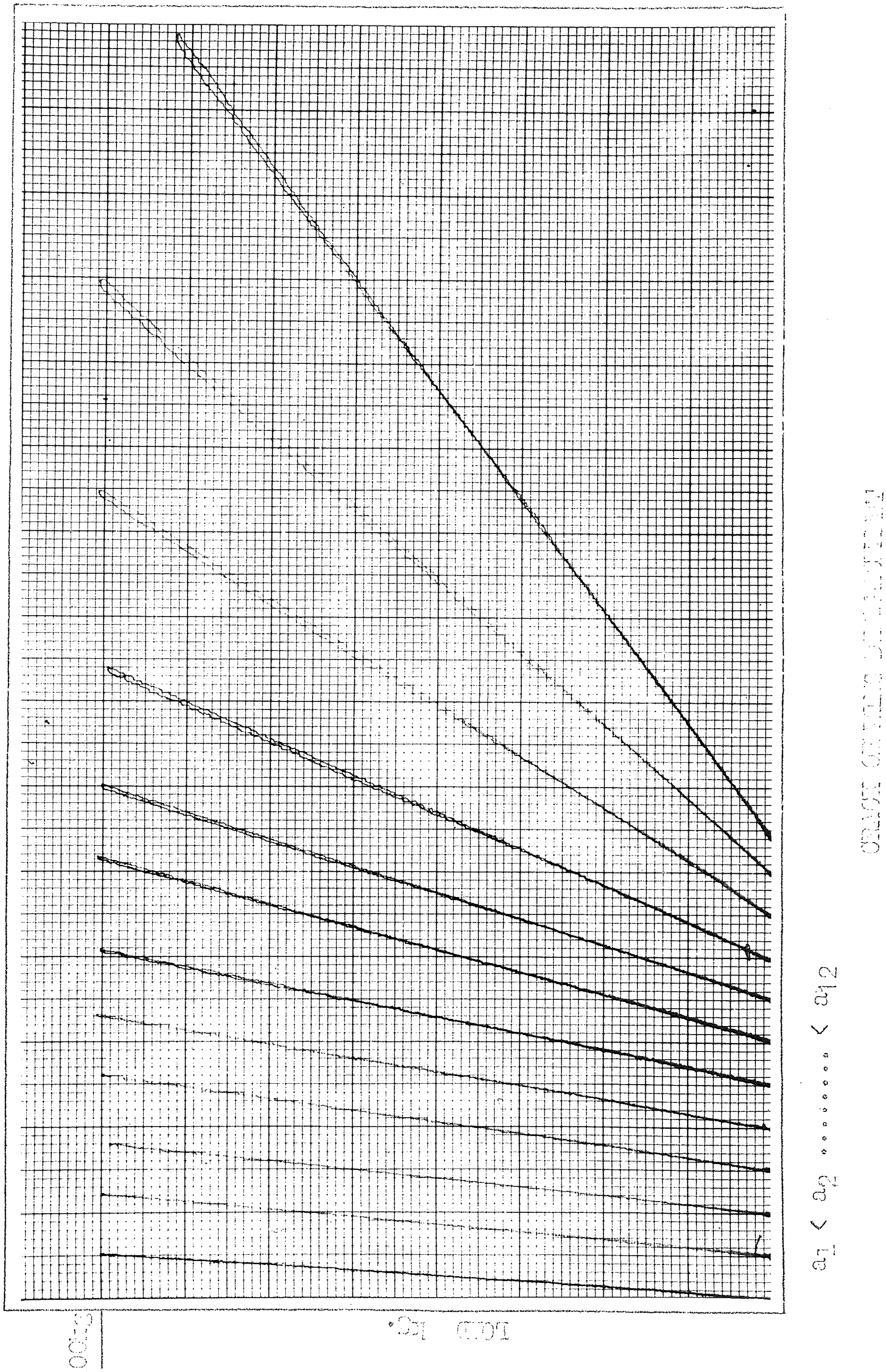

Fig. A3. Change in Compliance with Increasing Crack Length.

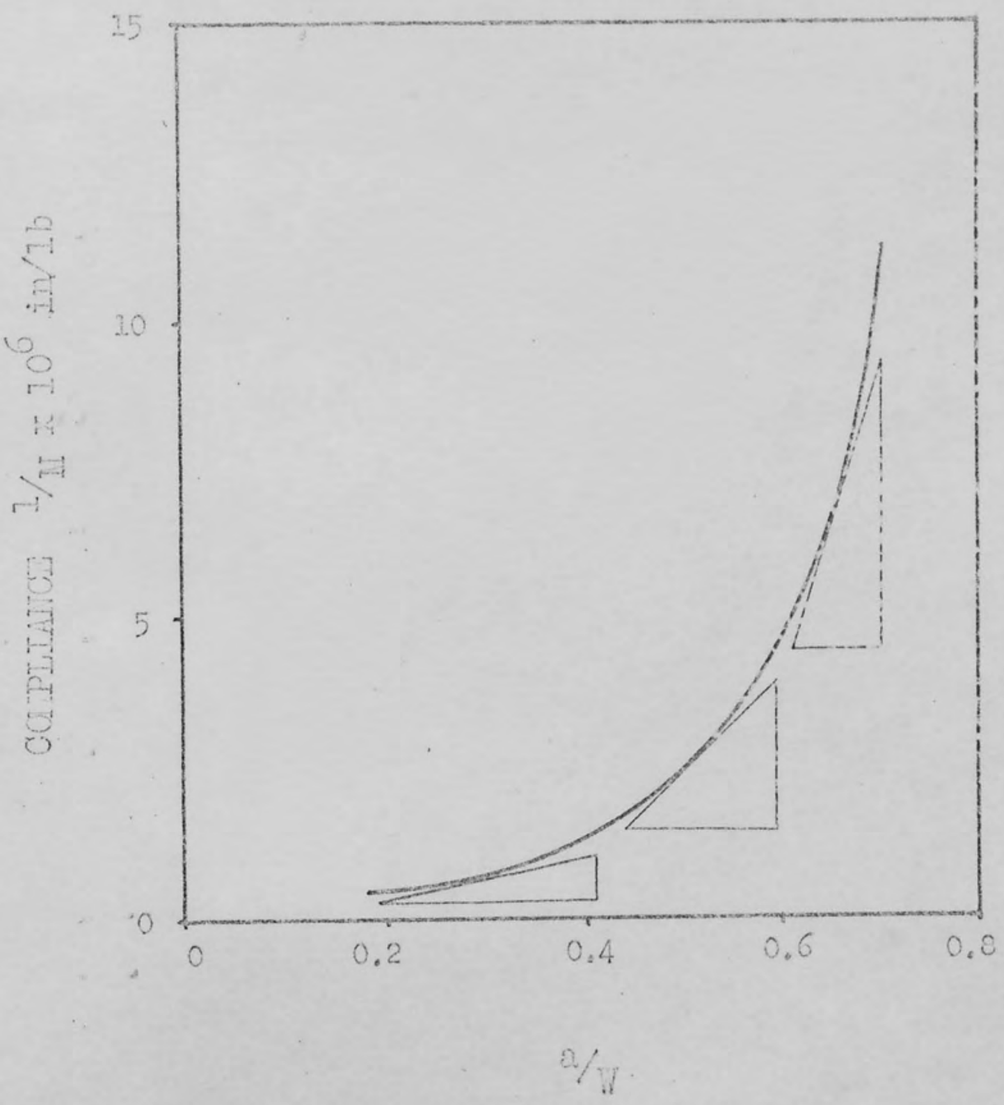

Fig. A4. Graphical Differentiation of Compliance/ $^a/_W$ Curve.

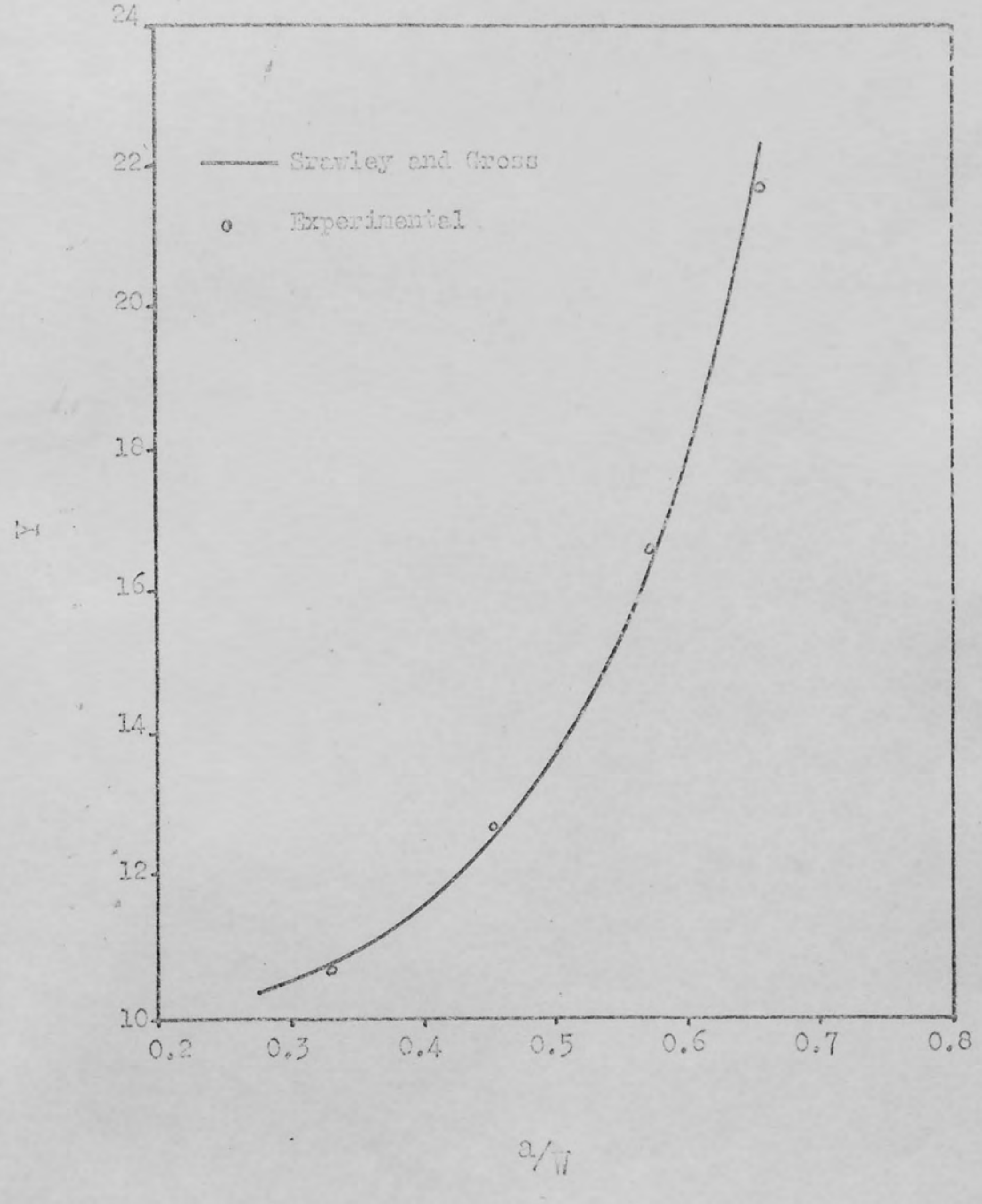

Fig. A5. Boundary Collocation(98) and Experimental Compliance Calibration Data.

ACKNOWLEDGMENTS.

The author thanks Dr. J.T. Barnby and Mr. J. Dodd for helpful discussions, and Bradley and Foster Ltd. for the facilities extended during the course of this work.

BIBLIOGRAPHY.

1. Avery. 'Handbook of Mechanical Wear.' Univ. of Mich. Press.

2. Wilson. 'The use of Abrasion Resistant Alloys in producing Underground Mine Scrapers.' S.A.E. National Farm Industrial and Machinary Papers. December, 1968.

3. Taggart. 'Handbook of Mineral Dressing.' Chapman and Hall.

4. Rey & Formanek. Int. Mineral Processing Cong. 1960. p.349.

5. Dodd & Jackson. Metallurgia. September, 1967. p.107.

6. Norman. Modern Castings. May, 1958. p.89.

7. Kempe. Symposium on Wear of Materials. Ottawa. March, 1967.

8. White. J.I.S.I. v.198, 1960, Discussion p.175.

9. Murakami. Oka & Nishigori. Tech. Rep. Tokoku Univ. 1930.(5) p 59.

10. Kinzel & Franks. 'Alloys of Iron and Chromium.' Vol. 1. Mcgraw Hill 1940.

11. Bungardt, Kunze & Horn. Arch. Eisenhüttenw. v.29, 1958. p.193.

12. Griffing, Forgeng & Healy. Trans. A.I.M.E. v.224, 1962. p.148.

13. Jackson. J.I.S.I. February, 1970.

14. Bradley & Foster. Internal Report Number. R.D. 66/17.

15. Kuo. J.I.S.I. v.173, 1953. p.363.

16. Lane & Grant. Trans. A.S.M. v.44. 1952. p.113.

17. Climax Molybdenum. Brochure 'The Role of Molybdenum in Abrasion Resistant Materials. 1962.

18. Bradley & Foster. Internal Report Number. R.D. 67/9.

19. Eichelman & Hull. Trans. A.S.M. v.45, 1953. p.77.

20. Andrews. J.I.S.I. v.203, 1965. p.721.

21. Grange. Met. Prog. April, 1961. p.73.

22. Holloway. PhD. Thesis, Univ. of Aston, 1970.

23. Irvine. 'The Effect of Cobalt in Steels.' Proc. of the Journees Internationales des Applications du Cobalt, Brussels 1964.

24. Hawkes & Mehl. Trans. A.I.M.E. v. 172, 1947. p.467.

25. Cohen. Trans. A.S.M. v.41, 1949, p.35.

26. Rickard. B.C.I.R.A. Report W.A. 16. May 1969.

27. Powell Trans. A.S.M. v.50, 1958, p.478.

28. Cina. J.I.S.I. v.406, 1954, p.177.

29. Karlson & Thomas. Trans. A.S.M. v.55, 1962, p.462.

30. Bressanelli & Moskowitz. Ibid. v.59, 1966, p.223.

31. Gerberich, Hemmings, Zackay & Parker. Paper 24. Int. Conf. on Fracture. Haifa 1969.

32. Gerberich, Hemmings, Mertz & Zackay. Trans. A.S.M. v.61, 1968, p.843.

33. Gold & Koppenaal. Ibid. v.62, 1969, p.607.

34. Zackay Parker, Fahr & Busch. Ibid. v.60, 1967, p.252.

35. Norman. Eng. and Min. J. v.158, 1957, p.102.

36. Pabiyn. A.F.S. Cast Metals Res. J. March 1969.

37. Bradley & Foster. Internal Report Number. R.D. 66/2.

38. Griffith. Phil. Trans. Roy. Soc. A221, 1920, p.163.

39. Inglis. Trans. Inst. Naval Architects. v.60, 1913, p.219.

40. Orowan. Trans. Inst. Eng. Shipbuilders. 1945, p.165.

41. A.S.T.M. S.T.P. 381.

42. Irwin. 'Fracturing of Metals' A.S.M. 1948, p.147.

43. Orowan. Welding Res. Suppl. v.20, 1955, p.157s.

44. Irwin. J. Appld. Mech. v.24, 1957, p.361.

45. Irwin. 'Structural Mechanics' Perg. Press 1968.

46. Neuber. Kerbspannungslehre. Berlin, 1958.

47. Kuhn. S.A.E. A.S.M.E. 1964.

48. Barenblatt. Advances in Appld. Mech. Volume Vll, 1962.

49. Barnby. Welding and Metal Fab. Feb. 1969, p.71.

50. Cottrell. Proc. Roy. Soc. A276, 1963, p.1.

51. Greenwood. 'Fracture Toughness Theory and Practice'. Symposium, Sheffield, 1968.

52. Irwin. Proc. 1st. Symp. on Naval Struc. Mech. Perg. Press, 1960.

53. Yukawa & McMullin. J. Basic Eng. v.83, 1961, p.451.

54. Weiss. Preprint 62-WA-270. A.S.M.E.

55. Jackson. Battelle Mem. Inst. D.M.I.C. Memo 178, 1963.

56. Srawley & Beachem. Rep. 5460 U.S. Naval Res. Lab. 1960.

57. I.S.I. Pub. 120. 'Fracture Toughness of High Strength Materials'.

58. Paris & Johnson. Eng. Fract. Mech. v.1, 1968, p.3.

59. Walker. 'Fracture Toughness Theory and Practice'.
Symposium, Sheffield. 1968.

60. Boyle, Sullivan & Krafft. Weld. J. Res. Supp. v.41, 1962, p.428s.

61. Irwin. J. Appld. Mech. C4E, v.4, 1962, p.651.

62. Irani, May & Elliott. B.I.S.R.A. Report, MG/A/81/67.

63. Petch. J.I.S.I. v.174, 1953, p.25.

64. Stroh. Proc. Roy. Soc. A223 1954, p.404.

65. Smith & Barnby. Met. Sc. J. v.1, 1967, p.1.

66. Cottrell. Trans. A.I.M.E. v.212, 1958, p.192.

67. Zener. 'Fracturing of Metals'. A.S.M. 1958, p.3.

68. Hull. Phil. Mag. v.3, 1958, p.1468.

69. McMahon & Cohen. Acta. Met. v.13, 1965, p.591.

70. Barnby. Int. Conf. on Fracture. Haifa, 1969.

71. Wells. Brit. Weld. J. v.10, 1963, p.563.

72. Cottrell. I.S.I. Pub. 69, 1960, p.281.

73. Burdekin & Stone. J. Strain Analysis. v.1, 1966, p.145.

74. Hahn & Rosenfield. Acta. Met. v.13, 1965, p.293.

75. Knott. Metallurgia. March, 1968, p.93.

76. Beachem. Trans. A.S.M. v.56, 1963, p.318.

77. Crussard. J.I.S.I. v.183, 1956, p.146.

78. Ashby. Bolton Landing Conf. New York, 1966.

79. Gurland. J. Trans. A.I.M.E. v.227, 1963, p.1146.

80. McKlintock. J. Appld. Mech. 1965.

81. Gurland & Plateau. Trans. A.S.M. v.56, 1963, p.442.

82. Edelson & Baldwin. Ibid. v.55, 1962. p.230.

83. Palmer & Smith. Bolton Landing Conf. New York, 1966.

84. Puttick. Phil. Mag. v.4, 1959, p.964.

85. Beeuwkes. Proc. 3rd. Sagamore, Met. Res. Conf., 1956, p.89.

86. Krafft. Appld. Mat. Res. April, 1964, p.88.

87. Birkle, Wei & Pellisier. Trans. A.S.M. v.59, 1966, p.981.

88. A.S.T.M. S.T.P. 410.

89. B.I.S.R.A. Proposed Spec. for Fracture Toughness Testing of High Strength Materials. Report MG/EB/312/67.

90. B.I.S.R.A. Recommended Clip Gauge Design for Fracture Toughness Testing. Report MG/E/308/67.

91. Dieter. 'Mechanical Metallurgy'. McGraw Hill, 1961, p.284.

92. Guthrie & Jolley. B.C.I.R.A. Journal. September, 1967.

93. Tipper. Metallurgia. v.39, 1949, p.133.

94. Barnby. Acta. Met. v.15, 1967, p.903.

95. Irwin & Kies. Welding Res. J. Supp., v.33, 1954, p.193s.

96. Sullivan. Mat. Res. Stds. v.4, 1964, p.20.

97. Roberts. Ibid. v.9, 1969, p.27.

98. Srawley & Gross. Ibid. v.7, 1967, p.155.

99. Wessell. J. Eng. Frac. Mech. v.1, 1968, p.1.

100. Terry & Richards, Private communication.